Kinetic Heating and Transition Studies at Hypersonic Speeds

Marcantony Zanchetta
April 1996

A thesis submitted for the degree of
Doctor of Philosophy
of the
University of London
and for the
Diploma of Imperial College

Department of Aeronautics
Imperial College of Science, Technology and Medicine
London

Abstract

The thesis reports on an experimental and computational study of kinetic heating at hypersonic speeds. Of particular interest is the transition of the laminar boundary layer to a state of turbulent motion.

The experiments are performed in a Mach 9 Gun tunnel with a 5 ° semi-angle cone geometry. Twelve hemispherically blunted nose radii are tested at three unit Reynolds numbers. Testing has indicated that as the nose is progressively blunted, the transition region moves downstream. Further amounts of bluntness enhance other instability mechanisms and transition events are witnessed in the near nose regions. There are clearly two transitional regimes, denoted the "small bluntness" and "transition reversal" regime, respectively.

This study investigates the structure of the transitional boundary layer in both regimes using thin film heat transfer rate gauges and liquid crystal surface thermography. The heat transfer measurements indicate that the small bluntness transition regime is governed by the rapid formation, growth and merging of turbulent events. Transition occurs over hundreds of boundary layer lengths. The reversal regime transition process is characterised by the birth of turbulent events in the nose and near nose regions. The temporal formation rate of the events is governed by roughness. In a low roughness environment, transition occurs over many model lengths. Increasing the roughness level, increases the spot formation rate, and transition is witnessed immediately downstream of the spherical nose region.

The role of roughness is further explored using boundary layer trips. The trip causes a laminar wake which rapidly undergoes transition and forms a turbulent wedge. Event circumferential spreading angles are found for a variety of trip geometries and locations. The heat transfer distribution in the wedge is mapped using the thin film gauges.

Computational work is used to perform laminar flow field predictions. Of interest is the entropy layer caused by the presence of the bow shock, and its interaction with the boundary layer. Heat transfer predictions in the transitional region are also performed aided with the experimentally obtained intermittency information.

Contents

1 Introduction **26**

1.1 Motivations 26

1.2 The breakdown of the laminar boundary layer 29

1.2.1 Receptivity and the linear region 30

1.2.2 The non linear region 31

1.2.3 The transition region 32

1.3 Review 32

1.3.1 Microscopic work 34

1.3.2 Macroscopic studies 36

1.3.3 The present work 39

2 Experimental techniques and models **41**

2.1 Techniques 41

2.1.1 Schlieren 41

2.1.2 Liquid crystal surface thermography 42

2.1.3 Pressure measurement 45

2.1.4 Heat transfer rate measurement 47

2.1.5 Data recording and signal conditioning 51

2.2 Models 52

3 Facility **58**

3.1 Description 58

3.2 Operation 59

3.3 Calibration 60

3.3.1 Calibration aims 60

3.3.2 Calibration tools 63

3.3.3 Calibration Methods 66

3.3.4 Results: barrel stagnation and total pressure 67

3.3.5 Results: Pitot pressure measurements 70

3.3.6 Results: cone pressure measurements 78

3.3.7 Results: stagnation point heat transfer measurements 85

3.3.8 Comparison of nozzle exit plane conditions with previous work 90

3.3.9 Results: Mach number field 94

3.3.10 Results: static pressure field 104

3.3.11 Results: total pressure Field 105

3.3.12 Results: flow angularity 110

3.4 Concluding remarks 111

4 Numerical analysis **113**

4.1 The computational method 114

4.1.1 Convection diffusion splitting 116

4.1.2 Convective terms 116

4.1.3 Viscous Terms 118

4.1.4 Block marching and mesh adaptation 120

4.2 Computational prediction of the blunt body flow field 121

4.2.1 Mesh and initial conditions 122

4.2.2 Inviscid solution 124

4.2.3 Viscous solution 127

4.3 Concluding remarks 129

5 Heat transfer database **131**

5.1 Heat transfer rate database, low pressure operating condition 133

5.1.1 Sharp Cone 133

5.1.2 12.5mm $\rightarrow$ 25mm cones, Re_n=93,900 $\rightarrow$ 187,800 133

5.2 Heat transfer rate database, medium pressure operating condition . . 135

5.2.1 Sharp cone 136

5.2.2 2mm cone, $Re_n = 25,200$ 136

5.2.3 3mm cone, $Re_n = 37,900$ 136

5.2.4 6.25mm $\rightarrow$ 25mm cones, $Re_n = 76,900 \rightarrow 315,500$ 136

5.3 Heat transfer rate database, high pressure operating condition 139

5.3.1 Sharp cone 139

5.3.2 2mm cone, $Re_n = 85,400$ 139

5.3.3 3mm cone, $Re_n = 142,200$ 139

5.3.4 4 and 6.25mm cones, $Re_n = 189,600$ and $296,300$ 142

5.3.5 9 and 12.5mm cones, $Re_n = 426,600$ and $592,500$ 142

5.3.6 15 $\rightarrow$ 25mm cones, $Re_n = 711,000 \rightarrow 1,185,000$ 143

5.4 Transition behaviour 143

5.5 Concluding remarks 152

6 The structure of the small-bluntness transitional boundary layer 153

6.1 Time resolved heat transfer rates 154

6.2 Transition front axi-symmetry 155

6.3 Intermittency 157

6.3.1 Effect of gauge size 159

6.3.2 Comparison with the Universal distribution 162

6.4 Time averaged statistical properties 164

6.5 Heat transfer prediction in the transitional region 167

6.6 Concluding remarks 169

7 The structure of the reversal regime transitional boundary layer 170

7.1 Reversal regime, test case 1 170

7.1.1 Reversal Regime transition zone modelling 177

7.1.2 Cross correlations 179

7.1.3 Dynamics of the reversal regime transition event 186

7.2 Reversal regime, test case 2 195

7.3 Concluding remarks 196

8 Roughness experiments in the reversal regime **199**

8.1 Some properties of the laminar base flow 200

8.2 Uniformly distributed roughness 201

8.3 3D roughness studies 208

8.3.1 Triangular trip geometry 208

8.3.2 Sand grain roughness elements 223

8.4 2D annular trips 229

8.5 Concluding remarks 231

9 Conclusions **233**

9.1 Summary 233

9.2 Further work 236

10 References **237**

A Derivation of p_c/p_∞ **250**

List of Figures

1.1 Illustration of the factors influencing transition, these are divided into triggering parameters and parameters prescribing the boundary layer shape. 27

1.2 Schematic of the blunt body field field, showing the boundary layer and entropy layer. 27

1.3 Effect of nose blunting on transition location, data of Softley et al. (1969). Horizontal axis, nose Reynolds number, Re_n, defined as the product of the nose radius and the unit Reynolds number; Vertical axis, transition Reynolds number, given by the product of the distance to transition times the unit Reynolds number. 28

1.4 Illustration of the breakdown of the laminar boundary layer and the formation of the turbulent boundary layer. 30

1.5 The universal intermittency distribution, after Narasimha (1957), compared with measured intermittency information at incompressible and compressible speeds. Data of Owen (1970), Clark et al. (1992) and Mee and Goyne (1994). 33

1.6 Stetson and Rushton's transition data (1967) at Mach 5.5. The transition Reynolds number, Re_{tr}, is based on freestream conditions. The distance to entropy swallowing, x_{sw}, is calculated using Rotta's expression (1968). 37

1.7 Ericsson's prediction method compared to the data of Sell (1992) obtained with a 5 ° cone at Mach 9. 39

2.1 Illustration of schlieren set-up, showing position of spark source, concave mirrors, knife edge and camera location. 42

2.2 Liquid crystal surface thermography, static test. Model is heated from lower left by a hot air source 43

2.3 Schematic of experimental set-up for liquid crystal surface thermography. 44

2.4 Pressure instrumentation module. The module is inserted flush in to the model surface. Transducers are mounted into the module, either in the screw-in or push-in fittings. 45

2.5 Resistance - temperature curve of gauge 02. 49

2.6 Illustration of manufacturing steps for construction of thin film heat transfer rate gauges. 51

2.7 Illustration of instrumented model, depicted in the tunnel test section. Clearly visible is the model, sting support arrangement, nozzle and diffuser. A selection of the interchangeable hemispherical nose radii is placed on the tunnel floor. 52

2.8 Engineering drawing of model, showing instrumentation slot and the selection of hemispherical noses, all dimensions in mm. 53

2.9 Illustration of three models reserved for liquid crystal visualisation purposes, all dimensions in mm. 56

2.10 Illustration of ceramic nose piece, used to obtain heat transfer rate data. 57

3.1 Schematic of a typical gun tunnel set up. 59

3.2 Calibration of barrel piezo resistive pressure transducer. 60

3.3 Schematic of a free piston mode of operation. 61

3.4 Illustration of measured pressure distribution and predicted flow angularity at the nozzle exit plane at the high pressure operating condition, after Hillier, Kirk and Millevoi. 62

3.5 Pitot probe and cone design for calibration work. Also shown in these drawings are the "screw - in" type transducers. 63

3.6 Choice of models for measurement of pressure, (a) sharp -nose cylindrical probe and (b) the sharp cone. 64

3.7 Stagnation point heat transfer probe design for calibration work. The Macor substrate insert and the two thin film gauges can clearly be seen. 65

3.8 Barrel reservoir pressure distribution, low pressure operating conditions. 68

3.9 Barrel reservoir pressure distribution, medium pressure operating conditions. 69

3.10 Barrel reservoir pressure distribution, high pressure operating conditions. 69

3.11 Pitot pressure time history, low pressure operating conditions. Steady run time is 16 - 21 ms. 72

3.12 Pitot pressure time history, medium pressure operating conditions. Steady run time is 18 - 23 ms. 72

3.13 Pitot pressure time history, high pressure operating conditions. Steady run time is 16 - 20 ms. 73

3.14 Radial profiles of normalised Pitot pressure at the nozzle exit plane. 73

3.15 Radial profiles of normalised Pitot pressure at the nozzle exit plane. 74

3.16 Pitot pressure profiles normalised by barrel stagnation pressure, (x - axis), against radial distance (y - axis) for five different axial locations, where z=0mm is the nozzle exit plane, low pressure operating conditions. 75

3.17 Pitot pressure profiles normalised by barrel stagnation pressure, (x - axis), against radial distance (y - axis) for five different axial locations, where z=0mm is the nozzle exit plane, medium pressure operating conditions. 76

3.18 Pitot pressure profiles normalised by barrel stagnation pressure, (x - axis), against radial distance (y - axis) for five different axial locations, where z=0mm is the nozzle exit plane, high pressure operating conditions. 77

3.19 Normalised Pitot pressure radial profiles for low, medium and high operating conditions, data from all five axial stations are plotted on each graph. 79

3.20 Average Pitot pressure at each axial station for low, medium and high pressure operating conditions, only data from core region included in average. 80

3.21 Schematic of pressure measurement system for cone pressure. 81

3.22 Cone probe pressure profiles normalised by barrel stagnation pressure, (x - axis) for five different axial locations, where z=0mm is the nozzle exit plane, low pressure operating conditions. 82

3.23 Cone probe pressure profiles normalised by barrel stagnation pressure, (x - axis) for five different axial locations, where z=0mm is the nozzle exit plane, medium pressure operating conditions. 83

3.24 Cone pressure profiles normalised by barrel stagnation pressure, (x - axis) for five different axial locations, where z=0mm is the nozzle exit plane, high pressure operating conditions. 84

3.25 Normalised cone pressure radial profiles for low, medium and high pressure operating conditions, data from all five axial locations are plotted on each graph, z=0mm is nozzle exit plane. 86

3.26 Average cone pressure at each axial station for low, medium and high pressure operating conditions, only data from core region included in the local averaging. 87

3.27 Time resolved heat transfer rates for probe 3, tested at low pressure operating condition. 89

3.28 Schematic of the compression process used in the analysis of total temperature. 93

3.29 Mach number profiles at five different axial locations, where z=0mm is the nozzle exit plane, at the low pressure operating conditions. Captions: squares (p02p01) method 1; circles (pcp01) method 2 and triangles (p02pc) method 3. 95

3.30 Mach number profiles at five different axial locations, where z=0mm is the nozzle exit plane, at the medium pressure operating conditions. Captions: squares (p02p01) method 1; circles (pcp01) method 2 and triangles (p02pc) method 3. 96

3.31 Mach number profiles at five different axial locations, where z=0mm is the nozzle exit plane, at the high pressure operating conditions. Captions: squares (p02p01) method 1; circles (pcp01) method 2 and triangles (p02pc) method 3. 97

3.32 Average Mach number each axial station for low, medium and high pressure operating conditions, only data from core region included in average. Captions: squares (p02p01) method 1; circles (pcp01) method 2 and triangles (p02pc) method 3. 98

3.33 Static pressure profiles, (in Pa), at five different axial locations, where z=0mm is the nozzle exit plane, at the low pressure operating conditions. Captions: Box, pressure estimate after Soltani (435 Pa); o, pressure estimate after Mallinson (451 Pa); lines with squares, (p02p01) method (1); lines with circles, (pcp01) method (2) and lines with triangles, (p02pc) method (3). 100

3.34 Static pressure profiles, (in Pa), at five different axial locations, where z=0mm is the nozzle exit plane, at the medium pressure operating conditions. Captions: Box, pressure estimate after Soltani (788 Pa); lines with squares, (p02p01) method (1); lines with circles, (pcp01) method (2) and lines with triangles, (p02pc) method (3). 101

3.35 Static pressure profiles, (in Pa), at five different axial locations, where z=0mm is the nozzle exit plane, at the high pressure operating conditions. Captions: Box, pressure estimate after Soltani (2813 Pa); o, pressure estimate after Mallinson (2825 Pa); $\triangle$, pressure estimate after Kirk (2986 Pa); lines with squares (p02p01), method (1); lines with circles (pcp01), method (2) and lines with triangles (p02pc), method (3). 102

3.36 Average static pressure (in Pa), at each axial station for low, medium and high pressure operating conditions, only data from core region included in average. Captions: squares (p02p01) method 1; circles (pcp01) method 2 and triangles (p02pc) method 3. 103

3.37 Total pressure profiles, (in Pa), at five different axial locations, where z=0mm is the nozzle exit plane, at the low pressure operating conditions. Captions: lines with circles, total pressure inferred from barrel pressure; lines with squares, total pressure, method (3). 106

3.38 Total pressure profiles, (in Pa), at five different axial locations, where z=0mm is the nozzle exit plane, at the medium pressure operating conditions. Captions: lines with circles, total pressure inferred from barrel pressure; lines with squares, total pressure, method (3). 107

3.39 Total pressure profiles, (in Pa), at five different axial locations, where z=0mm is the nozzle exit plane, at the high pressure operating conditions. Captions: lines with circles, total pressure inferred from barrel pressure; lines with squares, total pressure, method (3). 108

3.40 Average total pressure (in Pa), at each axial station for low, medium and high pressure operating conditions, only data from core region included in average. Captions: circles, total pressure inferred from barrel pressure; squares, total pressure, method 3. 109

3.41 Schematic of data mesh to be used to determine flow angularity, using centreline information. 110

3.42 Schematic of data mesh to be used to determine flow angularity, using model information. 111

4.1 Viscosity variation with temperature using the algebraic formulation of Sutherland, Keyes and the tabulated values of Hilsenrath. 115

4.2 Schematic of 1D problem, the discrete solution updates the cell properties **U** by calculating the fluxes **E** at both cell interfaces. 117

4.3 Reconstruction strategies, (a) piecewise constant, (b) piecewise linear. 118

4.4 Block marching strategy. Initial block (a) includes the subsonic nose region and the near nose supersonic region. Once solution is converged, the whole block is shifted downstream of the subsonic region (b), and the computation is continued. 121

4.5 Mesh details; top, near nose; and bottom, complete mesh, stretched vertically by a factor of three. Nose radius 1mm, mesh stand-off distance 0.2mm, body length=0.75m, There are 191 cells in the body direction and 101 in the body normal direction. 123

4.6 Mach number contours inviscid computation, contour intervals 1, levels 1, 2, 3 etc. 124

4.7 Schlieren image of flow around blunt cone, horizontal cut-off. The test conditions are $Re_{\infty/m}$ =47.4 $\times 10^6$, r_n=25mm. 125

4.8 Surface pressure along hemispherical portion of nose, left; and surface pressure over entire geometry, right; inviscid computations. 126

4.9 Shock angle against normalised distance along shock; inviscid computations. 126

4.10 Entropy profiles at two locations; left, upstream of point of minimum pressure, right downstream of point of minimum pressure. Vertical scale normalised by nose radius, computations performed at 9.16. . . 127

4.11 Mach number and Reynolds number at the boundary layer edge against distance. Computation performed at Mach 9.16, $Re_{\infty/m}$ = 54.06 $\times 10^6$, r_n=1mm. 128

4.12 Vorticity profiles based on normalised velocity for the blunt cone, at two different streamwise locations. Computation performed at Mach 9.16, $Re_{\infty/m}$ = 54.06 $\times 10^6$, r_n=1mm. 129

5.1 Time averaged heat transfer rates for the sharp, 12.5mm, 15mm, 18mm, 21mm and 23mm cases, tested at the low pressure operating condition. 134

5.2 Time averaged heat transfer rates for the 25mm case, tested at the low pressure operating condition. 135

5.3 Time averaged heat transfer rates for the sharp, 2mm, 3mm and 6.25mm cases, tested at the medium pressure operating condition. 137

5.4 Time averaged heat transfer rates for the 12.5mm 15mm, 18mm, 21mm, 23mm and 25mm cases, tested at the medium pressure operating condition. 138

5.5 Time averaged heat transfer rates for the sharp, 2mm, 3mm, 4mm 6.25mm and 9mm cases, tested at the high pressure operating condition.140

5.6 Time averaged heat transfer rates for the 12.5mm, 15mm, 18mm, 21mm, 23mm and 25mm cases, tested at the high pressure operating condition. 141

5.7 Schematic of boundary breakdown to turbulence and behaviour of some macroscopic quantity measured on the model surface. 143

5.8 Distribution of the heat transfer rate in the laminar, transitional and turbulent regions, (a) (b) and (c); and the corresponding change in signal intermittency (d), RMS (e) and skewness (f). 144

5.9 Determination of transition onset by extrapolation, transition onset is fixed at s=0.14m. Captions: squares, experimental data obtained at the high pressure operating conditions; dots, CFD laminar prediction; continuous line, curve fit used to obtain transition onset. 146

5.10 Determination of second transition length, x_{tr2}, The second transition onset length is given by the intersection of curve fit 1 and curve fit 2, and is 0.58m. Captions: squares, experimental data obtained at the high pressure operating conditions; dots, CFD laminar prediction; continuous line, curve fit to initial transitional region; dashed line, curve fit to second transitional region. 148

5.11 Transition Reynolds number against nose Reynolds number. 150

5.12 Transition behaviour against nose Reynolds number, data from present study is compared to the studies of Stetson and Rushton (1967), Softley (1969) and Sell (1992). 151

5.13 Intermittency map showing contours of constant γ obtained from the heat transfer database; x-axis, nose Reynolds number (10^{-3}) ; y-axis, wetted Reynolds number (10^{-6}). 152

6.1 Time resolved heat transfer traces for selected gauges tested with the 2mm nose radius tested at the medium pressure operating conditions. 154

6.2 Time resolved heat transfer traces for gauge 24 showing turbulent spikes, 2mm nose radius tested at the medium pressure operating conditions. 156

6.3 Shot 2612, surface heating patterns; 1mm nose radius high pressure operating conditions. 156

6.4 Time resolved heat transfer rate and intermittency at gauge 24, for the 2mm case, tested at the medium pressure operating condition. 158

6.5 Intermittency distribution with five different intermittency levels. . . 159

6.6 Time resolved heat transfer traces for gauges 30 and 32, showing the effect of gauge length in the transition region, 2mm nose radius tested at the medium pressure operating conditions. 161

6.7 PDF and intermittency distribution for the 2mm nose radius tested at the medium pressure operating conditions. 162

6.8 F function and the universal intermittency distribution for the 2mm nose radius tested at the medium pressure operating conditions. . . . 163

6.9 Statistical moments for the 2mm case, tested at the medium pressure operating condition. 164

6.10 Heat transfer prediction in the transitional region using two methods for the 2mm nose radius case tested at the medium pressure operating conditions. 168

7.1 Time resolved heat transfer rates for five selected gauges, for the 3mm case tested at the high condition. 171

7.2 Expanded view of the time resolved heat transfer rates for five selected gauges, for the 3mm case tested at the high condition. 172

7.3 Time resolved heat transfer rates for three selected gauges, for the 3mm case tested at the high condition, data obtained with ceramic nose piece.173

7.4 Schematic illustration of transition mechanisms. 174

7.5 Turbulent event passage frequency for the 3mm geometry tested at the high pressure operating conditions. 175

7.6 PDF and Intermittency for the 3mm case, tested at the high pressure operating condition. 175

7.7 Statistical moments for the 3mm case, tested at the high condition. . 176

7.8 Measured and predicted intermittency distribution, left; CFD predicted heat transfer; right. 3mm nose radius, high pressure operating conditions. 178

7.9 Time lag correlations functions for gauge 02, 3mm nose tested at the high condition, top figure, correlations with all sixty-five gauges; bottom figure, expanded view of selected gauges. 180

7.10 Time lag correlations functions for gauge 24, 3mm nose tested at the high condition, top figure, correlations with all sixty-five gauges; bottom figure, expanded view of selected gauges. 182

7.11 Time lag correlations functions for gauge 34, 3mm nose tested at the high condition, top figure, correlations with all sixty-five gauges; bottom figure, expanded view of selected gauges. 183

7.12 Time lag correlations functions for gauge 45, 3mm nose tested at the high condition, top figure, correlations with all sixty-five gauges; bottom figure, expanded view of selected gauges. 184

7.13 Time lag correlations functions for gauge 65, 3mm nose tested at the high condition, top figure, correlations with all sixty-five gauges; bottom figure, expanded view of selected gauges. 185

7.14 Trajectories for the ten transition events. 188

7.15 Modulus of the cross spectral density function for four cases. The CSD is computed between gauge 02 and gauge 02, between gauge 08 and gauge 02, between gauge 16 and gauge 08, and between gauge 24 and gauge 16. 3mm nose tested at the high condition. 191

7.16 Curve fit to phase of the cross spectral density functions for four cases. The CSD is computed between gauge 02 and gauge 02, between gauge 08 and gauge 02, between gauge 16 and gauge 08, and between gauge 24 and gauge 16. Test case is 3mm nose at high condition. 192

7.17 Quasi one dimensional illustration of the reversal regime transition event. 194

7.18 Artificially generated turbulent spot of Schubauer and Klebanoff (1956), note vertical scale. 194

7.19 Time resolved heat transfer rates, two test cases both obtained with the 9mm nose tested at the high pressure operating conditions. 197

8.1 Shot 1697, liquid crystal visualisation. r_n=25mm, Re_n=1185,000. . . 199

8.2 Boundary layer thickness, displacement thickness (a) and Mach number and Reynolds number against wetted distance (b). 202

8.3 Shot 2576, liquid crystal visualisation. r_n=25mm, Re_n=1185,000, matte finish. 203

8.4 Four liquid crystal visualisations, from shots 2617, 2618, 2619, 2620. r_n=25mm, Re_n=1185,000. 205

8.5 Shot 2647, liquid crystal visualisation. r_n=25mm, Re_n=1185,000. . . 206

8.6 Shot 2659, liquid crystal visualisation. r_n=25mm, Re_n=1185,000. . . 207

8.7 Shot 2627, liquid crystal visualisation. r_n=25mm, Re_n=1185,000. . . 209

8.8 Schematic interpretation of heating patterns downstream of trip in run 2627. 209

8.9 Physical interpretation of the flow field in the proximity of the trip elements in run 2627. 210

8.10 Further interpretation of the flow field behind the trip of shot 2627. . 210

8.11 Vortex structure and transition to turbulence of streak-like structures witnessed in shot 2627. 211

8.12 Trip movement relative to array of sensors 212

8.13 Time resolved heat transfer rates for six different triangular trip studies; test cases, from top to bottom are: no trip, 19mm circumferential separation, 15, 13, 7 and 0mm. Basic test geometry is 25mm nose radius tested at the high pressure operating condition. 213

8.14 Time averaged heat transfer rates and intermittency distributions for different locations of the triangular trip, with the 25mm nose radius tested at the high pressure operating condition. 214

8.15 Time averaged heat transfer rates, in W/cm^2 and intermittency map with the triangular trip, with the 25mm nose radius tested at the high pressure operating condition. The distance on the x-axis is measured form the stagnation point. 216

8.16 Shot 2629, liquid crystal visualisation. r_n=25mm, Re_n=1185,000. . . 216

8.17 Heating patterns around the trip with protruding tip 217

8.18 Flow field around trip with protruding tip 218

8.19 The effect of trip location, liquid crystal visualisations from runs 2635, 2636, 2637 and 2638; r_n=25mm, Re_n=1185,000. 219

8.20 The effect of trip location, liquid crystal visualisations from runs 2640, 2641 and 2642; r_n=25mm, Re_n=1185,000. 220

8.21 Transition behaviour for a 0.13mm high trip, on the 25mm cone, tested at the high pressure operating conditions. 223

8.22 Liquid crystal surface temperature visualisation from run 2644. Four sand grain roughness elements are located on the sphere-cone junction; r_n=25mm, Re_n=1185,000. 224

8.23 Time resolved heat transfer rates for five different sand grain trip studies, with the 25mm nose radius tested at the high pressure operating condition. 225

8.24 Time averaged heat transfer rates and intermittency distributions for different locations of the spherical trip, with the 25mm nose radius tested at the high pressure operating condition. 227

8.25 Time averaged heat transfer rates and intermittency map with the grain of a sand trip, with the 25mm nose radius tested at the high pressure operating condition. 228

8.26 Time resolved heat transfer rates for 2D "band" trips with the 25mm nose radius tested at the high pressure operating condition. 230

8.27 Time averaged heat transfer rates and intermittency distributions for different locations of the 2D triangular trip, with the 25mm nose radius tested at the high pressure operating condition. 231

A.1 Wall pressure against Reynolds number based on wetted distance for four viscous computations. 252

A.2 Ratio of viscous wall pressure to inviscid wall pressure against viscous interaction parameter for four computations. 252

Acknowledgements

This project was funded by the Defence Research Agency, under the DRA agreement 2037/399/MA. The comments and contributions of Dr. T. Cain, Dr. M. Collyer, Dr. M. Gilmore, Dr. P. Street and Dr. I. Wrisdale are warmly acknowledged.

The continued guidance, support and encouragement of Prof. R. Hillier, is gratefully and sincerely acknowledged, together with the careful assistance of Mr. R. Hutchins and Mr. S Johnson. The author has also had the fortune to collaborate with many accomplished scientists, in particular Dr. S. Soltani, who contributed extensively in developing many of the ideas presented in this study.

The assistance of Mrs. S. Clark, the librarian, and Mrs. R. Fairhurst, Ms. S. Payton and Ms. T. Hill, is acknowledged. The author also wishes to thank the departmental staff who have contributed to this project, amongst the many, Mr. R. Carter, Mr. J. Coles and Mr I. James.

The Hypersonic group has been enriched by the presence of many cherished colleagues, who the author wishes to thank for their friendship and advice. In order of appearance, they are: Dr. P. Asproulis, Dr. A. Pishevar-Esfahani, Dr. D. Smith, Mr. N. Ng, Dr. S. Mallinson and Mr. M. West.

Finally, a big thank you to the people of Aeronautics, especially those who have been fielded in the sensational and spectacular "Spartak Aero", a team yet to be rivalled.

to Mum & Dad
and Kal

Nomenclature

a	pressure tapping area	A	constant in turbulence model
a^+	constant	A	thin film sensor area
c	specific heat	C	Chapman - Rubesin parameter
c_p	specific heat, constant pressure	C_{cp}	constant in turbulence model
c_v	specific heat, constant volume	C_{kleb}	constant in turbulence model
c	speed of sound	C_{wk}	constant in turbulence model
d	probe diameter	F	intermittency function
dS	entropy rise	F_{kleb}	function in turbulence model
e	internal energy	F_{max}	function in turbulence model
i	imaginary number	F_{wake}	wake function in turbulence model
k	constant	H	enthalpy
k	thermal conductivity	L	operator to update CFD solution
l	pressure tapping length	M	Mach number
l	Prandtl Van Driest mixing length	Pr	Prandtl number
p	pressure	Q	threshold
q	heat transfer rate	R	gas constant
r	axis	R	normalised correlation function
r	radius	Re	Reynolds number
r	correlation function	S	entropy
s	wetted distance from model apex	St	Stanton number
t	elapsed time	T	temperature
u	velocity, x or z direction	V	voltage
v	velocity, y or r direction	Y	distance in turbulence model
v	pressure tapping volume	X	distance
x	axis	**E**	vector composed of flow variables
y	axis	**F**	vector composed of flow variables
y^+	normalised boundary layer height	**G**	vector composed of flow variables
z	axis (axial distance in tunnel)	**U**	vector composed of flow variables

Symbols

α	spatial growth rate, x direction
α_r	thin film sensor sensitivity
β	spatial growth rate, z direction
δ	boundary layer height
δ	thin film sensor thickness
η	mesh direction normal to body
γ	intermittency
λ	length scale for transition region
λ	bulk viscosity coefficient
ω	temporal growth rate
ω	vorticity
Ω	vorticity calculated with normalised velocity
μ	viscosity
μ	Mach angle
ν	Prandtl Meyer function
ρ	density
σ	area dependence parameter
σ	standard deviation
τ	dummy time variable
τ	shear stress
θ	angular distance around nose
θ	direction in cylindrical coordinate system
θ	flow inclination
θ	phase angle
θ	shock slope
ξ	normalised length through transition region
ξ	mesh direction aligned with body

Subscripts

0	stagnation conditions
1	initial barrel conditions
2	post-shock conditions
4	initial driver conditions
5	post reflected shock conditions
∞	freestream conditions
b	bridge
barrel	barrel conditions
a	adiabatic
b	reversal regime
c	cone
d	diffusion properties
e	edge conditions
inner	inner region in turbulence model
inv	inviscid conditions
h	Helmholtz type resonance
le	leading edge
n	nose
n	event formation rate
outer	outer region in turbulence model
p	platinum properties
p	organ pipe resonance
pen	penetration
r	reservoir conditions
res	reservoir conditions
s	wetted distance
s	small bluntness regime
shock	distance from shock to body along stagnation streamline
t	turbulent conditions
tb	reversal regime transition onset
te	trailing edge
tr	transition onset
tr1	transition onset of first transitional mechanism
tr2	transition onset of second transitional mechanism
tb	small bluntness regime transition onset
tu	transition completion
w	wall
H	hyperbolic terms
V	diffusive terms

Superscripts

—	time average
N	time level

Acronyms

CSD	cross spectral density
PDF	probability density function
PSD	power spectral density
RMS	root mean square

Chapter 1

Introduction

1.1 Motivations

The hypersonic transition problem is of acute practical importance and great scientific interest. Practically, the ability to predict the transition behaviour of complex hypersonic configurations at a variety of flight conditions is an arduous task, requiring ad hoc studies to be performed. Generally, there will be many factors influencing the transition location. These include: Mach number, Reynolds number, wall temperature, angle of attack, pressure gradients, shock impingement, nose blunting, roughness, free-stream turbulence and so on. Transition can be viewed as the triggering of a receptive boundary layer capable of sustaining turbulence. Any parametric study connected with transition must aim to investigate the effects of the triggering parameters and the role of the parameters prescribing the boundary layer "susceptibility" to turbulence. These parameters are illustrated in figure 1.1. The triggering parameters form the disturbance environment. They include convected turbulence, radiated acoustic waves, model vibration and surface roughness. Generally, the disturbance environment is difficult to control as it will depend on the test conditions and may vary from site to site, and between tunnel testing and free flight. The sole exception is surface roughness which can be controlled but not eliminated, by suitable manufacturing processes. The parameters prescribing the boundary layer shape will be constant from tunnel to tunnel and are those to be expected in free flight, as the boundary evolution is controlled by flight conditions, $Re_{\infty/m}$, M_∞ , T_∞ and body geometry. The objective of the present study is to isolate some of the phe-

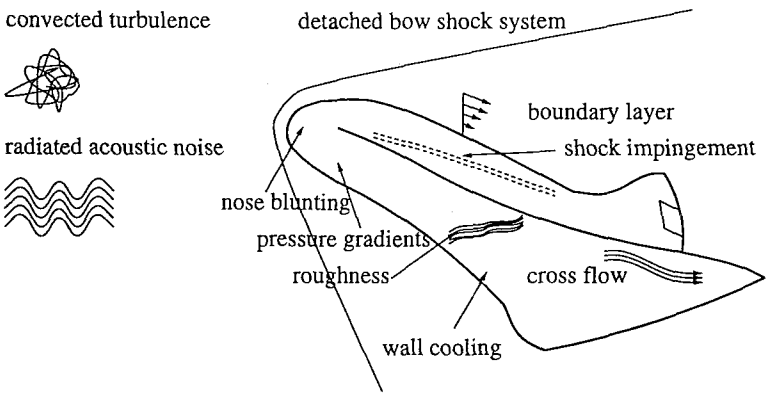


Figure 1.1: Illustration of the factors influencing transition, these are divided into triggering parameters and parameters prescribing the boundary layer shape.

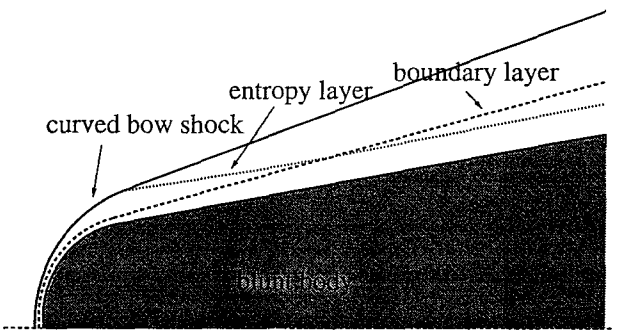


Figure 1.2: Schematic of the blunt body field field, showing the boundary layer and entropy layer.

nomena occurring in flight and examine their influence in a more rigorous fashion. The parameters analysed are nose blunting and surface roughness. At a fundamental level, nose blunting creates an entropy layer, vortical in nature, produced by the curved shock formed in front of the body, as illustrated in figure 1.2. The entropy layer surrounds the boundary layer for many nose radii downstream, until through growth, the boundary layer "swallows" the entropy layer, and sharp cone conditions are asymptotically approached. The presence of the entropy layer, and its interaction with the boundary layer, significantly alters the transition characteristics, as shown in figure 1.3.

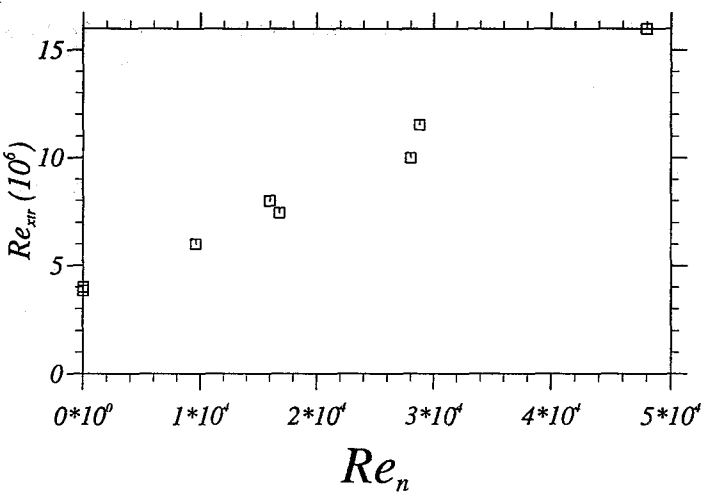


Figure 1.3: Effect of nose blunting on transition location, data of Softley et al. (1969). Horizontal axis, nose Reynolds number, Re_n, defined as the product of the nose radius and the unit Reynolds number; Vertical axis, transition Reynolds number, given by the product of the distance to transition times the unit Reynolds number.

Surface roughness is investigated and it is examined how, via the modification of the laminar "base - flow", the transition characteristics are altered.

The studies are performed experimentally, aided with the use of computational flow field predictions of the laminar flow field. In this chapter, firstly the breakdown to turbulent motion within the boundary layer will be described, before a review of the current state of transition knowledge is given. Having placed thus the current study in a more general context of transition research, the following chapters will then discuss the experimental facility, models and methods used, together with the numerical Navier - Stokes solver. The experimental results obtained will then be presented and the ideas arising will be discussed linking the contribution of the present study to general understanding of hypersonic transition.

1.2 The breakdown of the laminar boundary layer

The main events that can occur in the breakdown of the laminar boundary layer and the onset of turbulent flow are illustrated in the sketch of figure 1.4. One can recognise a linear region, in which instabilities enter the boundary layer. The key concepts arising are **receptivity** and **linear stability**. When these instabilities exceed a certain amplitude, the boundary layer is characterised by a region of non - linear breakdown, randomisation and formation of turbulent events. The key concepts are **non linear interactions, three dimensionalisation** and **event formation.** The region downstream of this location, is the transitional zone, which is governed by the intermittent production of turbulent events at Re_{tr}. In this region, the events grow and merge, both spatially and temporally, eventually forming a continuous region of turbulence at some location downstream, named the transition completion location, Re_{tu}. The key concepts to be examined here are **intermittency** and **event dynamics.**

This study is mainly cornered with the dynamics of the turbulent events, formed at Re_{tr}, however before examining the intermittent character of this region, the processes occurring upstream will be examined.

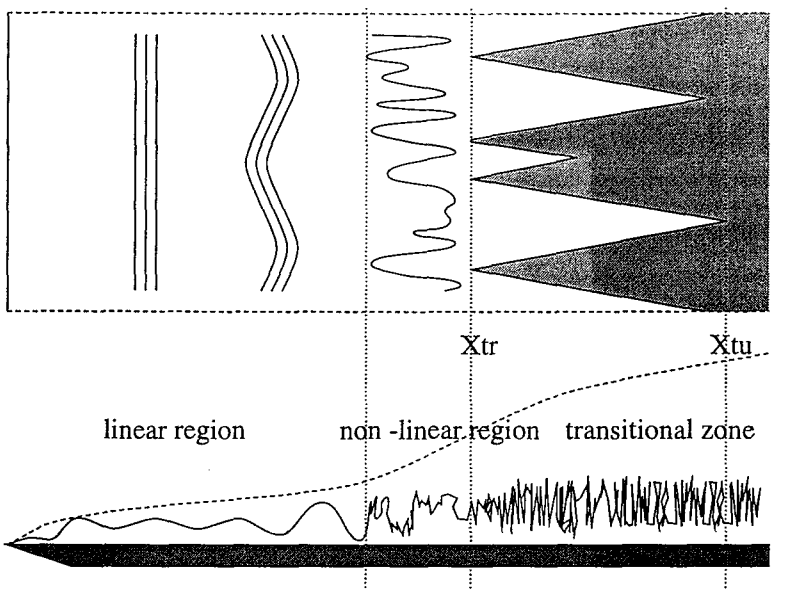


Figure 1.4: Illustration of the breakdown of the laminar boundary layer and the formation of the turbulent boundary layer.

1.2.1 Receptivity and the linear region

The laminar boundary layer can act as a linear oscillator, allowing sinusoidal disturbances to exist, superimposed upon the underlying mean flow. Receptivity is the name given to the process by which an external disturbance can enter the boundary layer, and generate these instability waves. The external disturbance environment, forcing the boundary layer, is typically composed of acoustic, vortical, entropy and vibrational fluctuations. Receptivity was first addressed by Morkovin (1969) and is discussed in detail by Reshotko (1976).

Linear stability theory attempts to address the physics of this region and describe the propagation and evolution in time and space of these small amplitude waves within the boundary layer. Typically, the boundary layer is stable if the waves are damped and is said to be unstable if the waves are amplified. The critical parameter is the growth rate of the disturbances. Waves of zero growth rate are said to be neutrally stable. In the analysis, any quantity, q say, is allowed to vary as:

$$q' = q(y) \exp\left[i(\alpha x + \beta y - \omega t)\right] \tag{1.1}$$

where x, y and z are an orthogonal coordinate system with x aligned in the direction of mean flow, and y is the direction normal to the surface; q(y) is the solution of q to the mean flow problem; α and β are the x and z components of the wave number k, and ω is a frequency. α, β and ω are complex and their imaginary parts represent the spatial and temporal amplification rates. The above expression is substituted in to the equation of motions. It is assumed that fluctuating quantities are very small, so that the quadratic terms of the disturbances can be neglected, and also that the mean flow solution does not vary significantly and the flow remains parallel. This leads to a set of ordinary differential equations, which are denoted the linear stability equations. There exists a hierarchy of linear stability equations. At one end, there is the Rayleigh equation, obtained by linearising the incompressible, Euler equations. This is a second order differential equation. At the other end of the scale, there are the fully two dimensional solutions to the compressible Navier stokes equations, which leads to a system of eighth order. Results from linear stability theory have contributed significantly to the understanding of pre-transitional behaviour, allowing the role of pressure gradients, surface cooling, etc. to be explored and also transition prediction methods to be developed (Van Ingen 1956).

By pass transition

It is known that if the external disturbance level is above some critical value, non - linear processes within the boundary layer occur immediately and transition to turbulence is witnessed within a short distance downstream. This process, mostly encountered in turbo-machinery, is denoted "by - pass" transition.

1.2.2 The non linear region

In this region, three dimensionality becomes important, as spanwise modulation of the mean flow occurs. Two breakdown regimes are recognised in which vortical structures develop and in turn, lead to smaller structures, and finally turbulent events. These are denoted the **K type** and **N type** regimes, after Klebanoff (1959), the worker who first observed the **K type** process, and after Novosibirsk, where the **N type** regime of breakdown was first witnessed. An excellent review of these processes can be found

in Kachanov (1994).

1.2.3 The transition region

In the transition regime, the departure from laminar behaviour becomes apparent at macroscopic scales, for instance a change in the boundary layer growth rate is first observable. Intermittency, γ, is the measure of the probability that the boundary layer motion be turbulent at any given point in this region, and must vary between 0, at the event inception point Re_{tr} and 1, at Re_{tu}. The first formulation of the intermittency distribution was provided by Emmons (1951). Successive work by Dhawan and Narasimha [Dhawan and Narasimha (1956), Narasimha (1957)], based on the hypothesis that breakdown occurs within a narrow chordwise region, lead to the familiar form for intermittency cited below:

$$\gamma(x) = 1 - \exp \frac{(x - x_{tr})^2 n\sigma}{u} \tag{1.2}$$

where x_{tr} is the location of laminar breakdown, the event inception point; n, is the event formation rate (number of events per second); and σ is the area dependence factor otherwise known as Emmons propagation parameter; and u is the velocity. Narasimha (1957), using the ideas of concentrated breakdown, expressed γ as a function of ξ, where

$$\xi = \frac{x - x_{tr}}{x(\gamma = 0.75) - x(\gamma = 0.25)} \tag{1.3}$$

and suggested the universal form of the intermittency distribution, written as:

$$\gamma(x) = 1 - \exp -0.412\xi^2 \tag{1.4}$$

The intermittency distribution of Narasimha can be seen plotted against some experimental data, at incompressible and compressible speeds in figure 1.5.

1.3 Review

In this section, a brief review of literature is given. It is divided into two parts, micro- and macroscopic studies. The microscopic work will be presented first.

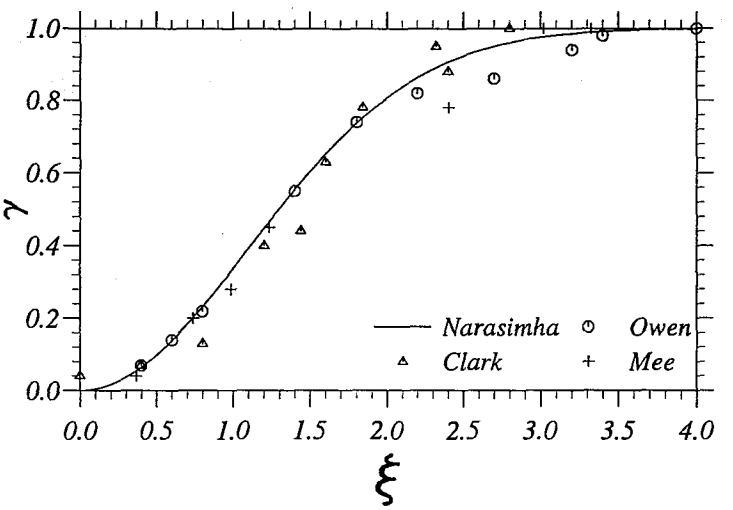


Figure 1.5: The universal intermittency distribution, after Narasimha (1957), compared with measured intermittency information at incompressible and compressible speeds. Data of Owen (1970), Clark et al. (1992) and Mee and Goyne (1994).

1.3.1 Microscopic work

Most microscopic approaches have investigated the linear stability of the laminar boundary layer, however with the increase in computational power, direct numerical simulations are performed allowing the physics of laminar breakdown to "drop - out".

Schubauer and Skramstad (1948) first proved experimentally the existence of linear small disturbances, conjectured by Tollmien and Schlichting. The first attempts at developing the compressible stability analysis was performed by Kuchemann (1938), followed by Lees and Lin (1948), who using an asymptotic extension to the inviscid equations, postulated that the presence of a generalised inflection point would be a sufficient condition for instability. However, the limits imposed by the asymptotic technique did not allow the contrasting differences between low speed and high speed flow to be uncovered. The first successful formulation and solution of the compressible stability equations was performed by Mack (1964). The most important observation is that at high Mach numbers, the mathematical nature of the stability equations changes, and the problem admits an infinite number of solutions. These other solutions are often referred to as the higher modes or Mack modes.

At high Mach numbers, the higher modes present large growth rates, in particular the second mode, which is seen to be the most important boundary layer destabilisation mechanism. Kendall (1975) presented the first microscopic experiments examining the relationship of the acoustic disturbance field and boundary layer stability behaviour. Kendall reports that for Mach numbers in the range of 3 to 5.6, there is strong evidence to suggest that the boundary layer is driven by the acoustic field. Kendall also notes the appearance of the second mode as the dominant instability mechanism and its role in creating "rope like" structures observable with shadowgraphs within the boundary layer.

A detailed five part study by Stetson, Thompson, Donaldson and Siler (1983, 1984, 1985, 1986 and 1989) investigated the linear stability behaviour of a 7 ° semi - angle cone at Mach = 8. The first part of their study concentrated on obtaining data for the sharp nose case. In agreement with Mack, the principle instability was a second mode disturbance. The wavelength of this disturbance was 2δ. The second study concentrated on the effect of bluntness. The findings indicated that significant

changes to the stability characteristics occur with the introduction of bluntness. The location of the critical Reynolds number, i.e. the first point at which instabilities can grow, was found to coincide with the location of entropy swallowing. In contrast to the sharp cone case, the blunt cone critical Reynolds number location occurred at a greater distances downstream, but the growth rates of the disturbances were considerably larger.

In the paper of Stetson et al. (1988), the authors address the problem of transition testing and transition prediction, commenting on the requirements for boundary layer stability experiments to better understand the relationship between the disturbance environment and transition characteristics. The high levels of background noise encountered in hypersonic wind tunnel testing has lead to the development of quiet flow tunnels. [Schneider et al. (1995), Chen et al. 1993)]. By delaying transition of the nozzle wall boundary layer, the acoustic disturbance environment is significantly reduced, however the levels encountered are still above those of hypersonic flight. Experiments performed (Stetson 1990) at hypersonic speeds have indicated that the growth rates of the second mode disturbances exceed the linear stability predictions and that possibly, non linear effects were present. This discrepancy has been linked to the effects of tunnel environment. Using the low disturbance Mach 3.5 wind-tunnel, transition Reynolds numbers are obtained an order of magnitude greater than those obtained in an ordinary wind-tunnel. Transition predictions based on linear stability theory were in excellent agreement with the measured data. The work of Wendt et al. (1993), and Stuckert and Reed (1992) have investigated the stability of the hypersonically travelling sharp cone. Herbert and Esfahanian (1992) have extended this analysis to blunted cones, and Heffner and Arnal (1994) have demonstrated the stabilising effect of slight to moderate bluntness. This result was in good agreement with parallel experiments performed in a Mach 7 blow-down tunnel.

The direct numerical simulation of Adams and Kleiser (1993) investigated the breakdown of a pair of oblique first mode waves, observing the non linear interactions which generated shear layers, which in turn roll up to form "rope like" structures. Doorly and Smith (1993) have studied the development of spots in the transition region and determined the dependence of the wake half angle on Mach number for the zero pressure gradient case. For high Mach numbers, the wave angle is given by:

$$\theta = 3^{-3/2} 2^{1/2} M^{-1} \tag{1.5}$$

1.3.2 Macroscopic studies

The main investigations into the macroscopic transitional processes have been performed experimentally. The first high speed experiments began after the second world war and initially concentrated on the change of macroscopic parameters through the transitional region, such as the increase in heat transfer rate. Brinich and Sands (1957), tested a variety of blunt cone and blunt plate configurations at Mach 3.1. They noted a downstream movement of transition with increasing bluntness for spherical noses. They also tested a variety of flat nosed bodies and witnessed a reversal in the transition delay above some critical bluntness. Stetson (1960), examined the transition characteristics of blunted bodies and noted that transition could occur in the subsonic region of flow in the hemispherical part of the nose for highly cooled boundary layers. Stetson also provided evidence of roughness in this region. Transition delay, trend reversal and re-reversal was discussed by Richards and Stollery (1966) in the context of decreasing the wall to recovery temperature ratio. Potter and Whitfield (1960) examined the effects of $Re_{\infty/m}$, nose bluntness and surface roughness at Mach numbers in the range of 3 to 8. An important observation was the similarity in the transition processes at sub- super- and hypersonic speeds. Using hot wire probes, they found an intense layer of fluctuations inside the boundary layer, and observed how this layer moved towards the boundary layer edge with increasing Mach number. A result which shows qualitative agreement with the linear stability analysis. The roughness studies at high Mach numbers indicated that large trip elements were required to successfully trip the boundary layer. Nagamatsu et al. (1967) investigated the transition behaviour of a 2 metre 5 ° semi - angle cone. The effects of M_∞ and roughness were also examined. In their study, turbulent bursts were detected using surface mounted thin film gauges, and it was concluded that they were convecting at 80 % to 90% of the edge velocity. They also noted that the greatest fluctuations were occurring in the laminar boundary layer at y/δ=0.8. Using hot film anemometry, Maddalon and Henderson (1968) also found a layer of maximum disturbance level in the outer regions of the boundary layer, with the speed of the disturbances being subsonic relative to the edge velocities. The authors proposed also that the origin of the turbulent bursts would be in this region, basing their arguments on the hot film measurements and schlieren visualisations.

Stetson and Rushton (1967) performed a comprehensive study of the transition be-

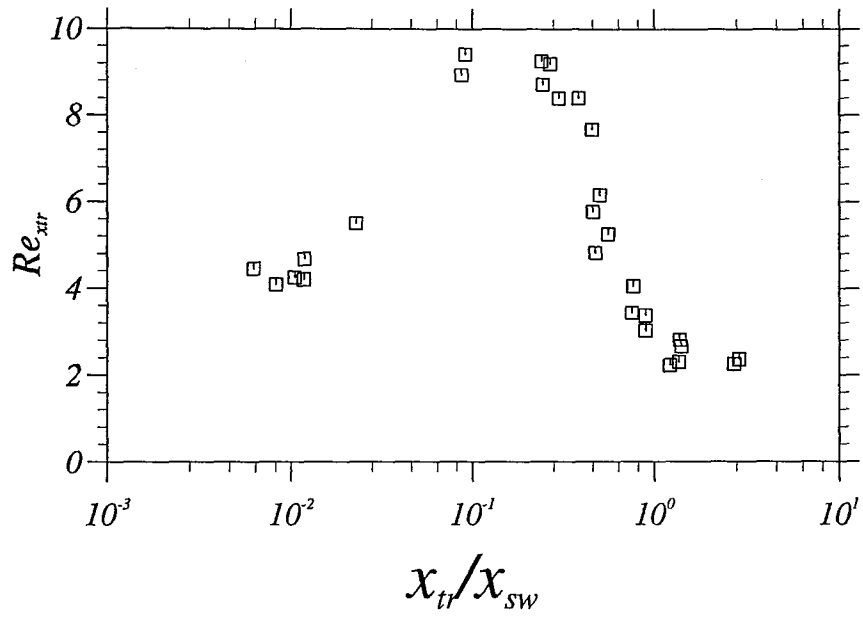


Figure 1.6: Stetson and Rushton's transition data (1967) at Mach 5.5. The transition Reynolds number, Re_{tr}, is based on freestream conditions. The distance to entropy swallowing, x_{sw}, is calculated using Rotta's expression (1968).

haviour on a 8 ° semi - angle cone at Mach 5.5. Their results suggested a rearward movement of the transition location for small amounts of bluntness. Greater blunting was found to cause the rearward movement of the transition point to cease, and with greater bluntness still, caused the transition location to move upstream, i.e. a transition "reversal". The distance to transition, x_{tr}, was correlated with the entropy swallowing distance, x_{sw}, as shown in figure 1.6. Three transition regimes were found. The first for $x_{tr}/x_{sw} > 0.4$, in which the transition Reynolds number, based on local edge conditions, remains equal to the sharp cone value. The second region, for $x_{tr}/x_{sw} < 0.02$, in which the transition Reynolds number, based on local edge conditions, is equal to some "blunt limit". The third intermediate region, for $0.02 < x_{tr}/x_{sw} < 0.4$, exhibits a monotonic decrease in the local edge condition transition Reynolds number, from the sharp value to the blunt limit. If the distance to transition Reynolds number based on freestream conditions is plotted, (as in figure 1.6), this is seen to be the region in which the maximum delay is found, occurring roughly

at $x_{tr}/x_{sw} = 0.2$. Martellucci et al. (1972) also reported a delay in transition with increasing blunting. Using schlieren, Fischer (1972), found turbulent structures present in the outer regions of the boundary layer at a streamwise station well upstream of the transition location detected by surface heat transfer measurements.

The transition behaviour for slender cones at angle of attacks were performed by Ericsson in 1974. The transition location on the windward side was found to be governed by the presence of the entropy layer and moved rearward with respect to the zero incidence position. On the leeward side, the cross flow effects were found to destabilise the boundary layer and dominate the transition process, moving the location of transition upstream.

The study of Softley et al. (1969), investigated the transition characteristics of a cone at Mach 10 and Mach 12. In this study, the location of peak disturbance was again found to be located in the external regions of the boundary layer. The studies examined also the effect of nose blunting and indicated a rearward movement of the transition location with increasing bluntness. In the cases examined, transition always occurred downstream of the entropy swallowing location, resulting in an increase of transition Reynolds number based on local edge conditions.

Owen's paper of 1970 concentrated on fluctuation measurements at Mach numbers in the range of 2.5 to 4.5. He noted that long before turbulent events are detectable in the boundary layer, fluctuations considerably larger than the freestream levels, are observable in the boundary layer. Again these appeared towards the outer regions of the boundary layer and moved outwards with increasing Mach number,

Ericsson (1988) discussed the role of the entropy layer as an inviscid mechanism controlling the blunt body transition behaviour, and proposed a correlation for the distance to transition x_{tr}, based on the sharp cone transition length $(x_{tr})_{sharp}$, and an entropy wake impingement parameter, x_{EWi}, and an experimental factor Δx_{tr}, as follows:

$$x_{tr} = (x_{tr})_{sharp} + x_{EWi} + \Delta x_{tr} \tag{1.6}$$

The distance x_{EWi} is an inviscid flow parameter, defined as the distance to the location where the blunt cone pressure has reached the sharp cone value. This prediction method has been used to predict transition using the data of Sell (1992) and the

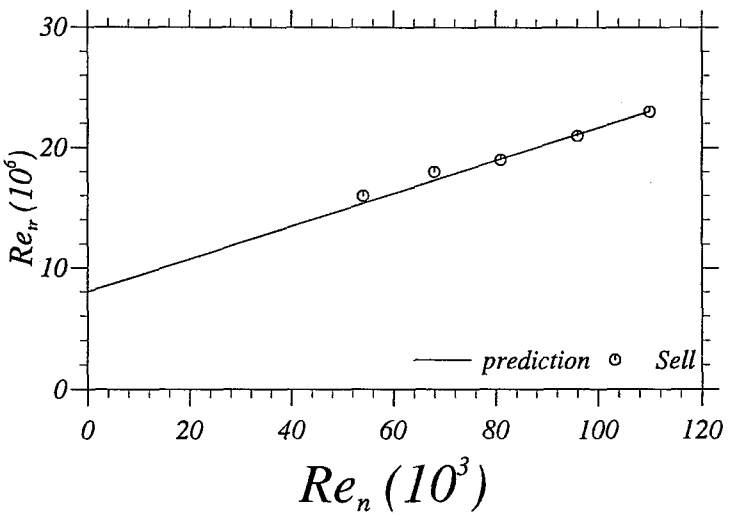


Figure 1.7: Ericsson's prediction method compared to the data of Sell (1992) obtained with a 5 ° cone at Mach 9.

outcome can be seen in figure 1.7. This model has been criticised by Stetson (1990), as the model uses an inviscid scaling parameter to correlate a viscous phenomenon. This is disputed by Ericsson (1990), who maintains that viscous phenomenon can be governed by the inviscid flow characteristics.

1.3.3 The present work

The present work is part of an ongoing transition testing program at Imperial College. The transition on a flat plate was investigated by Edwards in 1981. More recently, the work of Sell (1992) investigated the transition behaviour of sharp and blunted cones. He observed the distribution of time averaged heat transfer rates in the laminar, transition and turbulent regions. Sell concludes that the similarity between the sharp cone and flat plate transition processes indicate that first mode instabilities are the dominant transition mechanism, (Chen et al. 1989). This result is also supported by Reshotko (1969). The experiments indicated a progressive rearward movement of transition front with increasing bluntness. Sell proposes that the rearward movement

is linear with nose Reynolds number, but provides evidence to suggest that at higher nose Reynolds numbers, the transition front becomes three dimensional. At the highest nose Reynolds studied, it was speculated that the transition front was highly three dimensional and had moved upstream to the nose tip region, a reversal phenomenon. Evidently the appearance of three dimensionality with increasing bluntness is to be addressed, especially in the regions where transition reversal is expected to occur. The present study capitalises extensively on the models, instrumentation and data of Sell's study. This study intends to exceed Sell's work by obtaining and analysing time resolved data. The frequencies to be used are below those required to obtain stability information but are sufficient to monitor turbulent event formation processes, where it is felt that there is a distinct lack of information on transition event dynamics. This study aims to bridge that gap.

Chapter 2

Experimental techniques and models

2.1 Techniques

2.1.1 Schlieren

The schlieren technique is an optical flow investigation method. It depends upon the fact that the speed of light varies with the density of the medium through which it is travelling. If density gradients are present, due to shocks, shear layers or boundary layers, say, the light rays are bent in a manner proportional to the density gradient. In the schlieren system part of the deflected light is intercepted, causing the image to appear as bright and dark regions accordingly.

The present optical set-up is shown in figure 2.1. The system is composed of two 300mm diameter concave mirrors, m1 and m2, each with a focal length of 6.1m, one diameter 450mm planar mirror and one 2m focal length lens, l, for final focusing on to the camera plate. The illumination is provided by an Argon spark source and 35mm black and white film is used with a ASA rating of 60. In closing, it is noted that the density ratio across the boundary layer is greatly reduced if nose blunting is present, making the detection of the boundary layer more difficult.

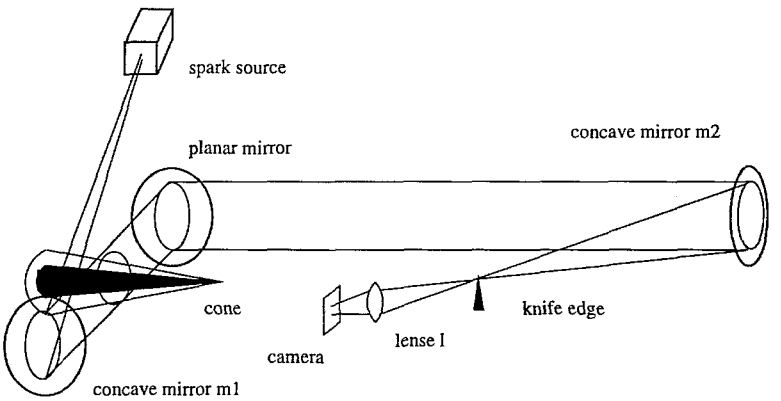


Figure 2.1: Illustration of schlieren set-up, showing position of spark source, concave mirrors, knife edge and camera location.

2.1.2 Liquid crystal surface thermography

Liquid crystal surface thermography is a qualitative technique, used to visualise surface temperature patterns. The liquid crystals are encapsulated polymer chains which are in equilibrium between the liquid and solid phase. When coated upon the model, the crystals respond to the model surface temperature evolution. At different temperatures within the thermo-chromic activity window, the crystals selectively absorb and reflect different wavelengths of the incident light. At temperatures above and below this window, they are inactive and the reflected light is unaltered. The models designed for surface thermography are made from wood and are heavily coated with several layers matte black paint, upon which the liquid crystals are applied. Polychromatic light sources are used to illuminate the model. If the surface temperature is below the lower threshold of activity, (usually required to be slightly above ambient), the model surface appears black. Once the temperature exceeds the lower limit, the shorter wavelengths of light are reflected and the model appears red. Further heating causes the wavelength of the reflected light to increase, and the apparent model colour changes through yellow, green to blue at the hot end of the window. Subsequent increases in temperature causes the paint to exceed the upper threshold of activity and the model returns to black once more. The concepts are best understood by examining figure 2.2. This is a static (flow off) test shot, in which the model is heated from the lower left by a hot air source. The jet impingement area (A), is hottest and the area is blue. Moving progressively away from this region, (B) and (C), the colour

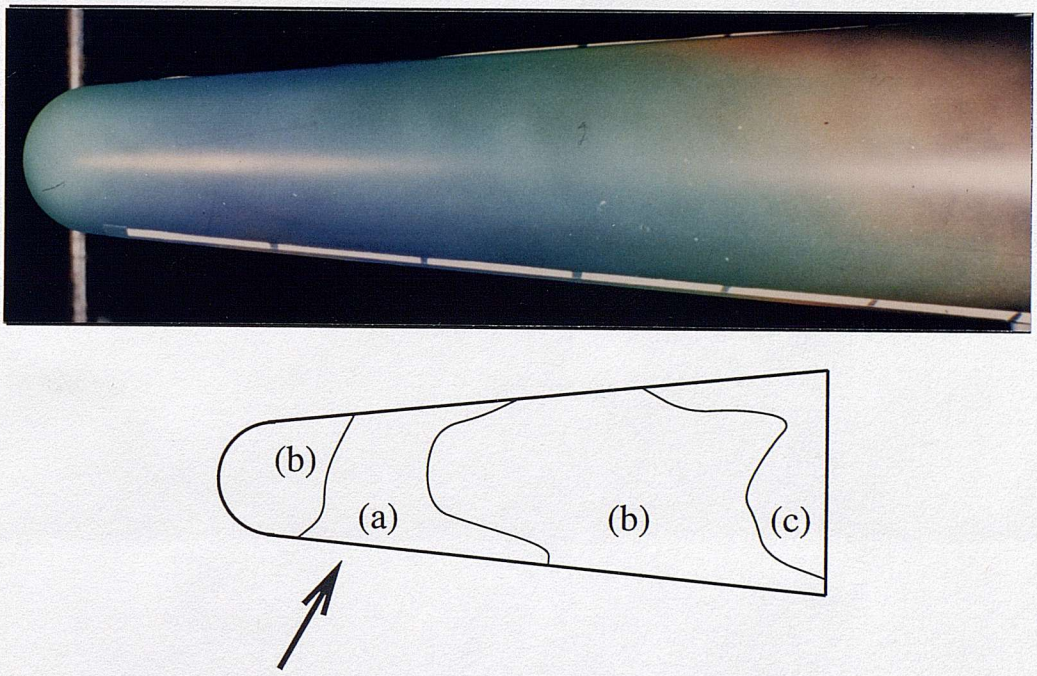


Figure 2.2: Liquid crystal surface thermography, static test. Model is heated from lower left by a hot air source .

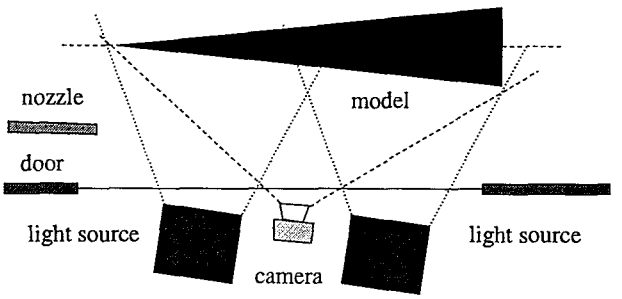


Figure 2.3: Schematic of experimental set-up for liquid crystal surface thermography.

changes through green to red and finally black in the region unaffected by the jet.

An important issue when testing in transient facilities is the history effect of the paints. Although the paints have a temporal response time better than a millisecond, they respond to temperature, not the instantaneous heat transfer rate. This has important implications in transition testing where the quantity of interest is q_w. However, it will be seen that the technique is of great use in the highly three dimensional transitional regions.

The lighting and camera arrangement are shown in figure 2.3. The camera is placed normal to the model frustum and the two light sources are arranged either side to provide uniform illumination. The film used is colour positive (slide) 35mm film, with an ASA rating of 400. A 50mm focal length lens is used, so that when the camera is located against the working section windows, the model fills the whole frame. The aperture is stopped down to f/4 and the depth of field is believed to be 20mm. Due to the model curvature, this is insufficient to keep the whole of the model surface in focus, so the camera is focussed to ensure that the nose and near nose regions are in the field of focus. Further problems are caused by the axi-symmetric shape of the model, most notably, the strong reflection of the incident light along the central portion of the model, causing a characteristic glare. Interpretation of the reflected colours becomes difficult in the regions away from the centre where the model surface is not parallel to the light source and camera, the colour of the reflected light changing with viewing angle. Other errors in colour interpretation can arise, for example if a strong temperature gradient exists across the thickness of the liquid crystal coatings, as this will lead to colour "bandwidth" problems; the hotter outer stratum will reflect

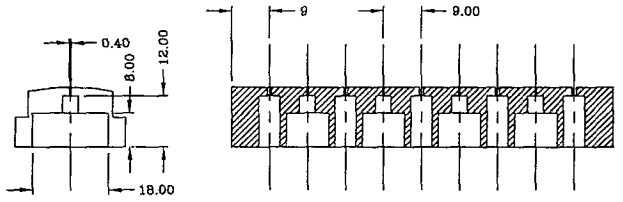


Figure 2.4: Pressure instrumentation module. The module is inserted flush in to the model surface. Transducers are mounted into the module, either in the screw-in or push-in fittings.

blue say, while the inner colder strata will reflect green. Finally, it is noted that in this thesis, prints obtained from the original colour slides will be presented. Due to printing process, involving the creation of an inter-negative, there is a loss in detail and a loss of colour intensity. For the majority of the cases presented, this does not impede the interpretation of the heating patterns.

2.1.3 Pressure measurement

Pressure is measured using Endevco and Kulite pressure transducers. The issues to be addressed are: transducer mounting, transducer calibration, transducer operation and measurement accuracy.

Transducer mounting

To minimise sensor response time, the transducers are located as closely as possible to the measurement location. Typically, for surface measurements, the transducers are mounted into "instrumentation modules", as shown in figure 2.4. To ensure good spatial resolution, the tapping, i.e. the opening at the surface, is kept as small as possible, the smallest choice of tapping diameter being dictated by the dead volume filling time. In addition to filling time, inside the measurement cavity, various resonances can occur, most importantly Helmholtz and organ pipe resonance. The Helmholtz resonance frequency is approximately given by:

$$f_h = \frac{c}{2\pi}\sqrt{\frac{a}{lv}} \tag{2.1}$$

where c is the speed of sound, a is the tapping area, l is the tapping length and v is the dead volume. Using typical values, (a=0.126mm^2, l=5mm, v=1mm^3), the Helmholtz resonance frequency is typically 5kHz. The organ pipe resonance frequency is given as:

$$f_p = \frac{c}{2l} \tag{2.2}$$

and is typically 15kHz.

Transducer operation

The transducer output is filtered and amplified and then passed to the analogue-to-digital converter. Prior to the run, the transducer output is recorded and the pressure is monitored as the departure from the pre-run baseline pressure. To obtain the absolute pressure, the pre-run pressure must be added. The latter is recorded with an Inficon capacitance manometer mounted in the test section.

Transducer calibration

For pressure differences within the operational range of the transducer, the sensor's voltage pressure relationship is linear. To obtain the voltage - pressure slope, the transducer is cross calibrated against a known pressure measurement. The latter is obtained using the Inficon manometer or using a Betz manometer. To reduce errors in calibration, the whole measurement chain, namely transducer, amplifier and A/D unit are calibrated together at ten pressure levels. The slope is calculated using linear regression. The calibrations are highly repeatable and show great linearity.

Measurement accuracy

A breakdown of the error sources is given in table 2.1. It is apparent that the strongest contribution to the measurement accuracy is the determination of the baseline pressure using the 1000 Torr Inficon manometer. This error reduces as the pressure to be measured increases, in such a manner that it is negligible for Pitot pressure measurements.

measurement chain calibration	± 5 %
run to run variation	± 3 %
errors in baseline pressure	
1000 Torr Inficon	± 5.5 %
100 Torr Inficon	± 1 %
Spatial accuracy	± 1 %

Table 2.1: Breakdown of pressure measurement errors.

2.1.4 Heat transfer rate measurement

To obtain the time resolved heat transfer rate, the thin film gauge technique is used. This method has been extensively used in short duration facilities and is discussed in Vidal (1962), Henshall and Schultz (1959), Edney (1967) and Schultz and Jones (1973). The thin film gauges are used to monitor the surface temperature evolution, which is related to the heat transfer rate. The presence of the film is not expected to change the temperature history of the substrate upon which it is mounted. For a semi-infinite substrate of density ρ, specific heat c and thermal conductivity k, the temperature and heat transfer distribution with time, t, are related by equation 2.3.

$$q_w(t) = \sqrt{\frac{\rho c k}{\pi}} \left[\frac{T(t)}{\sqrt{t}} + \frac{1}{2} \int_0^t \frac{T(t) - T(\tau)}{2(t-\tau)^{3/2}} d\tau \right] \tag{2.3}$$

For the assumption of semi-infinite substrate to be met, the penetration depth of the heat pulse must be small compared to the depth of substrate. The penetration depth, after Schultz and Jones, at which the heat transfer rate is negligible, i.e. less than one percent of the surface value, is given by:

$$x_{pen} = 4\sqrt{\frac{kt}{\rho c}} \tag{2.4}$$

substituting into the above expression the appropriate values, gives a penetration depth less than a millimetre, which is always less than the substrate thickness used in the present experiments. The response time of the platinum film is given as:

$$t_d = \frac{\rho_p c_p}{k_p} \delta^2 \tag{2.5}$$

where the subscript p indicates the properties of platinum to be used, For a hand painted film, δ, the paint thickness is of the order of microns, leading to diffusion times less than 10^{-9}s.

The temperature change of the platinum film during the run causes a resistance change which is monitored using a Wheatstone bridge. The appropriately conditioned bridge output is captured digitally by a Microlink transient capture system operating at up to 125kHz. After the run, the stored digital data is down loaded to a personal computer where the conversion is made from the bridge voltage imbalance, $\Delta V(t)$ to the temperature change, T(t), using the expression:

$$T(t) = \frac{4}{\alpha_r}\frac{\Delta V(t)}{V_b}\left(1 - 2\frac{\Delta V(t)}{V_b}\right)^{-1} \tag{2.6}$$

where V_b is the bridge supply voltage and α_r is the sensor sensitivity, related to the sensor resistance and resistance slope as follows:

$$\alpha_r = \frac{1}{R}\frac{\partial R}{\partial T} \tag{2.7}$$

The solution of equation 2.3 using the discrete temperature signal follows the method of Cook and Felderman (1966). The temperature distribution is considered to be piecewise linear, such that T(τ) is given by:

$$T(\tau) = T(t_{i-1}) + \frac{T(t_i) - T(t_{i-1})}{t_i - t_{i-1}}(\tau - t_{i-1}) \tag{2.8}$$

Substituting the above expression into equation 2.3 and noting that at t=0, T(t)=0, the following expression is found:

$$q(t_n) = \sqrt{\frac{\rho c k}{\pi}} \sum_{i=1}^{n} \frac{T(t_i) - T(t_{i-1})}{(t_n - t_i)^{1/2} + (t_n - t_{i-1})^{1/2}} \tag{2.9}$$

Gauge calibration

The calibration involves the determination of $\sqrt{\rho c k}$, a property of the substrate, and α_r, the thermo-resistivity of the film.

To determine α_r, the gauge is immersed in a thermostatic water bath and the resistance is monitored at a series of temperature intervals over the expected temperature

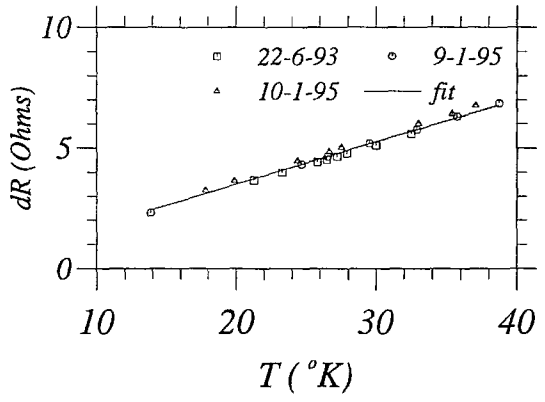


Figure 2.5: Resistance - temperature curve of gauge 02.

range. A resistance - temperature curve of a typical gauge can be seen in figure 2.5. Three calibrations performed at different dates are given, the linear fit to the measured data is obtained by linear regression.

To obtain an accurate estimate for $\sqrt{\rho ck}$, a pulse calibration technique is used, as suggested by Henshall and Schultz (1959), Bogdan (1964) and Skinner (1961). In this technique the gauge is placed in a resistance arm of a Wheatstone bridge and a known pulse is applied to the bridge. The sensor, due to resistive heating, will change in temperature and resistance, causing in a bridge imbalance. The change is senor temperature depends on the substrate thermal properties, $\sqrt{\rho ck}$, the sensor surface area, A, and the resistive heating, proportional to the sensor resistance and pulse voltage, V_p. The bridge imbalance depends on the resistance temperature slope and the pulse voltage. Equating the bridge imbalance ΔV_b to the resistive heating gives:

$$\frac{\alpha_r}{\sqrt{\rho ck}} \propto \frac{\Delta V_b}{\sqrt{t}} \frac{A}{V_p^3} \tag{2.10}$$

It is noted that as the left hand side of the above equation is constant, the bridge output with time $\Delta V_b(t)$ is parabolic. The determination of A, the surface area of the gauge is time consuming and if non uniformities in film thickness are present, the process can lead to serious errors. To overcome this, a two media approach was used, as presented by Skinner (1961). In this method, the gauge is first pulsed in air (as before) and the bridge imbalance slope $\Delta V_{b1}/\sqrt{t}$, is recorded. Then, in a second experiment, the gauge is pulsed in a medium in which $\sqrt{\rho ck}$ is known, and a second slope $\Delta V_{b2}/\sqrt{t}$ is measured. The decrease in resistance slope between $\Delta V_{b2}/\sqrt{t}$ and $\Delta V_{b1}/\sqrt{t}$ is a consequence of the presence of the second medium absorbing the heat

pulse. Maulard (1968) has shown that the substrate's thermal properties can be linked to the second medium's thermal properties, $\sqrt{\rho_2 c_2 k_2}$ as indicated below:

$$\sqrt{\rho ck} = \sqrt{\rho_2 c_2 k_2} \left(\frac{\Delta V_{b1}/\sqrt{t}}{\Delta V_{b2}/\sqrt{t}} - 1 \right)^{-1} \tag{2.11}$$

A variety of different gauge designs were successfully tested at a variety of pulse voltages. The mean estimate for $\sqrt{\rho ck}$ at 17 ° C is 0.2012 (J $cm^{-2}K^{-1}s^{-1/2}$), with a standard deviation σ_{N-1} of 1.6%. Jones' (1989) estimate for the Macor substrate is:

$$\sqrt{\rho ck} = 0.2 + T(°C) \times 0.00065 \tag{2.12}$$

The present estimate shows close agreement with the result of Jones.

Measurement accuracy

A breakdown of the error sources is given in table 2.2.

thermal properties, substrate	± 5 %
thermo-resistive property, film	± 1 %
run to run variation	± 3 %
amplifier accuracy	± 1 %
sampling accuracy and jitter	± 1 %
Spatial accuracy	± 1 %

Table 2.2: Breakdown of heat transfer measurement errors.

Gauge manufacture

Once the Macor substrate has been machined to the necessary shape, holes are drilled and countersunk through the substrate, as shown in figure 2.6 (a). The role of the countersinking is to create a surface of continuous curvature upon which the connecting gold paint is applied and baked, 2.6 (b). When this exercise is completed, the platinum sensor can be painted, 2.6 (c). To complete the gauge, connection pins are

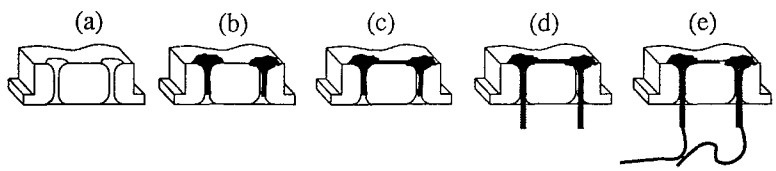


Figure 2.6: Illustration of manufacturing steps for construction of thin film heat transfer rate gauges.

inserted from the underside into the holes and are fixed in location with conducting epoxy, 2.6 (d). This ensures that as much surface area as possible is kept in contact with the gold, reducing significantly the contact resistance. The conducting epoxy is also used to fill any recesses left by the presence of the holes on the upper surface of the gauge. Finally wires are soldered to the solder buckets at the bottom of the pins, 2.6 (e) and the connections to the tunnel floor instrumentation plugs are made. All circuitry running external to the model is shielded and grounded to the tunnel earth. Typically, the connection resistance is less than 2% of the total gauge resistance.

2.1.5 Data recording and signal conditioning

The data recording is performed digitally. The facility can simultaneously sample and store 28 channels, at a maximum sampling rate of 125kHz with 12bit resolution. One channel of the A/D - storage equipment is reserved for the measurement of the barrel stagnation pressure. This pressure is used to trigger both the data capturing process and is also used to provide the input to the delay unit from which the spark sources are fired. Typically, the 4ms of data immediately before the trigger are saved and used as the pre-run zero level. The remaining memory is reserved to store the run time data. At run completion, the data are down-loaded from the A/D storage hardware onto a Personal computer. Further data analysis is performed on the departmental Workstations.

The signal conditioning units can be operated in a "bridge" and in "amplifier" mode. In the bridge mode of operation, used for heat transfer measurements, the units act as Wheatstone bridges and successively amplify and filter the bridge output. Filtering is used to avoid aliasing in subsequent A/D conversion. In the amplifier mode, the

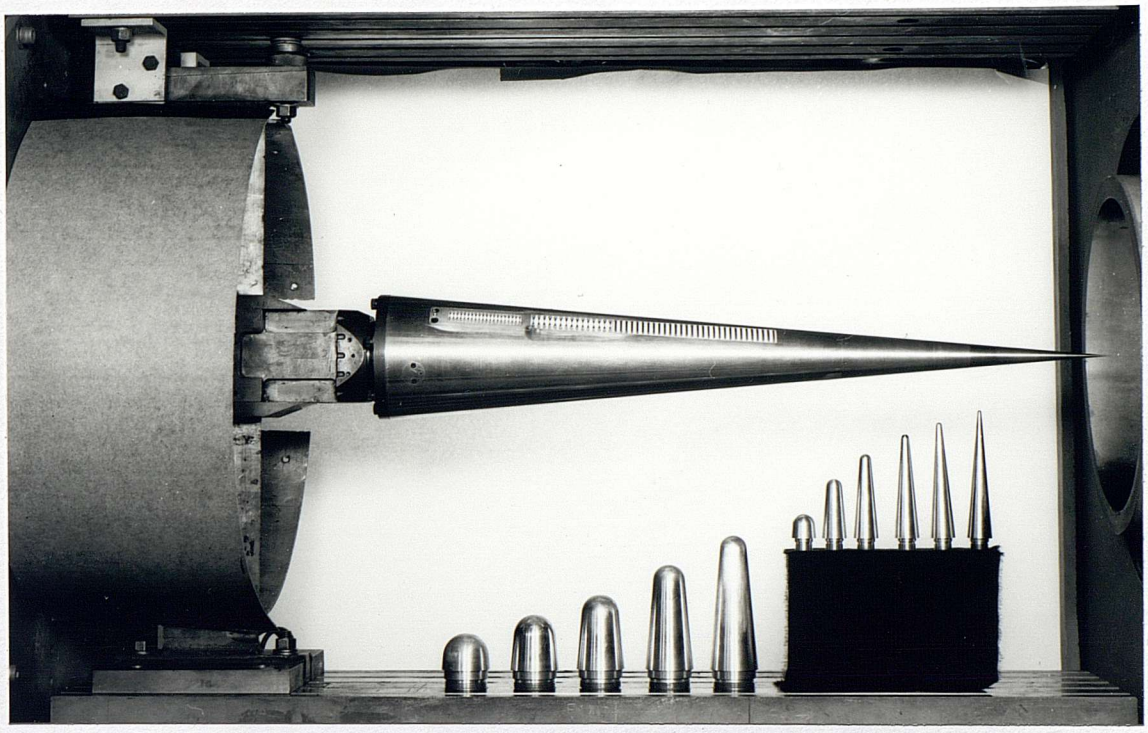


Figure 2.7: Illustration of instrumented model, depicted in the tunnel test section. Clearly visible is the model, sting support arrangement, nozzle and diffuser. A selection of the interchangeable hemispherical nose radii is placed on the tunnel floor.

unit provides a supply voltage to the transducer and more importantly amplifies and filters the transducer output.

2.2 Models

The main model used in this study is a 5 ° semi-angle cone, depicted in figure 2.7. The model presents an instrumentation slot aligned in a streamwise direction, into which heat transfer modules, pressure modules or blank units can be inserted. All modules are manufactured integral, (i.e. located in the instrumentation slot), and are machined flush to the model surface. Three pressure tappings, used to align the model, are located towards the rear of the model, positioned at 120 ° pitch around the circumference. The interchangeable hemispherical nose cones can be seen arranged along the tunnel floor in figure 2.7. These are screwed into the frustum portion, using when required the extension piece. An engineering drawing of the model and associated pieces of instrumentation can be found in figure 2.8.

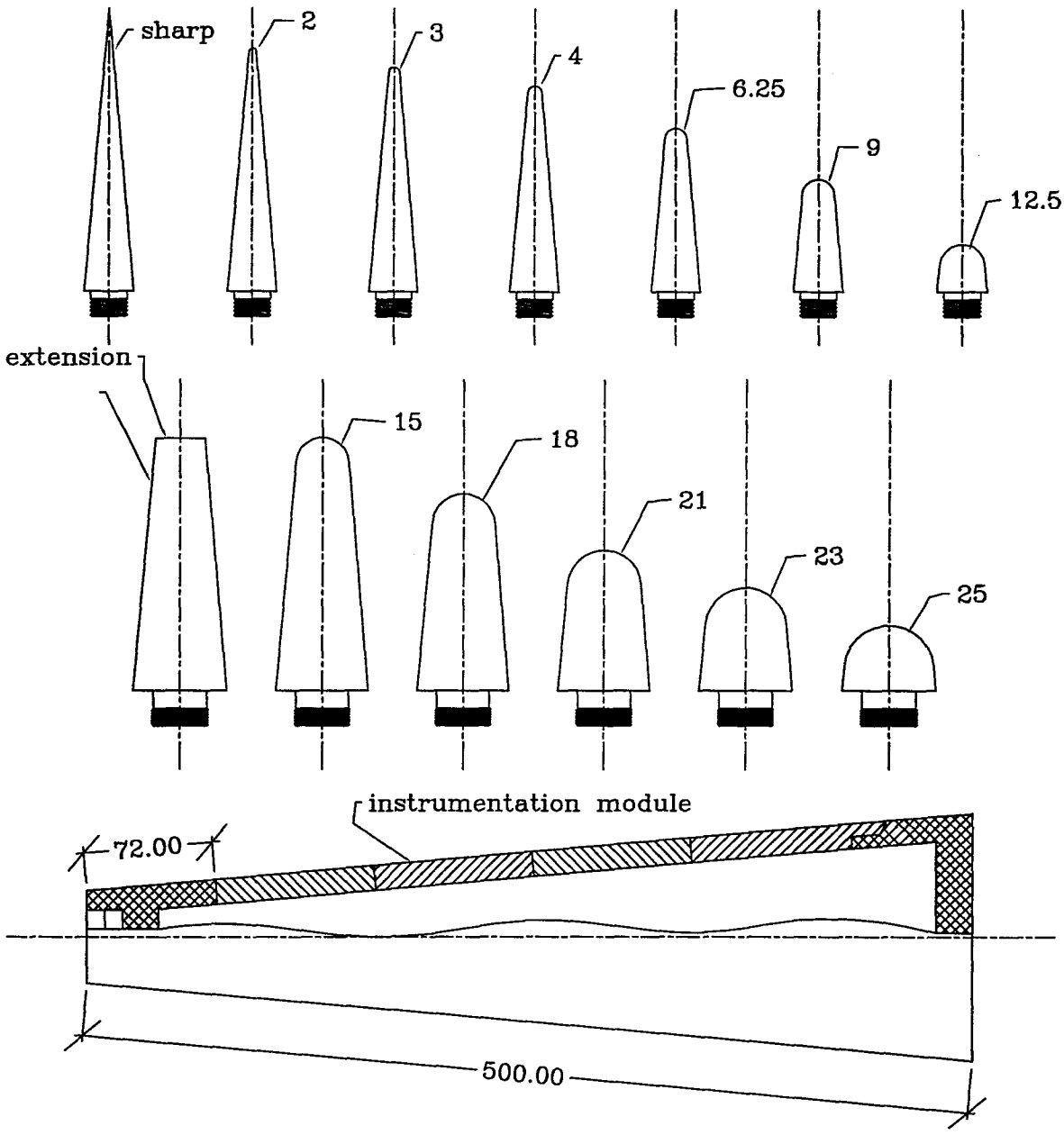


Figure 2.8: Engineering drawing of model, showing instrumentation slot and the selection of hemispherical noses, all dimensions in mm.

Model location and alignment

In all experiments, the model was located with the front end of the frustum portion, in the nozzle exit plane. Alignment, via the three circumferentially separated tappings located towards the end of the model, is better than $\pm 1\%$ in pressure at all three operating conditions.

Pressure measurement modules

The model has thirty six pressure tappings. These are located in groups of nine on four pressure modules. A typical pressure module is depicted in figure 2.4. The location of the tappings, with respect to the front end of the frustum, are given in table 2.3.

module 1

tapping number	1	2	3	4	5	6	7	8	9
s (mm)	81	90	99	108	117	126	135	144	153

module 2

tapping number	10	11	12	13	14	15	16	17	18
s (mm)	171	180	189	198	207	216	225	234	243

module 3

tapping number	19	20	21	22	23	24	25	26	27
s (mm)	261	270	279	288	297	306	315	324	333

module 4

tapping number	28	29	30	31	32	33	34	35	36
s (mm)	351	360	369	378	387	396	405	414	423

Table 2.3: Location of pressure tappings with respect to frustum datum.

Heat transfer measurement modules

The heat transfer gauges are painted on to four separate modules, made from Macor. The modules were machined and subsequently turned with the rest of the model to

ensure a flush fit. Sixty five gauges in total are located on the four modules. The gauges' locations, relative to the datum point at the beginning of the frustum, are given in table 4. The sensor length is 20mm for gauges 1 - 30, and 4mm for gauges

module 1

gauge number	1	2	3	4	5	6	7	8	9
s (mm)	75	81	87	93	99	105	111	117	123
gauge number	10	11	12	13	14	15			
s (mm)	129	135	141	147	153	159			

module 2

gauge number	16	17	18	19	20	21	22	23	24
s (mm)	165	171	177	183	189	195	201	207	213
gauge number	25	26	27	28	29	30			
s (mm)	219	225	231	237	243	249			

module 3

gauge number	31	32	33	34	35	36	37	38	39
s (mm)	255	251	267	273	279	285	291	297	303
gauge number	40	41	42	43	44	45			
s (mm)	309	315	321	327	333	339			

module 4

gauge number	46	47	48	49	50	51	52	53	54
s (mm)	354	358	362	366	370	374	378	382	386
gauge number	55	56	57	58	59	60	61	62	63
s (mm)	390	394	398	402	406	410	414	418	422
gauge number	64	65							
s (mm)	426	430							

Table 2.4: Location of heat transfer rates gauges with respect to frustum datum.

31 - 65. All gauges have a nominal 50 Ohms resistance and typically $\partial R/\partial T = 0.1$ $\Omega/^\circ$ K.

Other models

Four other models are used in this study. Three are reserved for liquid crystal visualisation purposes and are presented in figure 2.9. The models are made from wood. To remove the effect of wood grain causing variations in $\sqrt{\rho ck}$, the models were copiously covered with undercoat, before the final matte coat was added. When testing with

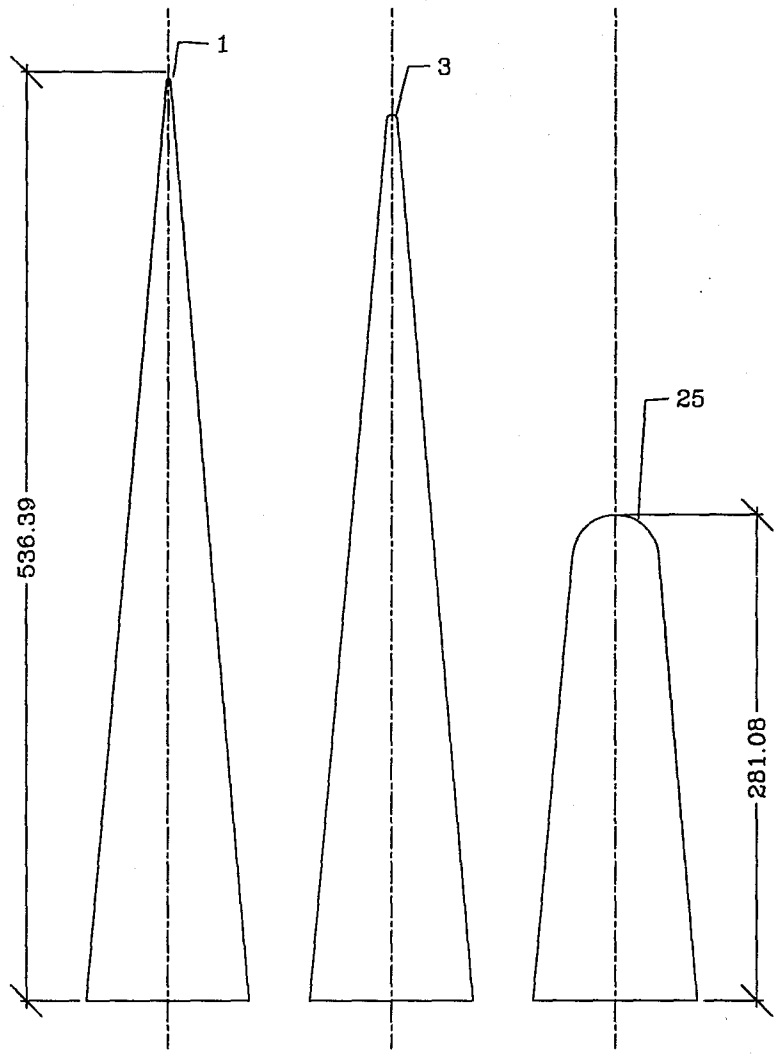


Figure 2.9: Illustration of three models reserved for liquid crystal visualisation purposes, all dimensions in mm.

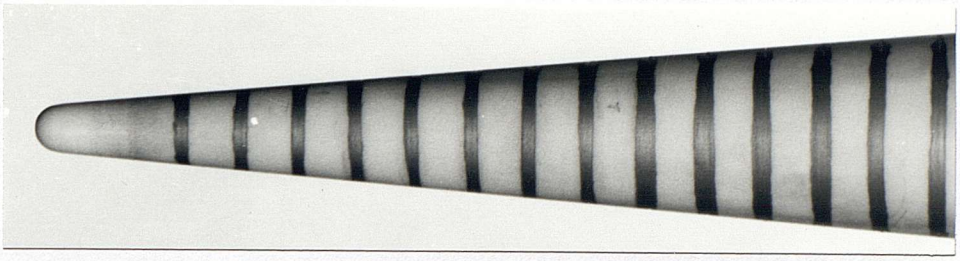


Figure 2.10: Illustration of ceramic nose piece, used to obtain heat transfer rate data.

these models, the model apex was located immediately downstream of the nozzle exit plane, allowing visualisation of the entire model surface heating patterns.

The fourth model has a 3mm radius ceramic nose, with fourteen gauges located between s=21mm and s=100mm, illustrated in figure 2.10. The apex was located at the same axial location in the tunnel as the equivalent test case with the main instrumented model (266mm inside nozzle).

Chapter 3

Facility

3.1 Description

The Imperial College number 2 gun tunnel is a nominal Mach 9 facility. It is capable of producing Reynolds numbers in the region $Re_\infty/m = 7.5*10^6 \rightarrow 55*10^6$. Operated in the free piston mode, run times exceed 20ms with a 4-7ms steady run window. The test gas is Nitrogen. The 280mm diameter core flow accommodates slender bodies up to chord lengths of 0.8m, allowing natural transition to turbulence to be achieved over a variety of free stream conditions and model geometries.

At present, three calibrated conditions exist, although the potential operational envelope extends well beyond this. Table 3.1 summarises the nominal operating conditions used in this study. A schematic of the gun tunnel is depicted in figure 3.1, where the

Run type	Driver p_4 (KN/m^2)	Barrel p_1 (KN/m^2)	Ratio p_4/p_1	M_∞	Re_∞/m	T_o $(°K)$
Low	11720	137.90	85	8.9	$7.5 * 10^6$	1060
Medium	22400	249.00	90	8.9	$12.6 * 10^6$	1090
High	97500	1055.00	92.4	9.0	$47.4 * 10^6$	1105

Table 3.1: Nominal operating conditions.

main elements including the driver, septum, barrel, throat, nozzle, test section and dump tank are shown.

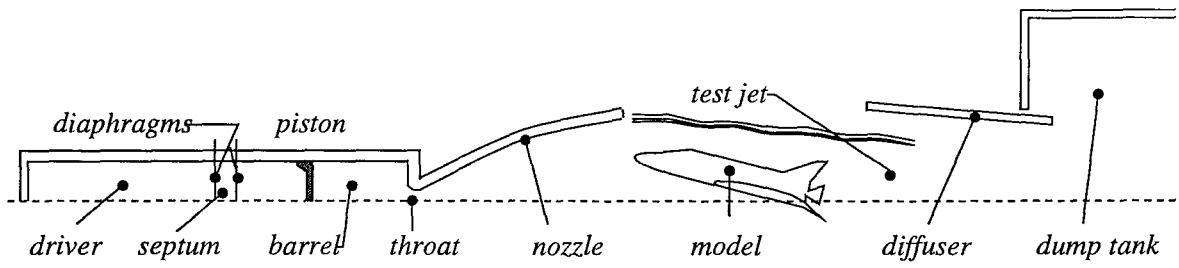


Figure 3.1: Schematic of a typical gun tunnel set up.

3.2 Operation

The operation manual [Needham et al. 1970] describes in detail the operational and safety procedures for the number 2 tunnel. When not in operation, the tunnel system is kept for obvious safety reasons at ambient pressure. Prior to a run, the nozzle, test section and the dump tank are evacuated of air until 1 *Torr* vacuum has been created. This promotes the starting of the flow and also ensures that at run completion the pressure in the test section is below atmospheric. The vacuum is separated from the high pressure gas in the barrel either by means of a Melinex membrane placed upstream of the throat or by a plastic plug inserted in the throat. Both devices are able to support an 11 *atm* pressure differential. At the two lower pressure operating conditions, the barrel is purged of air before pumping to the desired pressure to ensure a high nitrogen content. The driver and septum are then pumped to the required pressures, using the four compressors operated in series. Pressures are monitored using piezo - resistive transducers mounted in the driver, septum and barrel. These transducers are calibrated at regular intervals with precision dial gauges. The calibration slopes show high linearity and little hysteresis, as depicted in figure 3.2, for a series of barrel calibrations. The calibrations are highly repeatable with time showing no drift in zero reading.

Firing is controlled by the filling or venting of the septum chamber, which is located between the barrel and the driver. It is used to ensure repeatability in establishing p_4 and p_1, the driver and barrel pressures respectively and the repeatability of the run conditions. The front diaphragm is burst first, as it is felt that this provides better opening of the diaphragm petals [Elfstrom 1971].

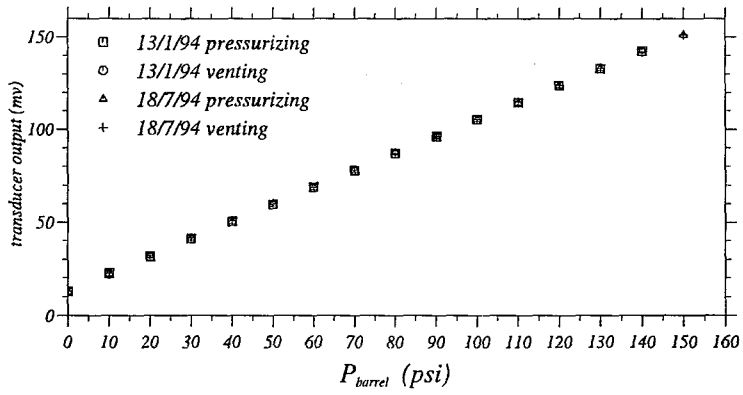


Figure 3.2: Calibration of barrel piezo resistive pressure transducer.

Upon bursting of the diaphragms, the driver gas accelerates the piston along the barrel, causing the gas ahead of it to be compressed by means of a shock wave, figure 3.3. This shock wave is reflected off the barrel end wall and returns to interact with the piston causing it to decelerate. There are several such like reflections and interactions between the piston face and barrel end wall, compressing the gas to some final end state, which is identified with the run time reservoirs conditions $p_{(0,r)}$, $T_{(0,r)}$. The run ends when all of the gas initially in the barrel, now compressed between the piston and the barrel end wall, has passed at sonic conditions through the throat.

3.3 Calibration

3.3.1 Calibration aims

The intention of the calibration is to provide, for experimental and computational use, a set of parameters describing the entire flow field at each of the three operating conditions. For the calibration to be complete, one must be able to identify, u_∞, v_∞, p_∞ and ρ_∞ at every point of interest in the test jet. As far as possible, it is desirable to measure the section properties directly, however, the experimental difficulties connected with the calibration of an intermittent hypersonic tunnel make the attainment of that goal rather difficult. Instead, it is proposed to obtain measurements allowing the calculation of the M_∞, $T_{(0,\infty)}$ and p_∞. These results can then be used to evaluate

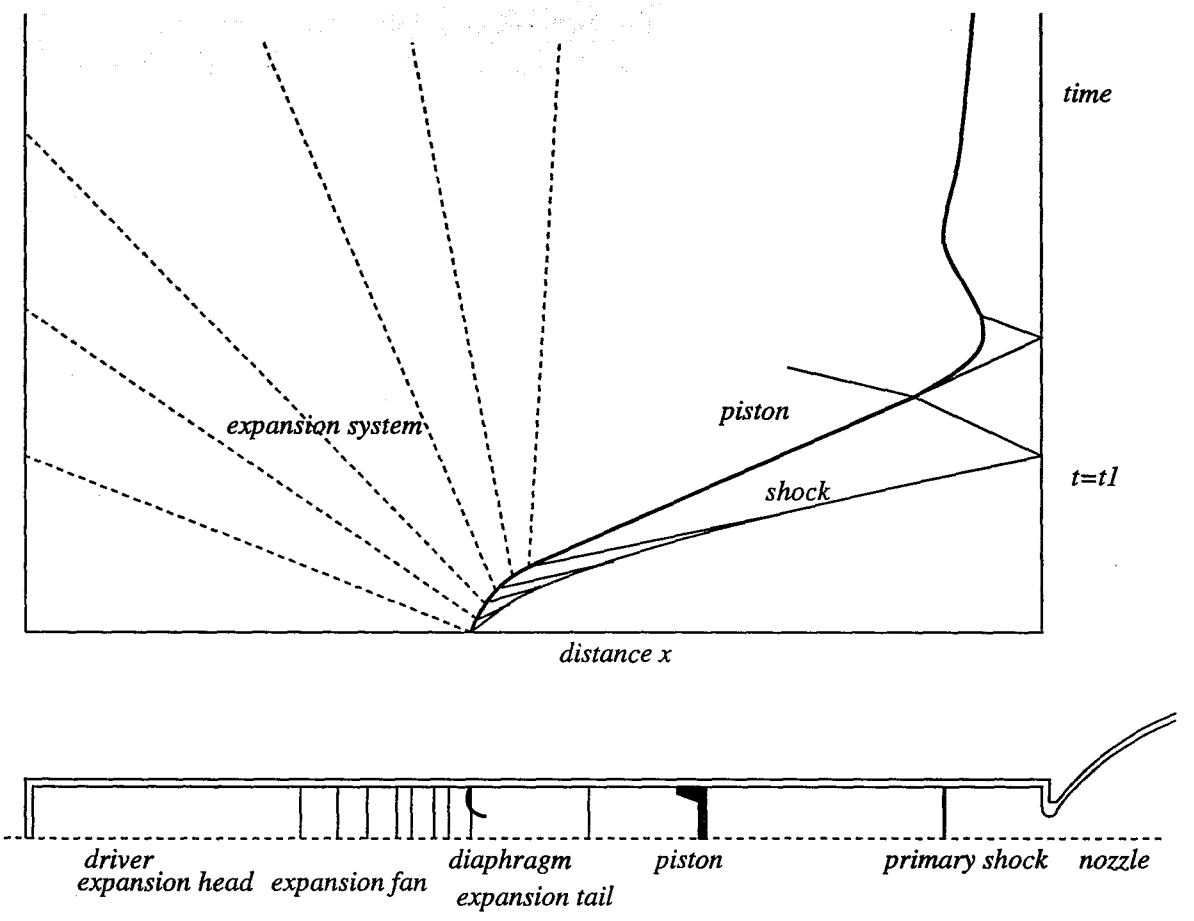


Figure 3.3: Schematic of a free piston mode of operation.

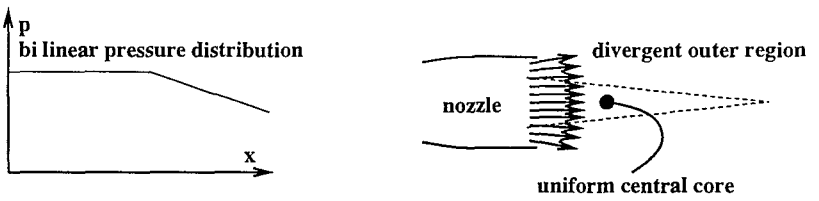


Figure 3.4: Illustration of measured pressure distribution and predicted flow angularity at the nozzle exit plane at the high pressure operating condition, after Hillier, Kirk and Millevoi.

u_∞, v_∞ and ρ_∞.

The four experimental measurements are to be made are: test section Pitot pressure, $p_{(0,2)}$; barrel total pressure, $p_{(0,res)}$; cone-probe surface pressure, p_c and stagnation point heat transfer rate, q_w . These four datasets provide three estimates for M_∞, $T_{(0,\infty)}$ and p_∞. The redundancy of estimates allows uncertainties associated with each individual method to be highlighted and ensures a high quality calibration. To obtain the velocity resolved in the two flow directions, u_∞ and v_∞, the flow angularity must be reconstructed from the Mach number and pressure information. This has been attempted previously by Millevoi and Hillier [Millevoi 1993, Kirk 1993, Hillier et al. 1993], using the pressure measurements on a hollow cylinder of Kirk to reconstruct the Mach number - flow direction field using the method of characteristics. The pressure distribution on the cylinder was found to be bilinear, constant in the upstream region, and then linearly decreasing with distance, as shown figure 3.4. The calculation indicated that the test core may present a central parallel core, surrounded by a divergent outer region.

The calibration will be performed at five stations, z=-150mm, 0mm (nozzle exit plane), 150mm, 300mm and 450mm. Radial resolution is set at 20mm and the whole width of the core (circa 300mm) will be covered. Flow axi-symmetry will be assessed in the nozzle exit plane and if a satisfactory level of axi-symmetry is obtained, the calibration will be performed at one azimuthal angle only. Run to run errors will be reduced by normalising each pressure by the stagnation pressure measured by the barrel transducer. Probe to probe calibrations will be performed.

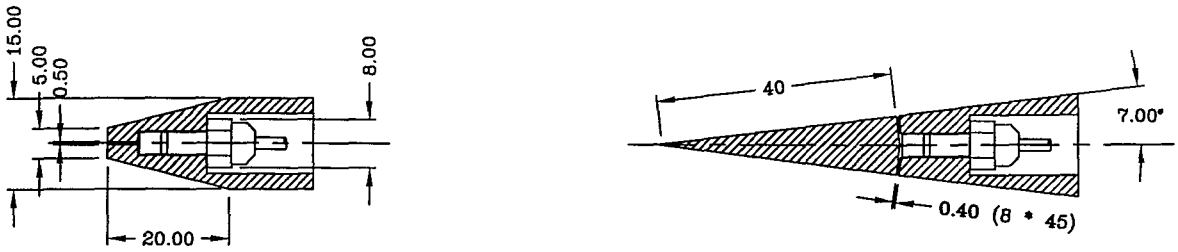


Figure 3.5: Pitot probe and cone design for calibration work. Also shown in these drawings are the "screw - in" type transducers.

3.3.2 Calibration tools

The measurement tools used in the calibration exercise include 5 Pitot probes, 6 7° semi angle sharp cones, 3 flat faced stagnation point probes, 1 traverse rake and 1 barrel stagnation pressure transducer.

In this subsection each calibration tool will be individually described.

Pitot probes

The Pitot probes are designed to achieve the highest possible spatial resolution. The lower constraint on dimensioning is the necessity to house Endevco type 8510 "screw - in" transducers. Further effort was made to ensure that dead volume and tapping length were as small as possible, in order to decrease filling time and increase probe response. The resulting design specifications can be seen in figure 3.5. Five Pitot probes were constructed and fitted with transducers. The transducers were inserted according to the manufacturers specifications, being sealed with both the suppliers " O - ring " seal and a quantity of silicone resin. Probe dead volume was further minimised by individually pairing transducers and probes.

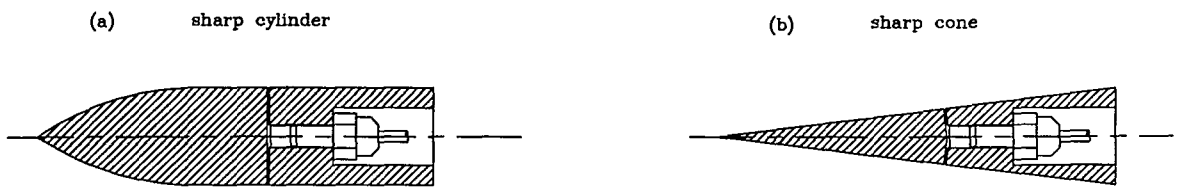


Figure 3.6: Choice of models for measurement of pressure, (a) sharp -nose cylindrical probe and (b) the sharp cone.

Cone probes for static pressure measurement

The cone surface measurement is to be used to infer surface pressure. The probe design is controlled by a variety of factors. Firstly, it must be wide enough to accommodate the Endevco 8350 type transducer. Secondly, the tapping location should be outside the region of strong viscous interaction, but upstream of the transition location. This sets an upper length constraint of about 50mm. Two design solutions are possible at this stage, as indicated in figure 3.6. The first proposal is a sharp nose - cylindrical - after-body design. The flow field is initially conical but is rapidly turned so that the pressure at the location of the tapping is comparable to p_∞. The ratio of the wall to freestream pressure will be dependent on geometry and the viscous interaction effect, hence a function of $f(p_\infty, M_\infty, Re_{\infty/m})$.

The sharp cone pressure depends more strongly on Mach number, but the viscous interactions are weaker. The geometry is easier to manufacture and as all the above criteria are meet, it was the chosen design. The probe can be seen in figure 3.5. This design angle was fixed at 7 ° . At Mach 9, the cones will typically recover three times the static pressure, and hence, they function as mechanical "amplifiers" making the quantity to be measured greater. This reduces significantly any errors connected with uncertainties in determining the baseline pressure.

The sharp 7° semi angle cones were designed with pressure tappings at $s = 40mm$. To minimise problems connected with small amounts of probe incidence, eight tappings were located at a circumferential spacing of 45°. The tips of the probes were manufactured from steel to ensure high mechanical strength and sharpness.



Figure 3.7: Stagnation point heat transfer probe design for calibration work. The Macor substrate insert and the two thin film gauges can clearly be seen.

Stagnation point heat transfer probes

The stagnation point heat transfer probes are of a flat face, sharp shoulder design, as illustrated in figure 3.7. The heat transfer gauges are painted on a Macor substrate machined integral to the probe surface. Gauge specification and construction was identical to heat transfer gauges destined for wall heat transfer measurements. The active sensing elements are painted with platinum and all connections are painted with gold. The initial design included one sensor per probe, but later, a second gauge was added. Computational studies, [Soltani 93], have indicated that heat transfer rates would be within 1% of stagnation point values over the entire length ($4mm$) of both gauges.

Rake design

The rake design requirements were to provide suitable structural stiffness and strength while creating as little blockage as possible. It presents a slender aspect ratio and a sharp leading edge to ensure shock attachment. The total radial span of the rake is $300mm$, allowing the rake to be inserted inside the nozzle. Before pressure measurements were made, schlieren photographs of typical rake configurations were taken to ensure no probe to probe interference occurred. The closest two probes can be placed on the rake is $20mm$. At this distance no interference between probes was found. A typical rake configuration would include five Pitot probes placed at $20mm$ intervals and five cone probes at $20mm$ intervals.

Barrel pressure measurement system

The barrel pressure is monitored using a Kistler piezo electric transducer mounted in the end wall of the barrel. The transducer is recessed to reduce damage from debris and is protected from the severity of reservoir conditions by an asbestos cap.

3.3.3 Calibration Methods

The three methods of calibration are:

Method 1 using $p_{(0,res)}$, $p_{(0,2)}$ and q_w

Method 2 using $p_{(0,res)}$, p_c and q_w .

Method 3 using $p_{(0,2)}$, p_c and q_w .

In this subsection each method will be described.

Method 1

The local Mach number is calculated using the Pitot pressure measurement and a total pressure estimate, $p_{(0,\infty)}$, inferred from the barrel reservoir conditions, $p_{(0,res)}$. The Mach number is uniquely linked to the ratio of Pitot to total pressure. The relationship can be prescribed via the supersonic Pitot probe equations:

$$\frac{p_{(0,2)}}{p_{(0,\infty)}} = \left[\frac{\gamma+1}{2}M_\infty^2\right]^{\gamma/(\gamma-1)} \left[\frac{2\gamma M_\infty^2-(\gamma-1)}{\gamma+1}\right]^{1/(1-\gamma)} \left[1+\frac{\gamma-1}{2}M_\infty^2\right]^{\gamma/(1-\gamma)} \quad (3.1)$$

It is important to note that the Mach number calibration is Reynolds number independent. To obtain the Reynolds number, the total temperature must be determined from the measured stagnation point heat transfer rate. The stagnation point heat transfer rate and total temperature can be linked by the formula of Fay and Riddell (1958), given below:

$$q_w = 0.763 Pr^{-0.6}(\rho_w\mu_w)^{0.1}(\rho_{(0,2)}\mu_{(0,2)})^{0.4}(h_{(0,2)}-h_w)\sqrt{\frac{du}{dx}} \quad (3.2)$$

Method 2

This method uses the locally measured cone pressure, p_c, the stagnation point heat transfer rate measurement, q_w, and the inferred total pressure, $p_{(0,res)}$, to provide an estimate for Mach number and Reynolds number. The method relates the freestream pressure, p_∞, to the cone pressure, p_c, using a set of relationships which are derived in appendix A, and given below:

$$\frac{p_c}{p_\infty} = \frac{p_c}{p_{(c,inv)}} \times \frac{p_{(c,inv)}}{p_\infty} \tag{3.3}$$

$$= (1 + 0.045\frac{M_\infty^3}{\sqrt{Re_s}}\sqrt{C}) \times (2.972 + (M_\infty - 9.0) * 0.378) \tag{3.4}$$

The solution strategy is to make an initial guess for $Re_{\infty/m}$ and M_∞ . This gives a value for p_∞, which is used together with $p_{(0,\infty)}$ to get an estimate for M_∞ using isentropic flow equation. This is then used to update the properties on the right hand side of equation 3.2, allowing a $Re_{\infty/m}$ estimate to be obtained. The updated M_∞ and $Re_{\infty/m}$ are then used in equation 3.4 and the process repeated until convergence.

Method 3

This method uses $p_{(0,2)}$, p_c and q_w to obtain Reynolds number and Mach number estimate. An initial guess for $Re_{\infty/m}$ and M_∞ are made and the static pressure is obtained using equation 3.4. This static pressure, together with the measured Pitot pressure, are used to obtain a Mach number estimate. This Mach number must satisfy both the total pressure estimates obtained using the measured Pitot pressure and the Mach number guess; and the estimated static pressure and the Mach number guess. This Mach number guess is then used to update the value of the properties appearing in equation 3.2, in order to obtain $T_{(0,\infty)}$ and hence updating the Reynolds number estimate. The process is repeated to convergence.

3.3.4 Results: barrel stagnation and total pressure

The total pressure is inferred from the barrel stagnation pressure, which is measured by means of a piezo electric transducer mounted in the barrel end wall. An important

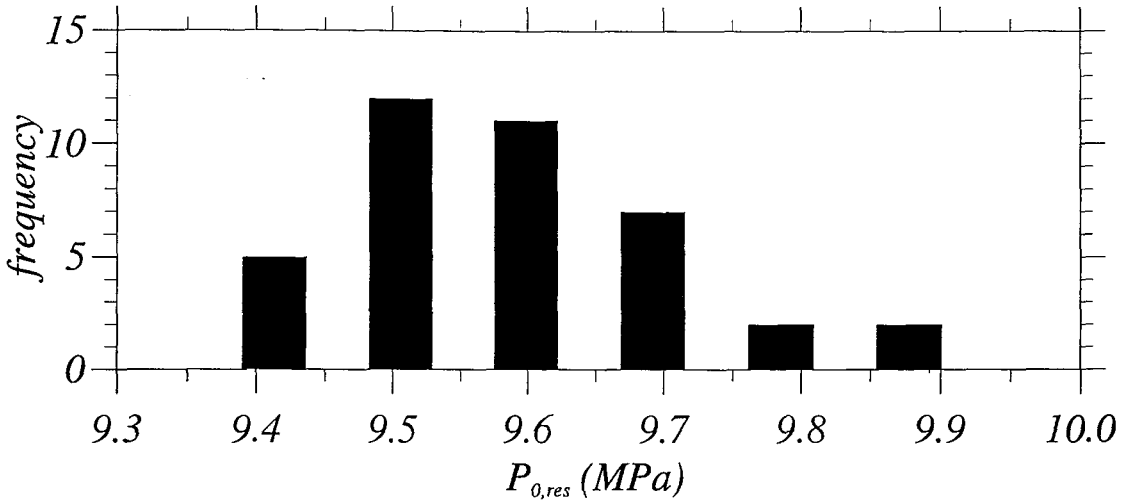


Figure 3.8: Barrel reservoir pressure distribution, low pressure operating conditions.

issue for calibration runs and test runs in general, is the ability to duplicate the steady run conditions. The repeatability of barrel reservoir pressure is an obvious indicator of this, showing how consistently conditions are attained. The stagnation pressure probability distribution at the low, medium and high pressure operating conditions, respectively, are shown in the figures 3.8, 3.9 and 3.10. The average pressure and the standard deviation for the three conditions are given in table 3.2 below.

Condition	n	$\overline{p_{(0,res)}}$ (MPa)	σ_n (MPa)	$\sigma_n/p_{(0,res)}$	$p_{(0,res)}/p_4$
Low	39	9.5358	0.1220	1.3 %	81.5 %
Medium	37	15.9666	0.4097	2.6 %	71.3 %
High	40	53.4294	1.0686	2.0 %	54.8 %

Table 3.2: Barrel reservoir conditions.

Also included in the table is the percentage of driver pressure recovered in the piston compression process. Cross referencing this information to the value of p_4/p_1 presented in table 3.1, it is seen that the lower driver to barrel pressure ratio used in the low operating condition leads to the greatest percentage of driver pressure recovery at stagnation conditions.

The upstream part of the nozzle flow and the throat flow are characterised by the nitrogen test gas being at high temperatures and pressures. The gas can no longer

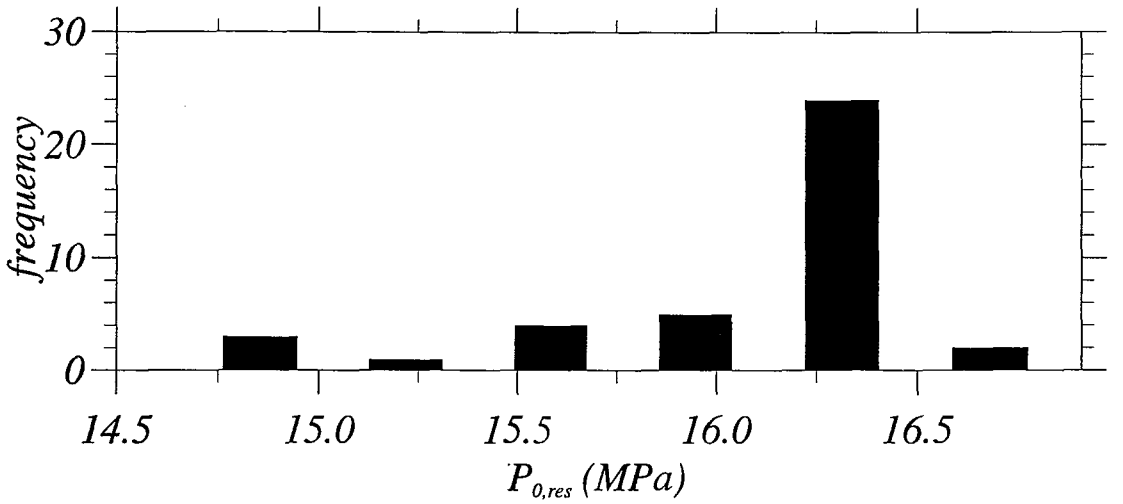


Figure 3.9: Barrel reservoir pressure distribution, medium pressure operating conditions.

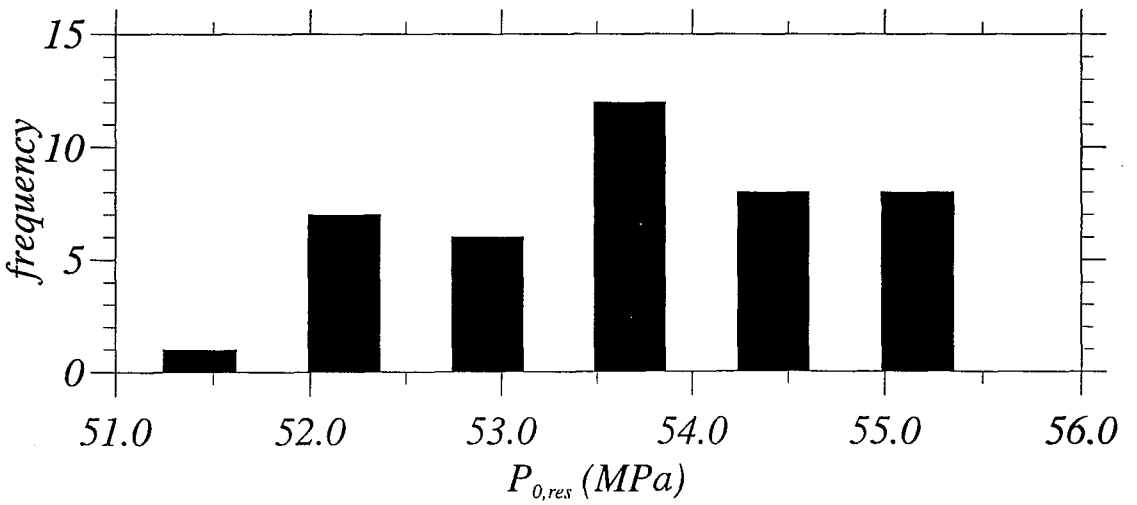


Figure 3.10: Barrel reservoir pressure distribution, high pressure operating conditions.

be treated as calorifically perfect and real gas effects are important. Culotta and Richards (1970) have analysed the problem of isentropic expansion of nitrogen at such conditions. They have calculated a series of correction factors allowing the total pressure to be related to the barrel stagnation pressure. The correction factors for temperature and pressure at the three working conditions of the number 2 gun tunnel are listed below.

Condition	$p_{(0,res)}(MPa)$	$T_{(0,res)}$ ° K	$p_{(0,\infty)}/p_{(0,res)}$	$T_{(0,\infty)}/T_{(0,res)}$
Low	9.5358	1060	1.00	1.06
Medium	15.9666	1100	0.99	1.06
High	53.4294	1060	1.12	1.09

Table 3.3: Real gas correction factors for Nitrogen gas.

3.3.5 Results: Pitot pressure measurements

Probe calibration

The pressure measurement chain includes transducer - amplifier - analogue to digital converter and is regularly calibrated against the Inficon pressure reading, during the pre - run test evacuation process. Two hundred digital samples of the system output (mv) are averaged at the given transducer supply voltage, gain and A/D setting to be used in the following runs, at ten pressure levels. The voltage - pressure slope is obtained by fitting a linear curve with the least squares method.

Probe to probe referencing

It is noted that when measuring the pressure at a given location by two different probes, they do not record the same pressure. For instance, one probe may read 2% below the other say. If the two probes are then moved to a different location, and again, one probe recovers 2 % less than the other, one can conclude that the two probes have different responses. To combat this problem, the probes were calibrated

relative to a "reference probe". It is noted that this procedure does not improve the absolute measure of pressure. The reference factors are given in table 3.4. It can be

Operating condition	probe 3	probe 4	probe 10	probe 11	probe 12	probe 13	probe 14	probe 15
Low	1.00	0.95	1.00	1.00	/	/	/	/
Medium	1.00	0.95	1.00	1.00	/	/	/	/
High	/	/	0.99	/	1.01	1.00	1.01	0.985

Table 3.4: Compensation factors for the Pitot probes used in the calibration experiment.

seen from table 3.4, that at the low and medium pressure conditions, only one probe necessitated correction. At the high pressure all the probes are slightly adjusted.

Reduction of run to run scatter

In order to reduce the run to run scatter, the steady run time Pitot pressure for each run is normalised by the steady run time barrel stagnation pressure. Three Pitot pressure time histories can be seen for the low, medium and high operating conditions in figures 3.11, 3.12 and 3.13. Typically, the steady run time for the low pressure operating condition is between 16 and 21 ms, between 18 and 23 ms for the medium and between 16 and 20ms for the high pressure operating condition. It noted, however that this is the elapsed time from the first data sample and hence triggering, caused the first shock reflection, occurs at t=4ms.

Tests for axi-symmetry

Tests were performed at nozzle exit plane at the low operating condition to establish the axi-symmetry of flow. The Pitot pressure was surveyed across the plane by rotating the rake through the following angles: 0°, 45°, 90°, 135°, 180°, 225°, 270°, 315°. The results of such measurements are found in figures 3.14 and 3.15.

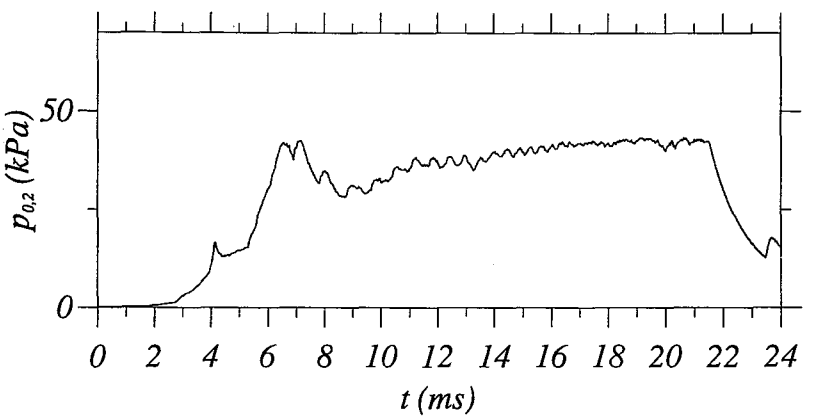


Figure 3.11: Pitot pressure time history, low pressure operating conditions. Steady run time is 16 - 21 ms.

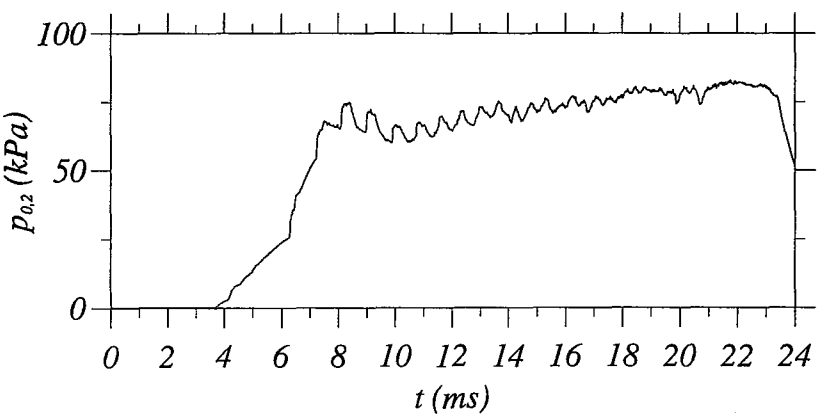


Figure 3.12: Pitot pressure time history, medium pressure operating conditions. Steady run time is 18 - 23 ms.

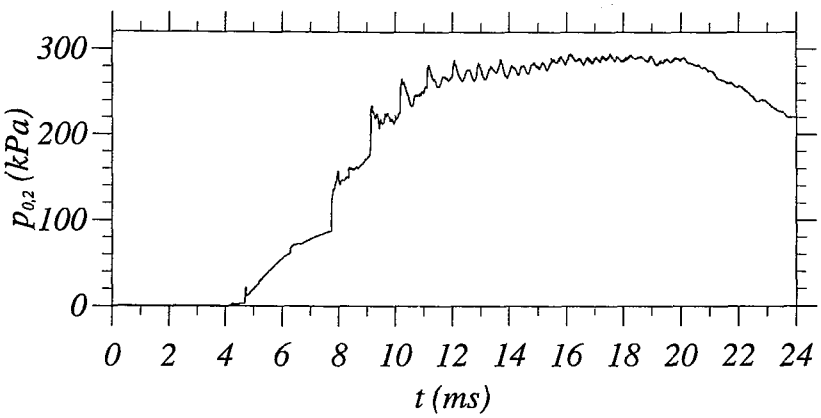


Figure 3.13: Pitot pressure time history, high pressure operating conditions. Steady run time is 16 - 20 ms.

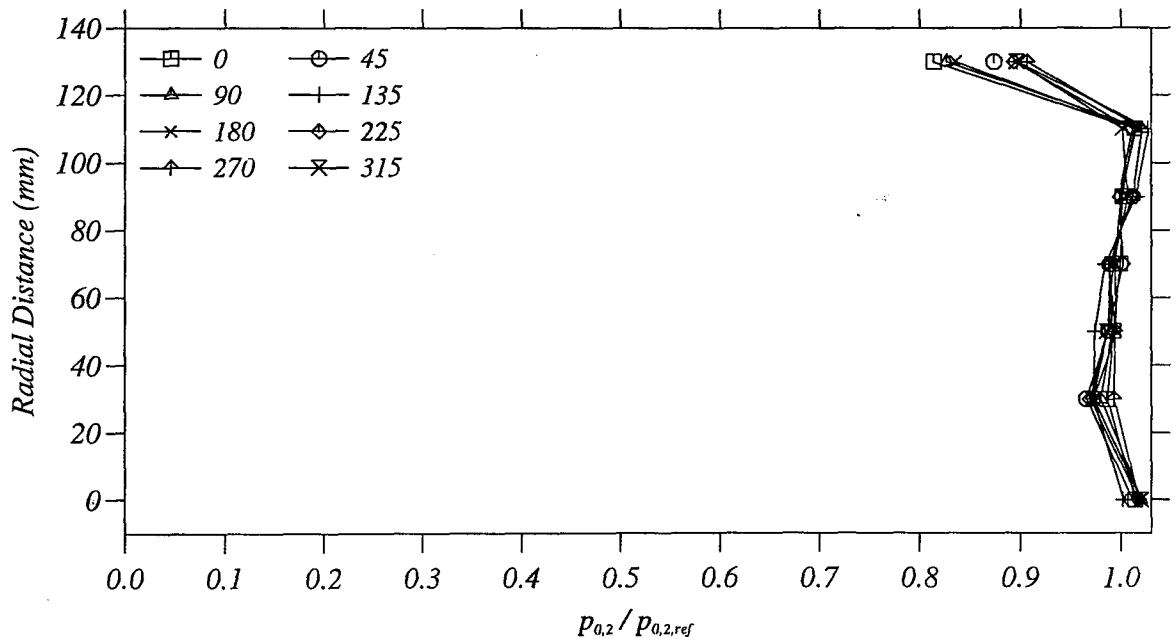


Figure 3.14: Radial profiles of normalised Pitot pressure at the nozzle exit plane.

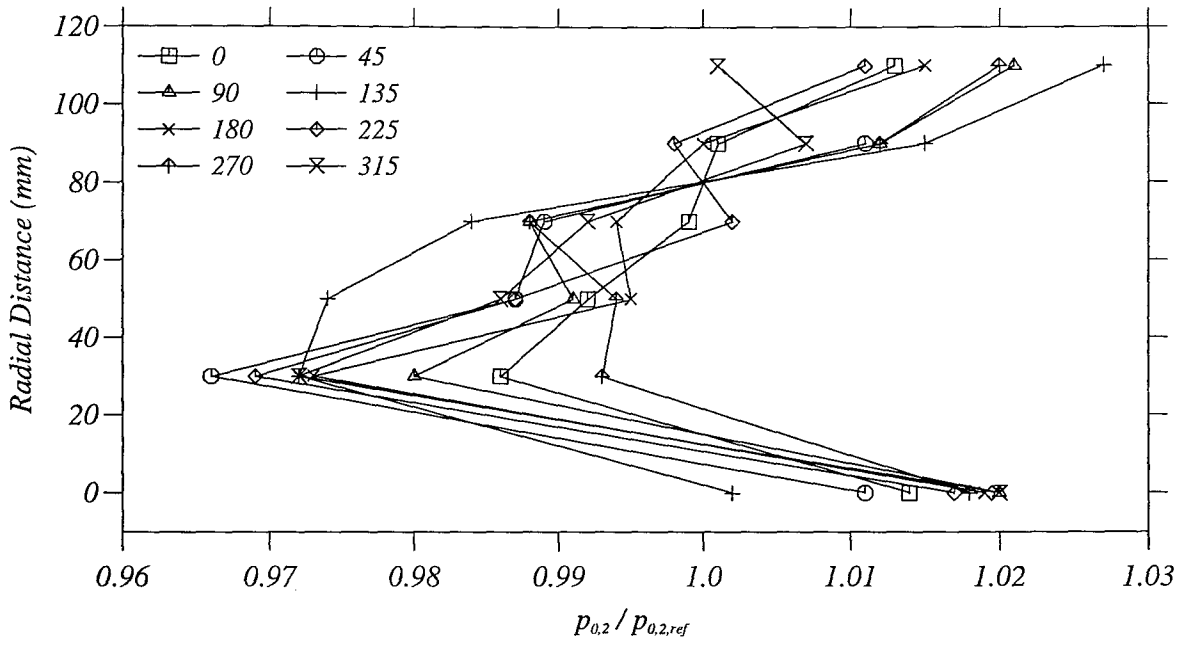


Figure 3.15: Radial profiles of normalised Pitot pressure at the nozzle exit plane.

The data are presented as normalised Pitot pressure, (x - axis), against radial distance, (y -axis). The normalisation value taken in this study is average pressure at each profile. Differences can be seen to be less than 2%. The profile trend is similar at all angles. Moving radially outwards from the centreline, the Pitot pressure drops until $r = 30mm$, then increases towards the edge of the jet. The effects of the jet boundary are present by $r = 130mm$, where the Pitot pressure drops significantly. It is concluded from figures 3.14 and 3.15 that the flow is highly axi-symmetric. From this evidence, it was decided that in the calibration process, pressure measurements need only be made at one azimuthal angle.

Pitot pressure profiles

The Pitot pressure profiles at the low, medium and high pressure operating conditions can be found in figures 3.16, 3.17 and 3.18 respectively. The data is presented as normalised Pitot pressure, $p_{(0,2)}/p_{(0,res)}$, against radial distance, $r(mm)$, at each of the measurements stations, ($z = -150mm$, $0mm$, $150mm$, $300mm$ and $450mm$). It is remarked that the horizontal scale is selected to resolve the spatial variations in

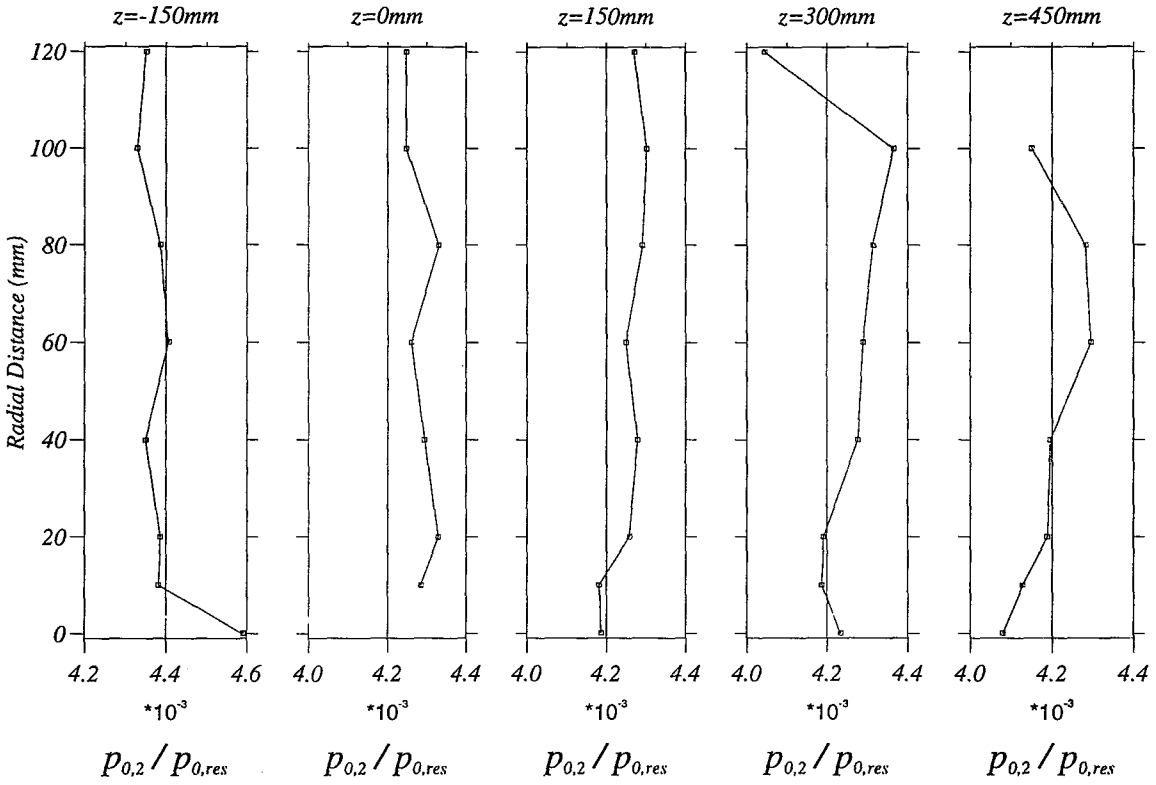


Figure 3.16: Pitot pressure profiles normalised by barrel stagnation pressure, (x -axis), against radial distance (y - axis) for five different axial locations, where z=0mm is the nozzle exit plane, low pressure operating conditions.

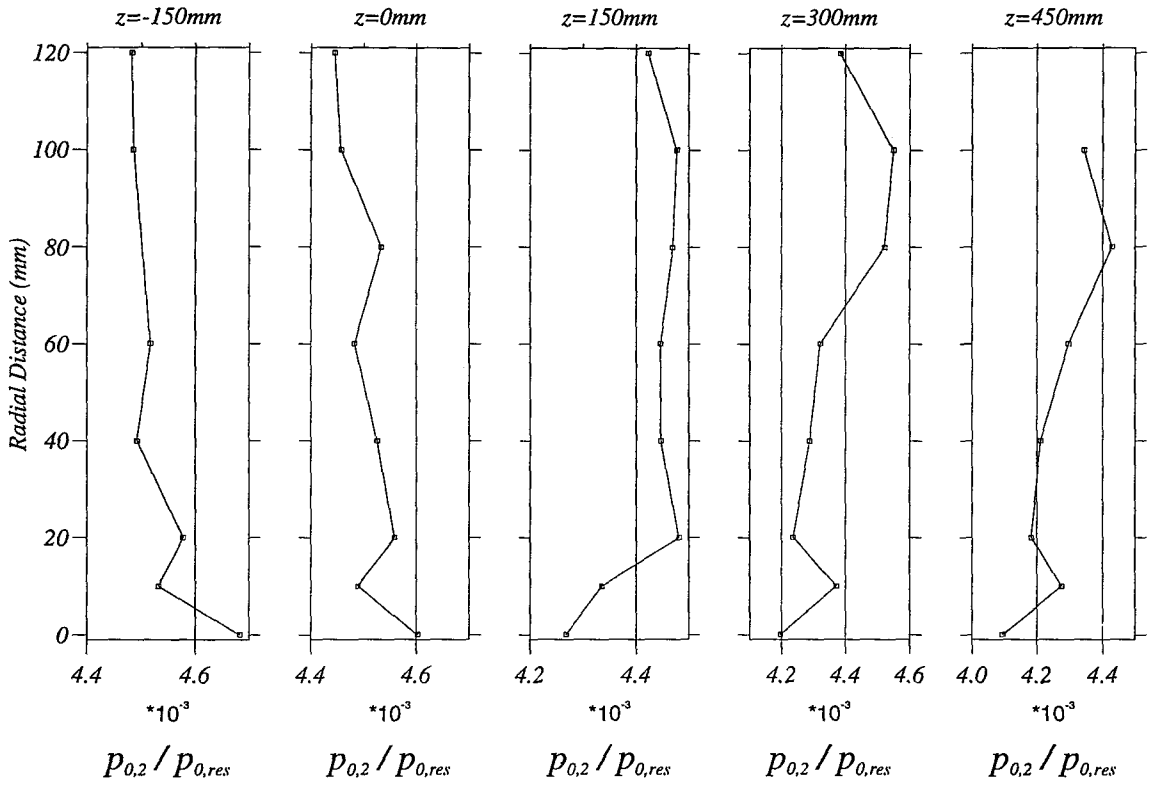


Figure 3.17: Pitot pressure profiles normalised by barrel stagnation pressure, (x-axis), against radial distance (y - axis) for five different axial locations, where z=0mm is the nozzle exit plane, medium pressure operating conditions.

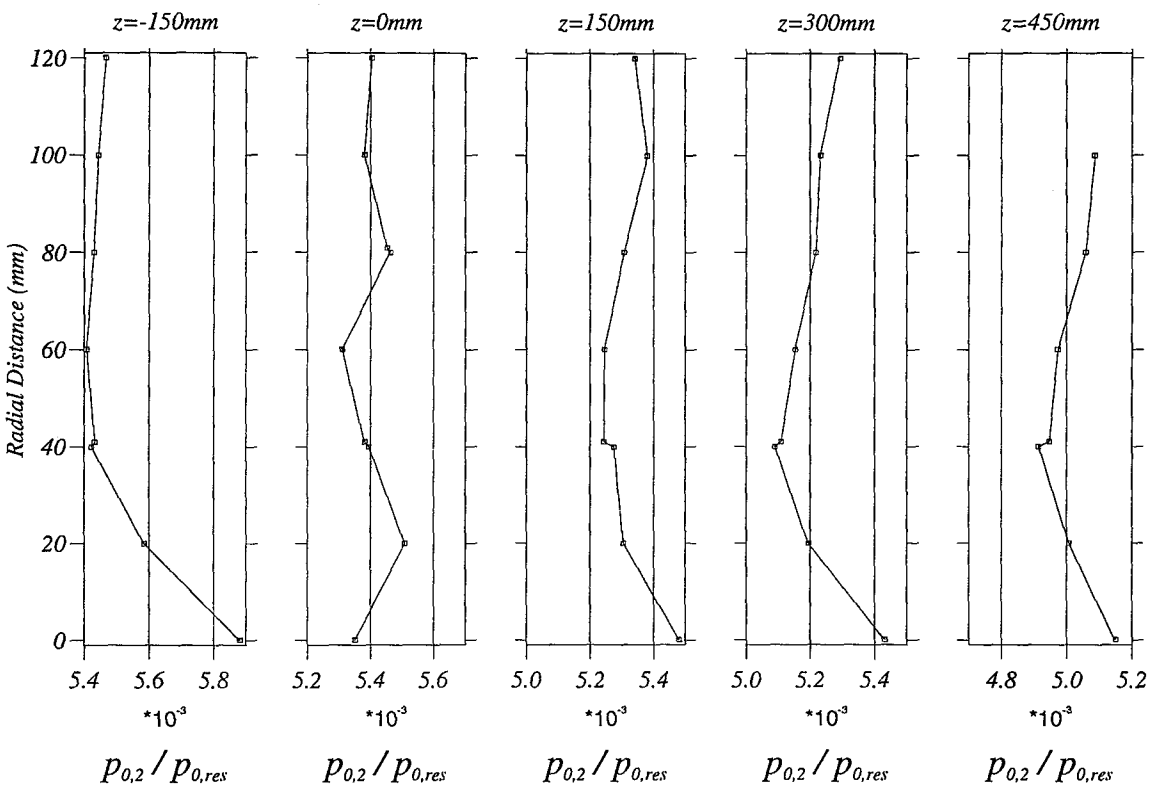


Figure 3.18: Pitot pressure profiles normalised by barrel stagnation pressure, (x -axis), against radial distance (y - axis) for five different axial locations, where z=0mm is the nozzle exit plane, high pressure operating conditions.

Pitot pressure. These are of the order of $\pm 2.5\%$ at the low and medium conditions and $\pm 2\%$ at the high pressure operating conditions. No definite radial trend can be witnessed at any given axial station. The effect of the test jet edge is noticed at the two most downstream stations at the outermost radial measurement locations.

In figure 3.19, the profiles from the five different stations are plotted on one graph. The horizontal axis, again showing normalised Pitot pressure, $p_{(0,2)}/p_{(0,res)}$, is plotted over the full range. The most apparent feature is the smoothness of the profiles, except at the outermost stations where the jet edge effects are apparent and on the centreline, $(r = 0mm)$, where the measured pressure differs considerably from the mean profile average. The latter is attributed to the focusing of the waves on the centreline.

Ignoring the centreline and edge effects, it is also seen that the Pitot pressure drops as the axial location increases, especially at the high pressure. In figure 3.20, the average normalised pressure at each of the five stations can be seen. The axial Pitot pressure gradient is now readily visible. The Pitot pressure drops by 3.87%, 5.15% and 8.37% of the nozzle exit plane value over $600mm$ for the low, medium and high pressure conditions respectively.

3.3.6 Results: cone pressure measurements

Probe calibration

The sharp cone probes are fitted with $2psi$ differential transducers. The static calibration is performed for each probe at the power supply and gain used in the successive experiments. A pressure differential is applied across the diaphragm via the reference port and the output of the transducer - amplifier system is recorded at ten pressure levels over the expected range of operation. The pressure is applied using a hand held pump and monitored using a Betz manometer. The data is used to construct the voltage - pressure slope.

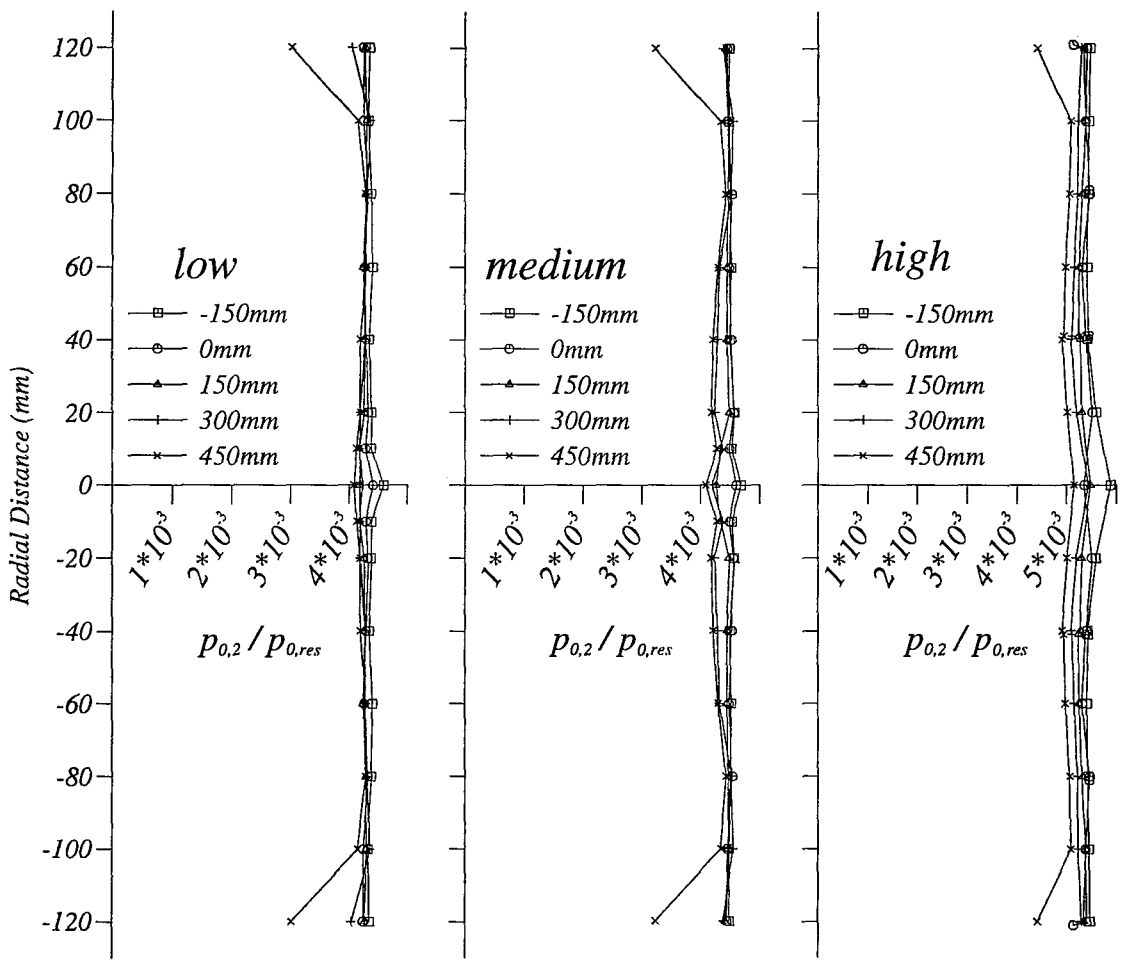


Figure 3.19: Normalised Pitot pressure radial profiles for low, medium and high operating conditions, data from all five axial stations are plotted on each graph.

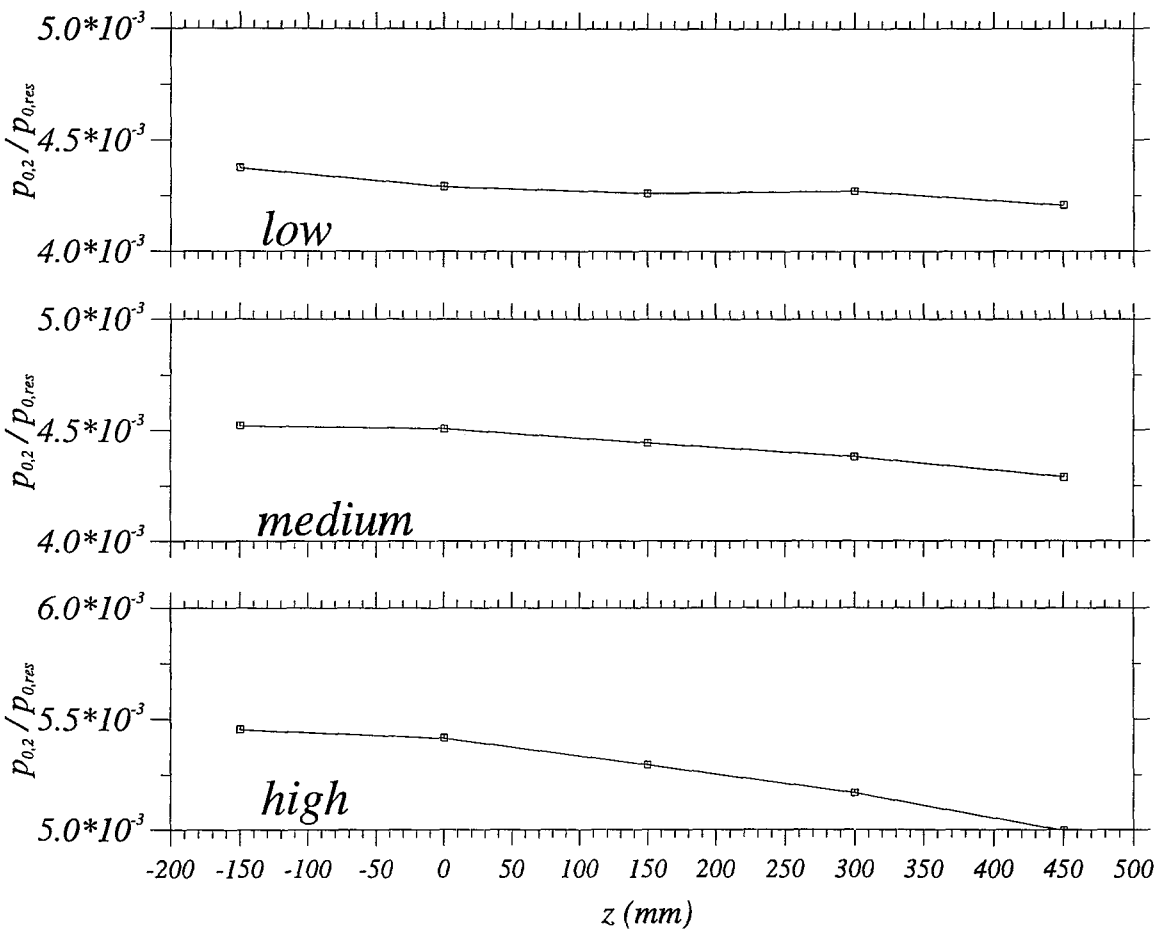


Figure 3.20: Average Pitot pressure at each axial station for low, medium and high pressure operating conditions, only data from core region included in average.

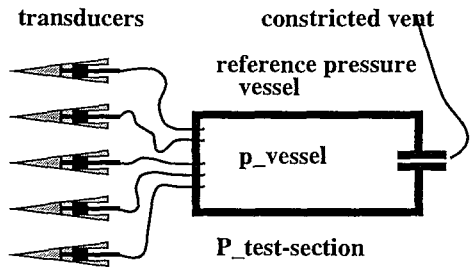


Figure 3.21: Schematic of pressure measurement system for cone pressure.

Probe operation

In operation, the reference ports are connected to a common reference pressure vessel, as indicated in figure 3.21. The reference pressure vessel is vented to the test section and the pressure in the vessel is equal to the pre run test section pressure. The vessel has however a constricted opening, such that the filling times are sufficiently long to maintain constant pressure in the vessel for the duration of a run ($20ms$) but sufficiently fast to allow the pressure to follow closely the post run re-pressurisation process (Soltani 1993). The latter is a necessary requirement as the transducer diaphragm can only support a $6psi$ pressure differential. The test section pre - run or "baseline" pressure is monitored with an Inficon pressure transducer. In the initial stages of the experiment, a 1000 Torr capacitance manometer used and was subsequently replaced by a 100 Torr manometer, more suited to the purposed of measuring typical pre run test section pressures.

Cone probe pressure profiles

The cone pressure survey for the low, medium and high pressure conditions can be found in figures 3.22, 3.23 and 3.24. The plots contain the normalised cone pressure, $p_c/p_{(0,res)}$, (x -axis), against radial location, $r(mm)$, (y -axis), at each axial location. The scales are chosen to resolve the pressure variation. The scatter can readily be seen to be less than $\pm 2\%$ at the low and medium pressure operating conditions and less than $\pm 2.5\%$ at the high pressure operating condition, comparable to the level of scatter found for the Pitot profiles. The effects of the boundary layer / jet edge are

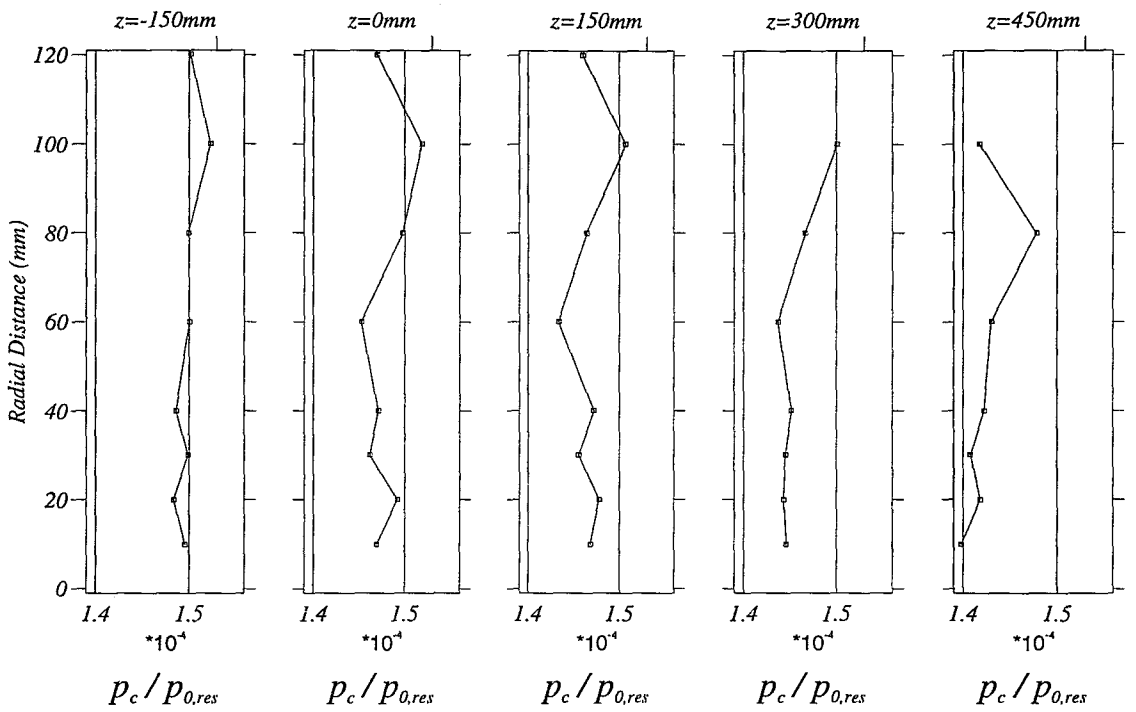


Figure 3.22: Cone probe pressure profiles normalised by barrel stagnation pressure, (x - axis) for five different axial locations, where z=0mm is the nozzle exit plane, low pressure operating conditions.

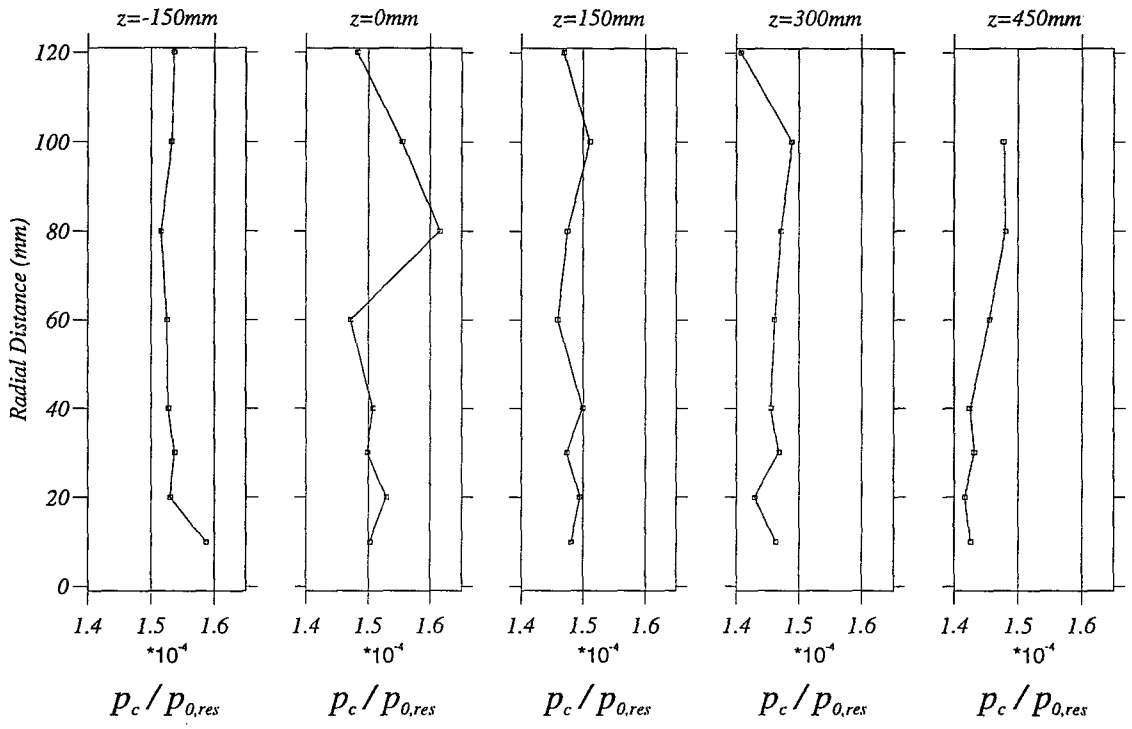


Figure 3.23: Cone probe pressure profiles normalised by barrel stagnation pressure, (x - axis) for five different axial locations, where z=0mm is the nozzle exit plane, medium pressure operating conditions.

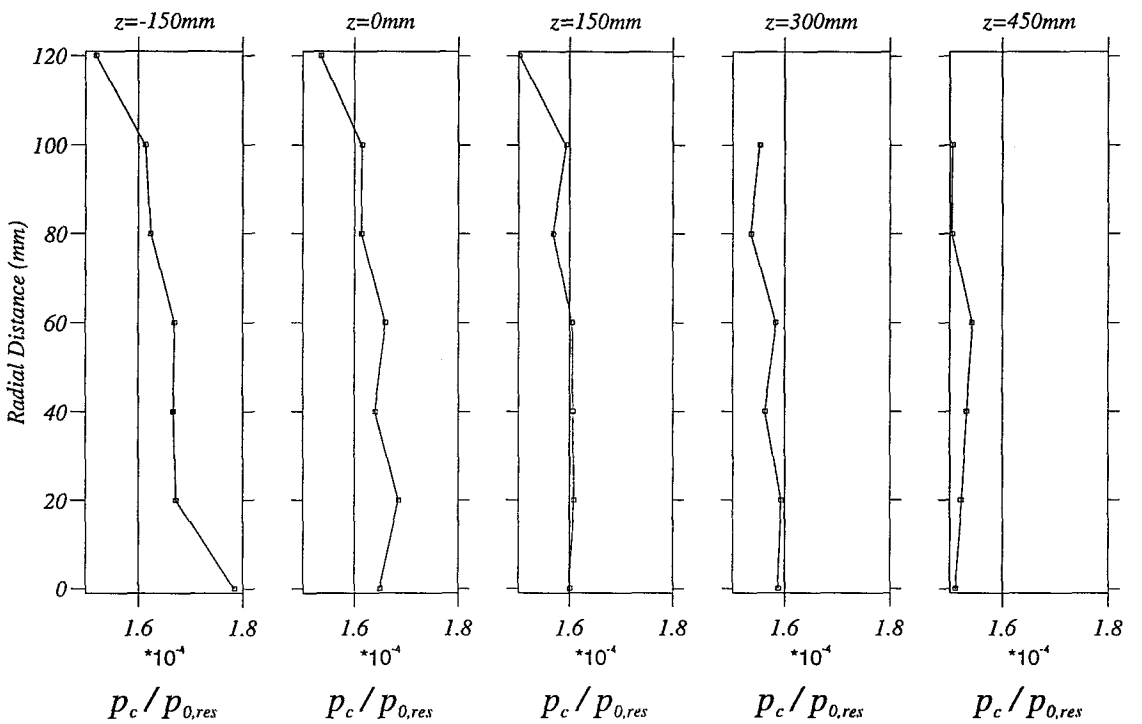


Figure 3.24: Cone pressure profiles normalised by barrel stagnation pressure, (x - axis) for five different axial locations, where z=0mm is the nozzle exit plane, high pressure operating conditions.

present at the outermost radial location ($r = 120mm$). At the two most downstream axial locations, ($z = 300mm$ and $450mm$), the jet edge is detected at the $r = 100mm$ radial station. At all stations, the profiles are smooth and show no radial trends. At the low and medium pressure operating conditions, the pressure decrease at the core boundary is contrasted by an increase at the next in-stream radial location, ($r = 100mm$). This higher pressure level may be associated with incidence effects due to flow divergence in the outer core regions. At the high pressure operating condition, the outermost probe, (r=120mm), is detecting the nozzle boundary layer when placed in the $z = -150mm$ station, the most upstream location. This indicates that the higher condition is characterised by a thicker nozzle boundary layer. Considerations about boundary layer growth imply that the boundary layer on the nozzle wall must be turbulent at the high pressure operating conditions while the low and medium pressure operating conditions may yield a laminar or transitional boundary layer over the entire nozzle wall. The state of the boundary layer has a strong importance in transition studies as it is the source of the radiated noise environment. The effects of jet edge are more readily apparent in figure 3.25, where the normalised pressure profiles have been plotted with true origin. The axial gradients in cone pressure are evident, and the average cone pressure through the core, (ignoring edge and centreline effects), at each station is plotted in figure 3.26.

3.3.7 Results: stagnation point heat transfer measurements

Total temperature and stagnation point heat transfer rate

The stagnation point solution is a classic aerodynamic problem. Various analytical solutions exist for this problem. Fay and Riddell (1958) have correlated the solutions for stagnation point heat transfer rate in terms of local properties at the boundary layer edge as follows:

$$q_w = 0.763 Pr^{-0.6} (\rho_w \mu_w)^{0.1} (\rho_{(0,2)} \mu_{(0,2)})^{0.4} (h_{(0,2)} - h_w) \sqrt{\frac{du}{dx}} \tag{3.5}$$

where Pr is the Prandtl number and the subscript w indicates properties to be evaluated at the wall conditions. To solve equation 3.5 for total temperature, it is noted that the stagnation temperature is equal to the total temperature and the equation

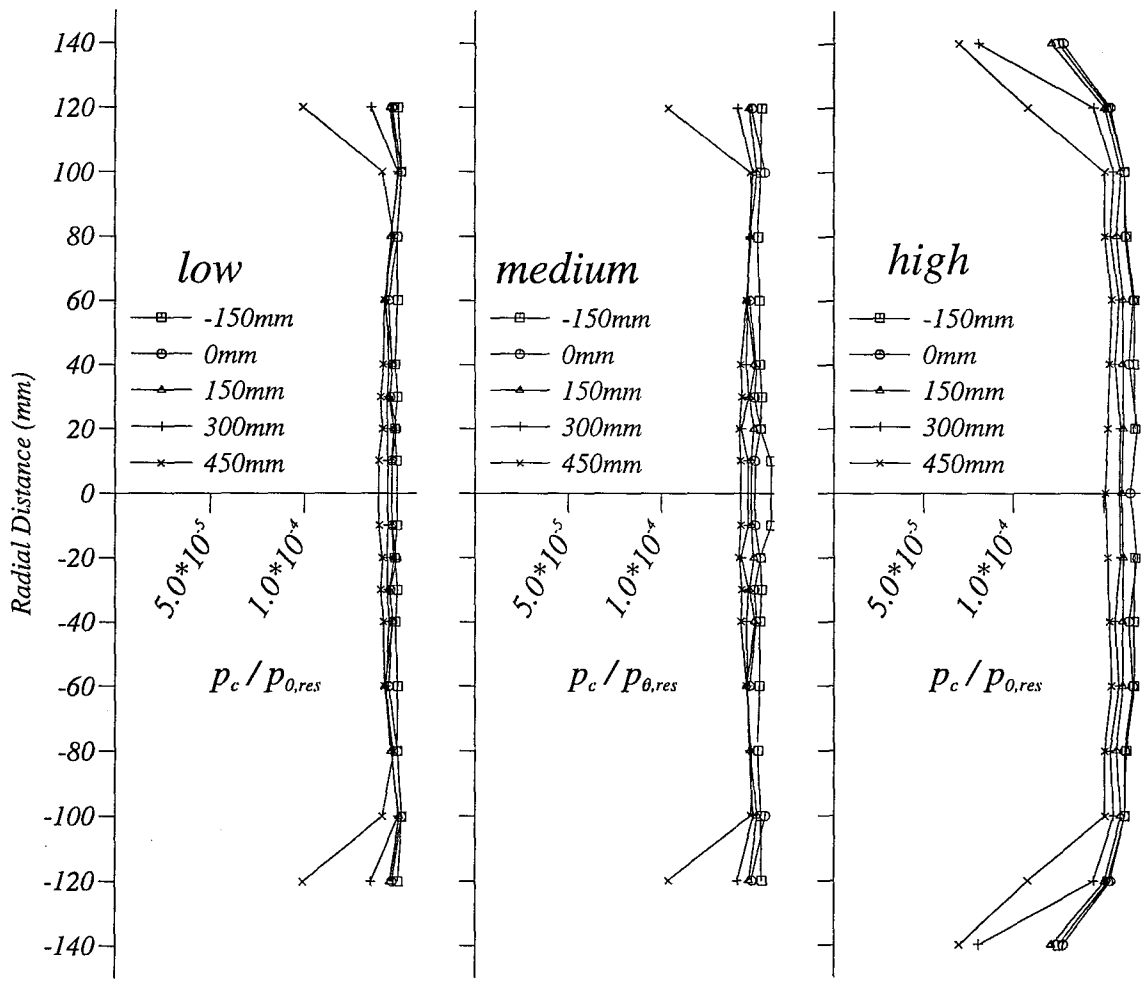


Figure 3.25: Normalised cone pressure radial profiles for low, medium and high pressure operating conditions, data from all five axial locations are plotted on each graph, z=0mm is nozzle exit plane.

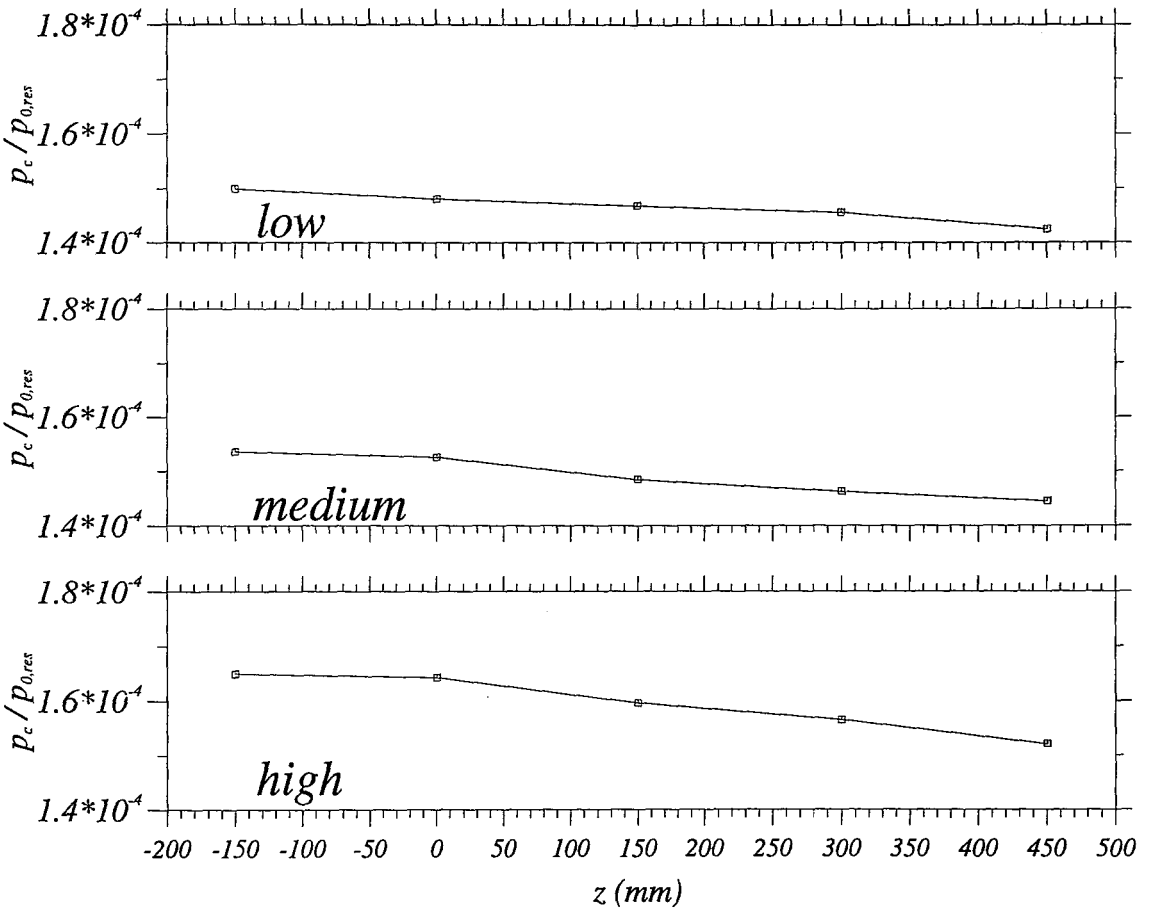


Figure 3.26: Average cone pressure at each axial station for low, medium and high pressure operating conditions, only data from core region included in the local averaging.

is re-written as:

$$q_w = 0.763 Pr^{-0.6} \left(\frac{p_{(0,2)}}{RT_w}\mu_w\right)^{0.1} \left(\frac{p_{(0,2)}}{RT_{(0,\infty)}}\mu_{(0,\infty)}\right)^{0.4} Cp(T_{(0,\infty)} - T_w)\sqrt{\frac{du}{dx}} \qquad (3.6)$$

In the calibration procedure, q_w , $p_{(0,2)}$ and T_w are measured and hence once the velocity gradient is found the total temperature can be evaluated. The term $\sqrt{du/dx}$ is calculated using CFD to obtain inviscid flow field predictions at a selection of Mach numbers, (see Soltani 1993). The normalised gradient is expressed purely as function of Mach number and probe diameter, d, as follows:

$$\frac{d(u/u_\infty)}{d(x/d)} = 458.8 + (M_\infty - 9.0) \times 10.8 \qquad (3.7)$$

Nozzle exit plane heat transfer rate measurements

Initial testing with the stagnation point heat transfer rate probes was unsuccessful. The probes were found to be readily damaged by particles in the flow. Over the period of a run, the resistance increase caused by erosion was typically 3%, compared to a 10 % increase due to actual temperature change. Clearly, the heat transfer rate averages obtained are erroneous and a more reliable set of measurements need be obtained. Two approaches are considered. The first approach is to minimise impact. The second approach, is to obtain a theoretical estimate of the total temperature by modelling the compression processes in the barrel during the run transient phase.

To reduce the probability of impact, the Melanex diaphragm at the throat was replaced by a plug. Furthermore, to increase the economy of the data acquisition process, the probes were repainted with two sensors in the stagnation region. The agreement between the two sensors on the same probe is within 2%, as shown in figure 3.27. The heat transfer traces also indicate that the gauges are generally responding to similar fluctuations in aerodynamic heating. This is apparent in figure 3.27. At present no cause can be found for the unsteadiness of the signal, it is concluded merely that they are aerodynamic in nature and not due to instrumentation or other sources of noise. A total of three runs were performed at each condition, using three probes, each with two gauges in the stagnation region. The probes were located at radial locations of -50mm, 0mm and +50mm in the nozzle exit plane. Total accumulated signal lengths in excess of $40ms$ were obtained at each condition. The mean stagnation point heat transfer rate obtained are listed in table 3.5.

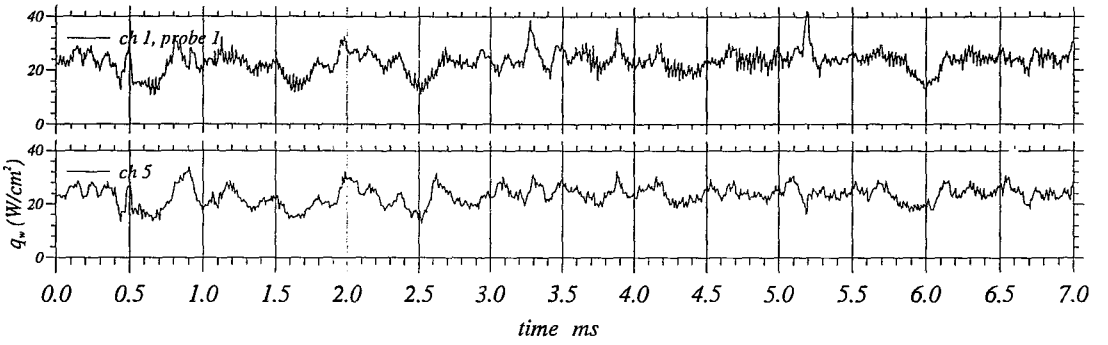


Figure 3.27: Time resolved heat transfer rates for probe 3, tested at low pressure operating condition.

low	medium	high
23.32 (W/cm^2)	33.25 (W/cm^2)	73.60 (W/cm^2)

Table 3.5: Average stagnation point heat transfer rates at nozzle exit plane for the three conditions.

Total temperature evaluation using the stagnation point heat transfer rate

The estimates for the stagnation point heat transfer rate of table 3.5 represent an average at the nozzle exit plane. The exercise of evaluating the total temperature is limited to this plane, using the average profile properties listed in table 3.6. The profile average does not include the centre line and jet edge measurements. The value obtained for total temperature at each condition will then be used to obtain a Reynolds number and Mach number distribution everywhere in the flow field in conjunction with the locally measured Pitot and cone pressure. The freestream estimates

	low	medium	high
$p_{(0,2)}$ (kPa)	45.03	78.35	294.94
p_c (kPa)	1.361	2.340	8.556
$p_{(0,1)}$ (MPa)	8.582	15.237	59.849
q_w (W/cm^2)	23.32	33.25	73.60

Table 3.6: Mean profile properties at the nozzle exit plane.

using the three calibration methods are listed for the low, medium and high pressure operating conditions in tables 3.7, 3.8 and 3.9 respectively.

3.3.8 Comparison of nozzle exit plane conditions with previous work

Extensive work has been performed at the high pressure operating condition, most importantly the work of Kirk (1993), in which surface and Pitot pressure measurements were made with a parallel body. The low pressure operating conditions were developed by Soltani (1994), and this calibration exercise represents the first attempt at calibrating the conditions. Similarly, the medium pressure operating condition was redefined for this present study and again this calibration exercise is the first attempt to measure the new stream conditions.

The previous and present estimates of the high pressure operating conditions are summarised in table 3.10. The present exit plane Mach number is in good agreement

	$p_{(0,2)}$ $p_{(0,1)}$ method	p_c $p_{(0,1)}$ method	$p_{(0,2)}$ p_c method
M_∞	8.89	8.89	8.87
p_∞ (Pa)	441.	441.	442.
$p_{(0,1)}$ (MPa)	8.582	8.582	8.473
T_0 $°K$	1028	1028	1028
Re_∞ $/m$	7.86 $\times 10^6$	7.6 $\times 10^6$	7.82 $\times 10^6$

Table 3.7: Mean profile properties at the nozzle exit plane at the low pressure operating conditions.

	$p_{(0,2)}$ $p_{(0,1)}$ method	p_c $p_{(0,1)}$ method	$p_{(0,2)}$ p_c method
M_∞	8.93	8.93	8.89
p_∞ (Pa)	760.	761.	766.
$p_{(0,1)}$ (MPa)	15.237	15.237	14.880
T_0 $°K$	1090	1090	1090
Re_∞ $/m$	12.62 $\times 10^6$	12.64 $\times 10^6$	12.50 $\times 10^6$

Table 3.8: Mean profile properties at the nozzle exit plane at the medium pressure operating conditions.

	$p_{(0,2)}$ $p_{(0,1)}$ method	p_c $p_{(0,1)}$ method	$p_{(0,2)}$ p_c method
M_∞	9.01	9.01	9.02
p_∞ (Pa)	2810.	2803.	2803.
$p_{(0,1)}$ (MPa)	59.849	59.849	59.603
T_0 $°K$	1184	1184	1184
Re_∞ $/m$	42.68 $\times 10^6$	42.66 $\times 10^6$	42.69 $\times 10^6$

Table 3.9: Mean profile properties at the nozzle exit plane at the high pressure operating conditions.

study	M_∞	$Re_{\infty/m}$ $(\times 10^6)$	$T_{(0,\infty)}$ (° K)	$p_{(0,\infty)}$ (MPa)
Needham et al. (1971)	9.00 $\pm$0.07	55.	1070$\pm$10	-
Elfstrom (1971)	9.	-	1070	-
Bartlett et al. (1979)	9.26	55	1064	-
Edwards et al. (1981)	9.21 $\pm$ 0.15	55.07	1064 $\pm$ 15	-
Sell (1992)	9.15	55.0	1063	600 $\pm$ 60
Kirk (1993)	8.9 $\pm$ 0.1	55.0 $\pm$ 0.5	1063 $\pm$ 5	600 $\pm$ 60
present study	9.01	42.7	1184	598

Table 3.10: Estimated tunnel conditions by various workers.

with the work to date, with the exception of Edwards et al. and Bartlett et al., who provide a higher estimate. It is felt that the present value of 9.01 is a more exact estimate. The static pressure computed using $p_{(0,\infty)}$ = 596 MPa and M_∞ =9.01 is p_∞=2810 Pa. This value is in close agreement with the estimate obtained from the model surface measurements of Soltani of 2813 Pa. The estimate of Soltani is obtained from the alignment pressure measurements, using CFD to obtain the ratio of wall pressure at the alignment station to the freestream pressure. The alignment pressure tappings were located in the nozzle exit plane.

There is a big discrepancy in the total temperature and Reynolds number estimate. The total temperature is 11% higher and the Reynolds number 14 % lower than the typical values previously reported. As the Mach number predictions are in agreement, this discrepancy must be a result of inaccuracies inherent to the method of evaluating total temperature or due to stagnation point heat transfer measurement problems. To appraise the validity of the Fay and Riddell formula, its predictive capability is matched against a full Navier - Stokes solution around a 1mm hemispherically blunted nose. The computational solution gives a stagnation point heat transfer rate of 436 W/cm^2, the Fay and Riddell formula, using the CFD predicted velocity gradient, yields 439.6 W/cm^2. The results are in excellent agreement, indicating that the Fay and Riddell formula can be used confidently. There is none the less strong evidence to suggest that the present total temperature estimate is incorrect, in particular the work of Bartlett et al. In their work, the total temperature was measured directly using shielded thermocouples probes: incorporating the real gas correction of Culotta and Richards, their data give a total temperature estimate of about 1100 ° K. To reconciliate this disturbing discrepancy, it has been attempted to infer $T_{(0,\infty)}$ directly. Firstly, an upper and lower temperature estimate can be made. The lowest total temperature is achieved when the compression process occurs isentropically. In this case, the barrel stagnation temperature, $T_{(0,res)}$, is given by:

$$T_{(0,res)} = T_{barrel}\left(\frac{p_{(0,res)}}{p_{barrel}}\right)^{\frac{\gamma-1}{\gamma}} \tag{3.8}$$

Using the appropriate pre run conditions, the estimate for reservoir temperature is 930 ° K. The upper limit arises when the test gas is compressed by a single shock (incident and reflected) which takes the test gas to some condition p_5 and T_5, as indicated in figure 3.28. The process is completed by a final isentropic compression from conditions (p_5, T_5) to ($p_{(0,res)}$, $T_{(0,res)}$). The pressure p_5 is evaluated using shock

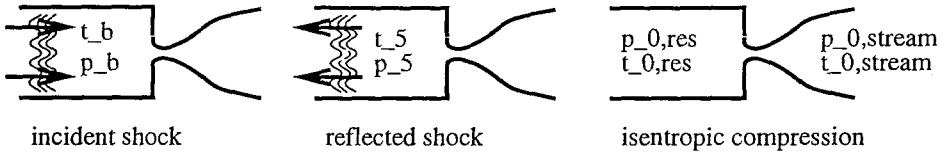


Figure 3.28: Schematic of the compression process used in the analysis of total temperature.

tube theory. For a pressure ratio of 92.4, this gives p_5/p_{barrel}=25. with T_5=953. ° K. Allowing the gas to compress then to $p_{(0,res)}$ gives $T_{(0,res)}$=1205. ° K.

The pressure ratio after the reflection of the first shock, p_5/p_{barrel} can also be determined from the barrel stagnation pressure time history. From a selection of traces analysed, it is found that p_5/p_{barrel}=15.1. Using this value to estimate T_5 and subsequently the stagnation temperature, a second better estimate for $T_{(0,res)}$ of 1096 ° K is found. This value is clearly in better agreement with the work of Bartlett et al. and in agreement with the estimate using stagnation point probes of Coleman, reported in Needham et al. (1970). The estimates above were performed assuming a perfect gas behaviour. The calculations have been extended to allow for real gas effects and also to allow two shocks to process and reflect through the test gas. Again, the pressure increases due to the passage of the first and second shock are obtained from the barrel pressure history and yield an estimate for the freestream total temperature of $T_{(0,\infty)}$ =1107 ° K, for an initial barrel temperature of 300 ° K.

The evidence presented above indicates that the total temperature at the high pressure operating conditions is overestimated using the stagnation point probe. Although the exact cause of this discrepancy has not been identified there are various possible sources, and it is felt that for the flow field calibration the total temperature will be fixed at 1105 ° K. At the low and medium operating pressure conditions, comparisons with other work are limited. The freestream pressure inferred by Soltani (1994) at the low pressure conditions is 435 Pa and the pressure inferred by Mallinson is 451 Pa. These values are in close agreement with the present estimate of 441 Pa. At the medium pressure operating conditions Soltani estimates p_∞= 788 Pa, close to the present value of 760 Pa. This suggests that at the low and medium pressure, the Mach number and total pressure deduced are correct, however doubts connected

operating condition	M_∞	$Re_{\infty/m} \times 10^6$	$T_{(0,\infty)}$ (° K)	$p_{(0,\infty)}$ (MPa)
low	8.89	7.51	1060	8.582
medium	8.93	12.62	1090	15.237
high	9.01	47.35	1105.	59.849

Table 3.11: Nozzle exit plane conditions

with the correctness of the total temperature estimates arise. It is felt that the total temperature estimate at the medium pressure operating condition need not be corrected, however, the low pressure operating condition total temperature is increased to 1060 ° K. Using these updated estimates, the nozzle plane exit conditions have been recalculated and are given in table 3.11. In conclusion to this subsection, it is noted that the total temperature estimates given provide good laminar heat transfer rate predictions for both the cone and flat plate geometries examined.

3.3.9 Results: Mach number field

The Mach number profiles can be found in figures 3.29, 3.30 and 3.31, for the low, medium and high pressure operating conditions respectively. For each condition, the three Mach number estimates are plotted against radial distance at five axial locations. Observing Mach number estimates for the low pressure operating conditions in figure 3.29, it is seen that method (1) and method (2) give close agreement everywhere in the flow field. The Mach number evaluated using method (3) shows greater fluctuations with radial distance, caused by the method's greater sensitivity to experimental error. It is also noted that the M_∞ profiles are uniform at the z=-150mm, z=0mm (nozzle exit) and z=150mm planes. At z=300 and z=450mm, there is an increase in Mach number at the outer (r=120mm) radial station. This is due to the presence of the jet edge which decreases the measured pressures locally and as $p_{(0,\infty)}$ is assumed constant, it leads to an increase in the calibrated Mach number. Considering only the uniform central core (r=0 to 100mm, typically), it can seen that there is a progressive increase in the Mach number estimate. The average Mach number at each location can be seen plotted in the top graph of figure 3.36. Again, it can be witnessed here that method (3) is prone to greater scatter. Using the values inferred from method (1), a Mach

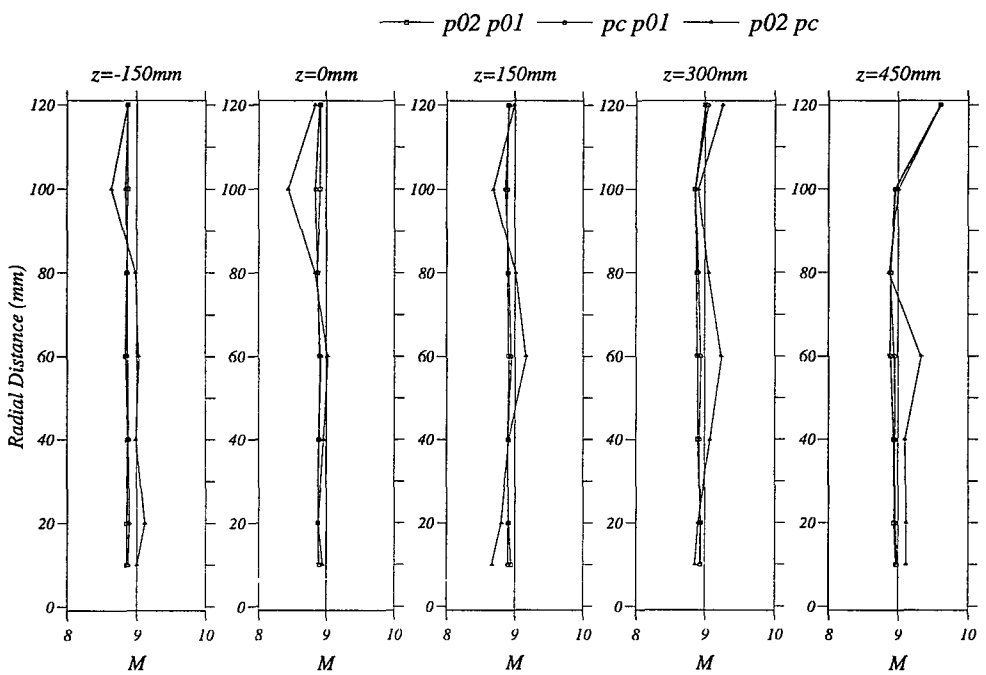


Figure 3.29: Mach number profiles at five different axial locations, where z=0mm is the nozzle exit plane, at the low pressure operating conditions. Captions: squares (p02p01) method 1; circles (pcp01) method 2 and triangles (p02pc) method 3.

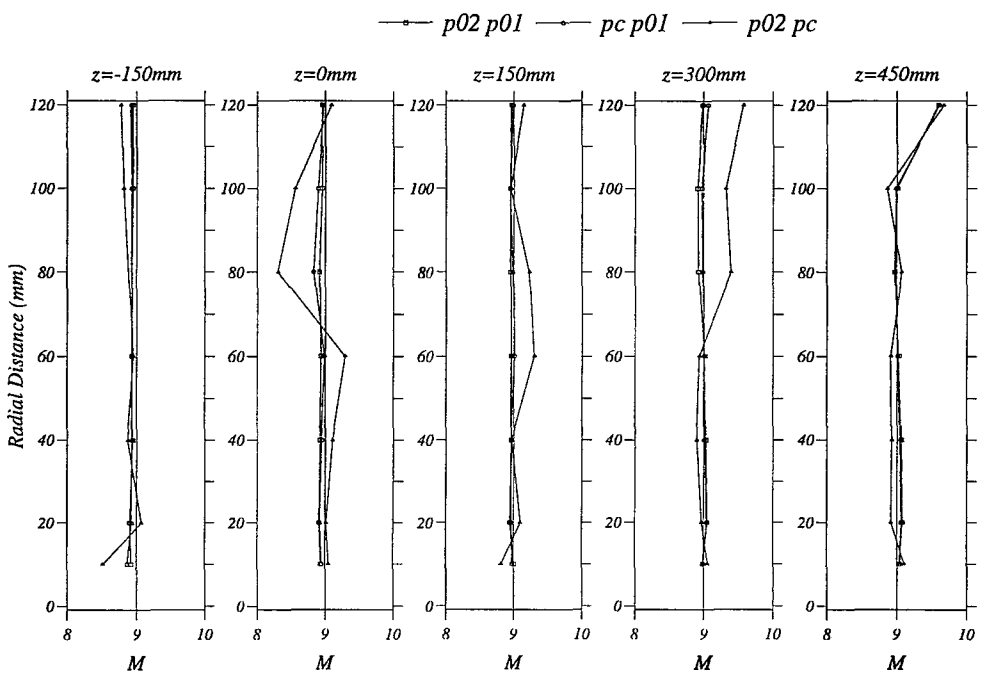


Figure 3.30: Mach number profiles at five different axial locations, where z=0mm is the nozzle exit plane, at the medium pressure operating conditions. Captions: squares (p02p01) method 1; circles (pcp01) method 2 and triangles (p02pc) method 3.

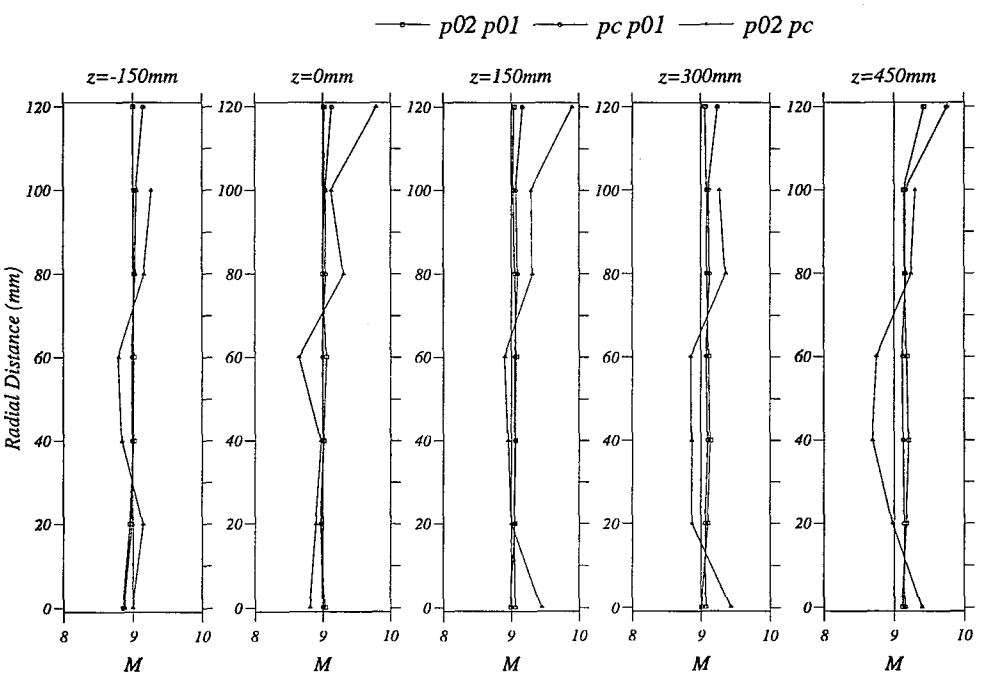


Figure 3.31: Mach number profiles at five different axial locations, where z=0mm is the nozzle exit plane, at the high pressure operating conditions. Captions: squares (p02p01) method 1; circles (pcp01) method 2 and triangles (p02pc) method 3.

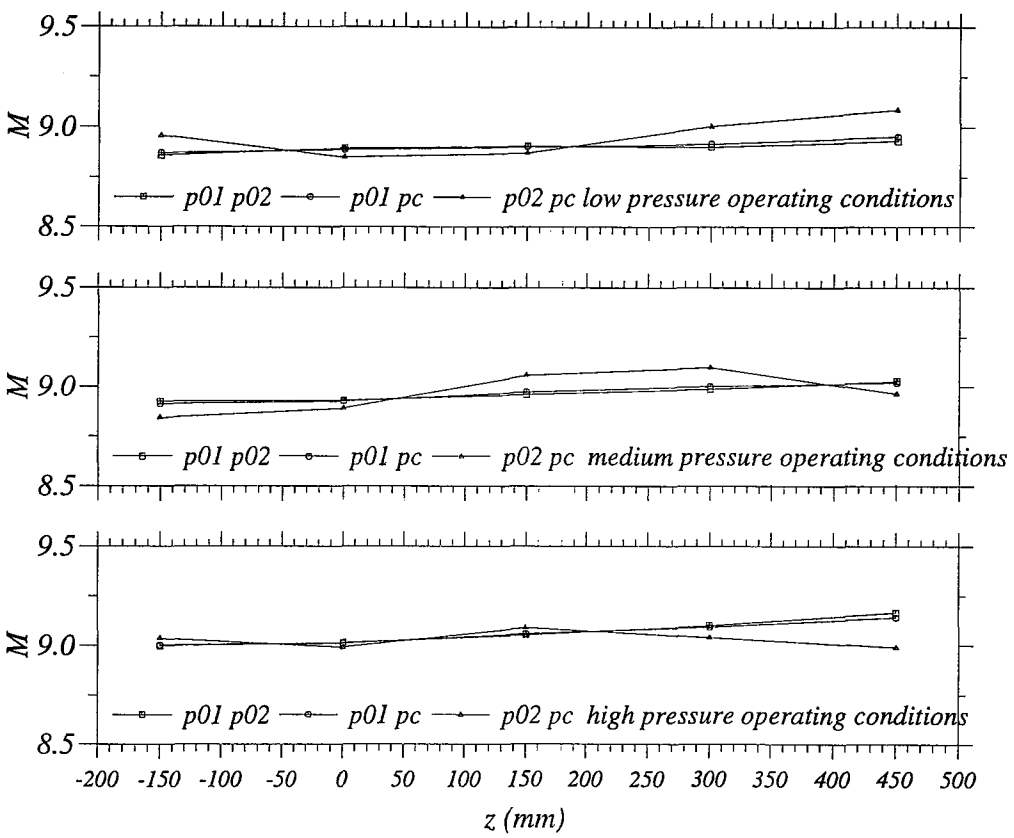


Figure 3.32: Average Mach number each axial station for low, medium and high pressure operating conditions, only data from core region included in average. Captions: squares (p02p01) method 1; circles (pcp01) method 2 and triangles (p02pc) method 3.

number test section gradient can be calculated. The average gradient, normalised by the exit plane Mach number for the low pressure operating condition, is 1.31 %/m.

At the medium pressure operating condition, figure 3.30, it is seen that the Mach number estimates by method (1) and method (2) are again in close agreement and indicate no radial trend. Method (3) shows greater variation, especially at the points where the other two methods show a degree of discrepancy. This indicates that the variation is not physical in origin and is a consequence of measurement error. An increase in Mach number can be found at the outermost location (r=120mm) at the two downstream locations (z=300mm and z=450mm), again attributed to jet edge effects. Also noted, is the greater divergence between method (1) and method (2) estimates immediately in-stream of these locations, possibly indicating greater local flow angularity, (from the probe dynamics, it is expected that method (2) is the most sensitive to angularity). The Mach number gradient, normalised by the nozzle exit plane Mach number, is estimated from the middle plot of figure 3.32. This is calculated to be 1.9%/m.

The high pressure operating condition Mach number profiles are shown in figure 3.31. Examining first the profile obtained at the station within the nozzle, (z=-150mm), a radial trend can be observed, a feature not encountered at any of the other operating conditions. The gradient shows an increase in Mach number as one moves outwards towards the nozzle wall, possibly indicating that the nozzle flow is still slightly divergent at this station. At the nozzle exit plane, the gradient appears less pronounced and it is felt that at the z=150, 300 and 450mm stations, no radial gradient is present. The jet edge is only apparent at the outermost radial location and the most downstream axial location, r=120mm, z=450mm. In the bottom plot of figure 3.32, the average Mach number for each axial location is plotted. The z=-150mm and z=0mm stations present a constant Mach number followed by a subsequent increase with distance downstream. The Mach number gradient for the entire test section is calculated to be 3.13 %/m, however, if a bi-linear fit is used, in which the Mach number is kept constant between z=-150 to 0mm and from thereon allowed to vary, the gradient is 4.2 %/m.

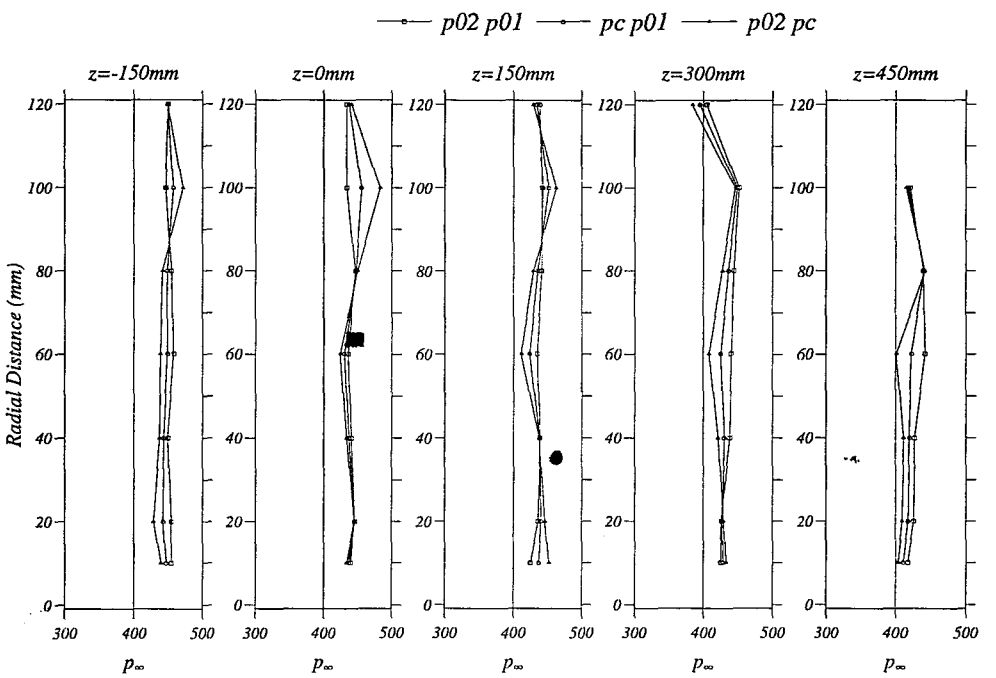


Figure 3.33: Static pressure profiles, (in Pa), at five different axial locations, where z=0mm is the nozzle exit plane, at the low pressure operating conditions. Captions: Box, pressure estimate after Soltani (435 Pa); •, pressure estimate after Mallinson (451 Pa); lines with squares, (p02p01) method (1); lines with circles, (pcp01) method (2) and lines with triangles, (p02pc) method (3).

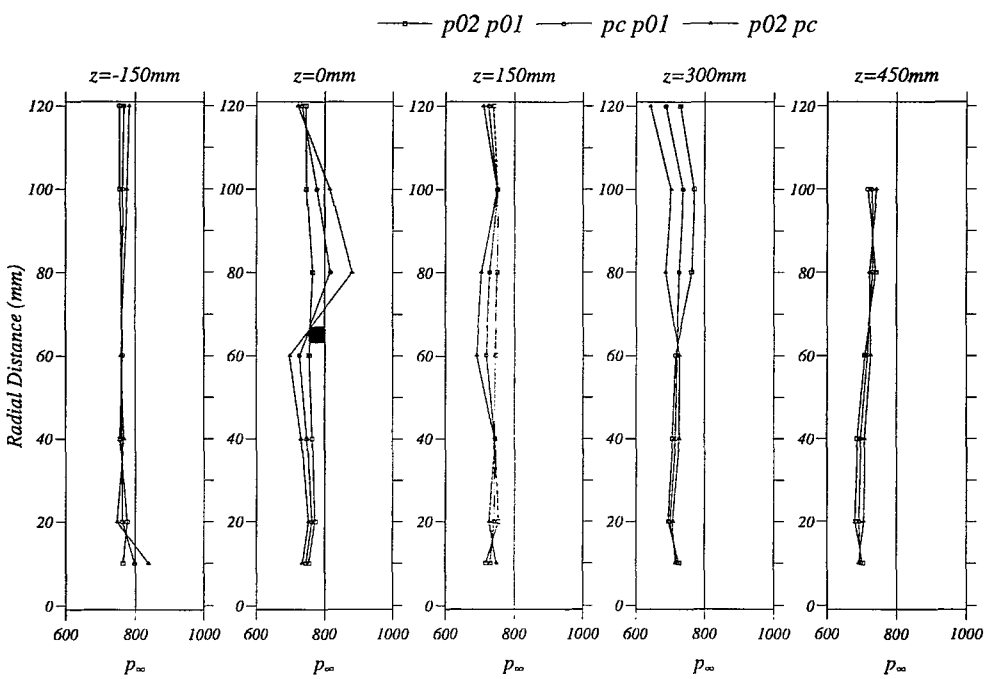


Figure 3.34: Static pressure profiles, (in Pa), at five different axial locations, where z=0mm is the nozzle exit plane, at the medium pressure operating conditions. Captions: Box, pressure estimate after Soltani (788 Pa); lines with squares, (p02p01) method (1); lines with circles, (pcp01) method (2) and lines with triangles, (p02pc) method (3).

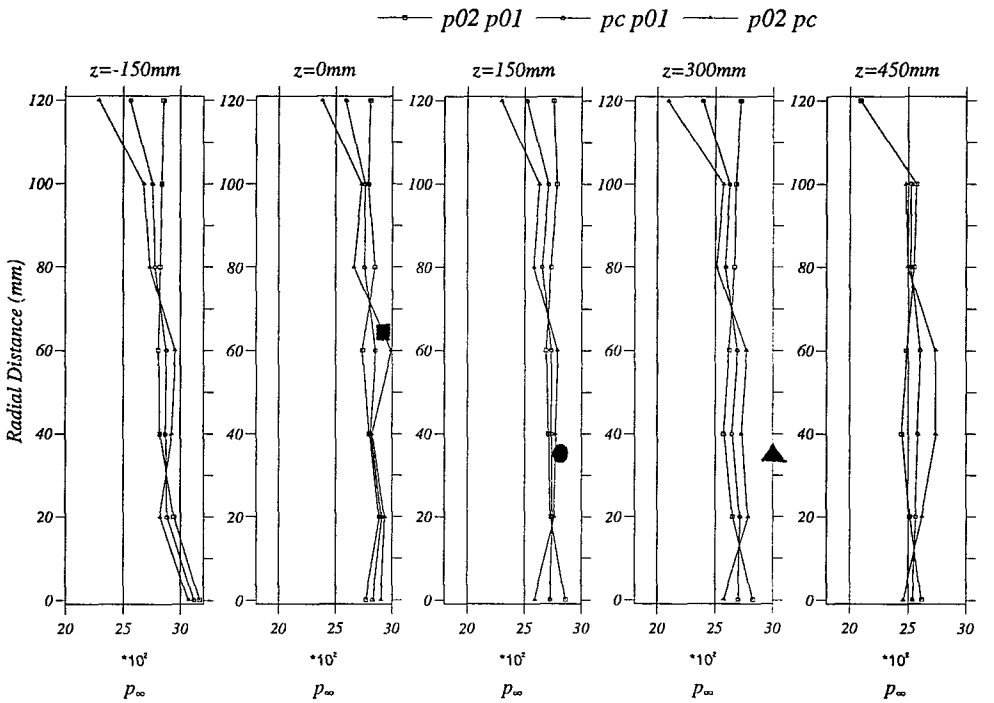


Figure 3.35: Static pressure profiles, (in Pa), at five different axial locations, where z=0mm is the nozzle exit plane, at the high pressure operating conditions. Captions: Box, pressure estimate after Soltani (2813 Pa); •, pressure estimate after Mallinson (2825 Pa); ▲, pressure estimate after Kirk (2986 Pa); lines with squares (p02p01), method (1); lines with circles (pcp01), method (2) and lines with triangles (p02pc), method (3).

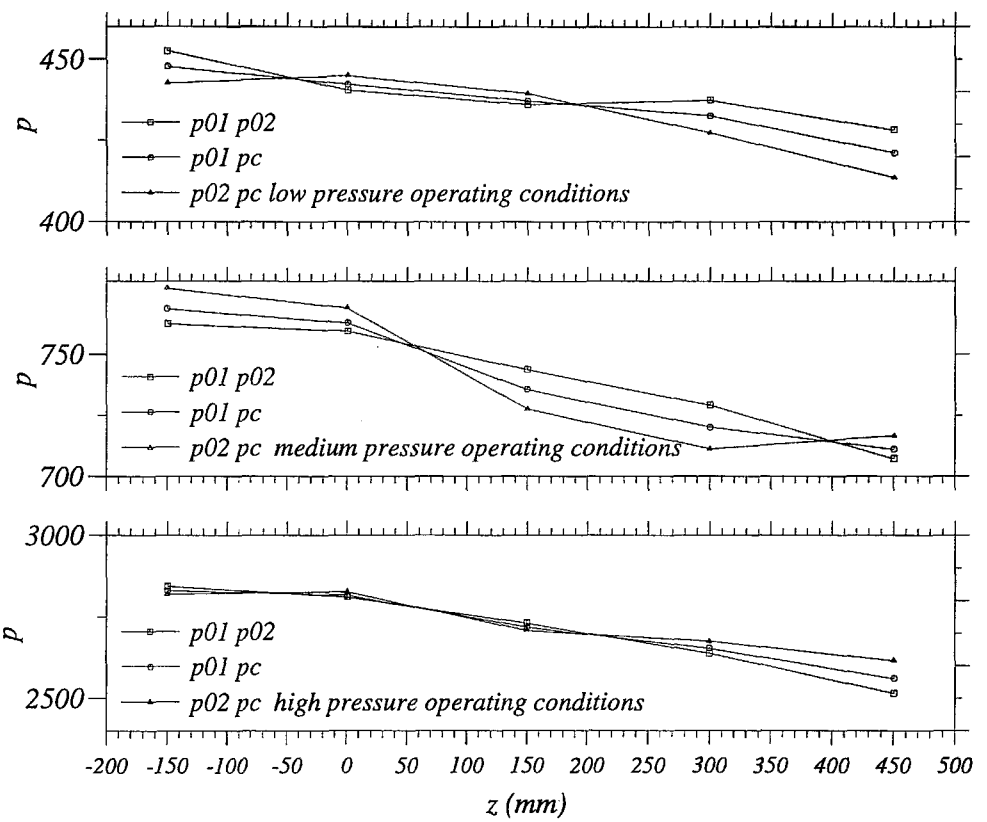


Figure 3.36: Average static pressure (in Pa), at each axial station for low, medium and high pressure operating conditions, only data from core region included in average. Captions: squares (p02p01) method 1; circles (pcp01) method 2 and triangles (p02pc) method 3.

3.3.10 Results: static pressure field

The static pressure profiles for the low pressure operating conditions can be found in figure 3.33. The horizontal scale has limits of 300 and 500 Pa, in order to resolve the radial and axial variations. At most points in the domain, the three methods give similar estimates for static pressure. Typically method (1) provides the highest M_∞ estimate, indicating that there may be some systematic error. In any case, the variation between estimates is small, and the exercise is felt to be successful. Included in figure 3.33 are two data points, obtained from test model surface pressure measurements (corrected for viscous effects) by Soltani (1994), indicated by the dark square, and Mallinson (1996), indicated by the dark circle. The presence of the models in the flow field obviously changes the flow field distribution, however, the pressure values indicated here are offered for comparison and are in good quantitative agreement with the static pressure predicted. At the three upstream calibration locations the pressure distribution is uniform in the radial directions., At the z=300 and 450mm stations, the jet boundary can be witnessed. The mean plane average static pressures are plotted against axial location, in the usual fashion in figure 3.36. Using method (1), the average pressure gradient, normalised by the exit plane pressure is -9%/m. This compares well to the calculated Mach number gradient, if one postulates the isentropic result that $p_\infty \propto -M_\infty^{-7}$.

The medium pressure operating condition static pressure profiles can be seen in figure 3.34. At the z=-150mm location, there is an excellent agreement between the three calibration methods. At other stations, the agreement is good, with method (3) presenting the greatest degree of scatter. The data point of Soltani, (square), is found to be in close agreement with the pressure predicted. No stations present any radial trend, with the pressure being constant with the exception of the locations where the jet boundary is impinging, (r=120mm, z=300 and 450mm). The axial trend indicates a decrease in static pressure in the core. This decrease in calculated using figure 3.36 to be -12.3%/m, based on nozzle exit values.

The static pressure field at the high pressure operating condition is shown in figure 3.35. The pressure predicted by the three different methods is typically within $\pm$ 5% and the agreement between method (1) and method (2) is generally better than $\pm$ 2%. At the most upstream radial location, there appears to be a decrease of

static pressure with increasing radius, consistent with the notion of increasing Mach number. The static pressure estimates after Soltani, Mallinson and Kirk have also been included in figure 3.35. The most noticeable feature is the drop of static pressure in the axial direction. This is clearly seen in figure 3.36. The pressure distribution, consistent with the Mach number distribution, would be best represented with a bi-linear curve, the gradient of which would present a maximum slope of -23.4%/m. This is equivalent to a gradient of -658 Pa/m^3, in agreement with the indirect estimates of Sell (1992) of -556 Pa/m^3; and Lin and Harvey (1987) of -861 Pa/m^3. Denman (1990) estimates a pressure gradient of -1540 Pa/m^3 which may be due to the fact that in these experiments a large angle cone was used, causing the surface pressure gradient to be related to the freestream pressure gradients arising at positions much further downstream.

3.3.11 Results: total pressure Field

The total pressure profiles for the low, medium and high pressure operating conditions are shown in figures 3.37, 3.38 and 3.39. The lines with circles indicate the total pressure inferred from the barrel stagnation pressure and the lines with squares indicate the total pressure calculated with method (3). The total pressure estimate inferred from $p_{(0,res)}$, is constant through the entire flow field, and this is one of the main assumptions of method (1) and method (2). The method (3) total pressure estimate is based on the local measurements, and albeit sensitive to experimental error, provides a true estimate for total pressure. In figure 3.37, 3.38 and 3.39, it is seen that the $p_{(0,\infty)}$ distribution calculated in this manner is, within the expected error band, constant both in the radial and axial direction. More importantly, the total pressure evaluated in this manner is good agreement with the $p_{(0,\infty)}$ obtained from $p_{(0,res)}$. This indicates firstly that there are no shocks present in the flow field, validating the assumptions of constant total pressure and also that all three Mach numbers, static pressure and total pressure estimates have converged to the same "calibration solution".

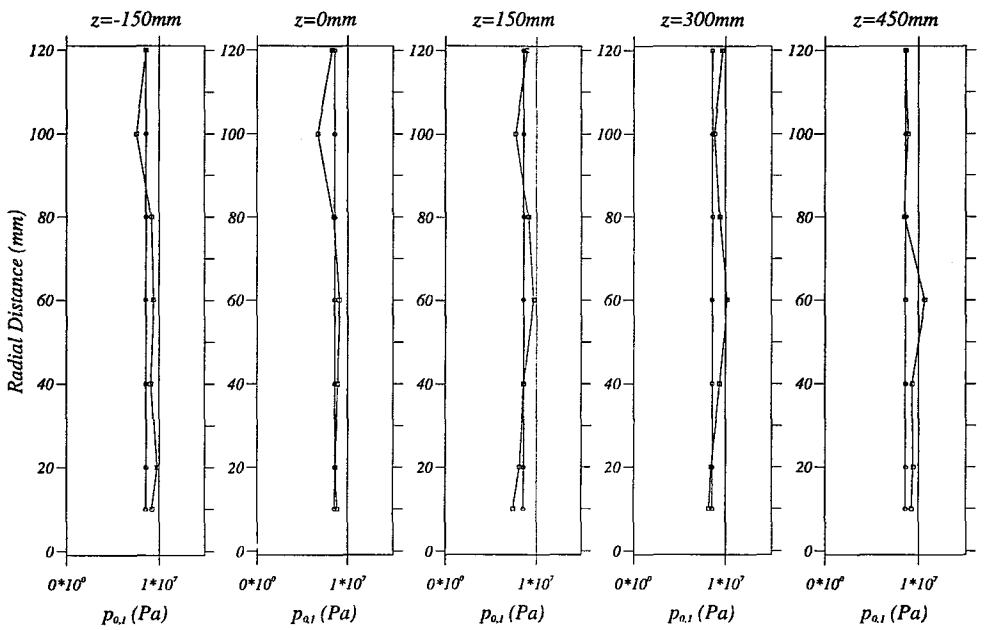


Figure 3.37: Total pressure profiles, (in Pa), at five different axial locations, where z=0mm is the nozzle exit plane, at the low pressure operating conditions. Captions: lines with circles, total pressure inferred from barrel pressure; lines with squares, total pressure, method (3).

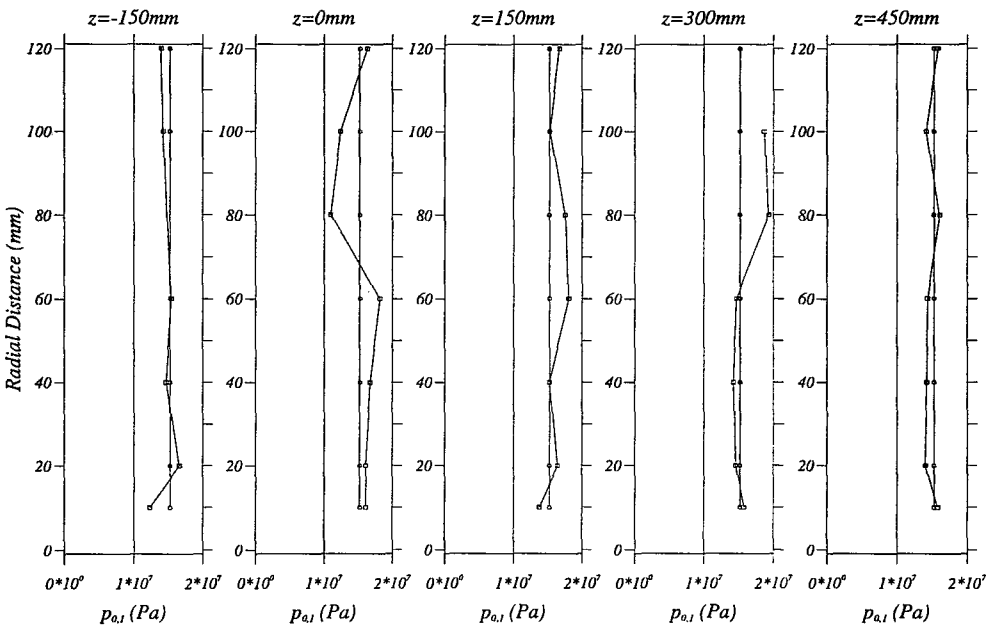


Figure 3.38: Total pressure profiles, (in Pa), at five different axial locations, where z=0mm is the nozzle exit plane, at the medium pressure operating conditions. Captions: lines with circles, total pressure inferred from barrel pressure; lines with squares, total pressure, method (3).

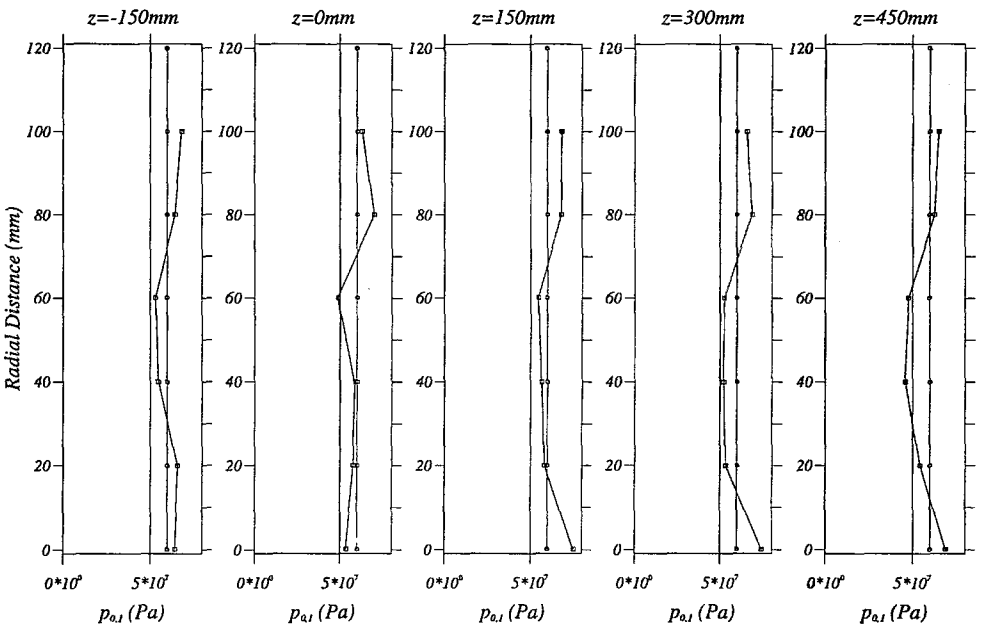


Figure 3.39: Total pressure profiles, (in Pa), at five different axial locations, where z=0mm is the nozzle exit plane, at the high pressure operating conditions. Captions: lines with circles, total pressure inferred from barrel pressure; lines with squares, total pressure, method (3).

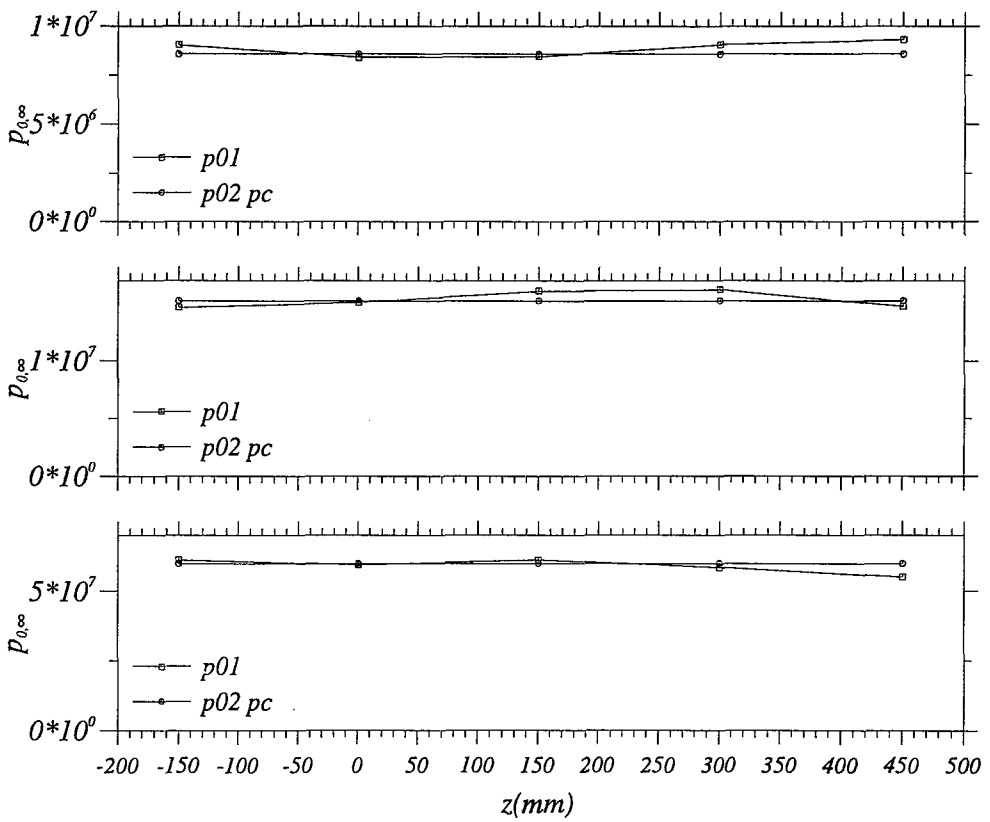


Figure 3.40: Average total pressure (in Pa), at each axial station for low, medium and high pressure operating conditions, only data from core region included in average. Captions: circles, total pressure inferred from barrel pressure; squares, total pressure, method 3.

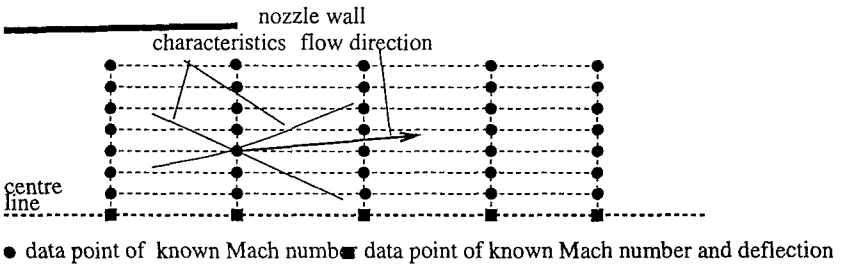


Figure 3.41: Schematic of data mesh to be used to determine flow angularity, using centreline information.

3.3.12 Results: flow angularity

The exercise of determining the flow angularity has not been completed, however sufficient information is available to performed the exercise. It is suggested to perform an axi-symmetric method of characteristics calculation to obtain the flow angularity. For an axi-symmetric flow, the characteristic directions are the Mach lines given by:

$$\left(\frac{dr}{dz}\right)_{char} = \tan(\theta \pm \mu) \tag{3.9}$$

where θ, is the streamline inclination to the z-axis, (the flow angularity) and μ is the Mach angle. Along the characteristic lines, the compatibility equations hold, these are given below, taking +, for the left running wave, and - for the right running waves:

$$d(\theta + \nu) = \pm \frac{1}{\sqrt{M^2 - 1} \pm \cot\theta} \frac{dr}{r} \tag{3.10}$$

where ν is the Prandtl - Meyer function. In the present problem, one can construct a mesh of data points at which the Mach number and Prandtl Meyer function are known, as indicated in figure 3.41. As the flow inclination, θ, is zero along the nozzle centre-line, characteristic lines can be found, allowing the solution to be marched between data points and the flow angularity determined. The centreline is however characterised by the focusing of Mach waves (characteristic lines) in axi - symmetric flow, which may present certain undesirable features. To overcome this, the present data can be used in conjunction with model surface information (Kirk 1993, Millevoi 1993), along which the flow defection can be equated to the displacement thickness slope, as shown in figure 3.42, and used as a boundary condition together with the known Mach number to march out the characteristics.

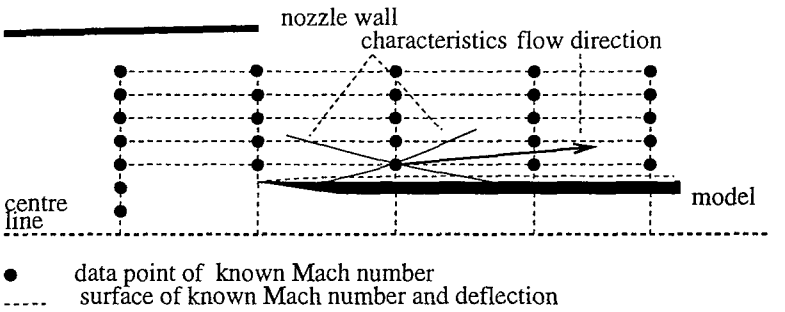


Figure 3.42: Schematic of data mesh to be used to determine flow angularity, using model information.

3.4 Concluding remarks

The calibration exercise has proved highly successful. The three methods have been used and show excellent agreement for estimated Mach number, static pressure and total pressure over the entire calibration domain. Axial trends at all conditions indicate a positive Mach number gradient. At the high pressure operating conditions, the calibrations indicated a radial increase in Mach number in the nozzle, (station z=-150mm). Difficulties were encountered in obtaining an accurate stagnation point heat transfer rate estimate with the flat faced probes. The time resolved signal is unsteady and furthermore, the probes were found to be prone to impact damage, causing an erroneous estimation. Due to these problems, a total temperature survey was not performed and in the flow field calibration exercise, the total temperature was postulated to be 1060, 1090 and 1105 ° K, at the low, medium and high pressure operating conditions respectively. It is felt that the flow field is free of shocks and that the core is in excess of 240mm in diameter, except at the z=300 and z=450mm planes where the jet boundary is encountered at r=120mm. At the low pressure operating condition, the nozzle boundary layer impinges on the outermost station, (z=-150mm r=120mm). The finalised conditions are summarised in table 3.12.

condition	M_∞	$Re_{\infty/m}$ $\times 10^6$	$T_{(0,\infty)}$ (° K)	$p_{(0,\infty)}$ (MPa)	$\frac{1}{M_\infty}\frac{dM_\infty}{dz}$ (%/m)
low	8.89	7.51	1060	8.582	1.3
medium	8.93	12.62	1090	15.237	1.9
high	9.01	47.35	1105.	59.849	3.1

Table 3.12: Nozzle exit plane conditions, including Mach number gradient estimates.

Chapter 4

Numerical analysis

The computational and experimental work in this study are closely integrated. The development verification and validation of the has been extensively documented by Kirk (1993), Hillier et al. (1993), Sell (1992), Hillier et al. (1992), Prodromou and Hillier (1991), Netterfield (1991) and Hillier and Netterfield (1990).

The solver had been used previously for the blunt body problem by Sell (1992), where the predictions were compared to the measured surface heat transfer, surface pressure, Pitot pressure profiles and schlieren images. In the present study, no further fundamental analysis was required. However, more than sixty blunt cone and cylinder geometries were analysed, requiring considerable effort in data handling and iterative development of highly resolved solutions. This chapter is divided in two parts. Firstly the features of the code are presented to familiarise the reader with the solution method. The description of the code is not intended to be exhaustive and the reader is referred to Kirk (1993) for a complete overview of the code. The second half of this chapter will examine how CFD is used to analyse the basic flow field considered in this study.

4.1 The computational method

The code is a high resolution Navier stokes solver for 2D planar and 2D axi-symmetric problems. In two dimensional cylindrical coordinates the governing equations are:

$$\frac{\partial \mathbf{U}}{\partial t} + \frac{\partial \mathbf{E}_H}{\partial x} + \frac{\partial \mathbf{F}_H}{\partial r} + \frac{(\mathbf{F}_H + \mathbf{G}_H)}{r} = \frac{\partial \mathbf{E}_V}{\partial x} + \frac{\partial \mathbf{F}_V}{\partial r} + \frac{(\mathbf{F}_V + \mathbf{G}_V)}{r} \tag{4.1}$$

where x and r indicate the axial and radial direction respectively and **U**, **E**, **F** and **G** are given by:

$$\mathbf{U} = \begin{bmatrix} \rho \\ \rho u \\ \rho v \\ \rho e \end{bmatrix} \mathbf{E}_H = \begin{bmatrix} \rho u \\ p + \rho u^2 \\ \rho uv \\ u(p + \rho e) \end{bmatrix} \mathbf{F}_H = \begin{bmatrix} \rho v \\ \rho uv \\ p + \rho v^2 \\ v(p + \rho e) \end{bmatrix} \mathbf{G}_H = \begin{bmatrix} 0 \\ 0 \\ -p \\ 0 \end{bmatrix}$$

$$\mathbf{E}_V = \begin{bmatrix} 0 \\ \tau_{xx} \\ \tau_{xy} \\ -q_{xx} + u\tau_{xx} + v\tau_{xy} \end{bmatrix} \mathbf{F}_V = \begin{bmatrix} 0 \\ \tau_{xy} \\ \tau_{yy} \\ -q_{yy} + u\tau_{xy} + v\tau_{yy} \end{bmatrix} \mathbf{G}_V = \begin{bmatrix} 0 \\ 0 \\ -\tau_{\theta\theta} \\ 0 \end{bmatrix} \tag{4.2}$$

Equation 4.1 is expressed in a time dependent form and the hyperbolic terms have been separated from the diffusive terms. To distinguish the essentially convective hyperbolic terms, the subscript $_H$ has been added. The diffusive terms are given the subscript $_V$.

The viscous stress τ_{xx}, etc. and the heat fluxes, q_{xx}, appearing in the terms on the right hand side of equation 4.1 take the usual form for laminar flow:

$$\tau_{xx} = (\lambda + 2\mu)\frac{\partial u}{\partial x} + \frac{\lambda}{r}\frac{\partial}{\partial r}(rv); \quad \tau_{xy} = \mu\left(\frac{\partial u}{\partial r} + \frac{\partial v}{\partial x}\right); \tag{4.3}$$

$$\tau_{yy} = (\lambda + 2\mu)\frac{\partial v}{\partial r} + \lambda\left(\frac{\partial u}{\partial x} + \frac{v}{r}\right); \quad \tau_{\theta\theta} = (\lambda + 2\mu)\frac{v}{r} + \lambda\left(\frac{\partial u}{\partial x} + \frac{\partial v}{\partial r}\right) \tag{4.4}$$

$$q_{xx} = -k\frac{\partial T}{\partial x}; \qquad q_{yy} = -k\frac{\partial T}{\partial r} \tag{4.5}$$

with

$$3\lambda + 2\mu = 0 \tag{4.6}$$

and

$$Pr = \frac{Cp\mu}{k} \tag{4.7}$$

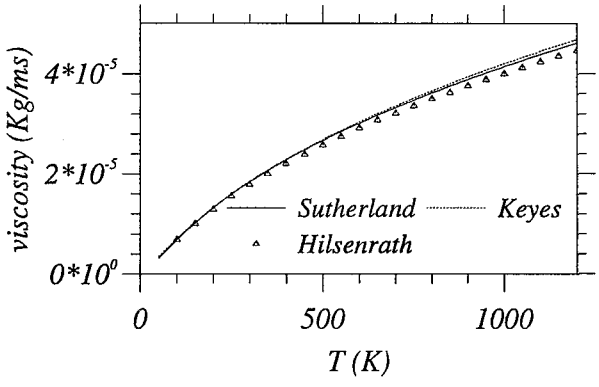


Figure 4.1: Viscosity variation with temperature using the algebraic formulation of Sutherland, Keyes and the tabulated values of Hilsenrath.

The Prandtl number, Pr, is considered constant over the temperature range of the computations, and taken as 0.72. The viscosity however, shows a more sensitive temperature dependence. In the paper of Hilsenrath (1960), the viscosity is tabulated against temperature, while Sutherland (1895) and Keyes (1952) have developed algebraic formulations, given in equations 4.8 and 4.9 respectively.

$$\frac{\mu}{\mu_{ref}} = \left(\frac{T}{T_{ref}}\right)^{3/2} \left(\frac{T_{ref}+C}{T+C}\right) \tag{4.8}$$

where for nitrogen μ_{ref}=1.711 $\times 10^{-5}$, T_{ref}=273.15 K and C equals 110.4 K.

$$\frac{\mu}{\mu_{ref}} = \frac{T^{1/2}}{1 + aT^{-1}10^{-(a_1/T)}} \tag{4.9}$$

with $\mu_{ref} = 1.418 \times 10^{-6}$, a=116.4 and a_1=5. The three distributions are plotted over the temperature range of the computations in figure 4.1. Both algebraic expression give a good representation of Hilsenrath's data. Sutherland's formulation follows more closely at the higher temperatures but as Keyes' formulation captures the behaviour better at lower temperatures, this method is favoured.

The solution to equation 4.1 is obtained by time marching to some steady state which is considered the final solution. The advancement at each time step employs "convection - diffusion" splitting. This concept is elaborated is more detail below.

4.1.1 Convection diffusion splitting

This is based on the premise that at the core of any good Navier-Stokes solver there must lie a good inviscid scheme. The practicality of splitting the convective and diffusive terms also reflects the development of the code, in which one first develops an Euler solver, capable of resolving all the "interesting" inviscid features, then one "adds on" the viscous extension. Given the operator $L_H(\Delta t)$, which advances the convective part of equation 4.1 and $L_V(\Delta t)$, the operator which advances in time the viscous part of equation 4.1 the solution vector $\mathbf{U}$, is updated between time levels N and $N+1$, as indicated in equation 4.10.

$$\mathbf{U}^{N+1} = L_V\left(\frac{\Delta t}{2}\right) L_H(\Delta t) L_V\left(\frac{\Delta t}{2}\right) \mathbf{U}^N \tag{4.10}$$

Equation 4.10 indicates that one first applies the operator $L_V(\Delta t/2)$ to $\mathbf{U}^N$ to update the solution in a viscous manner over half the time step, then the solution is advanced by a whole time step, ΔT using the convective operator, L_H, and finally the viscous operator is applied again to update the solution by the remaining half time step. The symmetrical nature of equation 4.10 is required to retain second order accuracy when the individual operators are themselves second order. Having illustrated the convection - diffusion splitting solution strategy, the inviscid and viscous terms can be discussed independently.

4.1.2 Convective terms

The inviscid part of equation 4.1 is given below:

$$\frac{\partial \mathbf{U}}{\partial t} + \frac{\partial \mathbf{E}_H}{\partial x} + \frac{\partial \mathbf{F}_H}{\partial r} + \frac{\overbrace{(\mathbf{F}_H + \mathbf{G}_H)}^{s}}{r} = 0 \tag{4.11}$$

This equation can be solved in two dimensions, or split into a sequence of "one-dimensional passes" in which the equation is solved in the two quasi-normal directions of the mesh, ξ, η. Again, one can formulate the sequence of operations which update the solution vector, $\mathbf{U}$, in the two mesh directions as follows:

$$\mathbf{U}^{N+1} = L_\eta\left(\frac{\Delta t}{2}\right) L_\xi\left(\frac{\Delta t}{2}\right) L_s(\Delta t) L_\xi\left(\frac{\Delta t}{2}\right) \ldots L_\eta\left(\frac{\Delta t}{2}\right) \mathbf{U}^N \tag{4.12}$$

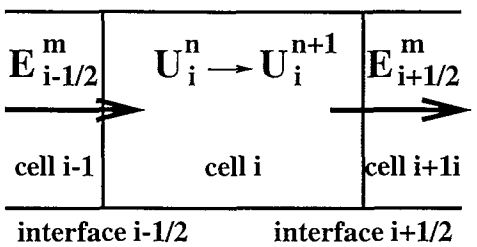


Figure 4.2: Schematic of 1D problem, the discrete solution updates the cell properties **U** by calculating the fluxes **E** at both cell interfaces.

---

where L_ξ and L_η are the operators which update the solution in the direction ξ and η respectively. The operator L_s updates the "source-like" terms indicated by the over-brace in equation 4.11. The strength of the method lies in its ability to accurately predict flux terms. The approach chosen follows the Godunov type scheme suggested by Ben-Artzi and Falcovitz (1983 and 1984) which in turn is closely related to the work of Van Leer (1979). To illustrate its implementation as a high resolution solver only the one dimensional time dependent formulation need be considered here. The equation to solve is thus:

$$\frac{\partial \mathbf{U}}{\partial t} + \frac{\partial \mathbf{E}_H}{\partial x} = 0 \tag{4.13}$$

with

$$\mathbf{U} = \begin{bmatrix} \rho \\ \rho u \\ \rho e \end{bmatrix} \quad \mathbf{E}_H = \begin{bmatrix} \rho u \\ p + \rho u^2 \\ u(p + \rho e) \end{bmatrix} \tag{4.14}$$

In the integrated form equation 4.13 is expressed as:

$$\int_{x_1}^{x_2} [\mathbf{U}(t + \Delta t) - \mathbf{U}(t)]dx - \int_t^{t+\Delta t} [\mathbf{E}(x_l) - \mathbf{E}(x_r)]dt \tag{4.15}$$

where $\mathbf{E}(x_l)$ and $\mathbf{E}(x_r)$ are the left and right fluxes. The problem is discretised, as suggested in figure 4.2 and formulated mathematically as:

$$(\mathbf{U}_i^{n+1} - \mathbf{U}_i^n)\Delta x_i = (\mathbf{E}_{i-1/2}^m - \mathbf{E}_{i+1/2}^m)(t^{N+1} - t^N) \tag{4.16}$$

If m=n, then the problem is first order accurate in time, if m=n+1/2, the problem is of second order accuracy. The discretisation in space can be of first order, in which cell properties are taken as piecewise constant, figure 4.3 (a); or second order accurate, in which cell properties are varied linearly over the cell, figure 4.3 (b).

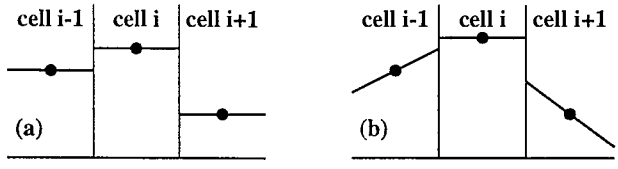


Figure 4.3: Reconstruction strategies, (a) piecewise constant, (b) piecewise linear.

In either case, there are discontinuities in flow properties at the cell interface. This problem is commonly termed the Riemann problem. The problem is solved iteratively for the exact solution to the Riemann problem, however less expensive, approximate methods, such as an acoustic solution can be used in regions in which $p_4 \approx p_1$. To avoid the smearing of discontinuities (for instance shocks), a second order formulation is used here. In the second order approach, the initial cell distribution is piecewise linear. This problem is typically called the generalised Riemann problem (Hillier 1996).

In conclusion to this section, it is noted that the alternating nature of the operator splitting scheme can cause noise due to the residual flux imbalances. This problem is overcome by replacing the inviscid fluxes with the perturbation from their averaged cell centre value at the beginning of the time step (Hillier et al. 1993).

4.1.3 Viscous Terms

The diffusive terms of equation 4.1 are recalled below:

$$\frac{\partial \mathbf{U}}{\partial t} = \frac{\partial \mathbf{E}_V}{\partial x} + \frac{\partial \mathbf{F}_V}{\partial r} + \frac{(\mathbf{F}_V + \mathbf{G}_V)}{r} \tag{4.17}$$

Examining in detail the terms appearing in equation 4.17, one can observe that there is no contribution to the mass conservation equation. The density remains constant therefore through a fractional viscous time step and solution is required only for the momentum and energy equations. If the thin shear layer approximation is made, identifying the "i coordinates" as the flow direction and the "j coordinates" as the flow normal, then the equations of momentum and energy can be decoupled. Momentum is solved first, followed by the energy equation (which requires knowledge of the "new"

velocities). In the code, these are solved implicitly, using a tridiagonal solver along a j-column.

Turbulence modelling

Turbulence is a time dependent chaotic phenomenon, in which one may recognise certain stochastic and statistical properties. The role of turbulence modelling will depend on the nature of the study at hand. The code at present includes a turbulent eddy viscosity model, to provide closure to the time-averaged Reynolds stress equations. In the eddy viscosity approach, the turbulent viscosity is added directly to the molecular viscosity, and the Navier Stokes equations are then solved as discussed previously. The eddy viscosity model used is that of Baldwin and Lomax (1978) The model defines an expression for both the inner and outer eddy viscosity, $(\mu_t)_{inner}$ and $(\mu_t)_{outer}$ respectively, and changes between them at the first location location at which $(\mu_t)_{outer} > (\mu_t)_{inner}$.

The inner viscosity is given by:

$$(\mu_t)_{inner} = \rho l^2 |\omega| \tag{4.18}$$

where $|\omega|$ is the magnitude of the vorticity and l is the Prandtl - Van Driest mixing parameter given by:

$$l = ky(1 - \exp -\frac{y^+}{a^+}) \tag{4.19}$$

in which a^+ and k are constants and y^+ is defined as:

$$y^+ = \frac{\rho_w u_\tau y}{\mu_w} \tag{4.20}$$

In the outer region the viscosity is defined as:

$$(\mu_t)_{outer} = KC_{cp}\rho F_{wake} F_{kleb}(y) \tag{4.21}$$

where K and C_{cp} are constants and F_{wake} defined as:

$$F_{wake} = \min(Y_{max}F_{max}; C_{wk}Y_{max}u_{dif}^2/F_{max}) \tag{4.22}$$

The values of Y_{max}, and F_{max} are the ordinate and abscissa as the following expression reaches a maximum:

$$F(y) = |\omega| y(1 - \exp - \frac{y^+}{a^+}) \tag{4.23}$$

F_{kleb} is given by the expression:

$$F_{kleb} = \left[1 + 5.5\left(\frac{C_{kleb}y}{Y_{max}}\right)^6\right]^{-1} \tag{4.24}$$

The term u_{dif} represents the velocity difference across the shear layer, and for the present case is equal to the boundary layer edge velocity. The values of the constants used in the code are as quoted in the source paper:

$$a^+ = 26 \quad C_{cp} = 1.6 \quad C_{kleb} = 0.3 \quad C_{wk} = 0.25 \quad k = 0.4 \quad K = 0.0168 \tag{4.25}$$

Closure for heat transfer is obtained by defining a turbulent Prandtl number, Pr_t, such that:

$$Pr_t = \frac{\mu_t Cp}{k_t} \tag{4.26}$$

with Pr_t taken to be 0.9 for this study.

The physics of the transitional region add further complications to the problems of turbulence modelling due to the time dependent intermittent nature of the boundary layer. Transition is addressed here by progressively introducing the eddy viscosity through the transitional region. The approach requires the transition onset and completion locations to be known, and some assumption about how to introduce the eddy viscosity in order to best capture the physics of the transition boundary layer to be made. This will be discussed in more detail later.

4.1.4 Block marching and mesh adaptation

The final features of the code to be addressed are the block marching and mesh adaptivity capabilities. The former takes advantage of the fact that in the supersonic regions of the flow, there is only a weak upstream influence in the boundary layer, and information is propagated mainly downstream. The computation can then be confined to a limited block of cells, once the most upstream portion of the flow is converged, the block is shifted by one or more cells downstream and the computation continued. The process repeated until the whole domain is converged. When computing flows over

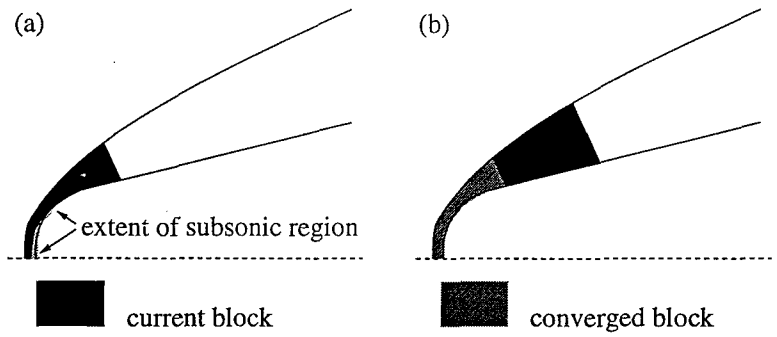


Figure 4.4: Block marching strategy. Initial block (a) includes the subsonic nose region and the near nose supersonic region. Once solution is converged, the whole block is shifted downstream of the subsonic region (b), and the computation is continued.

blunt bodies which present extensive regions of subsonic flow outside the boundary layer, the strategy used is to initially solve over a block containing the nose and near nose regions, 4.4 (a), such that the downstream end of the block is supersonic. When the block is converged, it is shifted so that the upstream end of the block is downstream of the subsonic region, 4.4 (b). From this point onwards, block marching can be allowed to continue in the usual fashion. In this manner, the solution is more efficient not only because one avoids computing in the already converged upstream regions, but also because the computation can continue at the optimum time step for the block in question, which can be significantly higher than the maximum time step allowable, controlled by the smallest cells in the flow field. The adaptivity, used in conjunction with the block marching, allows the mesh to be "shifted" permitting equal resolution of features at all streamwise locations. At present, the number of cells between the body and the boundary layer edge is kept constant and the number of cells between the boundary layer edge and shock are kept constant, enabling the grid to closely follow both the boundary layer and shock growth.

4.2 Computational prediction of the blunt body flow field

The intention of this section is to examine the flow field around the blunt cone using the computational results. Inviscid and Navier stokes solutions will be presented

in order to differentiate between inviscid entropy layer "rotational effects" and the viscous boundary layer effects.

4.2.1 Mesh and initial conditions

The same mesh was used for the inviscid and viscous computations. The mesh contains 191 cells along the body direction and 101 in the direction normal to the body. The mesh can be seen in figure 4.5. The mesh illustrated here is constructed around a 1mm nose radius, 0.75m long, 5° cone. Twenty cells are equi-spaced along the surface of the nose, and the remaining 171 are placed along the conical portion of the mesh. The mesh "stand-off" distance at the nose is 0.2mm, sufficient to ensure that the bow shock remains with the computational domain and still maintain good resolution. The body boundary conditions are set according to the computation; for the viscous study, no slip and isothermal wall conditions are imposed; for the inviscid study, reflective or zero normal velocity conditions are used. Symmetry is imposed along the stagnation streamline and the remaining boundaries are set as in-flow or as out-flow accordingly. The flow is initialised with uniform stream conditions, although Kirk (1993) and Hillier et al. (1993), together with the work of Millevoi (1993) have incorporated non uniform conditions which account for test section gradients. In the work presented below, the conditions are taken to be uniform and are $M_\infty = 9.16$, $Re_{\infty/m} = 54.06 \times 10^6$ and $T_0 = 1063°K$. These conditions differ from those outlined in the calibration work, due to the unfortunate fact that the calibration task was completed in the latter stages of this project when the present computational analysis was already complete. As the intent of this section is to illustrate the typical flow field around the blunt cone, the small differences in freestream conditions used are immaterial. The block marching technique is used and mesh adaption is imposed to keep the shock located at j=94. The first computational block extends over the first forty cells in the i direction, which extends to a chord distance of four nose radii. Once this region is converged, the upstream end of the block is moved to the sphere-cone junction, where the flow is supersonic. To ascertain whether the solution is converged , for the block in the upstream region, a residual is defined as follows:

$$Res = \sum_{j=1}^{jmax} \frac{\rho_j^N - \rho_j^{N-1}}{\rho_j^{N-1}} \tag{4.27}$$

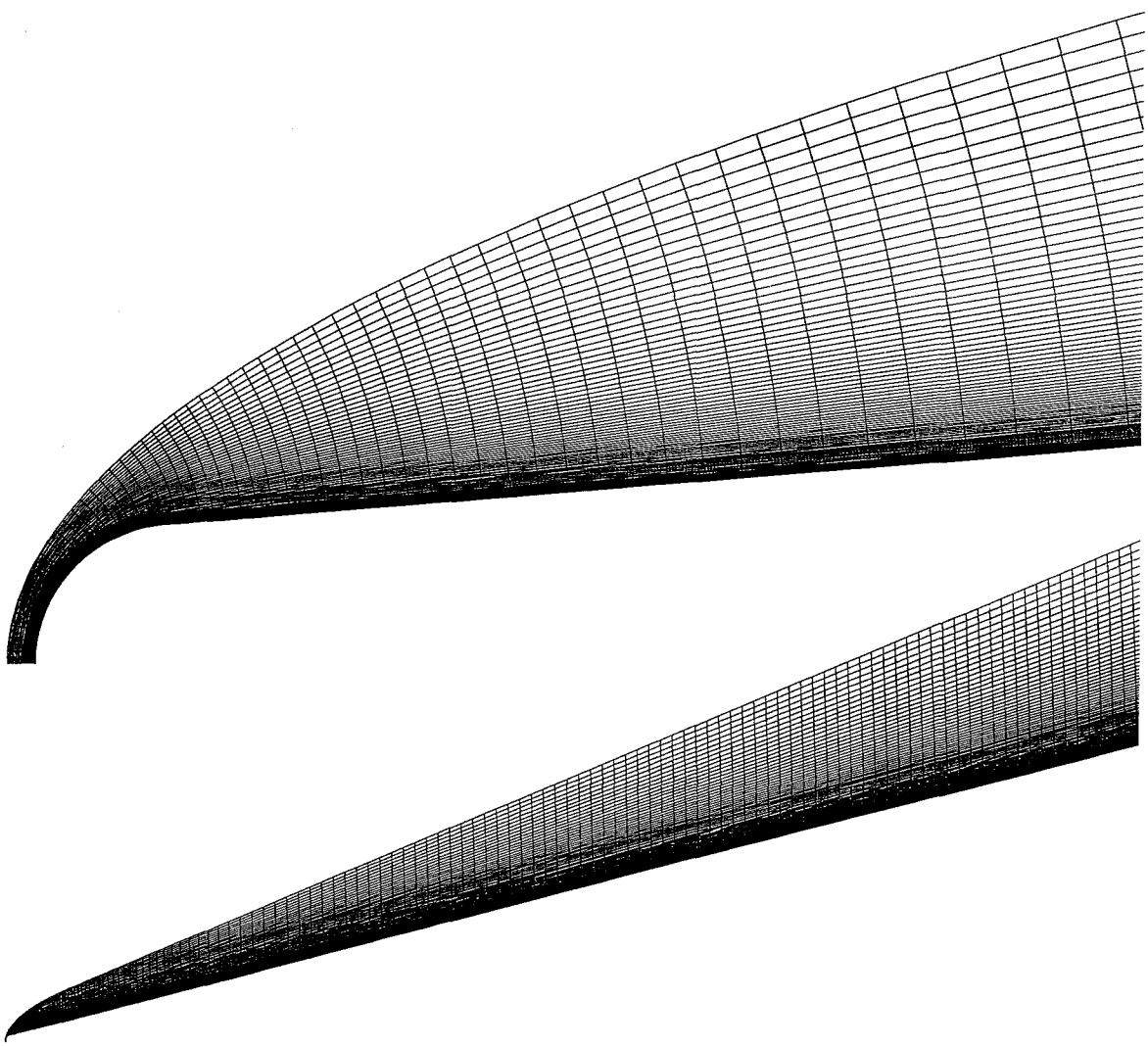


Figure 4.5: Mesh details; top, near nose; and bottom, complete mesh, stretched vertically by a factor of three. Nose radius 1mm, mesh stand-off distance 0.2mm, body length=0.75m, There are 191 cells in the body direction and 101 in the body normal direction.

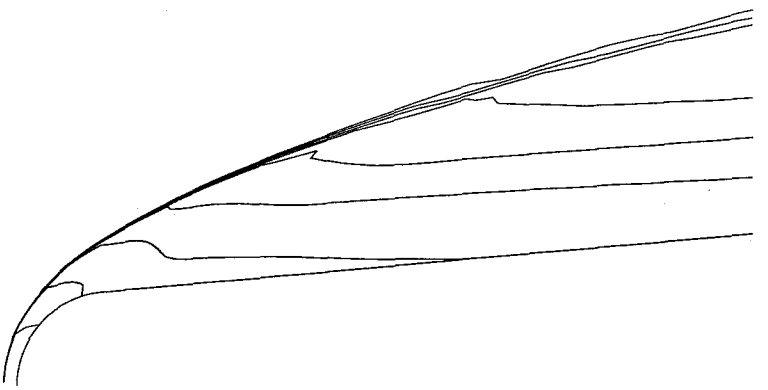


Figure 4.6: Mach number contours inviscid computation, contour intervals 1, levels 1, 2, 3 etc.

The convergence criterion allows the block to be moved when the residual is less than 1 part per million.

4.2.2 Inviscid solution

The shock shape for the inviscid computation can be found in figure 4.6. As the flow field is inviscid, the only length scale is the nose radius, r_n. Billig (1967), has correlated the shock stand-off distance, x_{shock}, against Mach number and nose radius as indicated below:

$$\frac{x_{shock}}{r_n} = 0.143 \exp\left(\frac{3.24}{M_\infty^2}\right) \tag{4.28}$$

Using the conditions for the computations, the above equation gives $x_{shock}/r_n = 0.149$. This compares favourably with the CFD standoff distance of 0.142. Using the schlieren image of figure 4.7, the estimated experimental stand-off distance, normalised by nose radius is 0.145 ± 0.09. All estimates show reasonable agreement.

The shock is normal to the axis of symmetry on the axis. The stagnation streamline can be linked to the freestream using the Rankine-Hugeniot expressions. At Mach 9.16, these give $p_{(0,2)}/p_\infty = 108.5$. The computationally predicted stagnation pressure ratio is 108.1, again in excellent quantitative agreement. More critical is the predic-

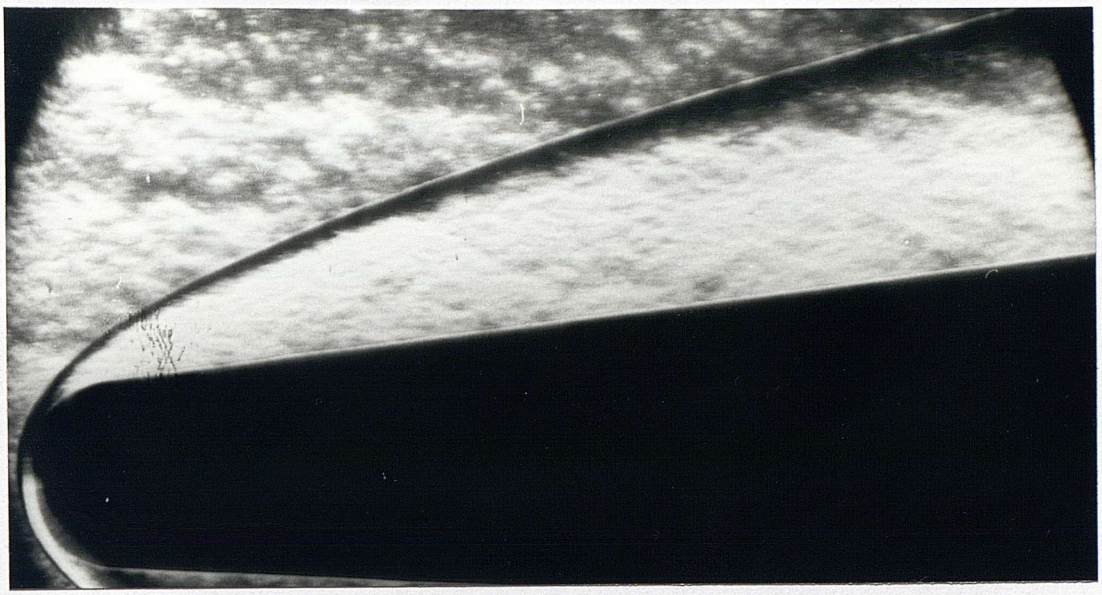


Figure 4.7: Schlieren image of flow around blunt cone, horizontal cut-off. The test conditions are $Re_{\infty/m}$ =47.4 $\times 10^6$, r_n=25mm.

tion of the stagnation density. Comparison indicates that the numerically predicted stagnation density is 0.66 % less than the exact value.

The computed surface pressure can be found in figure 4.8. The pressure drops rapidly over the hemispherical portion of the nose, from the stagnation value to a value slightly in excess of twice the freestream at the sphere cone junction. The surface pressure reaches a minimum at s/r=25, after which it asymptotes to the sharp cone value at many nose radii distance downstream. The minimum in surface pressure is connected with an over-expansion of the flow caused by over-turning of the flow around the hemispherical nose. In order to return the flow parallel to the body, a compression wave system is formed.

The shock slope is plotted against distance along the shock normalised by nose radius in figure 4.9. The slope decreases around the nose region and presents a minimum in shock angle at s_{shock}/r_n =100, before asymptoting again to the sharp cone slope. The minimum slope is located upstream of the interaction between the shock and the compression wave which originates on the model surface at s/r_n=25.

An important inviscid feature to be examined is the entropy layer. The entropy

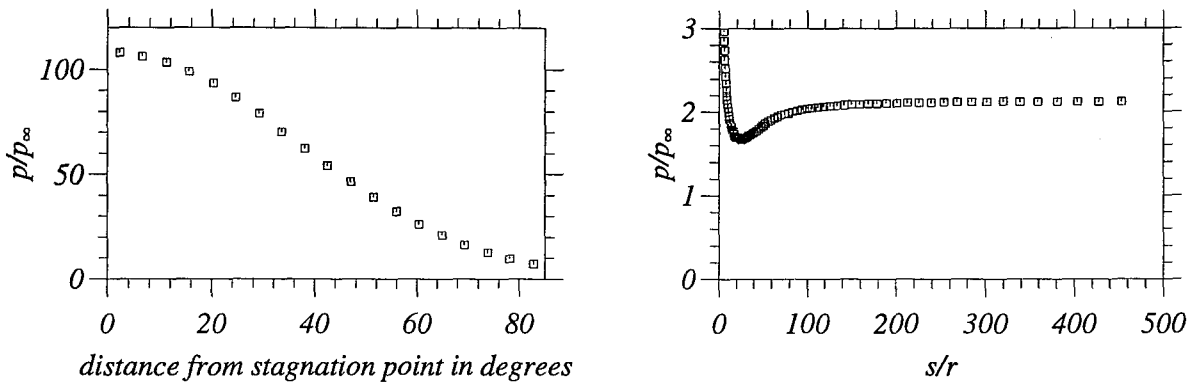


Figure 4.8: Surface pressure along hemispherical portion of nose, left; and surface pressure over entire geometry, right; inviscid computations.

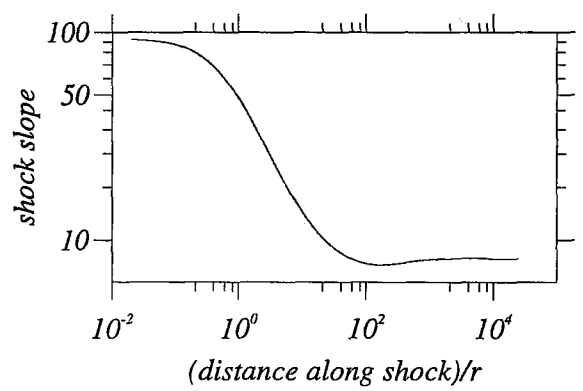


Figure 4.9: Shock angle against normalised distance along shock; inviscid computations.

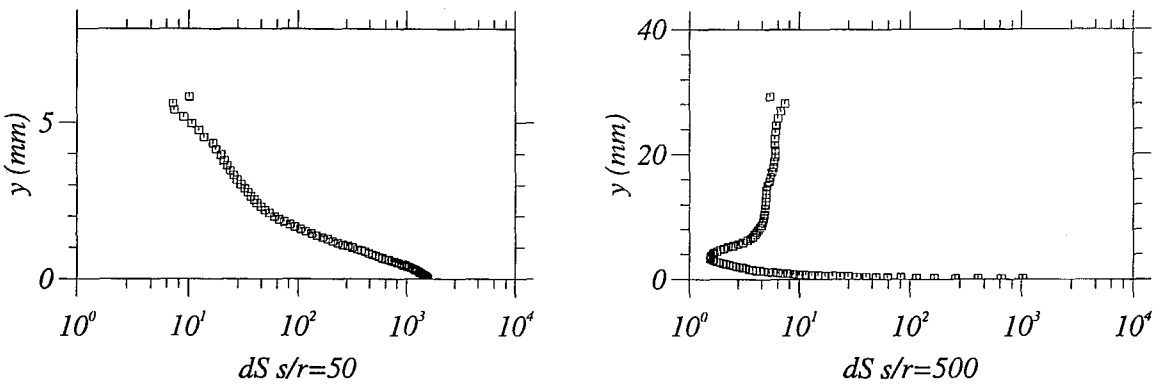


Figure 4.10: Entropy profiles at two locations; left, upstream of point of minimum pressure, right downstream of point of minimum pressure. Vertical scale normalised by nose radius, computations performed at 9.16.

change, measured relative to the freestream is:

$$\frac{S}{C_v} = \gamma \ln \frac{T}{T_\infty} + (\gamma - 1) \ln \frac{P_\infty}{P} \tag{4.29}$$

Within the entropy layer, differing streamlines have different amounts of entropy, such that the entropy is decreasing with distance away from the surface. If a profile of entropy is taken upstream of the point of minimum shock slope, then the entropy decrease in monotonic, as shown in figure 4.10. If the profile is taken downstream of the location of minimum shock slope, then the profile will present a minimum in correspondence of the streamline which passes through the location of minimum shock slope, which can be seen at y/r =4 in the right plot of figure 4.10. The location of minimum shock slope is often used to define the limit of the entropy layer, [Herbert and Esfahanian (1992)], as the streamline processed by this portion of the shock is characterised by the lowest entropy increase.

4.2.3 Viscous solution

The issue to be addressed here is the interaction between the entropy layer and the boundary layer. There are two main effects, firstly a retardation in edge properties at

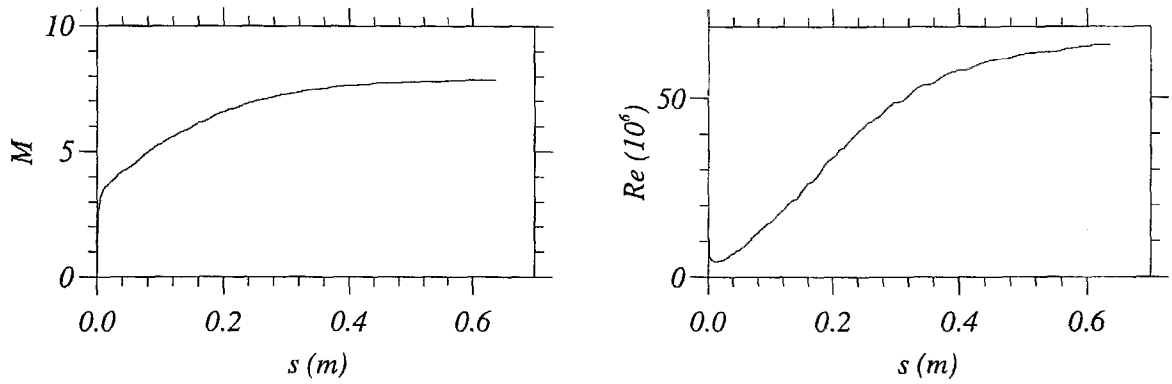


Figure 4.11: Mach number and Reynolds number at the boundary layer edge against distance. Computation performed at Mach 9.16, $Re_{\infty/m} = 54.06 \times 10^6$, r_n=1mm.

the boundary layer edge; and secondly, the presence of gradients in properties normal to the body surface.

The properties of two streamlines with an entropy difference, Δs, can be equated as:

$$\frac{\Delta S_{21}}{C_v} = \gamma \ln \frac{T_2}{T_1} + (\gamma - 1) \ln \frac{P_1}{P_2} \tag{4.30}$$

It can be seen that there is a strong dependence of temperature upon entropy, which considerably affects the boundary layer edge Mach number and Reynolds number distribution, as shown in figure 4.11. It can be seen in figure 4.11, that the Mach number and Reynolds number asymptotically approach the sharp cone values, as the boundary layer, through growth with distance downstream, entrains streamlines which will have progressively undergone an increasingly smaller entropy rise relative to the freestream.

The entropy layer is vortical in nature and gives rise to vorticity at the edge of the boundary layer. In figure 4.12, the vorticity profile is plotted for two different streamwise locations, for the viscous computation. The vorticity is computed using equation 4.31.

$$\Omega = \frac{1}{u_\infty} \left(\frac{\partial v}{\partial x} - \frac{\partial u}{\partial r} \right) \tag{4.31}$$

It can be seen in figure 4.12, vorticity is present outside the boundary layer edge at the s/r=50 station, where $\delta = 0.5mm$. Further downstream, as the entropy layer is

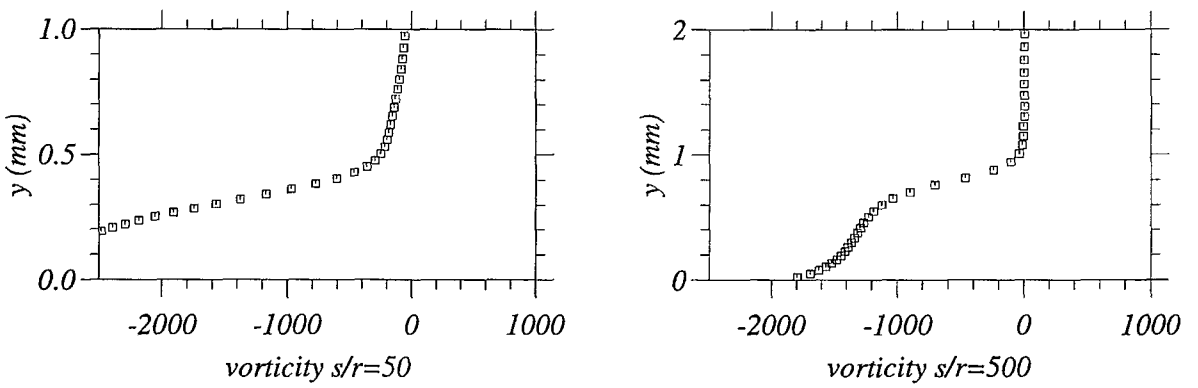


Figure 4.12: Vorticity profiles based on normalised velocity for the blunt cone, at two different streamwise locations. Computation performed at Mach 9.16, $Re_{\infty/m}$ = 54.06 $\times 10^6$, r_n=1mm.

progressively swallowed by the boundary layer, only a small amount of vorticity is observed outside the boundary layer, ($\delta = 1mm$).

4.3 Concluding remarks

In the first part of this chapter, a high resolution solver has been presented. The numerical method is a two dimensional axi-symmetric time marching scheme, with the calculation time split between the inviscid and viscous solvers. The inviscid solver is based upon a second order Godunov type algorithm which evaluates the fluxes assuming a generalised Riemann problem. The viscous solver utilises a thin shear layer approximation and is formulated implicitly. Turbulence is modelled using a Baldwin Lomax model. Block marching and mesh adaptivity features have been discussed.

In the second part of this chapter, the code was used to illustrate some features of the blunt body flow field. The flow field is composed of extensive regions of sub-, super- and hypersonic flow and is governed by the detached bow shock. The latter creates the so called entropy layer, a region of fluid with high entropy which interacts strongly with the boundary layer, both retarding the edge conditions and creating

gradients in the edge properties in the direction normal to the boundary layer.

Chapter 5

Heat transfer database

In this chapter, the time averaged heat transfer rate database is presented. The data is presented in three sets. Each set is distinguished by the operating conditions at which the tests were performed. In all plots, the data will be presented as time averaged heat transfer rate, q_w, against wetted distance, s. The units chosen for q_w are W/cm^2 and the wetted distance is measured in metres from the model apex. In addition, the data will also be plotted as Stanton number St, against the wetted Reynolds number Re_s. The Stanton number, a non-dimensional form of the heat transfer rate is given generally by:

$$St_e = \frac{q_w}{\rho_e u_e C_p (T_{aw} - T_w)} \tag{5.1}$$

where the suffix e indicates edge conditions; ρ and u are the density and the velocity; C_p is the specific heat at constant pressure; and T_{aw} and T_w are the adiabatic wall and wall temperatures respectively.

In this formulation, the term $T_{aw} - T_w$ is of strong physical significance as it is the temperature difference driving the heat transfer. Equation 5.1 cannot readily be used in the reduction of blunt cone data because of the strong variation of edge properties with distance. CFD can be used to prescribe the edge properties at any given point, but is recognised that as the intention is to provide an "engineering" database, it is best to use the following definition for Stanton number:

$$St_\infty = \frac{q_w}{\rho_\infty u_\infty C_p (T_{0,\infty} - T_w)} \tag{5.2}$$

where all properties are now based on freestream conditions. This formulation is physically less satisfactory, due to the presence of the term $T_{0,\infty} - T_w$ appearing in the denominator however it is noted that as the experiments performed here are characterised by a "cold wall" with $T_w \ll T_{aw} < T_{0,\infty}$, the formulation may be considered representative.

Similarly, for reasons discussed above, it is most appropriate to express the Reynolds number based on wetted distance as:

$$Re_s = \frac{u_\infty \rho_\infty s}{\mu_\infty} = Re_{\infty/m} \times s \tag{5.3}$$

The values used for the freestream properties are the nozzle exit plane averages obtained from the calibration experiments and are listed for convenience in table 5.1.

operating condition	ρ_∞ Kg/m^3	u_∞ m/s	$T_{0,\infty}$ ° K	$Re_{\infty/m}$
low	0.0238	1432	1060	7.5×10^6
medium	0.0402	1453	1090	12.6×10^6
high	0.1494	1464	11053	47.4×10^6

Table 5.1: Summary of conditions used in data reduction

Experiment classification

The data presented in the following chapter are classified by the experimental setup used. These are listed below, for the location of the gauges refer to table 2.4.

Set A In this series, gauges 01 to 24 were tested simultaneously.

Set B In this series, gauges 25 to 45 were tested simultaneously.

Set C In this series, gauges 46 to 65 were tested simultaneously.

Set E In set E, 27 gauges were selected evenly along the length of the model to obtain simultaneous measurements over the greatest possible wetted distance. The gauges tested were 2, 4, 6, 8, 10, 11, 14, 16, 18, 20, 22, 24, 26, 28, 30, 32, 34, 36, 38, 40, 42, 45, 46, 50, 55, 60 and 65.

Set F Set F uses the same gauge selection as set E, except experiments were performed with the "rough" surface finish, (machine finish, no polish).

Set H Ceramic nose piece with fixed 3mm nose. Gauges located in near nose region ($s \leq 0.01$m).

In addition to these datasets the numerically predicted heat transfer rate and the heat transfer rates measured by Sell (1992) will be included. For each test case, the graph presented will include a legend indicating the nose radius, the operating condition and the dataset to which the data belongs.

5.1 Heat transfer rate database, low pressure operating condition

5.1.1 Sharp Cone

The time averaged heat transfer rate distribution against wetted distance can be seen in figure 5.1 (a). The distribution is characterised by a rise in heat transfer, the attainment of a maximum at s=0.44m, Re_s=3.3 $\times 10^6$ and a subsequent decrease downstream. This is indicative of the final stages of the transition process and the commencement of the fully developed turbulent behaviour.

5.1.2 12.5mm → 25mm cones, Re_n=93,900 → 187,800

All test cases (figures 5.1 (b), (c), (d), (e), (f) and 5.2) show a monotonic decrease in heat transfer rate, indicating almost certainly laminar flow. For the 12.5mm (figure 5.1 (b)) and 25mm (figure 5.2), it can be seen that the numerically predicted laminar heat transfer rate agrees accurately with the measured values.

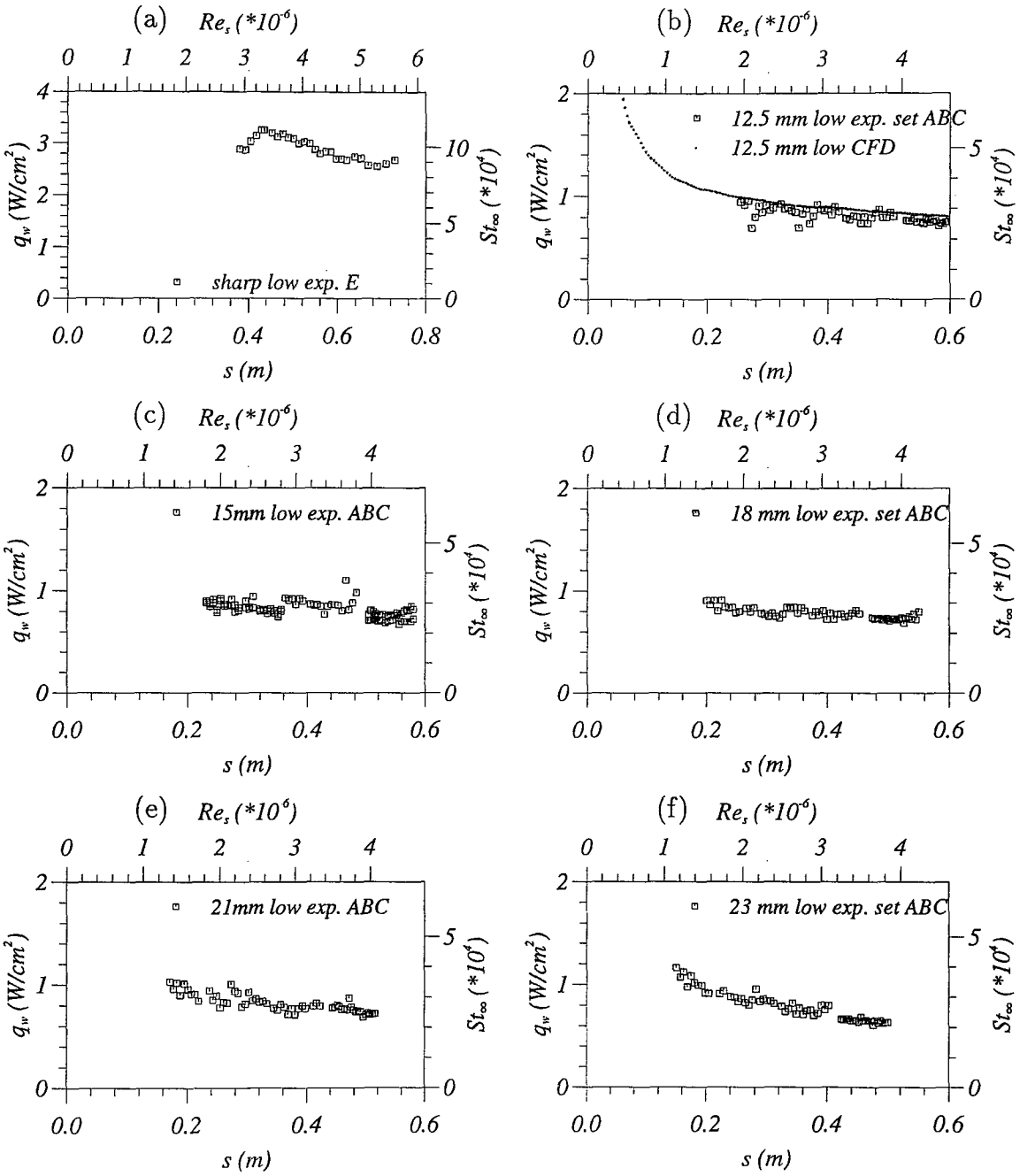


Figure 5.1: Time averaged heat transfer rates for the sharp, 12.5mm, 15mm, 18mm, 21mm and 23mm cases, tested at the low pressure operating condition.

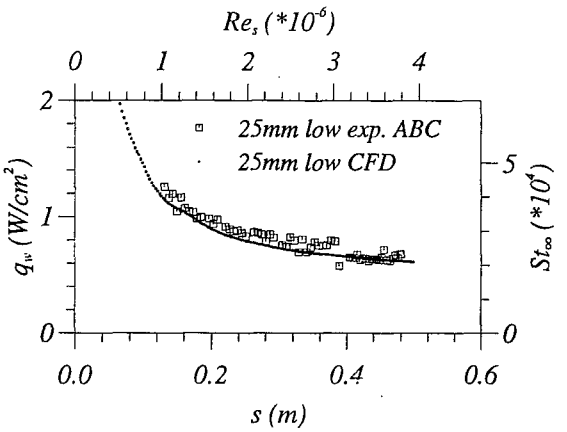


Figure 5.2: Time averaged heat transfer rates for the 25mm case, tested at the low pressure operating condition.

5.2 Heat transfer rate database, medium pressure operating condition

In total ten test cases were performed at the medium pressure operating condition. The 6.25, 12,5 and 25mm cases were also tested by Sell (1992) but it should be noted that the medium pressure operating condition were modified in 1993 prior to the present measurements. The modification was intended to increase the total temperature by increasing the driver to barrel ratio from 73.6 to 90. To avoid changing the diaphragm design, this was achieved by lowering the barrel pressure from 303kPa to 249kPa. In table 5.2, the new and previous conditions are compared. Of interest

	M_∞	$Re_{\infty/m}$	$T_{0,\infty}$ ° K	T_∞ ° K	$P_{0,\infty}$ (MPa)	P_∞ (Pa)	ρ_∞ Kg/m^3	u_∞ m/s
old	8.85	15.5 $\times 10^6$	996.5	59.8	15.2	804	0.0457	1388
new	8.93	12.6 $\times 10^6$	1090	64.3	15.2	760	0.0402	1453

Table 5.2: Comparison of operating conditions

are the changes to the term $\rho_\infty u_\infty (T_{0,\infty} - T_w) Cp$ appearing on the denominator of equation 5.2. Using the estimates of table 5.2, the term takes the value 4744 and

4542 W/cm^2 for the present experiments and those of Sell respectively.

5.2.1 Sharp cone

The heat transfer distribution for the sharp nose configuration can be seen in figure 5.3 (a). The results show decreasing heat transfer with distance, however, the high heating rates $St_\infty > 10^{-3}$, suggest that the boundary layer is turbulent at all measurement stations. This implies that transition onset and completion have occurred upstream of s=0.39, $Re_s = 4.5 \times 10^6$, the location of the most forward sensor. Further evidence to confirm that the sharp cone boundary layer is turbulent is obtained by analysing the signal RMS.

5.2.2 2mm cone, $Re_n = 25,200$

This test case, (figure 5.3 (b)) shows the heat transfer rate abruptly departing from the laminar value (depicted by the CFD) at s=0.38m, $Re_s = 4.80 \times 10^6$. The heat transfer rate rises to a maximum at s=0.6m, $Re_s = 7.57 \times 10^6$, and thereon decreasing as the boundary layer becomes fully developed turbulent. This exemplifies the classic picture of the variation of heat transfer through transition.

5.2.3 3mm cone, $Re_n = 37,900$

The measured q_w distribution, (figure 5.3, (c)) shows an initial region of laminar boundary layer growth until $s = 0.6m$, $Re_s = 7.5 \times 10^6$, where one can witness a rise in heat transfer rate associated with the beginning of transition.

5.2.4 6.25mm $\rightarrow$ 25mm cones, $Re_n = 76,900 \rightarrow 315,500$

These seven test cases, comprising the following nose radii, 6.25, (figure 5.3 (d), 12.5, 15, 18, 21, 23 and 25mm (figures 5.4 (a) to (f)), all show laminar trends. The

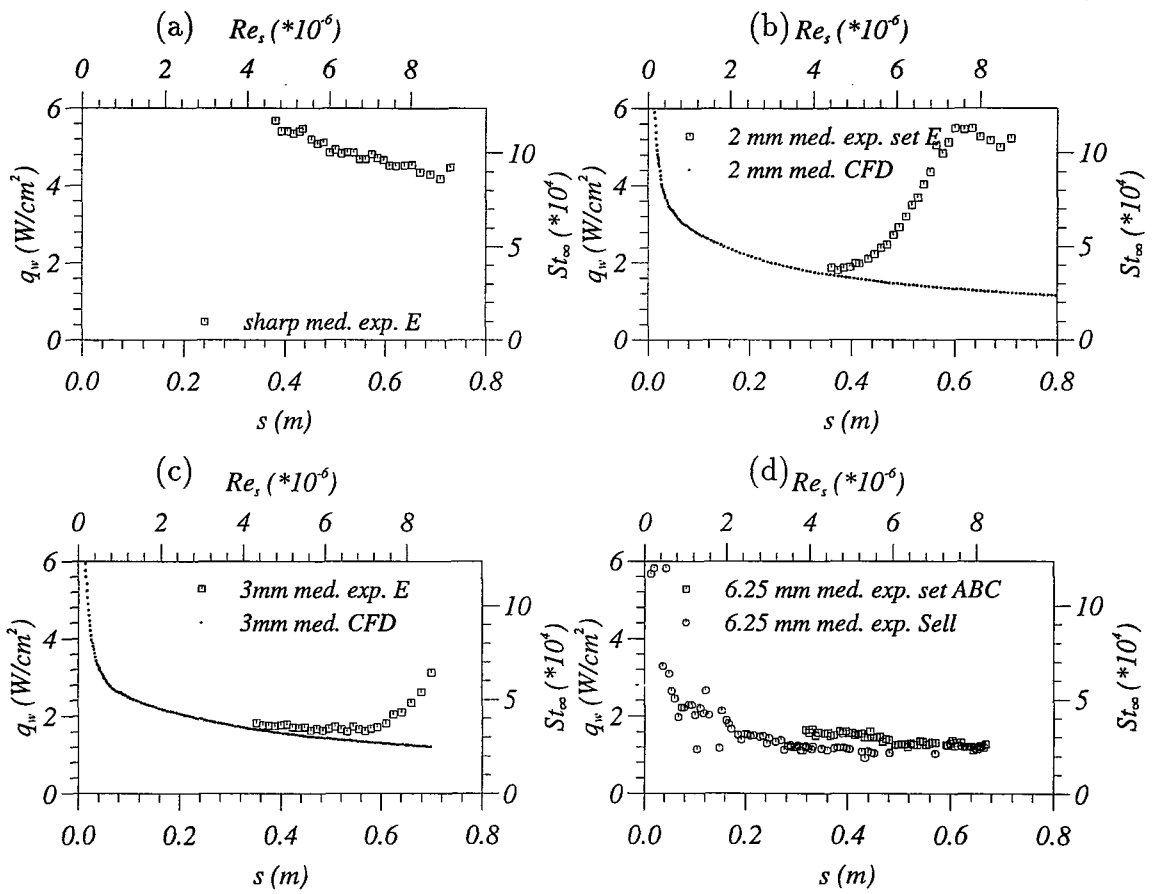


Figure 5.3: Time averaged heat transfer rates for the sharp, 2mm, 3mm and 6.25mm cases, tested at the medium pressure operating condition.

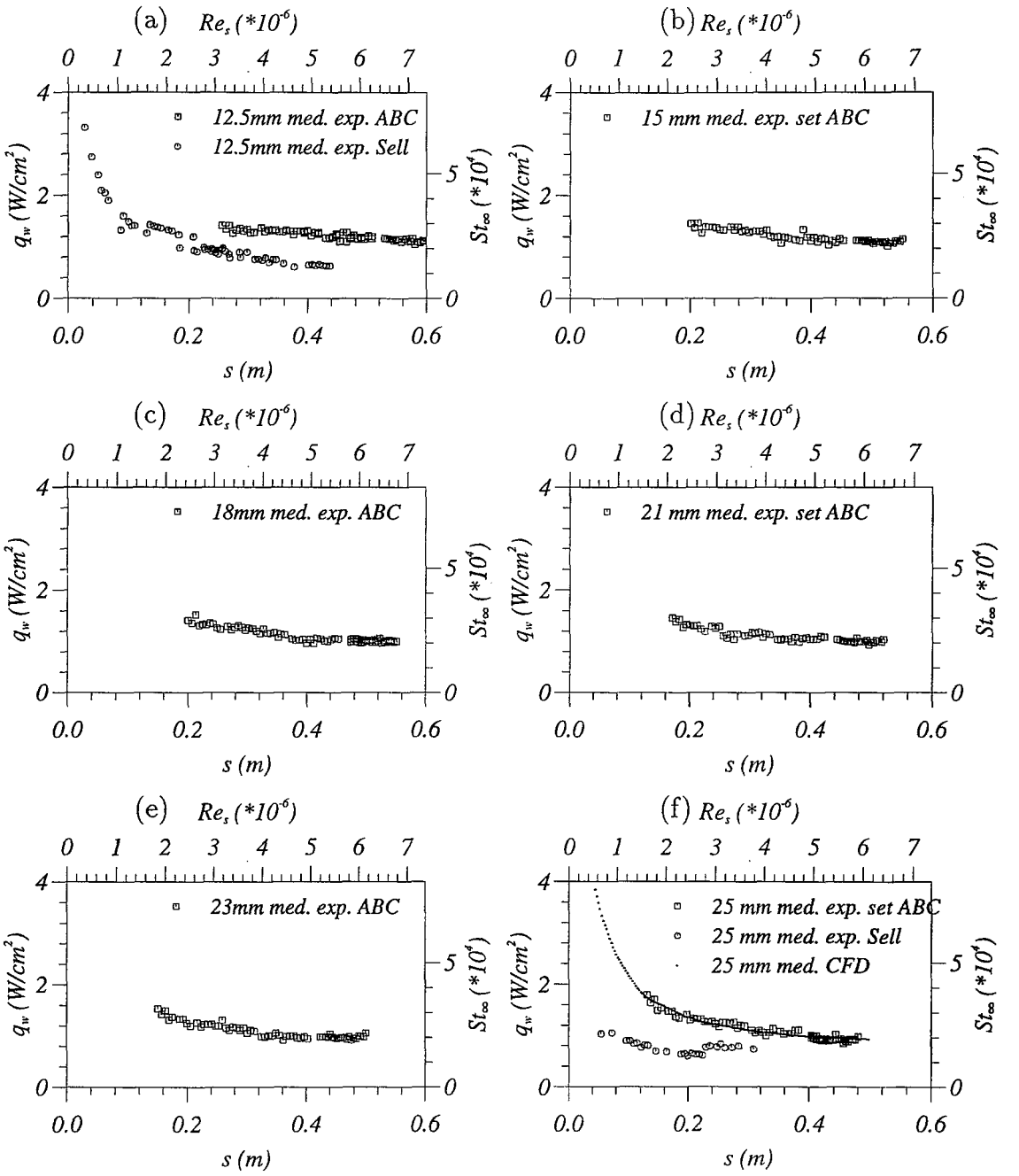


Figure 5.4: Time averaged heat transfer rates for the 12.5mm 15mm, 18mm, 21mm, 23mm and 25mm cases, tested at the medium pressure operating condition.

discrepancy with Sell's data although greater than the margin suggested earlier due to the change in operating conditions, is apparent where both datasets are presented.

5.3 Heat transfer rate database, high pressure operating condition

In total 12 test different noses were tested at the high pressure operating condition. The maximum Re_n tested exceeds 1,000,000 and for the small bluntness cases instrumentation extends up to wetted Reynolds numbers in excess of 30,000,000.

5.3.1 Sharp cone

The boundary layer is turbulent for the sharp nose case depicted in figure 5.5 (a). This conclusion is based upon the high Stanton numbers and the signal RMS (not shown).

5.3.2 2mm cone, $Re_n = 85,400$

The measured q_w, figure 5.5 (b), shows an increase in heat transfer rate until a maximum at s=0.48m, $Re_s = 22.9 \times 10^6$, followed by a subsequent decrease suggesting that the gauges are wetted initially by a transitional boundary layer and then by fully developed turbulent boundary layer motion.

5.3.3 3mm cone, $Re_n = 142,200$

For this test case, figure 5.5 (c), four data sets are presented. Dataset H shows that in the near nose region q_w is greater than the predicted (CFD) laminar value. This is echoed in dataset E, where the initial gauges, 0.34m<s<0.44m, show a definite departure from the laminar trend. Furthermore in this region, the heat transfer shows

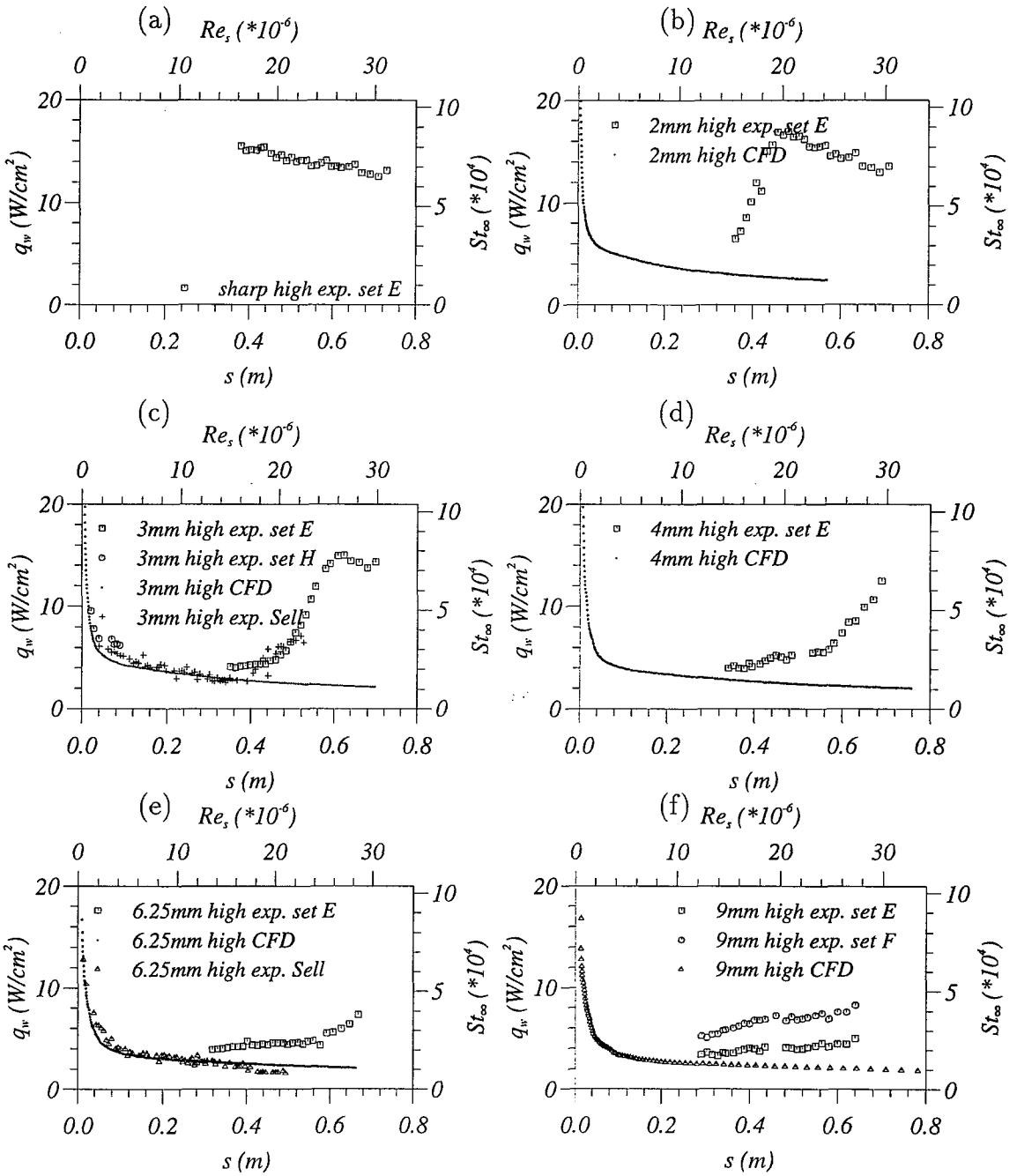


Figure 5.5: Time averaged heat transfer rates for the sharp, 2mm, 3mm, 4mm 6.25mm and 9mm cases, tested at the high pressure operating condition.

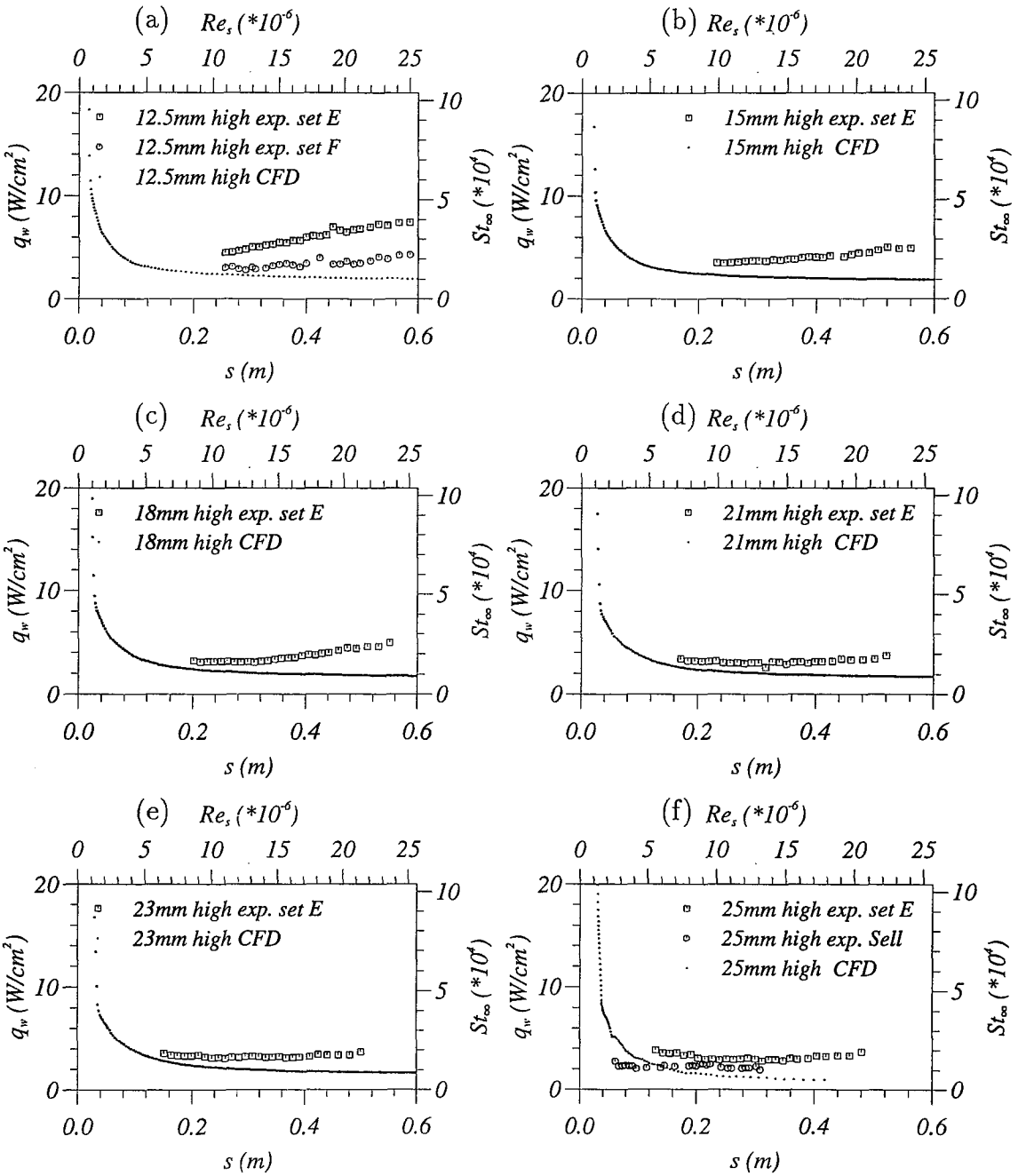


Figure 5.6: Time averaged heat transfer rates for the 12.5mm, 15mm, 18mm, 21mm, 23mm and 25mm cases, tested at the high pressure operating condition.

a mild but positive streamwise gradient, in distinct contrast with the predicted laminar trend. This departure is associated with low level transitional activity occurring in the nose and near - nose regions, producing turbulent events which are convected downstream. Downstream of s=0.44m, $Re_s = 21.0 \times 10^6$, there is an abrupt change of slope of q_w and the heat transfer rate rises sharply reaching a maximum at s=0.62m, $Re_s = 29.6 \times 10^6$. This rise is associated with a more rapid "switch on" of a second transition mechanism which readily causes the boundary to become fully turbulent over the downstream portion of the gauges (this subject will be discussed later).

5.3.4 4 and 6.25mm cones, $Re_n = 189,600$ and $296,300$

These two test cases, figures 5.5 (d) and (e), exhibit a region of mild heat transfer rate increase followed by a change in gradient downstream of which the heating rate is characterised by a more rapid growth. Again, it is concluded that the boundary layer is subject to an initially low level of transition activity and that at some streamwise location (respectively s=0.58m and s=0.56m for the 4mm and 6.25mm cases) the transitional activity increases with the corresponding rise in q_w. Transition completion is not witnessed despite the large chord of the model. For the 6.25mm nose case, it is noted that Sell's data does not exhibit this initial region of low level activity. Indeed the measured q_w show a monotonic decrease which is well predicted by the numerical simulation.

5.3.5 9 and 12.5mm cones, $Re_n = 426,600$ and $592,500$

For these two nose geometries, figure 5.5 (f) and figure 5.6 (a), two experimental configurations have been tested. Set E, the usual smooth nose setup and set F, with the rough nose finish. Again, it is noted that by "rough", one intends the non polished or "as machined" surface finish. Observing the heat transfer trends for both cases, one notes that all experiments exhibit the low - level transitional activity discussed above. The role of roughness is clearly to increase the transition activity, although the projected lengths to transition completion are still very long, possibly $>$ 1m.

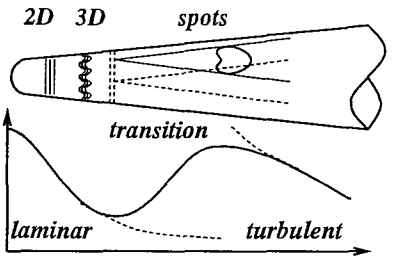


Figure 5.7: Schematic of boundary breakdown to turbulence and behaviour of some macroscopic quantity measured on the model surface.

5.3.6 15 → 25mm cones, $Re_n = 711,000 \rightarrow 1,185,000$

These five test cases are characterised by the weak transition process leading to a heat transfer distribution which gradually departs from the predicted laminar trend, as can be seen in figure 5.6 (b) to (f). It can be estimated from these that the lengths to transition completion would be many times the model length.

5.4 Transition behaviour

The heat transfer database presented a total 29 different test cases. The intent of this section is to analyse the outcome of those tests to determine the blunt cone transition behaviour. Transition from laminar to turbulent flow is characterised by certain "milestone" events. These may include the occurrence of two dimensional instability waves followed by more destabilising three dimensional waves, non linear breakdown and the formation, growth and merging of spots, as indicated schematically in figure 5.7. The true origin of transition is defined most generally as the location at which the boundary layer exhibits a "non-laminar" behaviour at some microscopic level. On the other hand, the transition information of use for the engineer involved in the design of a hypersonic vehicle will be based upon some detectable departure from the laminar behaviour of a given macroscopic quantity. This may be, for instance, the change in the boundary growth rate, shape factor, recovery factor and so on. The location of transition onset will be determined for the present experiments using the heat transfer database. The behaviour of heat transfer, through the transition

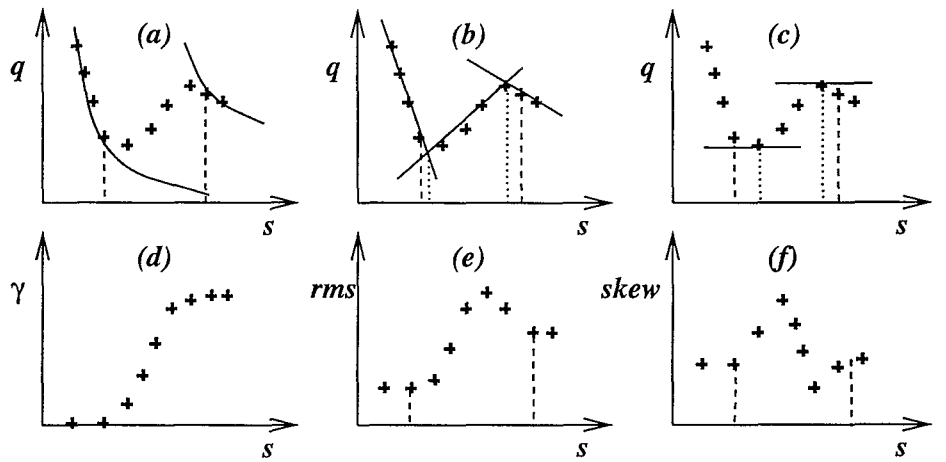


Figure 5.8: Distribution of the heat transfer rate in the laminar, transitional and turbulent regions, (a) (b) and (c); and the corresponding change in signal intermittency (d), RMS (e) and skewness (f).

region is shown in figure 5.8 (a). The distribution exhibits laminar behaviour until some location downstream of the breakdown point. The heat transfer then increases through the transitional region, reaching some maximum before transition completion, downstream of which, it follows the turbulent trend. The initial departure from the laminar trend will not be readily detectable, figure 5.8 (a), and often other methods to locate transition onset are used. In one method, straight lines are fitted to the laminar, transition and turbulent portions of the heat transfer trace, as indicated in figure 5.8 (b). The intersections of these lines are taken to be the transition onset and completion location. Other criteria use the location of the minimum and maximum heat transfer (c). A more accurate method is to examine the intermittency factor γ of the instantaneous heat transfer trace (d), the distribution of which gives a portrayal of the "amount" of non laminar activity present at any streamwise location. Finally, it is noted that the signal RMS (e) or, for instance, the signal skew (f) can be used to prescribe a location for transition.

All the above methods give useful indication concerning the transition location and the choice of which method to use depends upon the nature of the study.

To examine the data presented in this study, the transition onset and completion will be initially defined as using method (b). The outcome of the tests is given in tables

5.3 and 5.4.

$Re_{\infty/m} \times 10^6$	r_n (mm)	onset (m)	completion (m)
7.5	sharp	←	0.44
7.5	12.5	laminar	
7.5	15	laminar	
7.5	18	laminar	
7.5	21	laminar	
7.5	23	laminar	
7.5	25	laminar	
12.6	sharp	turbulent	
12.6	2	0.36	0.6
12.6	3	0.62	→
12.6	6.25	laminar	
12.6	12.5	laminar	
12.6	15	laminar	
12.6	18	laminar	
12.6	21	laminar	
12.6	23	laminar	
12.6	25	laminar	

Table 5.3: Transition behaviour, low and medium pressure operating conditions; ← indicates transition onset occurs upstream of instrumentation; → indicates transition completion downstream of instrumentation.

It can be seen in tables 5.3 and 5.4, that for the majority cases presenting transitional behaviour, the locations of onset and completion were not detected by the the instrumentation. This is especially true for the cases tested at the high pressure operating conditions where the heat transfer trace is seen to depart in a leisurely manner from the laminar trend. In all cases, the laminar heat transfer distribution has been computed. It is possible to extrapolate upstream the measured heat transfer curve and find the transition onset location as depicted in figure 5.9. This method, albeit not completely accurate, is simply an extension of the method proposed in this study and as such allows the analysis to be performed for all the transitional cases encountered.

The onset location for the transitional cases are given in table 5.5. To complete the information in this table, the Reynolds number and Mach number at the boundary

$Re_{\infty/m} \times 10^6$	r_n (mm)	onset (m)	completion (m)
47.4	sharp	turbulent	
47.4	2	←	0.48
47.4	3	←	0.62
47.4	4	←	→
47.4	6.25	←	→
47.4	9	←	→
47.4	12.5	←	→
47.4	15	←	→
47.4	18	←	→
47.4	21	←	→
47.4	23	←	→
47.4	25	←	→

Table 5.4: Transition behaviour, high pressure operating conditions; ← indicates transition onset occurs upstream of instrumentation; → indicates transition completion downstream of instrumentation.

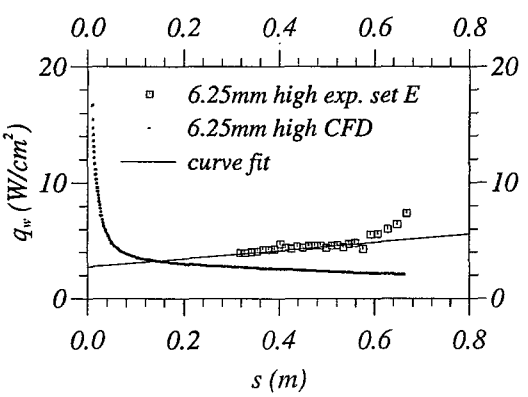


Figure 5.9: Determination of transition onset by extrapolation, transition onset is fixed at s=0.14m. Captions: squares, experimental data obtained at the high pressure operating conditions; dots, CFD laminar prediction; continuous line, curve fit used to obtain transition onset.

layer edge at the transition onset location are also given, together with the boundary layer and displacement thickness. These properties have been predicted using the Navier Stokes code with the pertinent nozzle exit plane conditions used in the computations. The final column in table 5.5 lists the entropy swallowing distance as calculated using the formula of Rotta (1968), given in equation 5.4.

$$\frac{x_{sw}}{r_n Re_n^{1/3}} = 26 \tag{5.4}$$

r_n	$Re_{\infty/m}$ $\times 10^6$	x_{tr} (m)	Re_e $\times 10^6$ (/m)	M_e	δ (mm)	θ (mm)	x_{sw} (m)
2	12.6	0.36	8.8	6.8	1.65	0.123	1.51
3	12.6	0.62	9.0	6.6	2.18	0.1	2.60
3*	47.4	0.20	6.4	4.0	0.92	0.076	4.26
4*	47.4	0.22	5.1	3.8	1.03	0.089	6.25
6.25*	47.4	0.14	3.6	3.5	1.07	0.098	11.33
9 *	47.4	0.18	3.5	3.5	1.27	0.115	18.42
12.5*	47.4	0.17	3.5	3.3	1.28	0.120	28.55
15*	47.4	0.12	3.6	3.2	1.17	0.110	36.40
18*	47.4	0.12	3.9	3.1	1.17	0.110	46.42
21*	47.4	0.10	4.3	3.0	1.06	0.101	57.01
23*	47.4	0.10	4.5	2.9	1.00	0.100	64.36
25*	47.4	0.08	4.8	2.8	0.87	0.090	71.93

Table 5.5: Transition behaviour; * indicates location determined by extrapolation.

Finally, the readers attention is drawn to the heat transfer distributions of the 3, 4 and 6.25 mm geometries tested at the high pressure operating condition, figures 5.5 (c), (d) and (e). In these tests, the most upstream measurements indicate that the the heat transfer trace is gradually departing from the laminar prediction. The divergence is mild and transition completion is expected to occur over many model lengths. However, the heat transfer rate measurements further downstream show an abrupt change in slope of the distribution. This indicates the presence of a second transitional zone of increased activity, caused by a change in the spot formation rate or growth parameter. For these test cases, it is possible to identify this second transition length x_{tr2} as indicated in figure 5.10. For the three test cases presenting the occurrence of the second transition mechanism the relevant boundary layer information is presented in table 5.6.

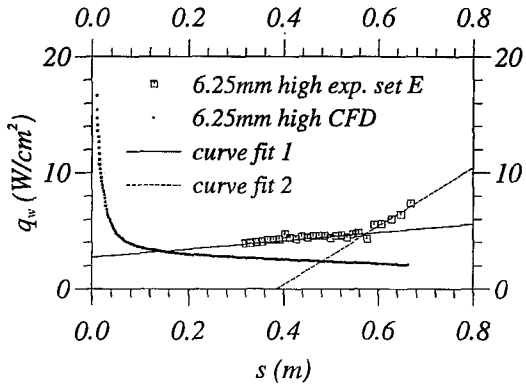


Figure 5.10: Determination of second transition length, x_{tr2}, The second transition onset length is given by the intersection of curve fit 1 and curve fit 2, and is 0.58m. Captions: squares, experimental data obtained at the high pressure operating conditions; dots, CFD laminar prediction; continuous line, curve fit to initial transitional region; dashed line, curve fit to second transitional region.

r_n	$Re_{\infty/m}$ $\times 10^6$	x_{tr2} (m)	Re_e $\times 10^6$ (/m)	M_e	δ (mm)	θ (mm)	x_{sw} (m)
3	47.4	0.46	15.7	5.3	1.11	0.076	4.26
4	47.4	0.56	13.1	5.0	1.30	0.089	6.25
6.25	47.4	0.58	7.62	4.2	1.61	0.098	11.33

Table 5.6: Transition behaviour; onset of second mechanism.

In the present series of experiments, the transition tests concentrated on the larger nose radii. In order to provide onset information for the sharp and small bluntness cases, the data of Sell is used. Three test cases have been chosen and the transition location and other flow field statistics are presented in table 5.4.

r_n	$Re_{\infty/m}$ $\times 10^6$	x_{tr} (m)	Re_e $\times 10^6$ (/m)	M_e	δ (mm)	θ (mm)	x_{sw} (m)
0	15.1	0.21	19.8	7.0	3.38	0.149	0.0
1	15.1	0.23	13.6	7.1	1.15	0.049	0.64
1	47.4	0.22	36	6.7	0.65	0.029	0.99

Table 5.7: Transition behaviour; data of Sell, 1992.

The final dataset of interest in the location of transition completion. In total four test cases showed transition completion. The data for those test cases are presented in table 5.8.

r_n	$Re_{\infty/m}$ $\times 10^6$	x_{tr} (m)	r_n	$Re_{\infty/m}$ $\times 10^6$	x_{tr} (m)
0	7.5	0.44	0	15.1	0.31
2	12.6	0.6	1	15.1	0.43
2	47.4	0.48	1	47.4	0.29
3	47.4	0.62			

Table 5.8: Transition completion data, data from present study, left; and Sell, right.

The data is presented in figure 5.11 as transition onset Reynolds number Re_{tr} (in millions) against nose Reynolds number. This is probably the most simple way to present and compare data obtained at a variety of unit Reynolds numbers and nose radii; the sharp, low unit Reynolds number cases lying to left of the curve and the blunt, high unit Reynolds number cases lying to the right. In figure 5.11, two distinct trends can be found. The first, for small bluntness, in which increasing the nose radii delays transition onset and transition completion. This trend is apparent up to Re_n=100,000. Transition onset Reynolds numbers are many times the sharp cone value. This region is denoted the small bluntness transition region. A second trend appears at higher nose Reynolds numbers, to the right of the graph. The transition onset location has moved forward, to values comparable to the sharp nose case. This

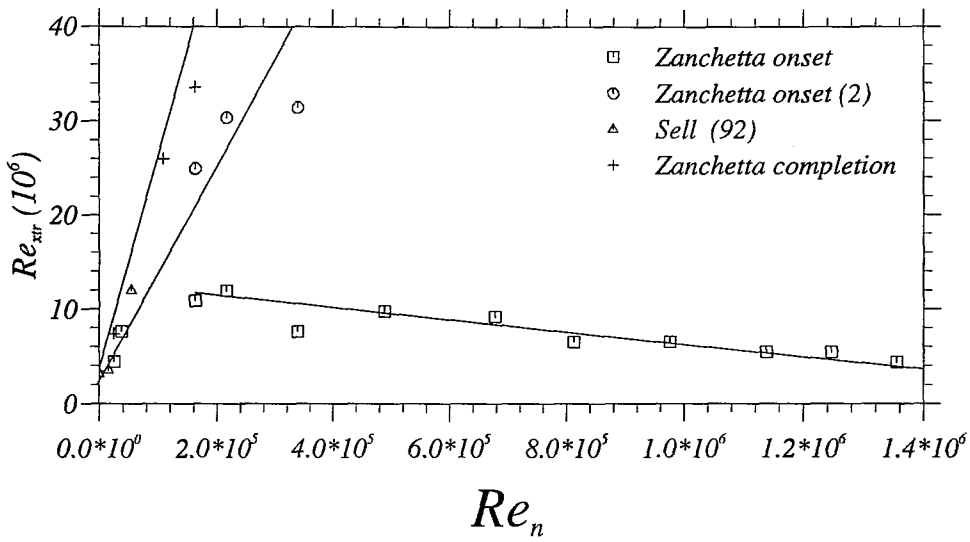


Figure 5.11: Transition Reynolds number against nose Reynolds number.

phenomenon occurs for nose Reynolds number greater than 400,000. Due to the forward movement of the transition front, it is believed that transition reversal is occurring, and this regime is denoted the reversal regime. Transition completion is not witnessed in this regime. There is no clear distinction between the two regimes, and it is seen that for Re_n between 100,000 and 400,000 both transition processes are present. Returning to figure 5.10, the heat transfer distribution can be better understood in light of the above remarks. At this particular nose Reynolds number, (300,000), reversal regime transition is occurring, with the characteristic early onset and slow growth of the transitional processes. At a location further downstream, the onset of the small bluntness transition mechanisms occurs, and acts in addition to the pre-existing reversal regimes process. The presence of a regime in which both events are present and acting concurrently is of extreme interest. The phenomenon presents a similarity with "sub-transitions", first noted in 1984 by Narasimha et al. in flows with pressure gradients (see also Narasimha 1985). Sub-transitions are characterised by a change in the spot formation rate. This topic will be dealt with in detail later.

The transition behaviour depicted in figure 5.11 follows the classic picture depicted by Stetson and Rushton (1967), in which small amounts of blunting delay transition, and at greater amounts of blunting a trend reversal is found. A comparison of the present data with that of Stetson and Rushton and Softley (1969) is offered in figure

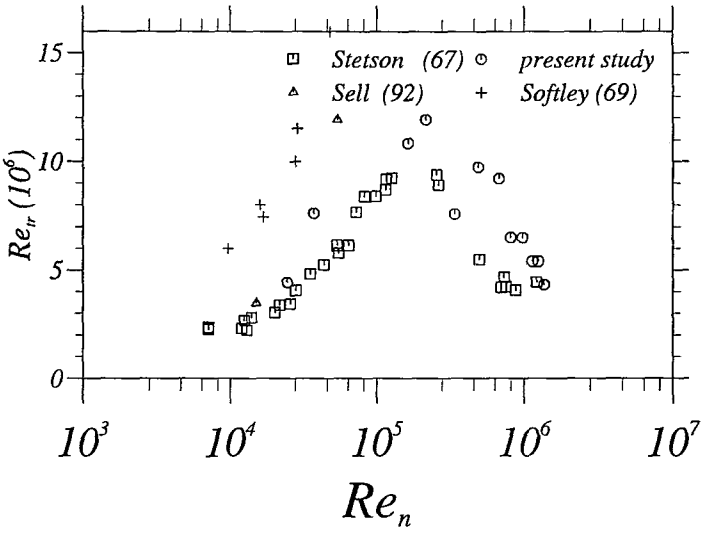


Figure 5.12: Transition behaviour against nose Reynolds number, data from present study is compared to the studies of Stetson and Rushton (1967), Softley (1969) and Sell (1992).

5.12. It is seen that the data are in reasonable quantitative agreement, and most definitely follow the same trend. Stetson's data indicate the occurrence of reversal of nose Reynolds of 100,000, which is also found to the critical nose Reynolds number in further experiments by Softley et al. (1969). However, if the intermittency distribution is plotted at various nose Reynolds numbers, it is is seen that the underlying transition processes have a more complex trend in the present experiments. This information is plotted in figure 5.13, where contours of intermittency are plotted against nose Reynolds number and wetted Reynolds number. The contours indicate that although the trend of transition onset does not continue to show a progressive rearward movement with increasing nose Reynolds number in the reversal regime, the transition activity is dramatically reduced. For Re_n in excess of 400,000, the measured intermittency never exceeds 40 %. This result is of strong importance both from a practical view point of say, the design engineer, but also from a more fundamental view, as the transition behaviour is being markedly altered. A detailed discussion of the processes at hand in the reversal regime are reviewed in the subsequent chapters.

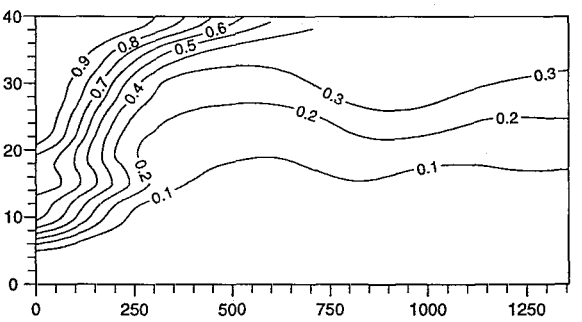


Figure 5.13: Intermittency map showing contours of constant γ obtained from the heat transfer database; x-axis, nose Reynolds number (10^{-3}) ; y-axis, wetted Reynolds number (10^{-6}).

5.5 Concluding remarks

In this chapter, the heat transfer distribution for thirty one test cases have been presented, yielding data for laminar, transitional and turbulent boundary layers. The numerical predictions have been presented and show excellent agreement at all three conditions. The majority of cases tested were transitional, however, often the onset of transition was not detected by the gauges. A method was developed to overcome this. Laminar boundary layer properties were computed using the numerical solver.

Transition onset information has been plotted against nose Reynolds number, and shows two distinct trends. For small nose Reynolds numbers, transition onset is delayed by increasing bluntness. This is denoted the "small bluntness" transition regime. At large nose Reynolds numbers, transition onset moves forwards to the near nose regions. Transitional activity is very low over the entire model length and transition completion does not occur. The maximum computed intermittency levels were always below 40 %. This is the so called "transition reversal" regime, and shows a greater sensitivity to roughness. There is no strong division between the small bluntness and reversal regimes, and two cases have been presented in which both mechanisms are occurring concurrently.

Chapter 6

The structure of the small-bluntness transitional boundary layer

In this chapter, an in-depth view into the small-bluntness transition process will be given. By small bluntness, one intends all the tests cases in which transition occurs in the final stages of the entropy layer swallowing process. These test cases lie to the left on the Re_{tr} vs. Re_n plot of figure 5.11. The test case investigated in this chapter is the 2mm nose radius case tested at the medium pressure operating conditions, with a corresponding nose Reynolds number of Re_n = 25,200. Examining figure 5.3, it seen that the the local minimum and maximum of time averaged heat transfer rate, associated with transition onset and completion as suggested by Owen 1975, are 4.54 $\times 10^6$ and 8.32 $\times 10^6$, respectively. The role of the bluntness in retarding the onset of transition, is apparent when one compares this to the sharp cone transition Reynolds number [Sell 1992] of 3.3 and 4.8 $\times 10^6$.

Using the result of Rotta (1968), the distance to entropy layer swallowing at Mach 9, for the case in question is 1.51m. This can be expressed as a Reynolds number by multiplying it by the free stream unit Reynolds number, giving a value of 19.02 $\times 10^6$. Of importance is the ratio of the distance to transition onset to distance to entropy swallowing, which for this case is 0.43.

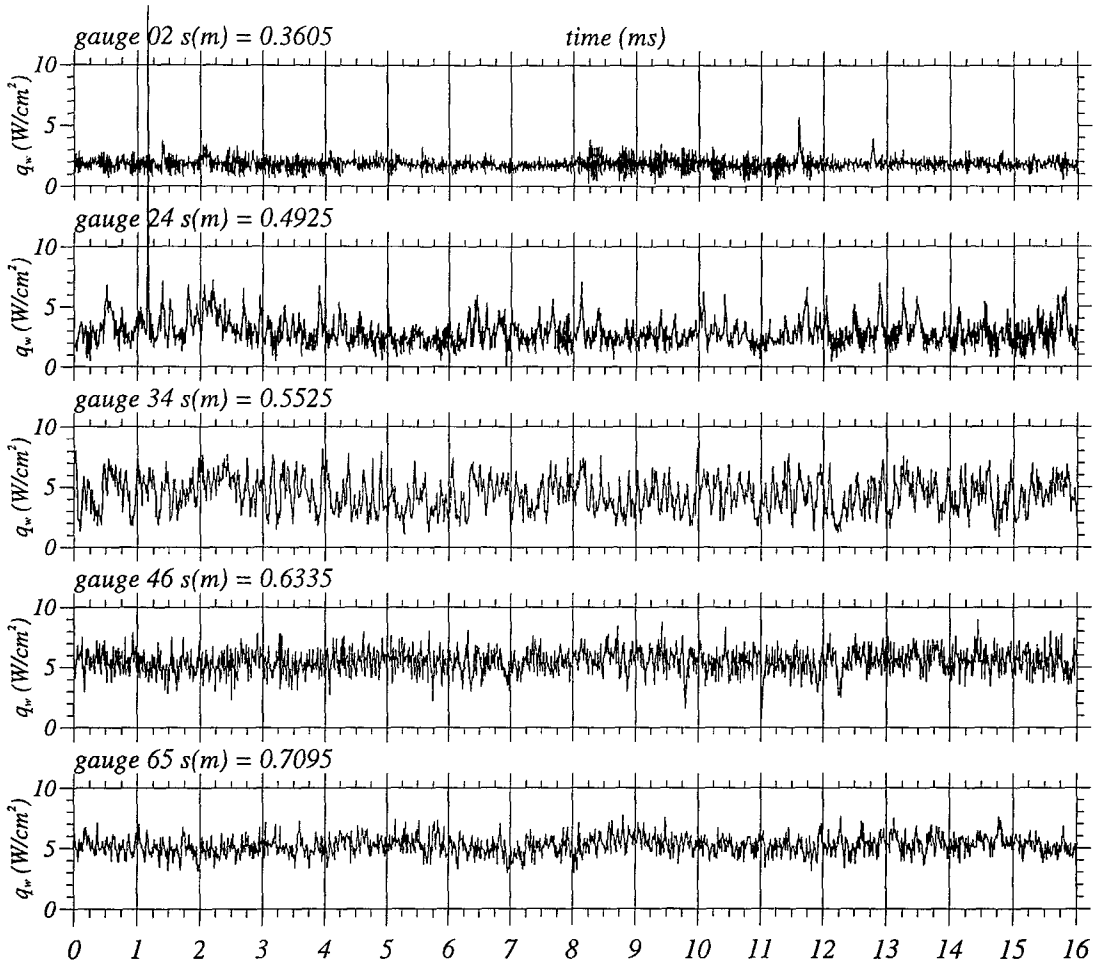


Figure 6.1: Time resolved heat transfer traces for selected gauges tested with the 2mm nose radius tested at the medium pressure operating conditions.

6.1 Time resolved heat transfer rates

In figure 6.1, the time resolved heat transfer rates traces are shown for a selection of five gauges at different axial stations. The data has been obtained by concatenating the steady run time signals for four separate runs, each of four milliseconds in length, to form an ensemble trace. At the most upstream location, (gauge 02, s=0.3605m), the boundary layer characteristics, predicted computationally are: δ = 1.65mm, θ=0.123mm, Re_e= 8.8 $\times 10^6$ (/m) and M_e=6.8. At gauge 02, the time resolved trace indicates that the boundary layer is almost entirely laminar exhibiting some degree of

fluctuations with time. These are believed to be a combination of both aerodynamic unsteadiness (to a small degree) and signal noise. The major contributing factors in the latter are connected with digitisation and integration of the temperature trace. Two spikes can be witnessed at t=11.6ms and 12.8ms, these are connected with the passage of transitional regions of flow over the gauge. At the next station downstream in figure 6.1, (gauge 24, s=0.4925m), the boundary layer has become transitional. The intermittent nature of the process readily apparent, with the heat transfer rate departing from the laminar value as regions of turbulent flow wash over the gauge. The temporal shape of these spikes can be seen in the expanded plot of heat transfer rate against time of figure 6.2. The time scale of the spikes is typically less than 1/10 ms and the spikes are resolved by 10 data samples. Moving further downstream to gauge 34, (s=0.5525m, central plot, figure 6.1), the highly intermittent nature of the transition process becomes more evident. The signal is seen to fluctuate between the lower laminar level of around 2 W/cm^2 and the upper turbulent level of 5 W/cm^2. In close detail, it is seen that all the events observed at gauge 24 are still present at this station and are now accompanied by transition events which have formed somewhere in between the two stations and also spread from neighbouring regions. (For example, the event witnessed at t=12.6ms at gauge 23 can be seen at t=12.64ms at gauge 34, the birth of new events can be seen at 5.5ms.) At gauge 46, (s=0.6335m), the time resolved signal indicates that the boundary layer is almost entirely turbulent showing the occasional passage of laminar flow, which is characterised by a downwards excursion in the heat transfer rate to the laminar value such as can be witnessed at 12.2 ms. At the most downstream location presented in figure 6.1, (gauge 65, s=0.7095m), the boundary layer is entirely turbulent. The signal fluctuation at this location is greater than at the purely laminar station (gauge 02) which is attributed to a greater degree of aerodynamic noise.

6.2 Transition front axi-symmetry

The model used above to capture heat transfer information contains instrumentation only along a single generator, making the task of assessing the axi-symmetry of the transition front very difficult. To obtain information concerning the whole of the boundary layer state, liquid crystal surface thermography was used. The model designed for this purpose was equipped with a 1mm nose radius, so it was not possible

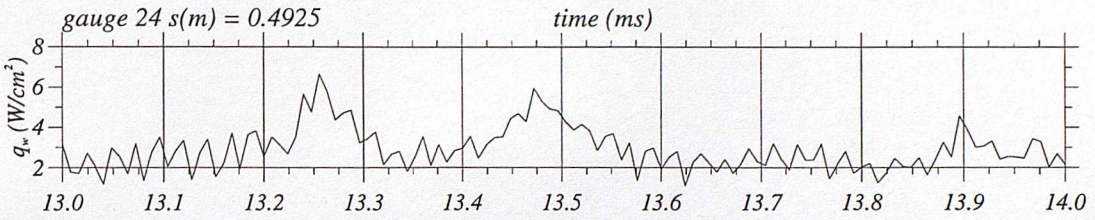


Figure 6.2: Time resolved heat transfer traces for gauge 24 showing turbulent spikes, 2mm nose radius tested at the medium pressure operating conditions.

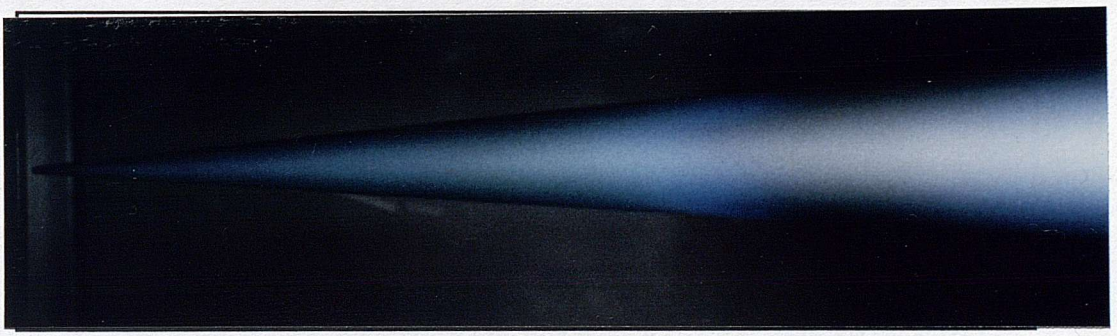


Figure 6.3: Shot 2612, surface heating patterns; 1mm nose radius high pressure operating conditions.

to re-create the exact nose Reynolds number conditions. Instead, two tests cases were performed, one at the medium and the other at the high pressure operating conditions, giving the following nose radius Reynolds numbers respectively: Re_n=12,600 and 47,400 (c.f. 25,200 for the instrumented case). The visualisation for the Re_n = 42,700 test case is presented in figure 6.3. The high heating levels in the stagnation and near nose region cause the paint to exceed the upper threshold of activity and the model surface appears black. Further downstream, the heating patterns indicate that the temperature is decreasing (bands of blue and green) with wetted distance. This is indicative of laminar boundary layer behaviour. The green temperature band is bounded on its downstream side by a second blue band, a black band and a further blue region, indicating that the temperature in this region is increasing to some local maximum (black band) before decreasing again. This increase in heat transfer rate is associated with the occurrence of transitional activity in the boundary layer. Transition onset and completion, (located by the local minimum and maximum of

time averaged heat transfer [Owen 75]) must lie somewhere within the green band and black band, respectively. The transition fronts may be taken as the upstream boundaries of these regions. The transition onset front (the border between the green and the blue bands) extends further forward in the centreline region and moves downstream towards the top and bottom of the model. This result may be caused any of the following reasons:

- inherent 3D nature of transition
- small angles of attack
- light source focusing on centreline
- the change in viewing angle at the different circumferential stations.

Repeat test cases have shown that the surface heating patterns in the transition regions are highly repeatable. If the transition front was three dimensional, one would not expect the transition location to be repeatable, hence the cause for the curvature must be sought elsewhere. To model is aligned geometrically in the tunnel and as it is not equipped with alignment taps any residual incidence cannot be quantified. From the alignment experiments performed with the aluminium model equipped with pressure taps, it is known that geometric alignment is precise to better than one degree of the true aerodynamic alignment. Using this information, it can be assumed that the model is at a near zero incidence. Thus the curvature of the transition front must be caused by the visualisation problem connected with bodies of small radius of curvature most importantly the effect of the change in model viewing angle. It is concluded that over the response time scales of the liquid crystal paint (<1ms) the transition front is axi-symmetric.

6.3 Intermittency

A key issue arising in the discussion of transition is intermittency. This parameter represents the probability of the boundary layer exhibiting turbulent behaviour at any given location. By definition, the intermittency, γ, varies between 0, for laminar

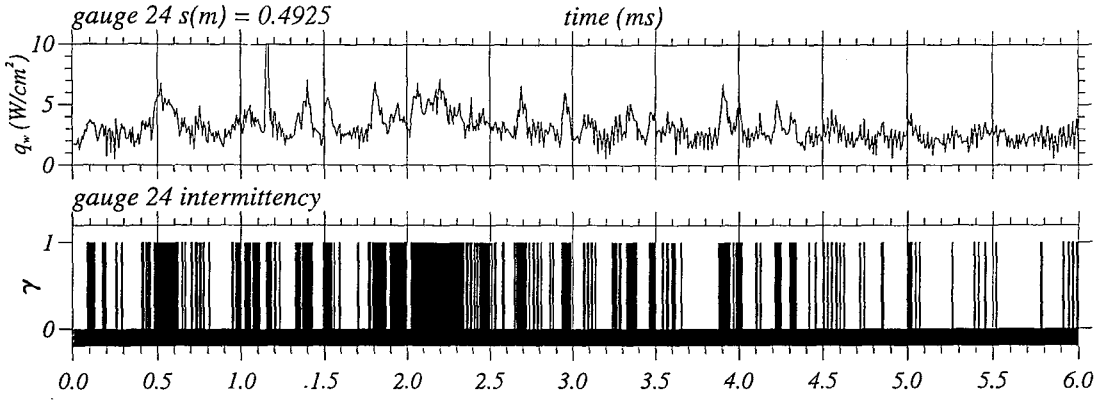


Figure 6.4: Time resolved heat transfer rate and intermittency at gauge 24, for the 2mm case, tested at the medium pressure operating condition.

flow and 1, for turbulent flow. Although the intermittency function is easily defined, it is not easily evaluated due to the difficulties arising when one tries to arbitrarily distinguish turbulent events. This important issue has been discussed recently by Schneider (1995) and as well as in the work of Hedley and Keffer (1974), Sreenivasan (1985), Corrsin and Kistler (1955).

In the cases examined in the present study, the ratio of heat transfer rate in the fully developed turbulent boundary layer to the laminar signal is typically 3 - 5. The large difference in signal level suggests the use of a threshold type intermittency criterion. In this method, some critical value of the heat transfer, Q, is arbitrarily set. If the heat transfer rate, q(t), is below this threshold, then the boundary layer is considered to be laminar at that moment in time and the intermittency function takes value 0. For heat transfer rates above this threshold, the boundary layer is considered "non laminar" and the intermittency function is set to 1. This is formulated into a simple algorithm as expressed in equation 6.1.

$$\gamma(s,t) = \begin{cases} 0 & q(s,t) \leq Q \\ 1 & q(s,t) > Q \end{cases} \tag{6.1}$$

When expressed as a function of time γ is a binary function. The time resolved heat transfer rates and intermittency function for one particular gauge can be seen in figure 6.4. Of particular importance is the time averaged intermittency function, or the intermittency distribution, $\gamma(s)$. This represents the probability, at the station s,

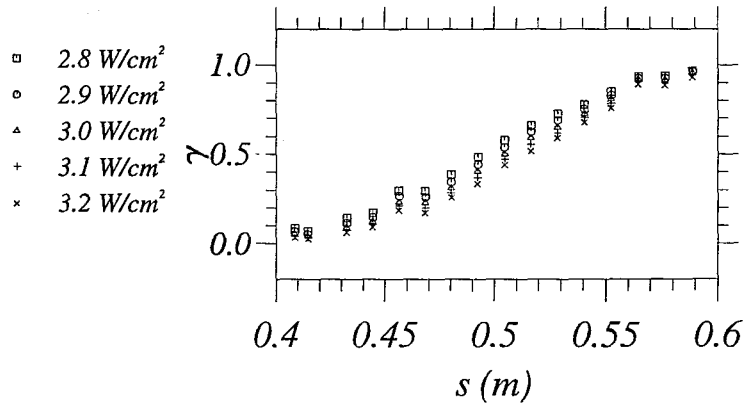


Figure 6.5: Intermittency distribution with five different intermittency levels.

of the boundary layer being turbulent, and can be derived as indicated in equation 6.2.

$$\gamma(s) = \frac{1}{T}\int_1^T \gamma(t,s)dt \tag{6.2}$$

The correct derivation of the intermittency function depends strongly on how Q is chosen. In figure 6.5, the effect of different threshold values, Q, on the intermittency distribution is investigated. In this study, five values of Q have been selected. By changing the threshold Q, the detection algorithm sensitivity is changed. Lowering Q makes the algorithm more sensitive while increasing Q has the opposite effect. The region in which intermittency distribution is most sensitive to the threshold level for moderate to medium levels of turbulent activity, say $0.25 < \gamma < 0.75$. To truly understand how to establish an objective and arbitrary threshold level, the event dynamics and the sensor - data system capabilities must be considered more closely.

6.3.1 Effect of gauge size

The sensitivity of the intermittency function to the threshold Q depends in essence on the sensitivity of the gauge to the passage of turbulent events. In order to best resolve the event features, it is desirable for the gauge to be completely wetted by the event. When, this occurs the signal will switch to the higher turbulent level,

q_t. If only a percentage, P say, of the gauge is wetted by the event, the resulting heat transfer rate can be thought as a linear sum of the laminar and turbulent heat transfer rates in the ratios 1-p:p, as expressed in equation 6.3.

$$q_{detected} = q_{laminar}(1-p) + q_t p \tag{6.3}$$

For gauges in the transitional region, the choice of sensor length depends on the main interest of the study. If the aim is to produce time averaged information, then it is best to use a long sensor which has the quality of a low pass temporal filter. If, as in the the present study, the interest is produce time resolved data, then the gauge is to be kept as small as possible. The constraints of gauge size are imposed by manufacturing capabilities and also be the frequency resolution of the data capturing system.

In the present case, two gauge sizes have been used. Gauges 1 - 30 have a nominal length of 20mm, and gauges 31 - 65 have a nominal length of 4mm. All gauges were sampled at 125kHz and information above $50Khz$ was filtered out to avoid aliasing. The lowest frequency events in a turbulent boundary layer will those associated with the large eddies, which are at most of size δ. Hence, an estimate for frequency, f, can be made using the expression below:

$$f = u_e/\delta \tag{6.4}$$

With boundary layer heights of the order of millimetres and edge velocities in excess of 1000m/s, the typical large eddy turnover frequency given by the above expression will be in the MHz regime. These are clearly beyond the reach of the present instrumentation. A more realistic aim, is to capture the passage of a transitional event over the gauges. The event passage time, t_t, depends on the distance between the gauge and the event origin, Δx_t and on the speeds of the leading and trailing edges of the event, u_l and u_t, respectively, as indicated in equation 6.5 [Mee (1995)].

$$t_t = \frac{\Delta x_t}{u_\infty}\left(\frac{u_l}{u_\infty} - \frac{u_t}{u_\infty}\right)\frac{u_\infty}{u_l}\frac{u_\infty}{u_l} \tag{6.5}$$

Using the values measured by Schubauer (1955) for u_l/u_∞ and u_t/u_∞, (0.88 and 0.5 respectively), the distance an event must propagate downstream from its origin before it can be detected by the present data can be evaluated. Assuming the event must be resolved by at least 3 data samples, (equal to 24 μs), to be distinguished from system noise, equation 6.5 can solved for Δx_t. The distance it must travel is 40mm.

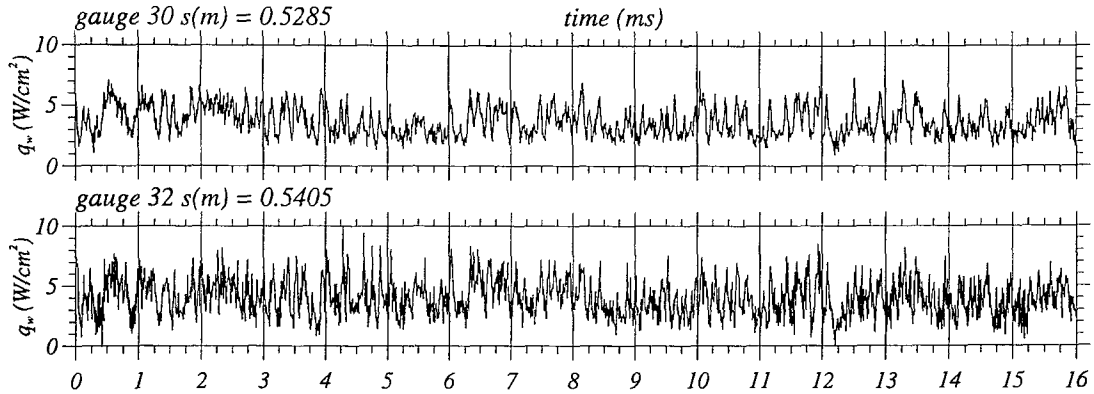


Figure 6.6: Time resolved heat transfer traces for gauges 30 and 32, showing the effect of gauge length in the transition region, 2mm nose radius tested at the medium pressure operating conditions.

Furthermore with increasing distance downstream, the spanwise width of the event increases (after Doorly and Smith (1993), the wedge spreading semi-angle is 2 ° , indicating a circumferential width of 3mm). The transition region is generally of the order of 100 δ (100 mm) in length, and hence the problem of gauge resolution (both temporal and spatial) are not encountered in the latter stages of the intermittency process. This result is confirmed in figure 6.5, in which all five curves collapse towards the end of the transition region, $\gamma > 0.75$. It is the initial stages of event formation that the gauge size is most crucial.

Returning to issue of gauge length the signal from two adjacent gauges of differing length have been plotted, in figure 6.6, The top trace is the signal from gauge 30 of nominal 20mm length and the bottom trace from the nominally 4mm gauge 32. Gauge 32 is located 12mm downstream of gauge 30. Both gauges are located in the region of maximum transitional activity, ($\gamma = 0.5$). The two traces show similar event activity, the main difference being the better capability of gauge 32 to respond to the switching between laminar and turbulent states of the boundary layer.

Setting the intermittency threshold

The sensitivity of the intermittency distribution to the threshold was illustrated in figure 6.5. To set the threshold in a controlled manner, information from the prob-

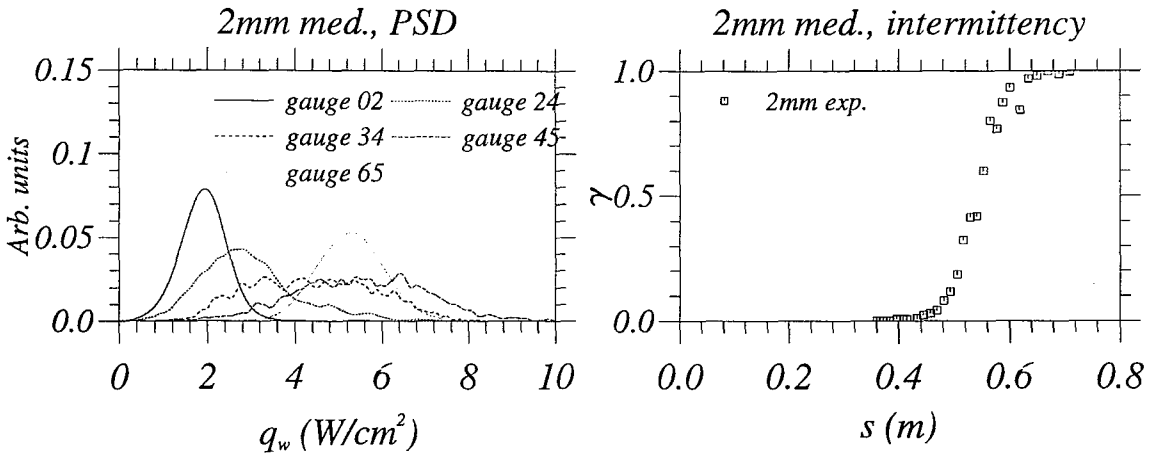


Figure 6.7: PDF and intermittency distribution for the 2mm nose radius tested at the medium pressure operating conditions.

ability density functions (PDF), given in figure 6.7 (left), was used. It can be seen here that the heat transfer rate is symmetrically distributed around some mean value at the station where the boundary layer is laminar (gauge 02). The threshold is established such that it is above the highest laminar levels found to the right of the distribution for gauge 02 in figure 6.7.

6.3.2 Comparison with the Universal distribution

The universal intermittency distribution, based on the concept of concentrated breakdown, was first proposed by Narasimha (1957). It is given as:

$$\gamma(x) = \exp[-0.412\xi^2] \tag{6.6}$$

with

$$\xi = \frac{x - x_t}{\lambda} \tag{6.7}$$

and

$$\lambda = x(\gamma = 0.75) - x(\gamma = 0.25) \tag{6.8}$$

where x_t is the transition onset location. To compare the intermittency distribution measured for the present case, it is necessary to specify x_t and λ. λ is easily measured

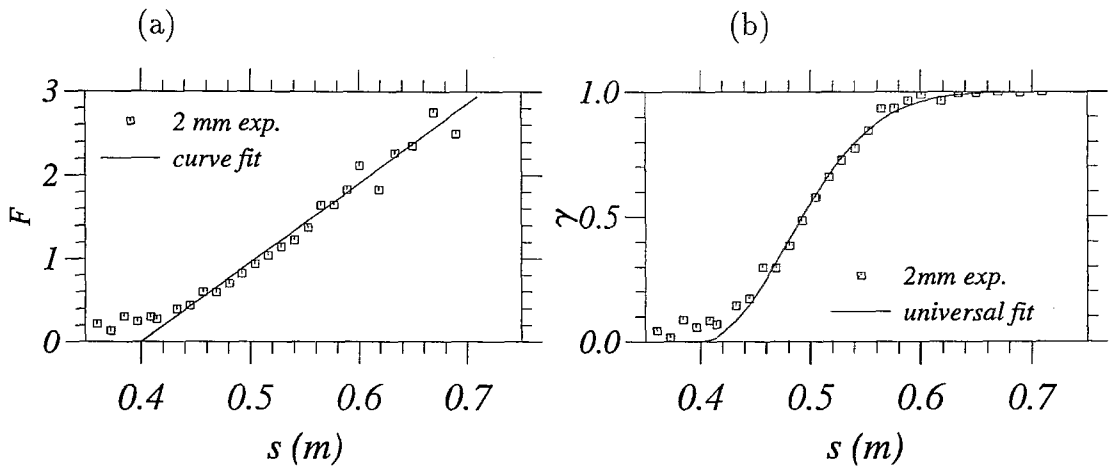


Figure 6.8: F function and the universal intermittency distribution for the 2mm nose radius tested at the medium pressure operating conditions.

from the intermittency distribution. The exact location of transition onset is difficult to specify, firstly because the intermittency criterion is most prone to error in this region, and secondly because, rather than being a unique location of laminar breakdown, there is a narrow belt within which events first originate. To best determine x_t, Narasimha suggests plotting the function F,

$$F(\gamma) = [-\ln(1-\gamma)]^{1/2} \tag{6.9}$$

as given in equation 6.9 and extrapolating to find the zero value. The function F can be seen in figure 6.8 (a) together with the universal fit obtained using equation 6.7 with x_t=0.4 and λ=0.0713. The universal fit, figure 6.8 (b), closely matches the experimentally measured intermittency distribution in the middle and final stages of the transition region; however the agreement in the early part of the transition is poor. Indeed, using the F function, the predicted distance of transition onset is 0.4m, which is greater than the previously observed value of 0.36m. This discrepancy is attributed to the deficiency of the intermittency criterion at low levels of transitional activity to accurately distinguish between system noise and turbulent events. It is concluded that the universal distribution still appears to hold for this high Mach number small-bluntness transition case.

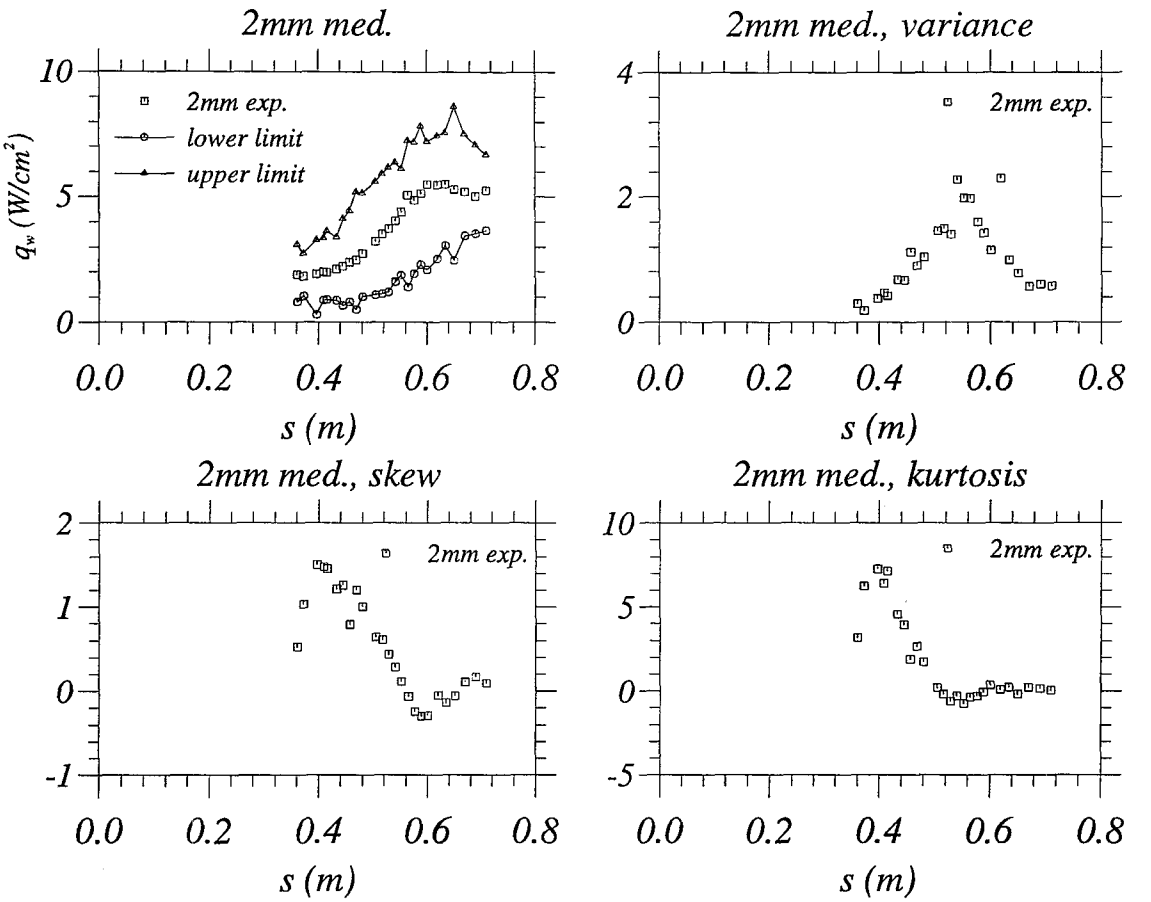


Figure 6.9: Statistical moments for the 2mm case, tested at the medium pressure operating condition.

6.4 Time averaged statistical properties

In figure 6.9, the mean, variance, skew and kurtosis distribution against wetted distance can be found. The time averaged heat transfer rate information has been presented earlier, together with the laminar CFD prediction. In figure 6.9, in addition to the time averaged heat transfer, the extent of the heat transfer excursions, both upper and lower are also included. The heat transfer rate (figure 6.9) measurements have been made such that they present information mainly in the transitional region. Transition begins at s=0.36m and the heat transfer rate has minimum at x=0.37m and rises to a maximum at s=0.6m. At this location, this intermittency function,

figure 6.7 (b) is 0.75. This indicates that the peak in heat transfer occurs upstream of the transition completion point (γ=1, s=0.64m). The extent of the signal fluctuation at any point is given by the difference between the upper (triangles) and lower (circles) limits of the probability density distribution. In the laminar region, the signal fluctuations result primarily from signal noise (digitisation and integration), and the upper and lower bounds are located symmetrically around the mean. This is evident when one analyses the PDF for gauge 02, shown on the left of figure 6.7. In the transition region, the transition process causes the boundary layer to alternatively switch between a laminar and turbulent state, and the extent of signal fluctuation is greatest. The maximum spread occurring between $\gamma = 0.25$ and $\gamma = 0.75$.

The signal variance (figure 6.9) also indicates an increase in signal activity. The minimum signal variance is encountered in the laminar region, and the maximum is achieved at s=0.54m. At this location the intermittency function takes a value of 0.5, i.e. the "middle" of the transition region. In addition this is also the location in which the gradient of time averaged heat transfer is maximum, and indeed the location where the passage frequency of events is greatest. After this location, the signal variance decreases with distance downstream, however even at the most downstream location, where the boundary layer is thought to be fully developed turbulent, the variance level remains higher than the unperturbed laminar level. This result is in accordance with the findings of Owen (1975, 1970), who noted:

- turbulent RMS > laminar RMS
- peak RMS occur between laminar and turbulent region
- peak RMS in correspondence of maximum of turbulent burst frequency

Similar behaviour for hot wire output has been found by Potter (1961) and by Hall (1991) using constant temperature thin films.

In figure 6.9, one can also find the distribution of signal skew and kurtosis. Their definition is given in equations 6.10 and 6.11.

$$Skew = \frac{1}{N}\sum_{1}^{N}\left(\frac{x-\bar{x}}{\sigma}\right)^3 \tag{6.10}$$

$$Kurt = \frac{1}{N}\sum_{1}^{N}\left(\frac{x-\bar{x}}{\sigma}\right)^4 - 3 \tag{6.11}$$

where $\bar{x}$ is the mean and σ is the standard deviation. Both the skew and the kurtosis are non dimensional and indicate the asymmetry and flatness of the signal distribution respectively.

The behaviour of the skew indicates that the signal is changing from the symmetrically distributed noise encountered in the laminar region to a positive skewed distribution occurring in the early part of the transition region (s<0.48m). This is due to the passage of the transitional spikes causing a bias towards positive values. The skew has a zero value at s=0.56m, the location of 50 % intermittency, indicating that at the point of maximum transitional intermittency the signal is evenly distributed between the passages of laminar and turbulent flow. As turbulent activity increases the skew function becomes negative and reaches a local minimum ($\gamma = 0.75$), before returning to zero. The negative values of skew are caused by the passage of laminar regions over the gauge, at a location where for the majority of the time the sensor is wetted by turbulent flow.

The kurtosis gives information concerning the flatness of the distribution with respect to a Gaussian. Positive values indicating that the curve is "sharper" and negative values indicating that the distribution is "flatter" . It is noted that the distribution closely follows the shape of the skew function. Starting from some non-zero positive quantity, reaching a positive maximum at the beginning of the transition region and exhibiting a negative minimum in the middle of the transition region before returning to a near zero reading when the boundary layer becomes fully developed turbulent. This implies a "flat" distribution in the transition region as the signal spreads between laminar and turbulent values.

In table 6.1 the results discussed above are summarised.

s (m)	$\Delta x/\delta$	γ	comment
0.36	0	0	transition begins
0.37	6	< 10 %	minimum time averaged q_w
0.49	78	$= 50$ %	maximum rate of increase of heat transfer rate
0.56	121	> 75 %	maximum RMS minimum skew and kurtosis
0.60	121	> 90 %	maximum time averaged q_w
0.66	182	$= 100$ %	transition completion

Table 6.1: Properties of the small bluntness transitional boundary layer.

6.5 Heat transfer prediction in the transitional region

The capability of the Navier stokes code to perform laminar flow field predictions has been extensively documented (Hillier et al. 1992, Hillier et al. 1993, Soltani and Hillier 1994). Kirk (1992) and Hillier (92) developed a algebraic eddy viscosity model based on the Baldwin Lomax model (1978) and incorporated it into the code. The main interest of Kirk's work was the study of the effect of pressure gradients on turbulent boundary layers (Kirk 1992, Smith 1995). In the early work, the transition region was modelled using a linear "switch-on" of the eddy viscosity, μ_t, such that the viscosity to be used in the computation at any time is prescribed by:

$$\mu = \begin{cases} \mu_{lam} & x < x_t \\ \mu_{lam} + \frac{x-x_t}{\Delta x_t}\mu_t & x_t < x < x_t + \Delta x_t \\ \mu_{lam} + \mu_t & x_t + \Delta x_t < x \end{cases} \tag{6.12}$$

where μ_{lam} is the molecular viscosity, and x_t and Δx_t are the transition onset distance and transition length respectively. The model, albeit satisfactory for Kirk's study, does not reflect the physics of the transition region. In this section, two better models are examined. These are a linear combination method and an up-graded formulation of the switch on of eddy viscosity given in equation 6.12. Linear combination models were first proposed by Dhawan and Narasimha in 1958. They are based on the hypothesis that any mean flow property in the transition region is a linear combination, in the ratio of $1-\gamma : \gamma$ of the laminar boundary layer property and the turbulent boundary layer property. The second method, based upon the success of modelling the eddy viscosity in the turbulent regions, introduces the eddy viscosity in an amount

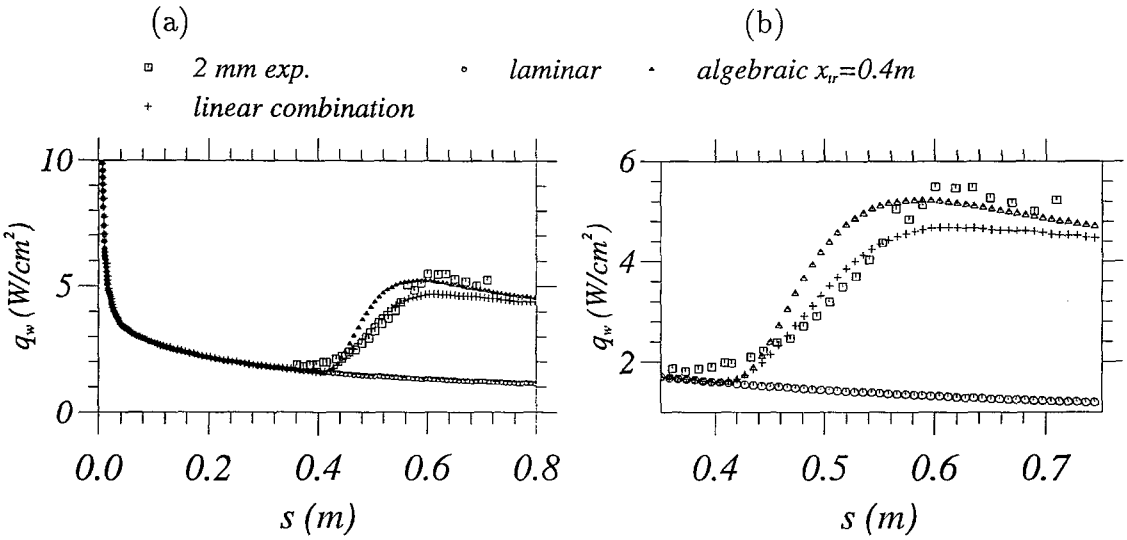


Figure 6.10: Heat transfer prediction in the transitional region using two methods for the 2mm nose radius case tested at the medium pressure operating conditions.

prescribed by the intermittency distribution, $\gamma(x)$, as indicated in equation 6.13.

$$\mu(x) = \mu_{lam} + \gamma(x)\mu_t \tag{6.13}$$

In figure 6.10 (a), the heat transfer predictions are presented over the entire body. Four datasets are shown, namely: the measured heat transfer rate (squares); the laminar CFD prediction (circles); the turbulent CFD prediction with x_t=0.4m; and the final dataset (crosses) which is the heat transfer estimate using the linear combination. In the laminar region, all the estimates are in good agreement with the experimental data. Observing in detail the transitional region, figure 6.10 (b), it is seen that the algebraic eddy viscosity model increases too rapidly, departing readily from the measured trend, but successfully predicts the turbulent heat transfer rate. The linear combination model follows quite closely the heat transfer behaviour in the transitional region, but under-predicts the turbulent heating levels. Neither approach would seem to be capturing the true distribution through the transition region, but the algebraic eddy viscosity model is preferred because it is more representative of the transitional physics.

6.6 Concluding remarks

The heat transfer distribution in a small-bluntness type transitional boundary has been analysed. It is observed that the transition process is governed by the birth and growth of transition events. The transition front is considered to be axi-symmetric and unaffected by roughness. Intermittency distributions have been presented and compared favourably to Narasimha's universal distribution. A strong similarity between properties in sub-, super- and hypersonic transitional boundary layers is observed. Heat transfer predictions in the transitional region favour the algebraic eddy viscosity approach.

Chapter 7

The structure of the reversal regime transitional boundary layer

The experiments reported on previously have noted that an increase in the nose Reynolds number Re_n causes an increase in the length to transition, Re_{tr}, [see also Stetson 1967, Ericsson 1974, Potter 1961, Brinich 1957, Softley 1969 and Owen 1970, for instance]. The retardation of transition onset is caused by the stabilisation of the small-bluntness type transition mechanism. It is proposed that as the boundary layer sensitivity to this mode of transition decreases, the effectiveness of a second transition mode is increased. This second method is denoted the reversal regime transition mechanism. Viewed as a "race to transition" [Reshotko 1990] of different instability modes, there is clearly a change in the leading transition mechanism with increasing nose bluntness.

In this chapter two test cases will be presented, the first, at Re_n=142,200, in which both transition mechanisms are occurring concurrently; and the second at Re_n = 426,600 in which the small-bluntness type transition mechanism has been completely stabilised and the reversal mechanism is explored.

7.1 Reversal regime, test case 1

This test case corresponds to the 3mm nose radius tested at the high pressure operating conditions. In total seven runs were performed to achieve an ensemble steady run

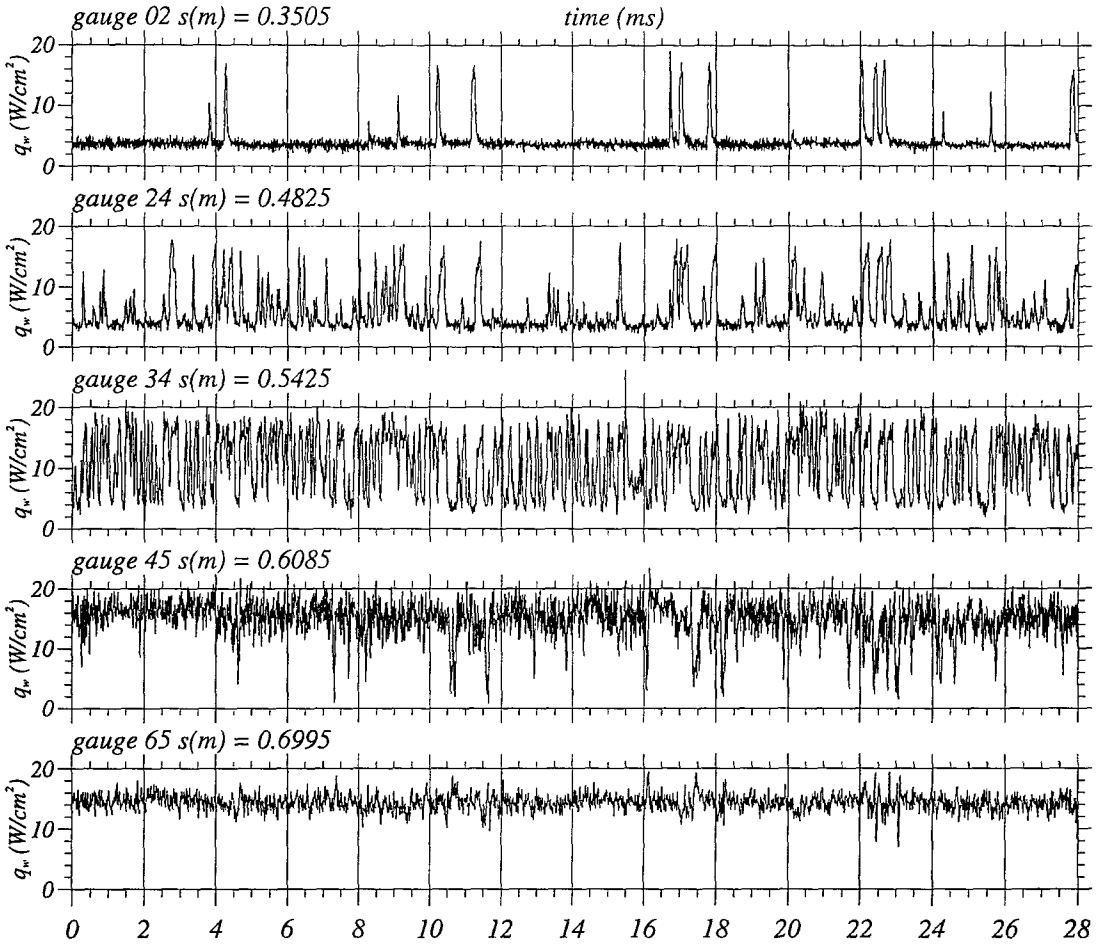


Figure 7.1: Time resolved heat transfer rates for five selected gauges, for the 3mm case tested at the high condition.

time trace of 28ms. The data is concatenated sequentially, so that the time resolved heat transfer rate trace for gauges 02, 24, 34, 45 and 65 of figure 7.1, is composed of seven distinct datasets, each of four milliseconds. The five traces show the boundary layer at different stages in the transition process. Gauges 24, 34, 45 and 65 show the onset and completion of the small-bluntness transition mechanism, (which continuing with the race analogy would be the dominant mode), which can be recognised by its characteristic high frequency intermittent signal. Gauge 02 shows the passage of reversal regime transition events. At this location the boundary layer exhibits a low level of transition activity, and the passage of the events occurs at a much reduced frequency. The temporal structure of these events differs considerably from the

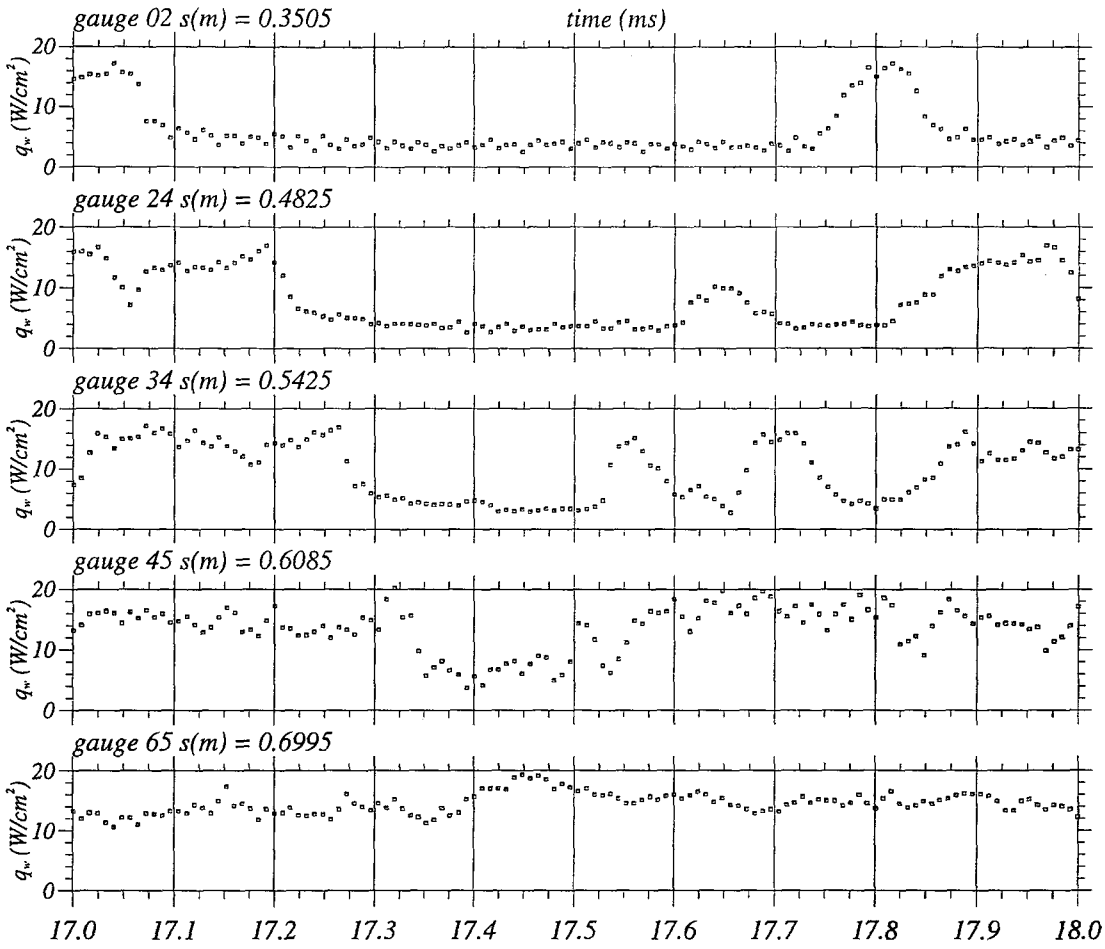


Figure 7.2: Expanded view of the time resolved heat transfer rates for five selected gauges, for the 3mm case tested at the high condition.

transitional spikes encountered in the small-bluntness transition process depicted in figure 6.2. The reversal regime events are seen in a time expanded view in figure 7.2. They rise rapidly from the laminar heating levels (circa 4W/cm^2) to the turbulent level (16W/cm^2) where they exhibit a plateau of duration in excess of 1/10ms before switching back to the laminar heating rates. The event can be separated into three regions; the leading edge, the central plateau and the trailing edge. The leading edge is well defined, showing a very rapid switch to turbulent flow. This indicates that the gauge is completely wetted by the event, suggesting circumferential scales in excess of 20mm. The plateau is characterised by near constant heating followed by the trailing edge in which there is a relaxation of the boundary layer back to laminar flow.

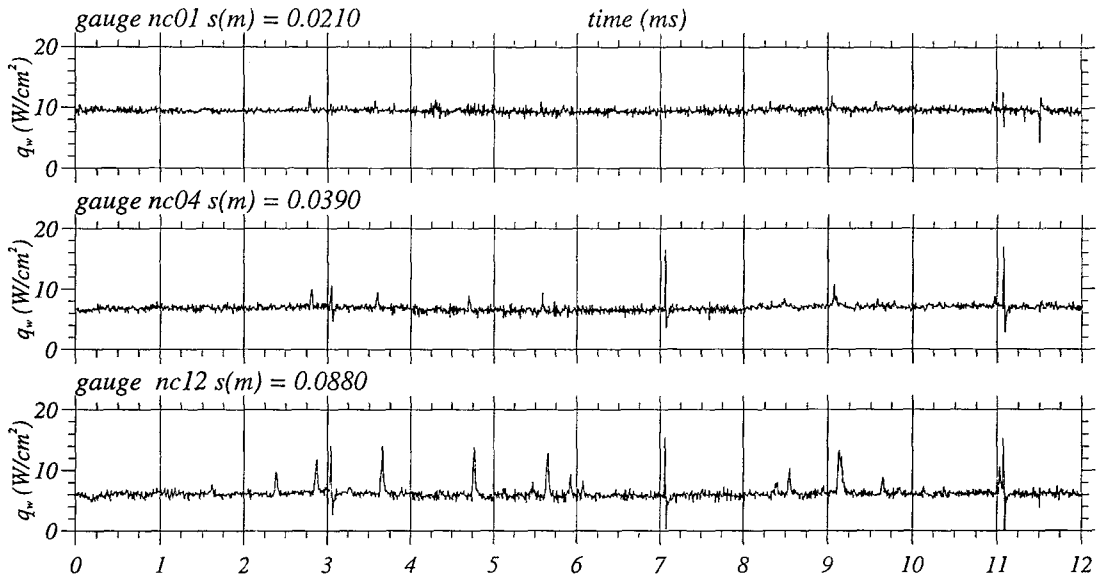


Figure 7.3: Time resolved heat transfer rates for three selected gauges, for the 3mm case tested at the high condition, data obtained with ceramic nose piece.

The relaxation shows the typical "tail off" associated with the passage of the calmed region.

The visualisation experiments (chapter 8, and Zanchetta 1994 and 1995) give details of the event spreading angle. From the known position of gauge 02, it transpires that the event must originate somewhere upstream of s=0.2m. To confirm the presence of the reversal events in the near nose region, a ceramic nose piece, with gauges located between 0.021m and 0.09m downstream (7 - 30 nose radii), was used. The time resolved heat transfer rate traces for three gauges can be seen in figure 7.3. Before analysing the results, it is worth noting that the gauges were all painted to a length of 35mm. This imposes serious problems of gauge resolution, especially as one approaches the model nose. Gauge nc13 (s=0.088m) spans circa 50 % of the circumference and the most upstream gauge covers 2/3 of the local circumference. Finally, it is noted that these experiments were performed in conjunction with schlieren visualisation. The spark trigger voltage contaminates the heat transfer trace at t=3.1, 7.1 and 11.1 ms.

The transition events are most visible, for the reasons of gauge resolution, at gauge nc12. At this station, 11 transition events can clearly be distinguished, and in two

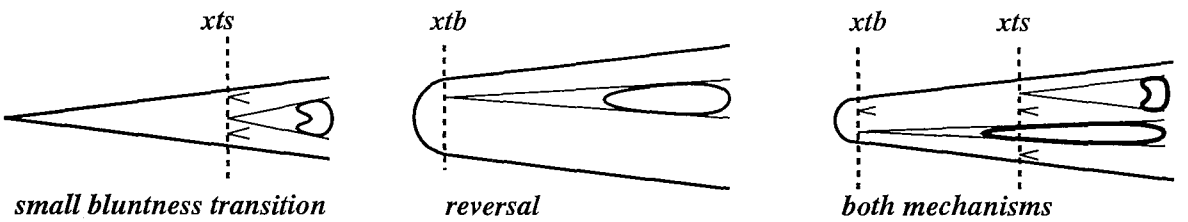


Figure 7.4: Schematic illustration of transition mechanisms.

particular cases (t=3.75 and 9.2 ms) they can be traced upstream to gauge nc01, where the associated rise in heat transfer can still be detected.

This study clearly supports the hypothesis that turbulent events are being formed by two distinct processes. The first process, the small-bluntness mechanism, is stabilised by increasing Re_n; and the second, reversal regime process, promoted by increasing bluntness, in which events originate in the nose and near - nose regions. The superimposition of transition mechanisms, characteristic of this test case, is depicted in figure 7.4. In figure 7.4, it can be seen that the events originating at x_{tb} are joined by further event formation at x_{ts}. When events are formed at x_{ts}, they will not wet the entire sensor length and hence initially will not produce well defined changes in the time resolved heat transfer rate trace. This makes the exact identification of the location of x_{ts} difficult. Furthermore it is noted the inception point is physically a narrow band of finite length, in which the boundary layer breaks down to form events rather than some unique chordwise position. It is proposed that the best method to find the wetted distance of x_{ts} is to monitor the event passage frequency, defined as the number of turbulent events (or laminar) to wet a particular gauge in a unit of time. This curve will show a change in slope downstream of x_{ts}, as the second higher frequency mechanism commences. The event passage frequency is plotted against gauge location in figure 7.5. The curve shows a low but non-zero level of activity up to s=0.42m (in correspondence of gauge 20), after which the event passage frequency rises to a maximum value of 5000Hz at s=0.52m and then returns to zero, (effectively the boundary layer becomes a continuous burst of turbulent activity). Comparing the turbulent event passage frequency to the intermittency distribution, figure 7.6, it is seen that the maximum event passage frequency occurs in correspondence of the 50 % intermittency location (s=0.52m).

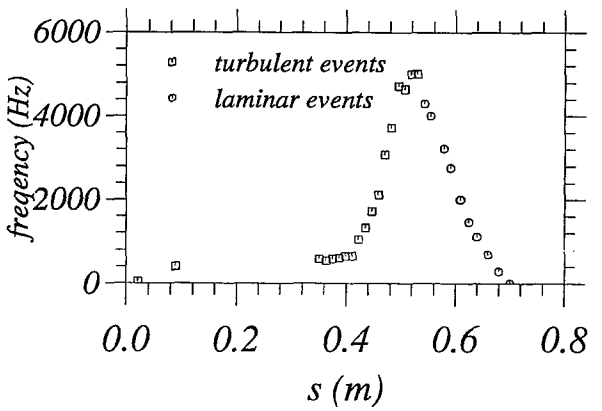


Figure 7.5: Turbulent event passage frequency for the 3mm geometry tested at the high pressure operating conditions.

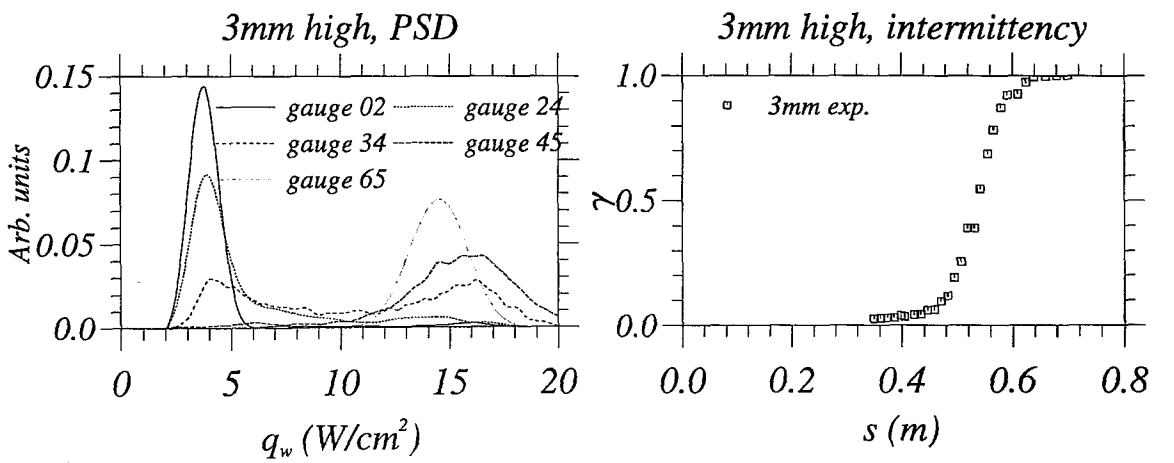


Figure 7.6: PDF and Intermittency for the 3mm case, tested at the high pressure operating condition.

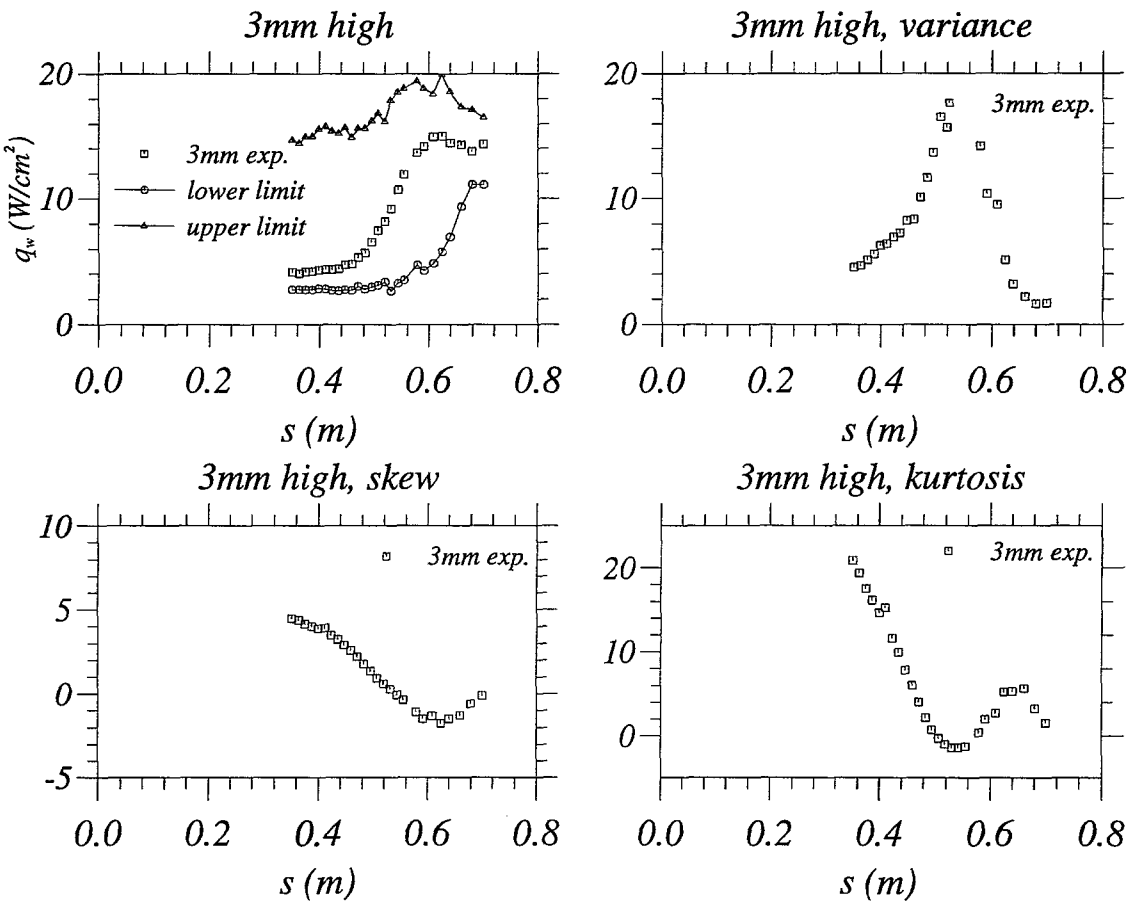


Figure 7.7: Statistical moments for the 3mm case, tested at the high condition.

The presence of the reversal regime events causes significant changes in the distribution of intermittency function and of the statistical moments. The main differences are listed below.

- The presence of a non zero intermittency in a perturbed "laminar region", between x_{tb} and x_{ts}.
- "laminar" signal variance > greater than turbulent variance

The events can also be detected in the PDF plot (left, figure 7.6) where the distribution for gauge 02 shows two distinct peaks. The first centred around the laminar heating level (4W/cm^2) and a second centred around the turbulent heating rate (15W/cm^2) corresponding to the upper heating limit shown in time averaged heat rate plot of figure 7.7. Moving downstream of X_{ts}, the breakdown location for the sharp cone transition mechanism to gauge 24 (γ=0.15), 34 (γ=0.55) and 45 (γ=0.90), it is seen that the effect of the boundary layer transition is to redistribute the PDF from the laminar value to the turbulent value. At the most downstream location, gauge 65 the boundary layer is entirely turbulent and the distribution is centred entirely around the average turbulent level.

7.1.1 Reversal Regime transition zone modelling

In subsection 6.3.2, Narasimha's universal intermittency distribution was presented. The intent of the present subsection is to extend his formulation to model the reversal regime intermittency distribution. At high Re_n, when only the large bluntness mechanism is present, equation 6.6 is still applicable, the notable difference being that the scale of λ, (equation 6.7) is comparable to or greater than the model scale. If the small-bluntness mechanism is also present, it will cause intermittency in the remaining laminar part of the signal, such that at any point in the boundary layer the intermittency will be given by:

$$\gamma = \gamma_b + (1 - \gamma_b)\gamma_s \tag{7.1}$$

where γ_b and γ_s refer to the reversal regime and small-bluntness intermittency distributions respectively as indicated in equations 7.2 and 7.3:

$$\gamma_b(x) = 1 - \exp[-0.412\xi_b^2] \tag{7.2}$$

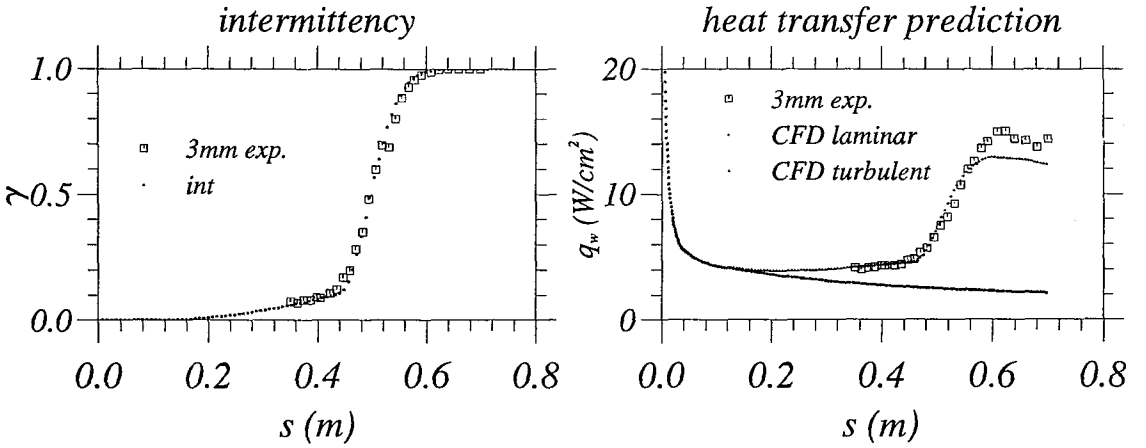


Figure 7.8: Measured and predicted intermittency distribution, left; CFD predicted heat transfer; right. 3mm nose radius, high pressure operating conditions.

$$\gamma_s(x) = 1 - \exp[-0.412\xi_s^2] \tag{7.3}$$

in which ξ is prescribed by equation 6.7. Substituting equations 7.2 and 7.3 into equation 7.1, the intermittency behaviour is prescribed as follows:

$$\gamma(x) = \begin{cases} 0 & x < x_{tb} \\ 1 - \exp[-0.412\xi_b^2] & x_{tb} \leq x < x_{ts} \\ 1 - \exp[-0.412(\xi_b^2 + \xi_s^2)] & x_{ts} \leq x \end{cases} \tag{7.4}$$

The success of equation 7.4 in predicting the intermittency distribution can be seen in figure 7.8. The values used in equation 7.10 are $x_{tb} = 0.1m$, $\lambda_b = 0.65m$, $x_{ts} = 0.44$ and$\lambda_s = 0.05m$.

Equation 7.4 can also be used to prescribe the intermittency distribution for turbulent computations. The resulting heat transfer prediction can be seen in figure 7.8.

The computational results shows good agreement at the lower intermittency levels. The discrepancies become greatest in the terminal stages of the transition process and in the turbulent regions, suggesting that the problem may indeed rest in the limitations of the turbulence model.

7.1.2 Cross correlations

The cross correlation function, $r_{12}(\tau)$, of two heat transfer rate signals, q_1 and q_2 say, describes the general dependence of one data set upon the other. It is defined as:

$$r_{12}(\tau) = \frac{1}{T}\int_0^T q_1'(t)q_2'(t-\tau)dt \tag{7.5}$$

where $q_1'(t) = q_1(t) - \bar{q}_1$ with $\bar{q}_1$ taken as the mean signal level of the period T. The cross correlation function is made non dimensional by dividing by the root mean squared values for each signal, $\overline{q_1'}$ and $\overline{q_2'}$, as follows:

$$R_{12}(\tau) = \frac{r_{12}(\tau)}{(\overline{q_1'})(\overline{q_2'})} \tag{7.6}$$

The root mean square takes the usual definition:

$$\overline{q_i'} = \left[\frac{1}{T}\int_0^T (q_i'(t))^2\, dt\right]^{1/2} \tag{7.7}$$

Using the definition of equation 7.6, forces the correlation function to be contained in the interval [-1,1]. In the present experiment, it is possible to construct the correlation functions between any two of the twenty seven gauges tested simultaneously. The correlation between gauge 02 and all the other gauges tested has been computed using equation 7.6 and is presented in figure 7.9. Gauge 02 is in the perturbed laminar region characterised by the passage of the reversal regime events. The correlation function of gauge 02 with gauge 02, otherwise called the autocorrelation, presents a maximum of 1 at τ=0. As τ is increased, the correlation weakens, such that at separation times of 0.1ms, the signals show very little correlation. Consider the correlation between gauge 04 and 02, (broken line), best seen in the bottom plot of figure 7.9. It is seen that the correlation maximum is lower and shifted to a positive τ of 0.008ms. The delay in peak correlation is a consequence of the physical separation between the gauges and is indicative of the time taken for events to convect between sensors, (in this case 12mm). The decrease in correlation amplitude is caused by the change in character of the structures wetting the two sensors. This means that the events occurring are not "frozen" as they convect downstream boundary layer. The boundary layer, at the streamwise locations of gauge 02 and gauge 04 is mainly characterised by the passage of the long (>100mm) turbulent reversal events, which are of sufficient scale to add positive contribution to the correlation function. Further downstream at station 20, the small-bluntness transition process begins and the heat transfer signal changes

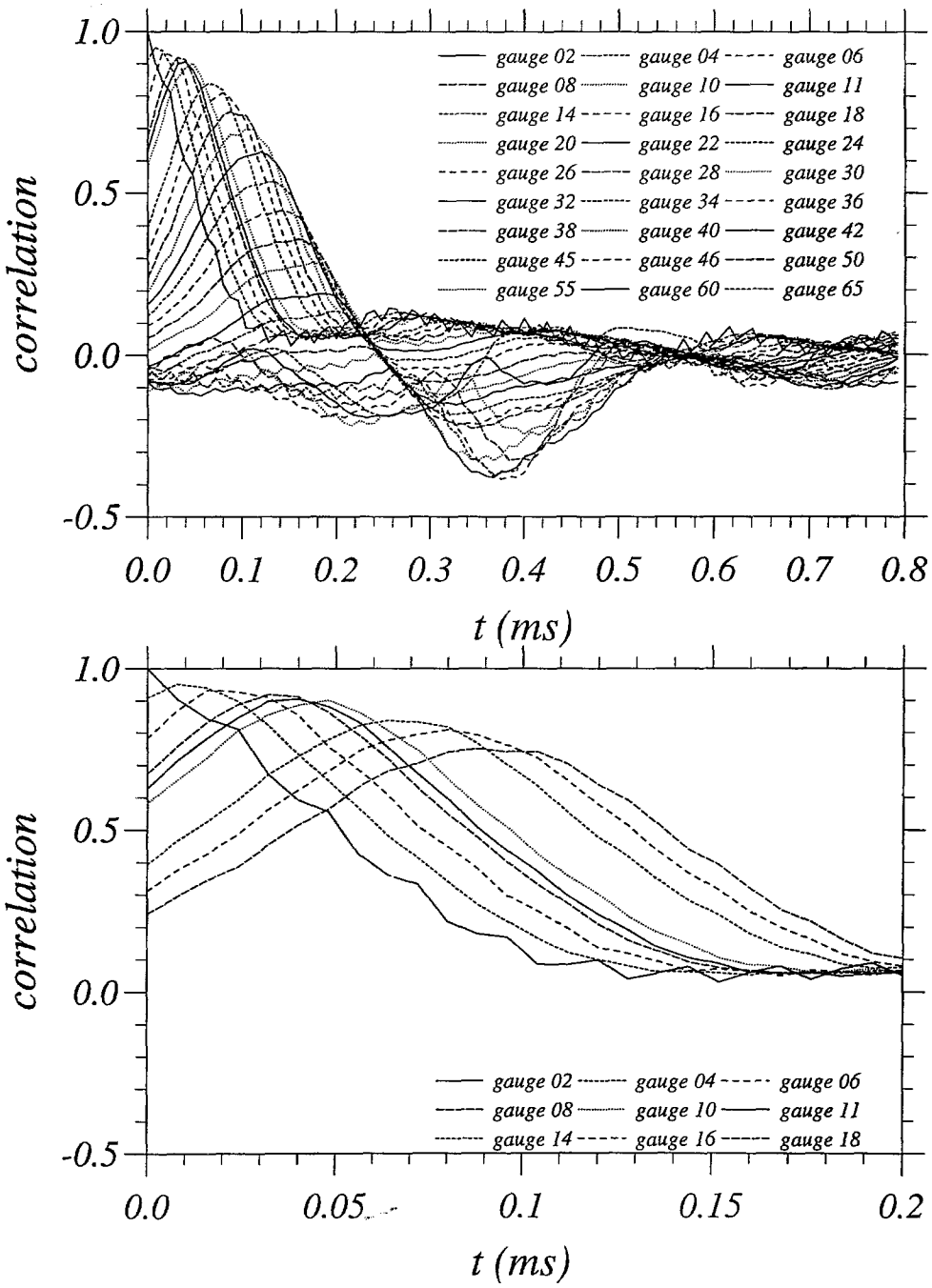


Figure 7.9: Time lag correlations functions for gauge 02, 3mm nose tested at the high condition, top figure, correlations with all sixty-five gauges; bottom figure, expanded view of selected gauges.

rapidly. This is reflected in the behaviour of the correlation function of gauge 02 with gauge 20, which shows a decrease in signal coherency made evident by the smaller extent of positive correlation. Entering further into the transition region and the boundary layer nature is changing substantially. This is such that the last gauge location to show any confident level of correlation with gauge 02 is gauge 32. At this station, the intermittency level is at the 50 % mark.

Figure 7.10 shows the correlations with gauge 24. Gauge 24 is at the beginning of the small-bluntness transition region (s=0.4825m, γ=0.15). Again the autocorrelation function, (the correlation of gauge 24 with gauge 24), shows a maximum of unity at zero time delay. For gauges in the perturbed laminar region, located upstream of gauge 24, it is noted that there is a good level of correlation, for the reasons outlined above. The only difference being that the peak correlation now occurs at negative τ, due to the fact that the events giving a positive contribution to the function convect with the flow, passing first over the upstream gauges (02 - 22). For the gauges located downstream, the correlation function rapidly decreases with increasing separation. This is due to rapid change in the temporal nature of the heat transfer rate trace through the transition region, in particular the formation of new transition events dramatically alters the temporal footprint of the boundary layer.

The correlations with gauge 34, (figure 7.11, s=0.5425m, $\gamma = 0.55$), illustrate further how the transition process is causing a rapid decrease in correlation, for both the gauges located upstream and downstream of station 34. It is noted that the correlation drops most rapidly for gauges located downstream. Similar comments apply to the cross correlation function computed with gauge 45, (figure 7.12, s=0.6085m, γ=0.90), which shows correlation only with the three stations located immediately upstream and downstream of itself. As the turbulent structures are of a scale insufficient to provide any positive correlation, the correlation is a result of the laminar "events", which still persist at this location.

The correlations obtained with gauge 65, the most downstream gauge are given in figure 7.13. This gauge is located in what is believed to be the fully developed turbulent region. Once more, the correlation function is seen to drop rapidly moving upstream, however the presence of non zero correlation with these gauges indicates that certain structures are present at these stations. A possible indication of the nature of these structures is best sought in the time resolved heat transfer rates plots

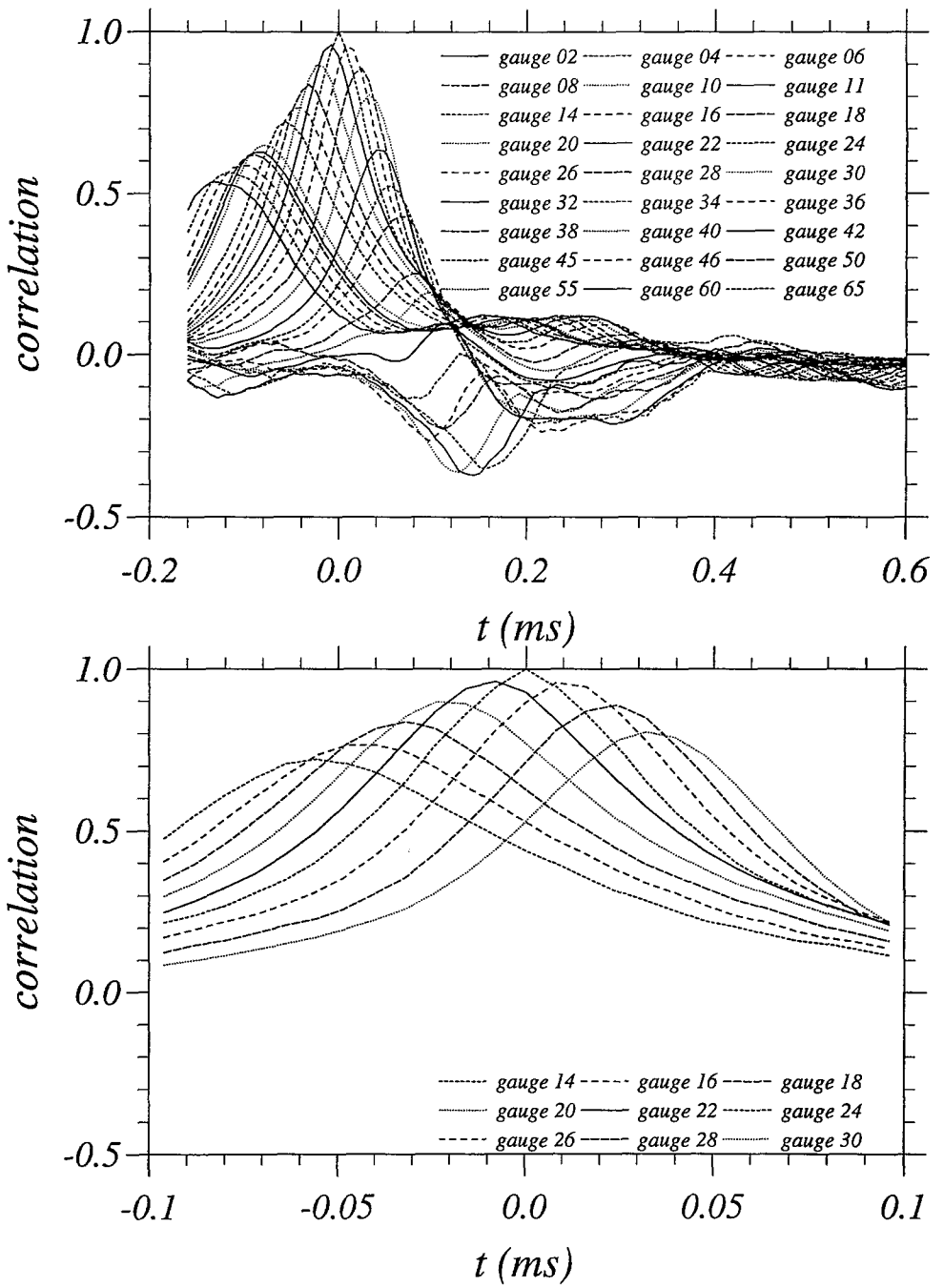


Figure 7.10: Time lag correlations functions for gauge 24, 3mm nose tested at the high condition, top figure, correlations with all sixty-five gauges; bottom figure, expanded view of selected gauges.

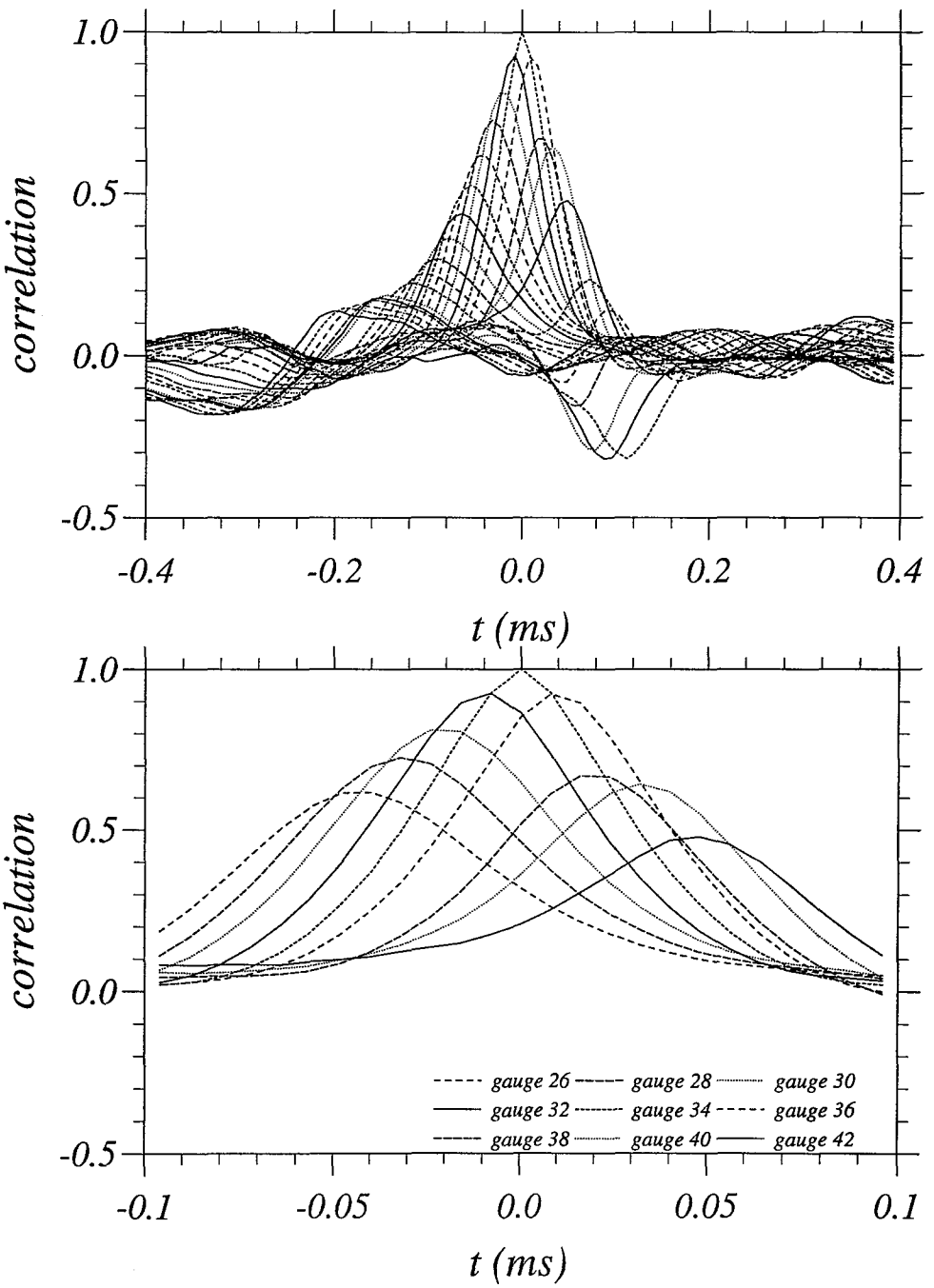


Figure 7.11: Time lag correlations functions for gauge 34, 3mm nose tested at the high condition, top figure, correlations with all sixty-five gauges; bottom figure, expanded view of selected gauges.

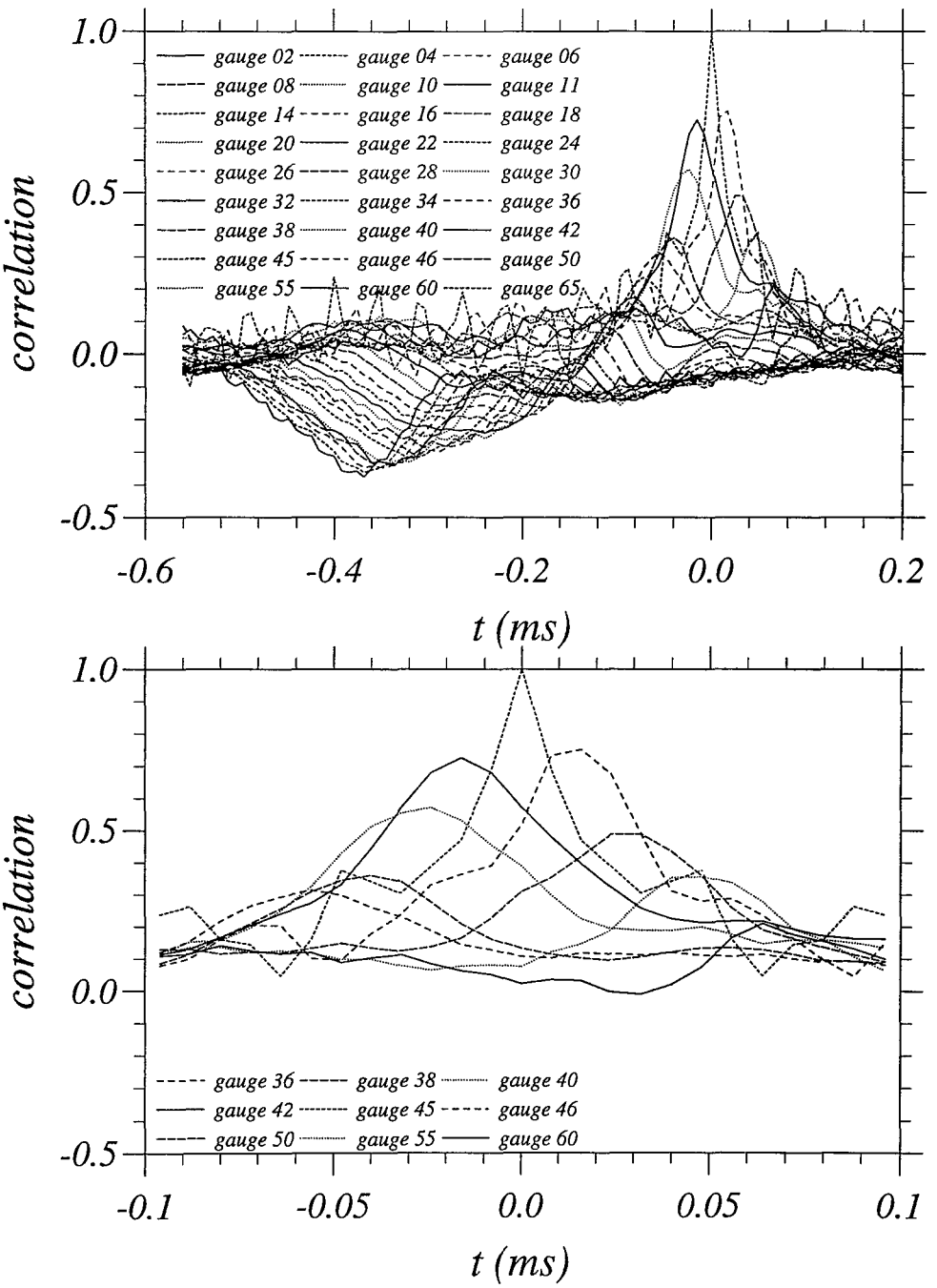


Figure 7.12: Time lag correlations functions for gauge 45, 3mm nose tested at the high condition, top figure, correlations with all sixty-five gauges; bottom figure, expanded view of selected gauges.

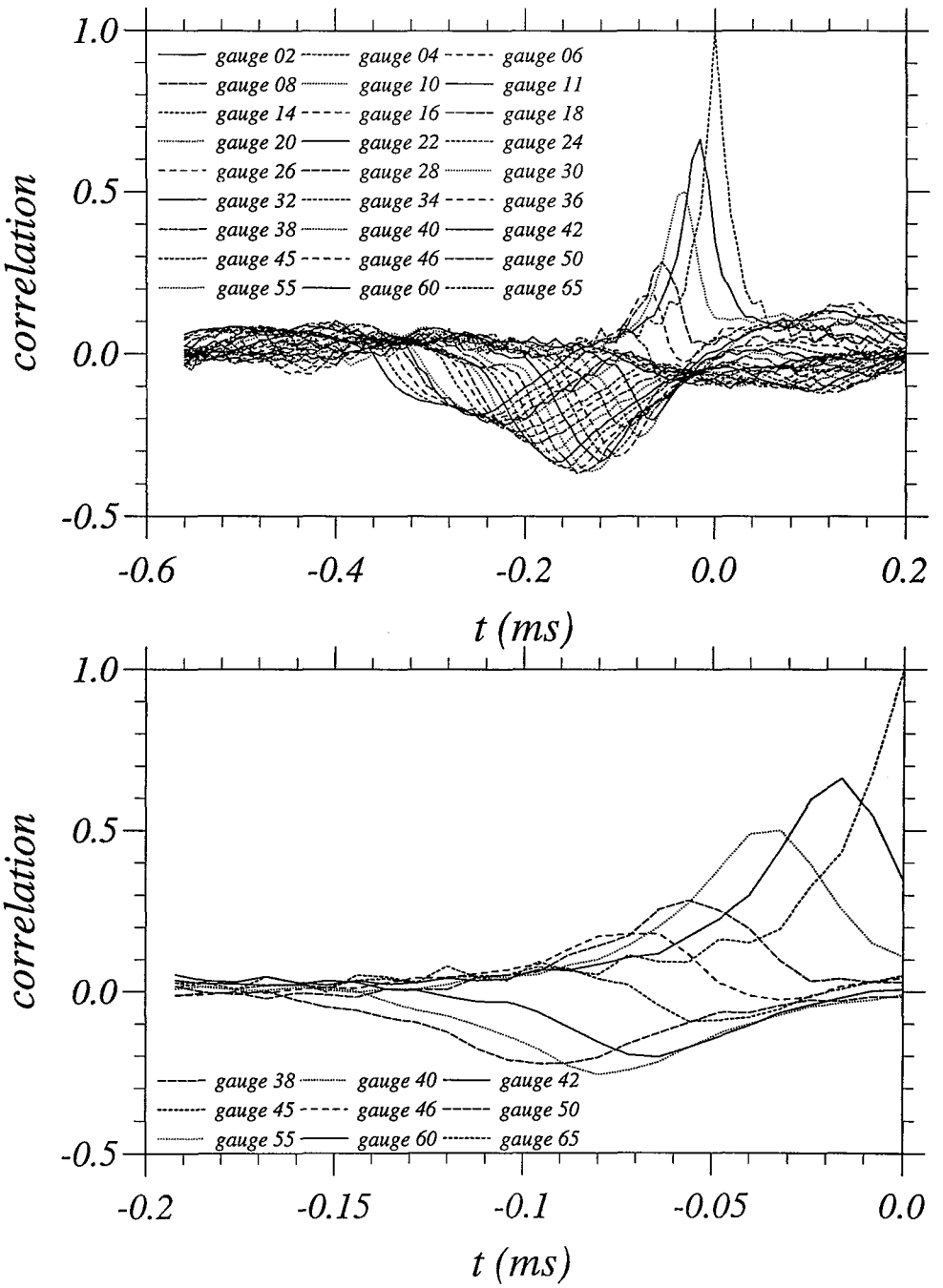


Figure 7.13: Time lag correlations functions for gauge 65, 3mm nose tested at the high condition, top figure, correlations with all sixty-five gauges; bottom figure, expanded view of selected gauges.

of figure 7.1.

7.1.3 Dynamics of the reversal regime transition event

Three methods are used to obtain the propagation characteristics of the reversal regime transition events. Firstly, the event passage at stations 02, 08, 16, 20 and 24 is tracked. Using the intermittency criterion to indicate the presence of an event, both the leading edge and trailing edge passage time are recorded. The difference between the leading and trailing edge arrival times at any particular location gives information about the temporal length of the transition event. The difference in time of passage at different stations yields the propagation velocities of the leading and the trailing edge. Finally from the known speeds and disturbance length, the spatial scale of the event can be found.

The second method is to examine the cross correlation functions presented earlier. This method takes advantage of the fact that only structures of scales greater than the spatial separation of the gauges will give a positive contribution to the correlation function. These structures are the reversal events. The time-lag $\Delta\tau$, corresponding to the maximum correlation between two gauges, can be found and using the known spatial separation of the gauges Δs, a mean convection velocity can be found.

The final method is to examine the phase content of the cross spectral density function calculated between two gauges of known spatial separation Δs. Here, the phase angle delay, $\Delta\theta$ at a given frequency f, is proportional to the time delay $\Delta\tau(f)$ of events of frequency f. Hence a frequency resolved estimate of the mean convection speed can be found.

Event tracking

Ten transition events were tracked between gauge 02 and 24. The leading edge and trailing edge arrival times are given below in tables 7.1 and 7.2.

The leading edge and trailing edge passage times, referenced to gauge 02 (Δ s=0.0m) can be found in figure 7.14. The average speeds based upon curve fits to the mean

	station 02	station 08	station 16	station 20	station 24
Event no. 1	3.792	3.816	3.856	3.872	3.896
Event no. 2	4.232	4.256	4.296	4.304	4.320
Event no. 3	9.096	9.120	9.152	n/a	n/a
Event no. 4	10.176	10.208	10.240	10.248	n/a
Event no. 5	11.160	11.184	11.224	11.240	11.256
Event no. 6	16.960	16.976	17.016	17.040	n/a
Event no. 7	17.736	17.776	17.808	17.824	n/a
Event no. 8	21.960	21.984	22.008	22.024	22.040
Event no. 9	22.344	22.368	22.400	22.424	n/a
Event no. 10	22.576	22.600	22.640	22.656	22.672

Table 7.1: Event leading edge passage time in milliseconds.

	station 02	station 08	station 16	station 20	station 24
Event no. 1	3.380	3.920	3.968	3.992	4.016
Event no. 2	4.328	4.368	4.424	4.448	4.472
Event no. 3	9.144	9.192	9.248	9.272	9.300
Event no. 4	10.280	10.328	10.368	10.408	10.424
Event no. 5	11.304	11.352	11.392	11.424	11.448
Event no. 6	17.080	17.128	17.176	17.208	17.232
Event no. 7	17.864	17.904	17.952	17.984	18.016
Event no. 8	22.088	22.128	22.176	22.200	22.224
Event no. 9	22.480	22.504	22.560	22.592	22.608
Event no. 10	22.704	22.744	22.792	22.816	22.848

Table 7.2: Event trailing edge passage time in milliseconds.

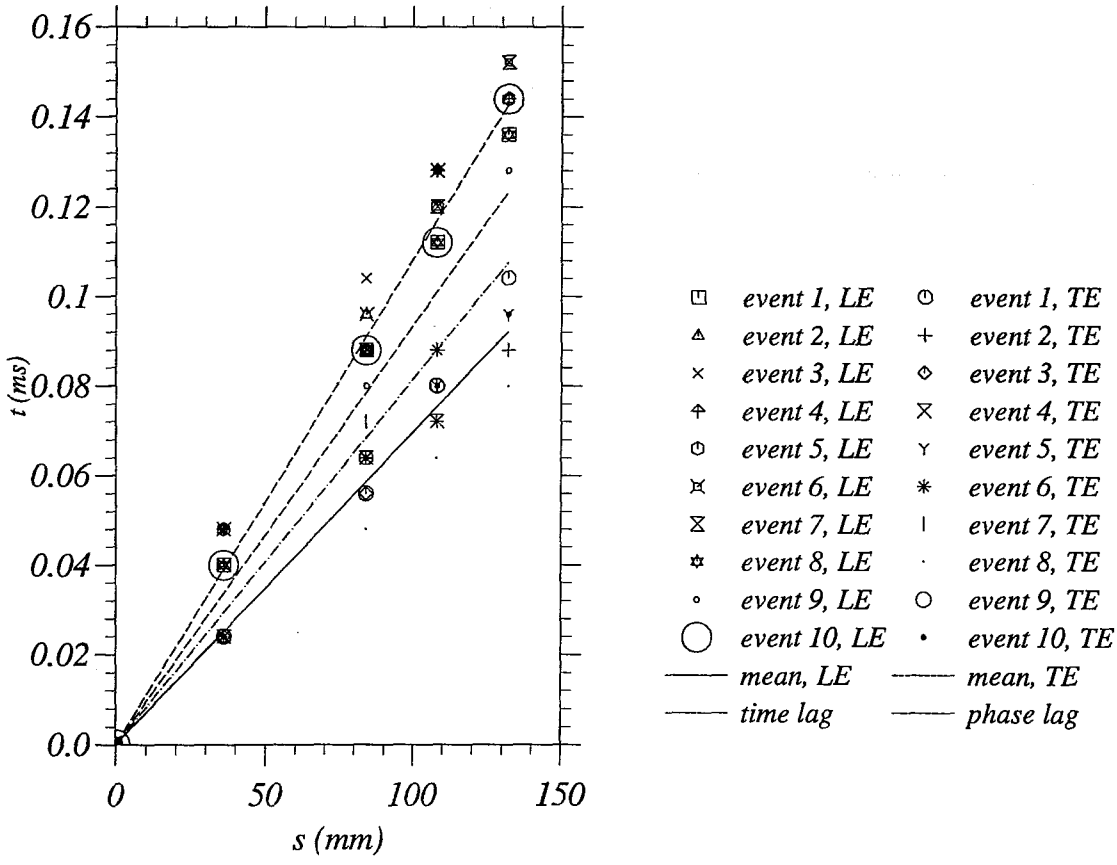


Figure 7.14: Trajectories for the ten transition events.

data of figure 7.14 are given in table 7.3. The mean leading and trailing edge values

	gauge 08	gauge 16	gauge 20	gauge 24	all
Δs (mm)	36	84	108	132	-
$\Delta\tau$ (ms) leading edge	0.0257	0.0609	0.0775	0.0921	-
V_{le} (m/s), leading edge	1402	1379	1393	1433	1402
$\Delta\tau$ (ms) trailing edge	0.0369	0.0900	0.1189	0.1429	-
V_{te} (m/s), trailing edge	975	933	908	924	935

Table 7.3: Event characteristics (mean), referenced to gauge 02.

(1402 and 935 m/s) have also been included in figure 7.14.

The average time the events wetted the tracking stations are given in table 7.4. If

station 02	08	16	20	20
.112 ms	.128 ms	.142 ms	.160 ms	.164 ms

Table 7.4: Event mean duration at the five tracking stations

one assumes that at the breakdown point, located at some distance s_{trans} upstream from the station, the transition event is of finite but very small duration then the following relationship can be derived:

$$s_{trans} = \frac{V_{le}V_{te}}{V_{le} - V_{te}}\Delta\tau \tag{7.8}$$

Using the appropriate values for the leading and trailing edge velocities and the passage time at station 02, equation 7.8 indicates that the breakdown or reversal regime transition event inception point is 314mm upstream. Given that station 02 is 0.351m downstream from the stagnation point it is found that the reversal regime events are forming within the first 30mm i.e. within ten nose radii of the nose. This result is in accordance with the findings of figure 7.3. As the origin of the event is now known, the spatial length of the event can be found, or as the spatial length is a function of distance, the growth rate can be found. The temporal growth rate is the algebraic difference of the leading and trailing edge speeds, 467m/s. The spatial growth rate (based on leading edge position) is 0.333. A typical event is 106mm in length when the leading edge arrives at station 02.

Cross correlation method

The time lags at the peak correlation (taken from figure 7.9) are given in table 7.5, together with the corresponding mean velocity.

	gauge 08	gauge 16	gauge 20	gauge 24	all
Δs (mm)	36	84	108	132	-
mean $\Delta\tau$ (ms)	0.032	0.080	0.104	0.128	-
mean velocity (m/s)	1125	1050	1038	1031	1061

Table 7.5: Peak time lags, and corresponding velocities.

Cross spectral density method

The concept of cross spectral density function evolves directly from the cross correlation function. In a similar manner to which the PSD is the Fourier transform of the autocorrelation function, the CSD is the Fourier transform of the cross correlation function. The cross spectral density will typically have a real and imaginary part, as indicated below:

$$G_{xy} = C_{xy}(f) - iQ_{xy}(f) \tag{7.9}$$

As stated, G_{xy} represents the Fourier transform of the correlation function expressed in equation 7.5. The correlation function is always real and in the special case of the autocorrelation will also be even. The CSD function F, will contain both real and imaginary parts for the general correlation but only a real part for the autocorrelation case. It is preferred however to express G_{xy} in polar coordinates with of modulus $|G_{xy}|$ and phase θ. These are expressed as:

$$|G_{xy}| = \sqrt{C_{xy}^2 + Q_{xy}^2} \tag{7.10}$$

$$\theta = \tan^{-1}\frac{Q_{xy}}{C_{xy}} \tag{7.11}$$

The modulus and phase parts for the CSD calculated using equation 7.11 can be found in figures 7.15 and 7.16. The data are plotted for four CSD studies, namely gauge 02 and gauge 02: gauge 08 and gauge 02; gauge 16 and gauge 08 and gauge

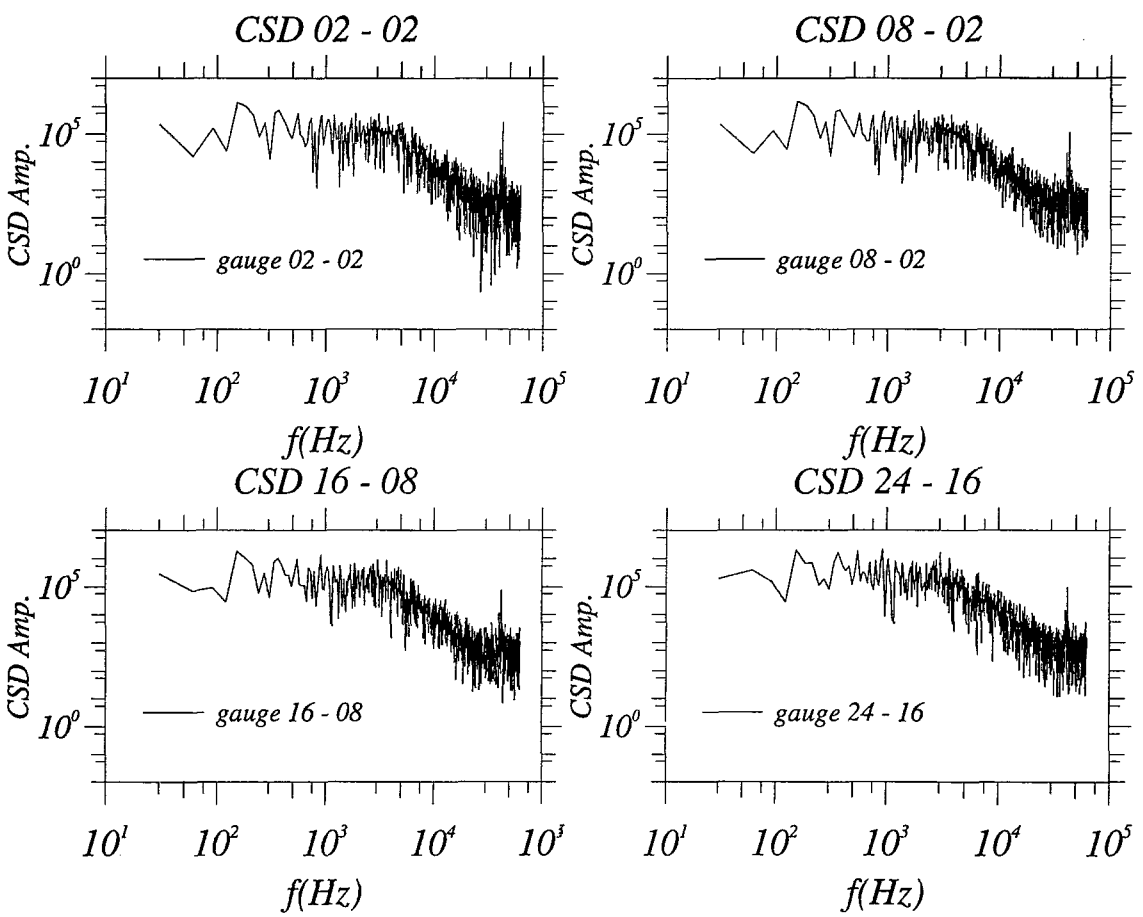


Figure 7.15: Modulus of the cross spectral density function for four cases. The CSD is computed between gauge 02 and gauge 02, between gauge 08 and gauge 02, between gauge 16 and gauge 08, and between gauge 24 and gauge 16. 3mm nose tested at the high condition.

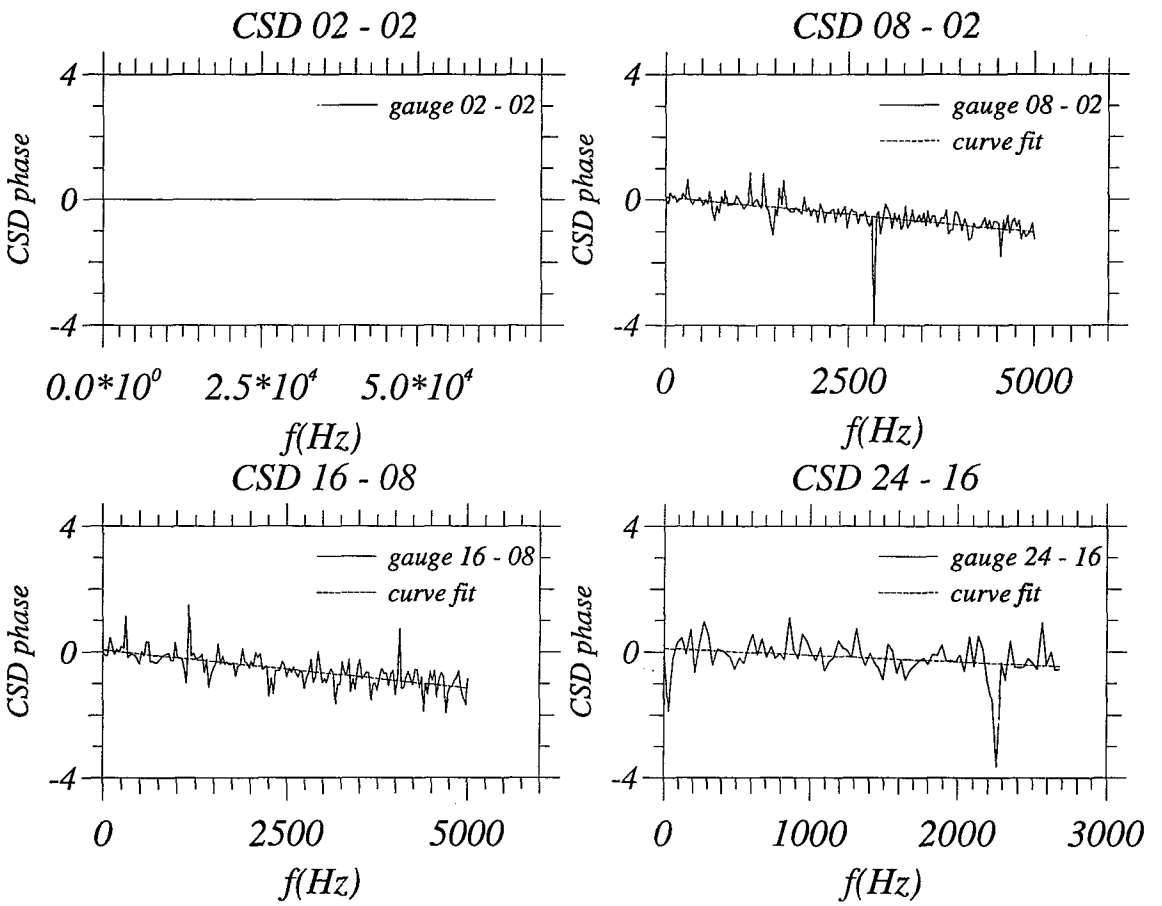


Figure 7.16: Curve fit to phase of the cross spectral density functions for four cases. The CSD is computed between gauge 02 and gauge 02, between gauge 08 and gauge 02, between gauge 16 and gauge 08, and between gauge 24 and gauge 16. Test case is 3mm nose at high condition.

24 and gauge 16. The phase plots are restricted to frequencies in the kHz range, in which the information is most relevant to the physical processes at hand. The first study represent the cross spectral density of the autocorrelation function of gauge 02. This represents a "benchmark" as it is known that the modulus of the CSD reduces to the PSD and that the phase information of the CSD must be zero.

In general the time lag $\Delta\tau(f)$ at any frequency is given by equation 7.12.

$$\Delta\tau(f) = \frac{\theta(f)}{2\pi f} \tag{7.12}$$

In the following analysis, the phase lag is assumed to increase linearly with frequency with zero time lag for events of zero frequency. Furthermore, this will restricted to a range of frequencies. The phase frequency relationship is thus expressed as:

$$\theta = cf \qquad\qquad f < f_{max} \tag{7.13}$$

where c represents the phase versus frequency slope. Substituting the above expression into equation 7.12, one obtains:

$$\Delta\tau = \frac{c}{2\pi} \tag{7.14}$$

The value of the constant c is obtained by fitting curves to the plots of figure 7.16 and for the three cases examined above the convection speeds are given in table 7.6.

CSD	gauge 08 - 02	gauge 16 - 08	gauge 24 - 16
c (rad/Hz $\times 10^6$)	223.9	241.8	212.3
f max (Hz)	5000	5000	2500
$\Delta\tau$ (ms)	0.0356	0.0385	0.0339
Δ s (mm)	36	48	48
V (m/s)	1017	1247	1416

Table 7.6: Phase lags and corresponding velocities.

The spatial structure

Having obtained the leading and trailing edge velocities of the event and two estimates for the mean convection speeds, one can collate the information to build up a quasi

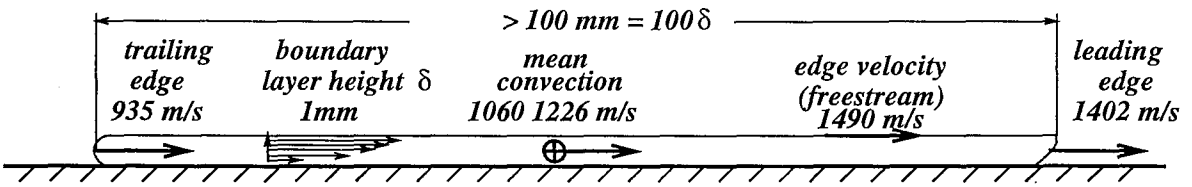


Figure 7.17: Quasi one dimensional illustration of the reversal regime transition event.

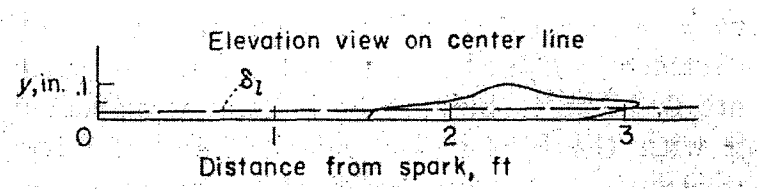


Figure 7.18: Artificially generated turbulent spot of Schubauer and Klebanoff (1956), note vertical scale.

one dimensional picture of the event. This is depicted in figure 7.17. The image compares favourably with the turbulent spot visualised by Schubauer and Klebanoff (1956). This artificially generated spot has leading and trailing edge speeds of 88% and 50 % of the freestream respectively, and can be seen in figure 7.18. The high leading edge celerity found by spot tracking suggests that the event leading edge must be in proximity of the boundary layer edge, this result is in agreement with figure 7.18 and also the work at high Mach numbers of Fischer in 1972. The long spatial scales of the disturbance found in this work are also in agreement with the size suggested in figure 7.18, where the local boundary layer height is $\approx$ 1.3mm and the spot length $>$ 300mm, a ratio $\approx$ 200.

In table 7.7, the leading and trailing edge velocities of various experiments are collected. It can be seen that the present results agree well to the previous estimates. When the present study is compared to the work of Cantwell, it appears that the effects of Mach number are minimal. This is in contrast with the results for event spreading angle angle which shows a strong Mach number dependence (Doorly and Smith, 1993).

This illustration of figure 7.17 has been reconstructed purely from the surface mea-

Study	spot type	M_∞	u_{le}/u_∞	u_{te}/u_∞
Schubauer (1955)	Artificial	0.03	0.88	0.5
Wygnanski (1976)	Artificial	0.05	0.89	0.5
Cantwell (1978)	Artificial	≈ 0	0.98	0.69
Cole (1980)	Artificial	0.03	0.82	0.69
Matsui (1980)	Artificial	≈ 0	0.8	0.56
Gutmark (1987)	Artificial	0.01	0.93	0.6
Sankaran (1991)	Artificial	0.01	0.84	0.58
Clark (1993)	Natural	0.24	0.86	0.56
Clark (1993)	Natural	0.55	0.81	0.56
Clark (1993)	Natural	1.32	0.85	0.54
Clark (1993)	Natural	1.86	0.83	0.53
Zanchetta (1995)	Natural	9	0.94	0.63

Table 7.7: Event leading and trailing edge velocities for a selection of experiments

surements. To construct the complete profile of the event, it is necessary to obtain information in the spanwise (circumferential) and normal direction to the wall. It will be seen latter that if there is continuous and sustained bursting of turbulence (as caused by a roughness element), it is possible to visualise the circumferential growth using liquid crystals. To obtain the growth patterns in a direction normal to the wall, one must traverse a fast response probe through the boundary layer, or alternatively to take schlieren images of the complete event. Unfortunately, both techniques have been applied with little success at Imperial College.

7.2 Reversal regime, test case 2

In this case the nose radius has been increased to 9mm. In doing so, the small-bluntness transition mechanism has been completely stabilised, such that the only transition mechanism at work is the reversal process.

The tests were performed for a total of four runs, two runs with a "smooth" model finish and two runs with a "rough" model finish. Smooth and rough are used in a qualitative manner, smooth indicating a polished finish (roughness height R_a=1.7 μm) and rough indicating that no polishing was performed after machining (R_a=5

μm) The time traces for the heat transfer rates for both cases are given in figure 7.19. In both cases the transition events discussed above are present and can be seen to grow and merge as they move downstream.

In the "rough case", the initial temporal spacing of the events is close, as the events readily merge to form an almost continuous turbulent burst by the most downstream gauge. For the "smooth" case, the initial amount of turbulent bursts present is smaller and furthermore they occur mostly within the initial 2ms. At the most downstream station this leads causes the heat transfer history to appear as a 1ms burst of continuous turbulence, followed by a millisecond of intermittent flow and finally 6 milliseconds of laminar flow in which 3 transition events are present. This low frequency switching of the boundary layer state is sufficiently long to be detected by the thermo-chromic liquid crystal paints, and leads to ghost-like heating patterns which show the footprint of turbulent wedges which are no longer present have switched themselves off.

Further experiments, at different nose Reynolds number, have highlighted the marked influence of roughness on turbulent event formation rate in the reversal regime. An interesting observation is that the first two milliseconds of the steady run time, (data segments 0-2ms and 4-6ms in figure 7.19) also present greater levels of intermittent activity. At this point it rests to speculate upon the origin of this. Certainly, the evidence is sufficient to ascertain that this phenomenon is systematically occurring. Furthermore, the stagnation point heat transfer rate probes have indicated a certain unsteadiness during the steady run window. Indeed, the gun tunnel is a transient facility in which conditions are varying with time and hence it is be expected that at a microscopic level, events can vary with time. For instance, an unsteady behaviour in the transition behaviour of the nozzle boundary layer could significantly alter the disturbance environment of the test jet.

7.3 Concluding remarks

In this chapter evidence has been provided to support the claim that increasing nose radius inhibits the small-bluntness type transition mechanism and promotes the reversal regime transition mechanism. The latter is characterised by the formation of

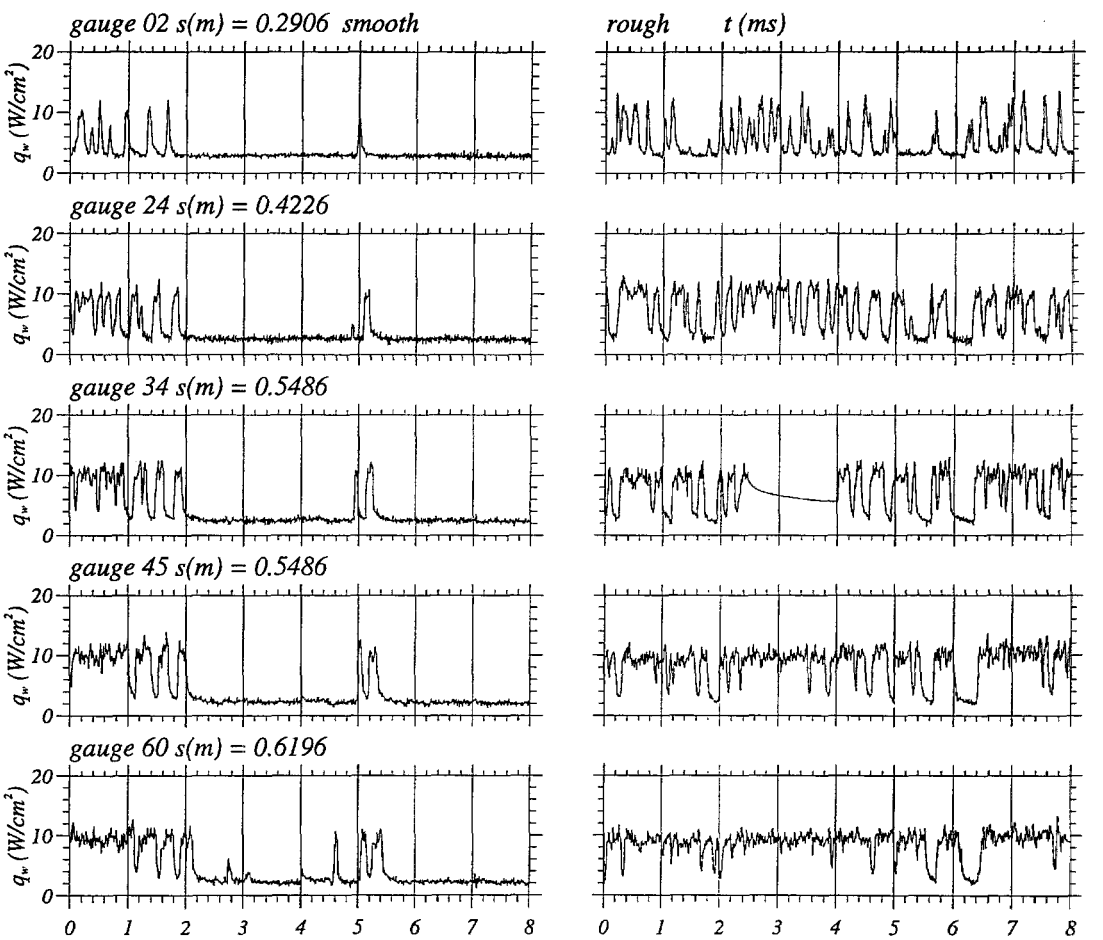


Figure 7.19: Time resolved heat transfer rates, two test cases both obtained with the 9mm nose tested at the high pressure operating conditions.

events in the nose and near nose regions and is highly sensitive to roughness. A case has been presented in which the two mechanisms are occurring concurrently. The experiments have allowed the pre- and transition reversal regime transition dynamics to be compared. In the pre- reversal or small-bluntness regime, the transition process is governed by the birth and growth of turbulent spots at a very high frequency. In the reversal regime, the events show a longer time scale and the distance to transition completion depends strongly upon the initial event formation rate. The latter is strongly connected to the roughness in the nose region. The reversal regime events have leading edge speed equivalent to 94 % of the edge velocity and a trailing edge velocity equivalent to 63 % of the edge velocity, and lengths in excess of 100 δ.

It has been postulated and shown in this chapter that there is a clear link between the reversal regime event formation rate and severity of the roughness environment. This dependence is pursued further in the following chapter.

Chapter 8

Roughness experiments in the reversal regime

Introduction

The experiments of section 7.2 have highlighted the role of roughness in the transition reversal regime. The surface temperature visualisation experiment of figure 8.1 with the 25mm nose cone tested at the high operating pressure conditions, illustrates the highly three dimensional nature of transition front, a further feature characteristic of the reversal regime transition problem.

In the experiment of figure 8.1, one can see three hotter wedge-shaped structures superimposed on the laminar "base" flow. The top and bottom wedges originate from

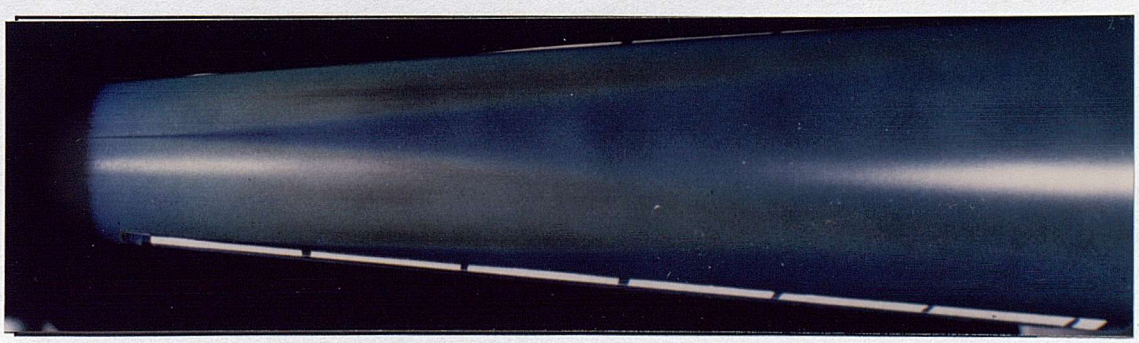


Figure 8.1: Shot 1697, liquid crystal visualisation. r_n=25mm, Re_n=1185,000.

the scale indicator trips which stand 0.2mm proud of the surface. The third wedge is the main feature of interest. In close detail, one can observe that it has evolved from a thin streak-like wake visible in the near nose region, immediately downstream of the sphere cone junction. In addition, several other such structures are present, the majority of which are attenuated and blend back into the laminar background. The exception is the feature of interest which develops into the wedge which remains visible over the entire model surface. The wedge can be divided into two regions. The first region is characterised by little circumferential grow other than that of the natural streamline divergence. In this region, it is felt that the wake is essentially laminar in nature. The region of laminar growth persists for 2/3 of a nose radii downstream of the sphere cone junction at which point the flow within the wake becomes turbulent. Once turbulent, the wake begins to spread with a semi-angle of about 5°, which combined with the natural streamline divergence means that the wake can readily contaminate the surrounding laminar regions. The reason why this wake became turbulent, unlike the others which eventually decayed back into the laminar base flow, was found after the run when the model was inspected. Examination showed that, consistent with the wake origin, the model had sustained an impact from tunnel debris. This impact was of sufficient strength to remove the paint locally and increase local roughness, providing therefore an enhanced disturbance environment capable of promoting transition and sustaining turbulence.

When the transition front is three dimensional, the interpretation of the heat transfer data obtained with instrumentation located along a single generator of the cone may lead to incorrect conclusions. To overcome this problem, the approach used in the following studies are a combination of visualisation and measurement. All experiments were performed with the 25mm nose geometry and, if it not otherwise stated, tested at the high pressure operating condition. This gives a nose Reynolds number of Re_n=1,185,000. This chapter concentrates on the effects of two type of roughness, the 2D distributed roughness and the isolated 3D roughness element.

8.1 Some properties of the laminar base flow

Before examining the experimental results, the CFD will be used to predict the unperturbed laminar flow, otherwise known as the "base flow", which is later distorted

by the roughness elements in the experimental work. The computations were performed using the Navier Stokes solver and taking for input conditions the nozzle plane exit conditions obtained in the calibration. For convenience, these are summarised in table 8.1.

M_∞	$Re_{\infty/m}$	T_0	p_∞
9.01	47,350,000	1105 °K	2815 N/m^2

Table 8.1: Summary of nozzle exit plane conditions, high pressure operating condition

In figure 8.2, the boundary layer height, displacement thickness, edge Mach number and edge unit Reynolds number are given against wetted distance. The top two graphs show the behaviour over the entire wetted length of the model while the bottom two focus on the nose region (s=37mm is the wetted distance to the sphere cone junction). The boundary layer remains of near constant height in the proximity of the stagnation point. In this region the flow is subsonic but rapidly accelerating. At s=0.018m ($\theta = 41.25°$), the flow at the boundary layer edge becomes sonic. At this point the $Re_{e/m}$ reaches a local maximum of 70 million. Downstream of the sonic point, the flow is supersonic and the boundary layer undergoes a more rapid growth as a result of the expansion of the flow around the nose. The rapid growth of the boundary layer and displacement thickness continues until the sphere cone junction is reached, at which point, they begin to grow in a near parabolic fashion and the recovery to sharp cone conditions begins. The Mach number and Reynolds number distributions illustrate the severity of entropy layer effect for this particular case. Indeed, at the most downstream location, the Mach number is only 3.4 and the edge Reynolds is 7×10^6, a factor of ten below the sharp nose case. Using Rotta's expression, entropy swallowing and recovery to sharp cone conditions will occur at s/r_n=2750, (s=68.8m).

8.2 Uniformly distributed roughness

Various distributed roughness environments have been investigated. In the first instance, the distributed roughness effect was created by using a matte undercoat.

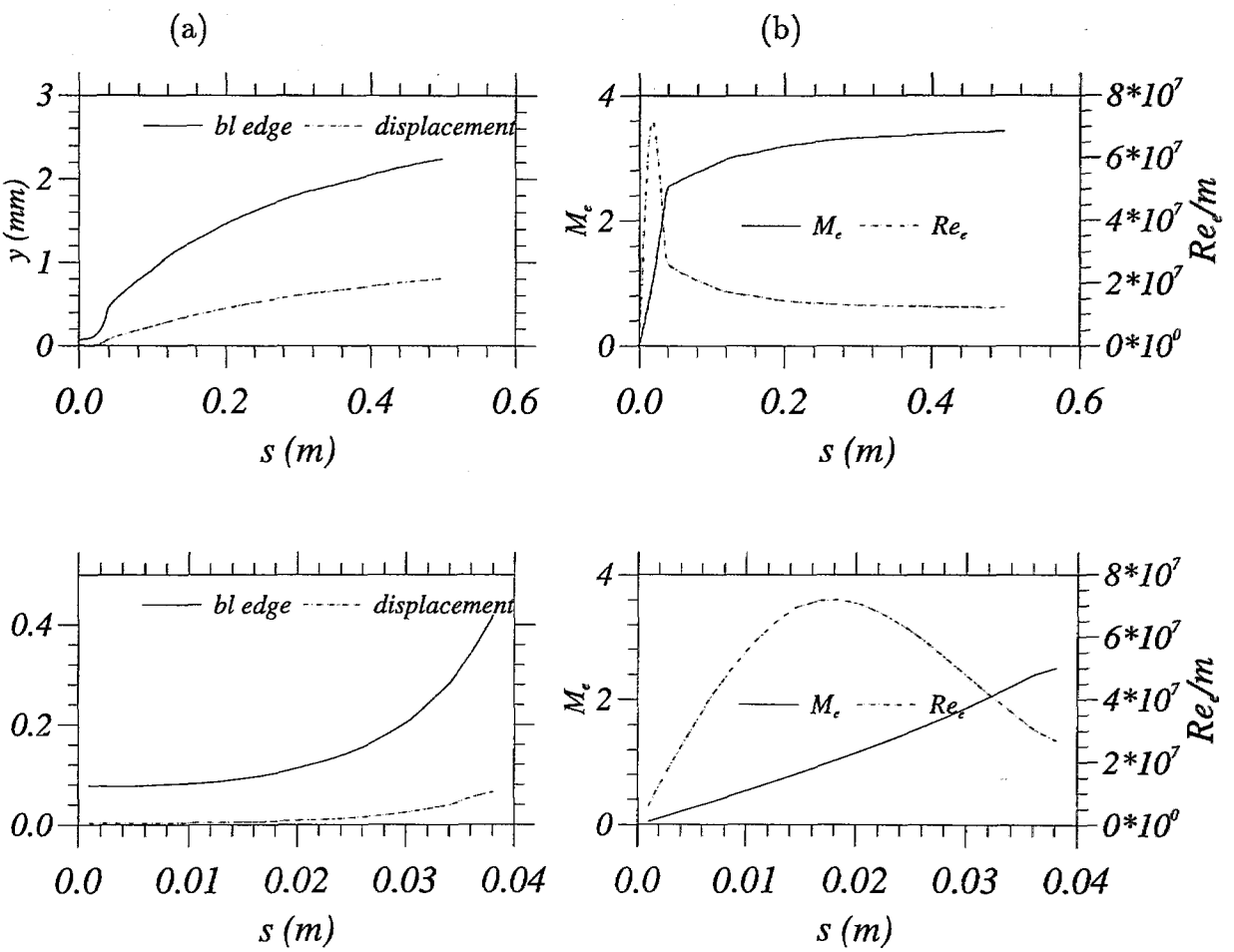


Figure 8.2: Boundary layer thickness, displacement thickness (a) and Mach number and Reynolds number against wetted distance (b).

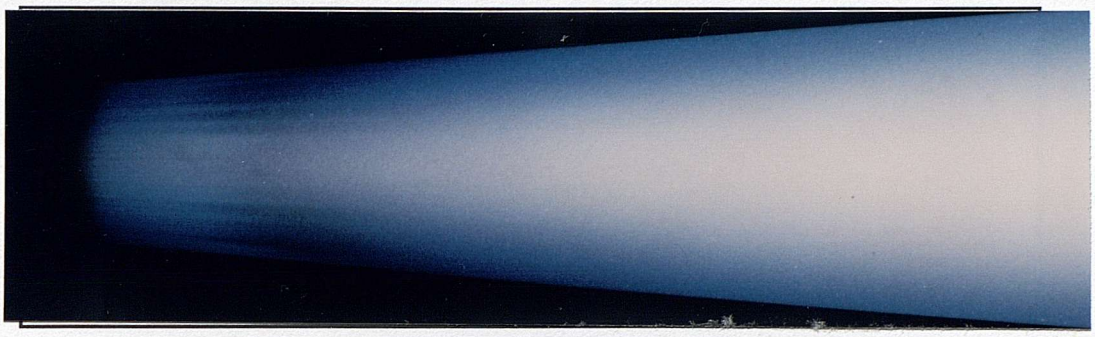


Figure 8.3: Shot 2576, liquid crystal visualisation. r_n=25mm, Re_n=1185,000, matte finish.

Upon this layer the liquid crystal paints were applied. It is believed that the roughness height of the undercoat was circa 50 μm. The resulting heating patterns for this case can be seen in figure 8.3. The model is black in the nose region, where the temperature has exceeded the upper threshold of activity. In the near nose region, the model is cooling, (dark blue followed by a lighter blue band); and further downstream a second hot band is encountered (dark blue) after which the temperature decreases again. The patterns indicate that the boundary layer is laminar in the nose region and becomes turbulent at two nose radii downstream from the sphere-cone junction. At a microscopic level, the flow in the shoulder region is characterised by the presence of hotter (darker blue) axially aligned streaks. These structures have spacing between 0.2 - 1 mm and a density of 5 - 10 per mm. The streaks undergo a change in circumferential spreading rate between 2/3 and 1 nose radii downstream of the sphere - cone junction. This is associated with transition. The streaks, once turbulent, merge as they spread downstream. The distance at which the whole boundary layer becomes turbulent is dependent on the initial spanwise spacing of the streak-like structures. One can identify two distances to transition completion. At small scales, transition of the streak, highlighted by the change in spreading angle, occurring at Re_{tr}=2,640,000; and at larger scales, transition completion is associated with the coalescence of the turbulent wedges, the Reynolds number for which is Re_{tr}=3,722,000.

The matte undercoat is successful in providing a distributed roughness environment but does not prove to be a flexible test base for parametric studies. In a second series of experiments, the model under-surface was returned to its smooth state and by

using a different painting technique, the liquid crystal paints were re-applied, forming roughness elements of 50 μm in diameter, evenly distributed over the surface. The paints serve a double use, firstly providing a flexible and easily applicable disturbance environment and secondly visualising the resulting heating patterns. It must be noted that in all other applications, the typical roughness height of the paints is 10 μm, but for this particular use, the painting technique enabled the user to deposit agglomeration of capsules 50 μm in diameter. As the paints can readily be applied and removed in a spiral manner from the surface, their use, as both the roughness generator and visualisation tool, is highly profitable and in total twenty experiments were performed.

In the sequence of photographs of figure 8.4, the effect of roughness in the hemispherical region of the model is explored. In all four studies, the top half of the model is painted with Merck TCA 1005 paints and the bottom half with Hallcrest paints BM22/R22/C5W/C17-10. The boundary between the paints appears as a darker line running horizontally down the model. The paints differ slightly in activity range and were applied together to appraise their respect merits.

In the first image of the series the whole model is coated with the "enhanced-roughness" paint. Shot 2617, 8.4 (a), shows that this roughness size and distribution is sufficient to promote transition in the near nose region. Again the transition process is characterised by the appearance of streak-like structures immediately after the sphere - cone junction. The structures again undergo transition between 1 and 1 1/2 nose radii downstream of the sphere - cone junction and transition is complete by two nose radii downstream.

In shot 2618, 8.4 (b), the paint has been removed in the nose region to reveal a circular portion of the smooth model surface centred around the model nose. The paint present downstream of an angle 50° measured with respect to the apex. The resulting surface heating pattern indicates the presence of the hot streak-like structures, but transition of these structures is not witnessed. One concludes that the reduced roughness environment does not sufficiently perturb the boundary layer to promote transition.

The paint has been removed to the 70° degree mark in shot 2619, 8.4 (c). The effect is to reduce the occurrence of the roughness wakes and diminish their intensity. Present

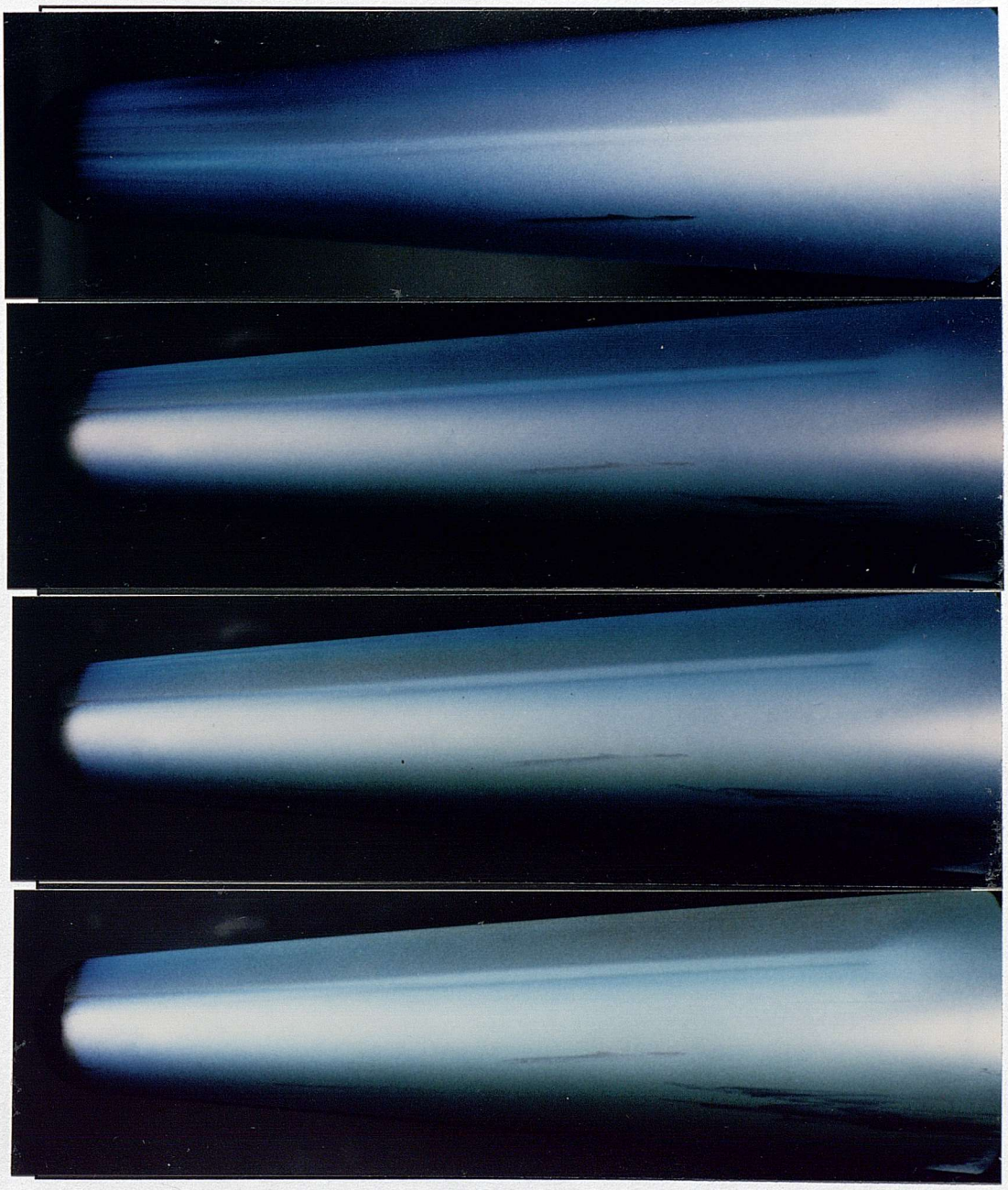


Figure 8.4: Four liquid crystal visualisations, from shots 2617, 2618, 2619, 2620. r_n=25mm, Re_n=1185,000.

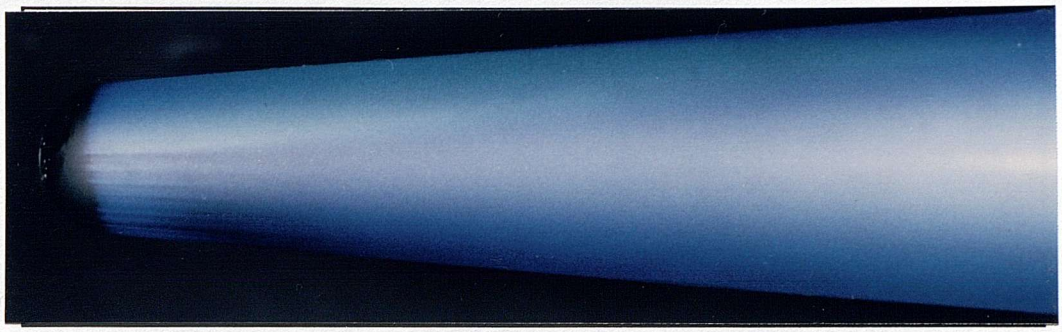


Figure 8.5: Shot 2647, liquid crystal visualisation. r_n=25mm, Re_n=1185,000.

in the lower portion of the model is a turbulent wedge. The wedge is caused by the presence of a piece of Melanex debris, produced by the rupturing of the throat diaphragm. This Melanex is located immediately downstream of the sphere cone junction. The wake developed downstream of the impacted particle presents an initial region of laminar growth extending for 1 3/4 to 2 nose radii downstream, until the spreading rate changes indicating completion of the transition to turbulence process.

In shot 2620, image (d) in the sequence of figure 8.4, the paint has been completely removed to expose the smooth model under-surface over the complete hemispherical nose region. The boundary layer for this case remains entirely laminar.

The spirit of the four tests presented in figure 8.4 is reflected in the visualisation of shot 2647, shown in figure 8.5. In this test, the paint has been progressively removed in the nose region, in such a manner as to reveal increasing amounts of the smooth model surface. The paint extends forward to the 45° mark along the bottom generator, 65° at the middle generator and 85° (the sphere cone junction) along the top generator. In the bottom portion of the image, one observes the presence of streaks, the change in the wake angle linked with the transition process and the merging of the wakes to form an entirely turbulent boundary layer. Removal of the paint (moving towards the centreline) reduces the effectiveness of the disturbance environment and the streaks remain laminar. Moving away from the centreline towards the top of the model, the further reduction in the roughness environment causes the streaks to disappear, and boundary layer remains laminar. However, at some downstream station, the turbulent wedge spreading from the lower region of the model will spread into this region.

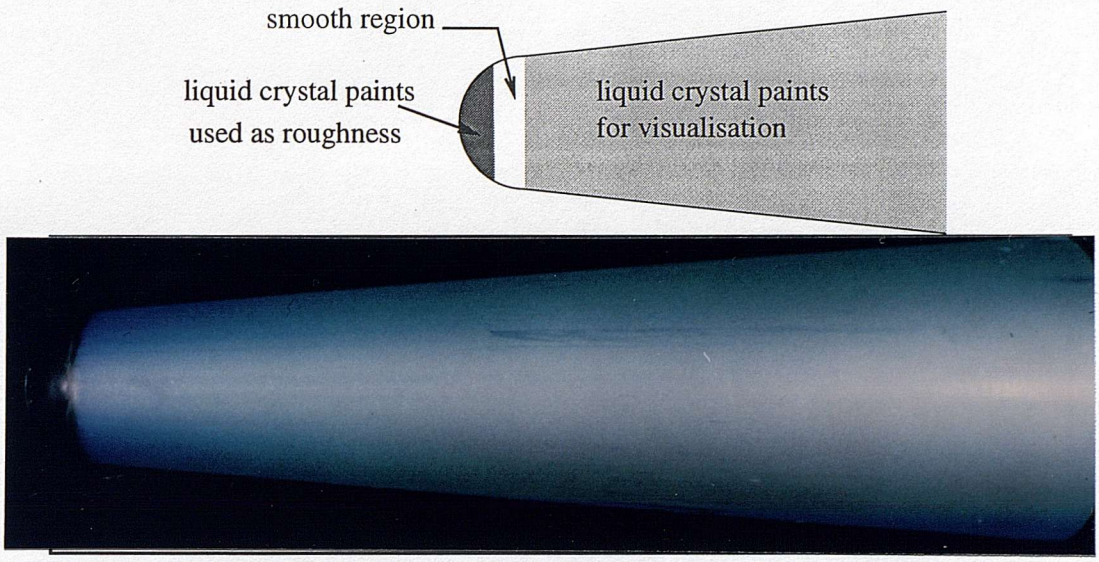


Figure 8.6: Shot 2659, liquid crystal visualisation. r_n=25mm, Re_n=1185,000.

For the level of roughness used, the above experiments indicate that the boundary layer will undergo transition when the roughness is present upstream of 70°, or s=30.5mm. This gives an effective roughness Reynolds number, based on local edge conditions of Re_{Keff}=2500, at a wetted Reynolds number of 1.45 $\times 10^6$ based on freestream conditions, and 1.37 $\times 10^6$ on local edge conditions.

The final part of this study is to assess the sensitivity to roughness in the sub- and transonic region (s<22mm). In these experiments, a polar "cap" of paint is applied to the nose while downstream the model surface is kept smooth up to the sphere cone junction where the paint is re-applied to enable visualisation. The location of the roughness and the outcome of one such test is shown in figure 8.6. The monotonic decrease of temperature indicates the boundary layer is laminar. This is also confirmed by contrasting the colour play in the rear portions with the hotter turbulent wedge wrapping itself around the bottom of the model, caused a protruding impact crater on the hidden part of the model. The presence of roughness in the subsonic region does not perturb the boundary layer with sufficient intensity to promote transition but streak structures are visible in the near nose regions which attenuate downstream.

In conclusion, the distributed roughness studies have indicated that for the given

roughness height (50 μm) used, the effective location for the roughness to promote transition is in the supersonic region on the spherical nose. When roughness is present here, distortions to the laminar base flow occur which form wakes aligned with the mean flow. These wakes will undergo transition at Re_{tr}=3,450,000.

8.3 3D roughness studies

In this section, all experiments with isolated roughness elements, or trips, are presented in conjunction with the step type-trip geometries which extend around the whole model circumference. Two isolated trip geometries have been considered. The first trip geometry is a triangular prism. The second trip geometry is a sand grain.

8.3.1 Triangular trip geometry

The studies with the triangular trip concentrated on the following issues: effect of trip planform to height ratio and the effect of trip location. The trips, irrespective of planform area, are all 0.13mm in height. Returning to figure 8.2, one can see that the roughness elements are comparable to the boundary height over most of the spherical nose region and greater than the displacement thickness until s=0.2m.

The trip flowfield: visualisation

In run 2627, figure 8.7, two triangular trips have been located at the sphere - cone junction, s=37mm. To eliminate any other possible roughness upstream of this location, the model nose has been kept clean of paints and polished to a smooth finish with optical lens grinding paste. The trip geometry is an isosceles triangle with a 3mm length base and a 8mm side length, the height is 0.13mm. In figure 8.7 the heating pattern 2ms into the steady run time can be seen. The trips produce two hot wakes which remain highly visible against the "cold" laminar background. The wake structures show a high degree of organisation and are repeatable from run to run. An interpretation of the heating patterns at six stations immediately downstream of one

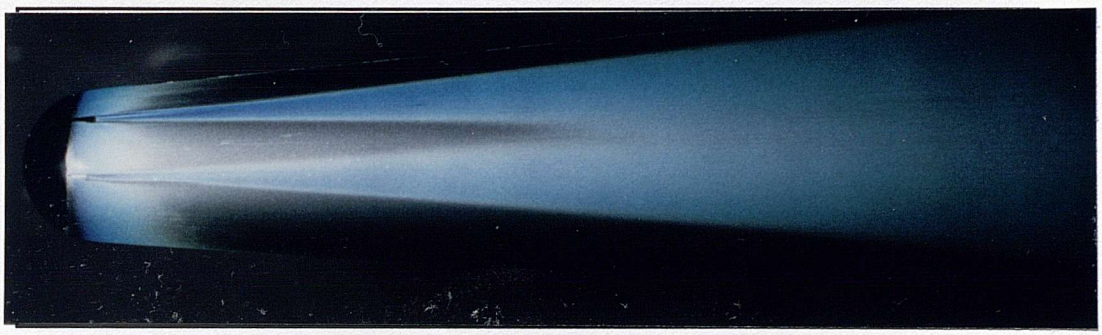


Figure 8.7: Shot 2627, liquid crystal visualisation. r_n=25mm, Re_n=1185,000.

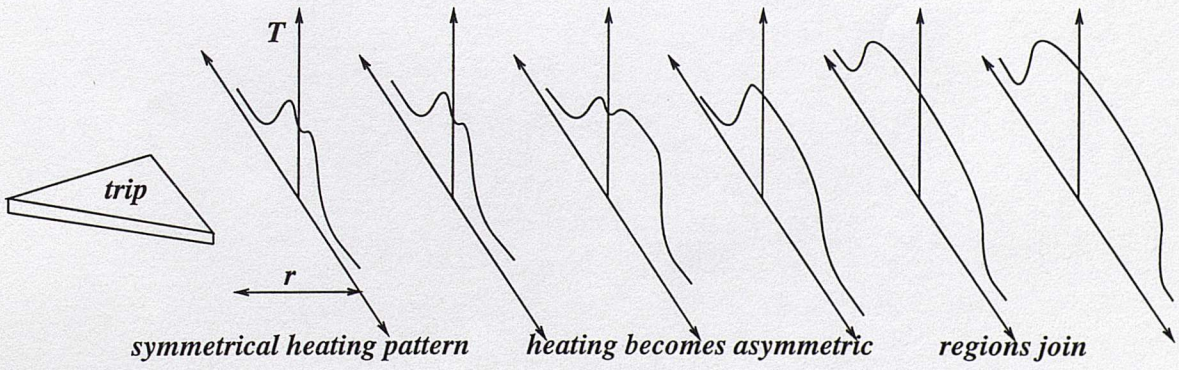


Figure 8.8: Schematic interpretation of heating patterns downstream of trip in run 2627.

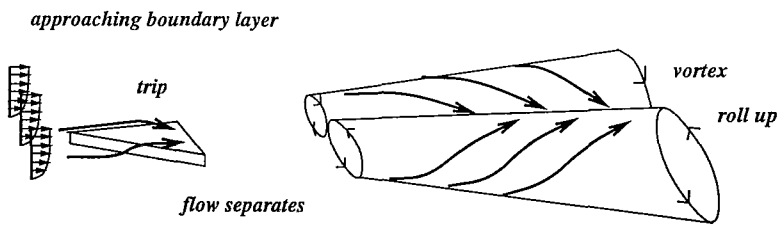


Figure 8.9: Physical interpretation of the flow field in the proximity of the trip elements in run 2627.

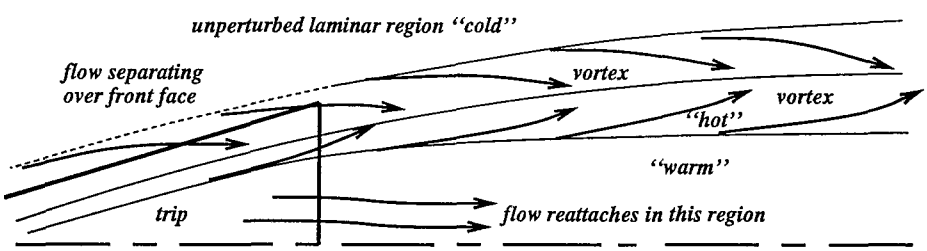


Figure 8.10: Further interpretation of the flow field behind the trip of shot 2627.

trip is offered in figure 8.8. The trip causes a wake which remains almost parallel for 1.25 nose radii downstream. In this initial phase, the wake shows a small degree of spanwise growth, comparable to the natural divergence of streamlines encountered on conical bodies. Inspection of the wake indicates that the temperature is not uniform in the spanwise direction, showing hotter streaks at the outer boundaries of the wake. The physical interpretation for the near field flow structure is given in figure 8.9. It is believed that the boundary layer separates over the leading edge of the trip and rolls up to form a vortex structure which trails downstream. A more detailed picture of the possible flow pattern is given in figure 8.10. Here, it is conjectured that two vortical structures (probably composed of a set of counter rotating vortices) are shed from the trips' rear corners. In between these structures, the boundary layer, which has separated from the back of the trip, re-attaches. The heating in this region is higher than the unperturbed laminar flow external to the wedge but less than the heating associated with the vortical structures. The re-attachment region divides the vortical structures, allowing their evolution to remain independent. Around one nose radius distance downstream from the wake inception point, one structure begins to

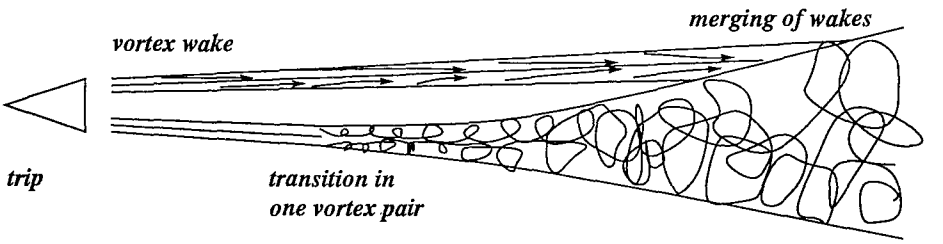


Figure 8.11: Vortex structure and transition to turbulence of streak-like structures witnessed in shot 2627.

spread at a greater circumferential rate. This is connected with the breakdown to turbulence within the vortex. Once the spreading angle has increased, the turbulent vortex "contaminates" the laminar vortex coming from the other side of the trip, with the two wakes interacting and merging to form a single turbulent wedge. This process is illustrated in figure 8.11. Once turbulent, the wake spreading angle is estimated at 4°, this is in addition to the natural streamline divergence. The structure is very similar to the wake of a raised tile inferred from infrared thermography by Charbonnier (1993). The work Morrisette et al. (1969) also shows a highly organised wake structure behind a spherical roughness element, however, both works indicate that the two vortical structures undergo transition simultaneously.

The wake characteristics are summarised in table 8.2.

Re trip origin	Re_{tr}	spreading angle	M_e
1,585,000	3,722,000	4°	$2.2 \rightarrow 3.4$

Table 8.2: Wake characteristics with 0.13mm trip placed at sphere cone junction. 25mm nose radius case, high pressure operating conditions.

The trip flowfield: measurements

In the following experiments a geometrically identical trip to that of the previous text, has been used on the instrumented model. By varying the circumferential separation

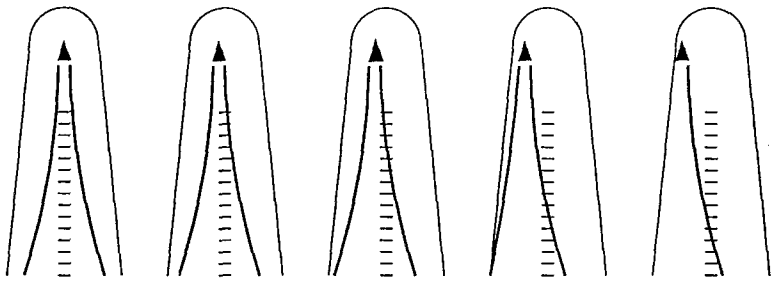


Figure 8.12: Trip movement relative to array of sensors

between the trip and the instrumentation array, the heat transfer distribution in different "slices" of the wake can be analysed as suggested in figure 8.12. Obvious problems arise due to the large spanwise scales of the sensor; however as the the spirit of the tests is mainly exploratory this is not considered to be limiting factor. The gauges are located at chord distances between 0.13m and 0.48m. At these locations, the flow in the wake of the trip is fully turbulent. In order to classify each test case, a convention has been established. Each test case is defined by the spanwise distance between the trip centre and the centre of the gauges, measured at the sphere cone junction.

Figure 8.13 shows the time resolved heat transfer rates at five different streamwise locations for six different test cases. The first test case is the heat transfer distribution without a trip. The remainder are cases in which the trip is present, and moved progressively closer to the gauge centre-line. The bottom trace (f) of figure 8.13, corresponds to the case when the trip is in front of the gauges. The trip is >100mm upstream of the first gauge, allowing transition in the wake to occur and the wedge to become turbulent and spread to encompass all the gauges in turbulent flow. All heat transfer traces show heating levels and signal RMS characteristic of turbulence. Experiment (e) figure 8.13, with 7mm separation, shows turbulent behaviour for the four most downstream gauges. The most upstream, gauge 02, presents a heating level below the expected turbulent level yet above the laminar value and furthermore the signal has a turbulent RMS level. This is caused by the gauge being only partially wetted by the turbulent wedge and in consequence, the measured heating rate is a linear combination of laminar and turbulent values in a proportion equal to the amount of gauge wetted by each region respectively. When the circumferential separation

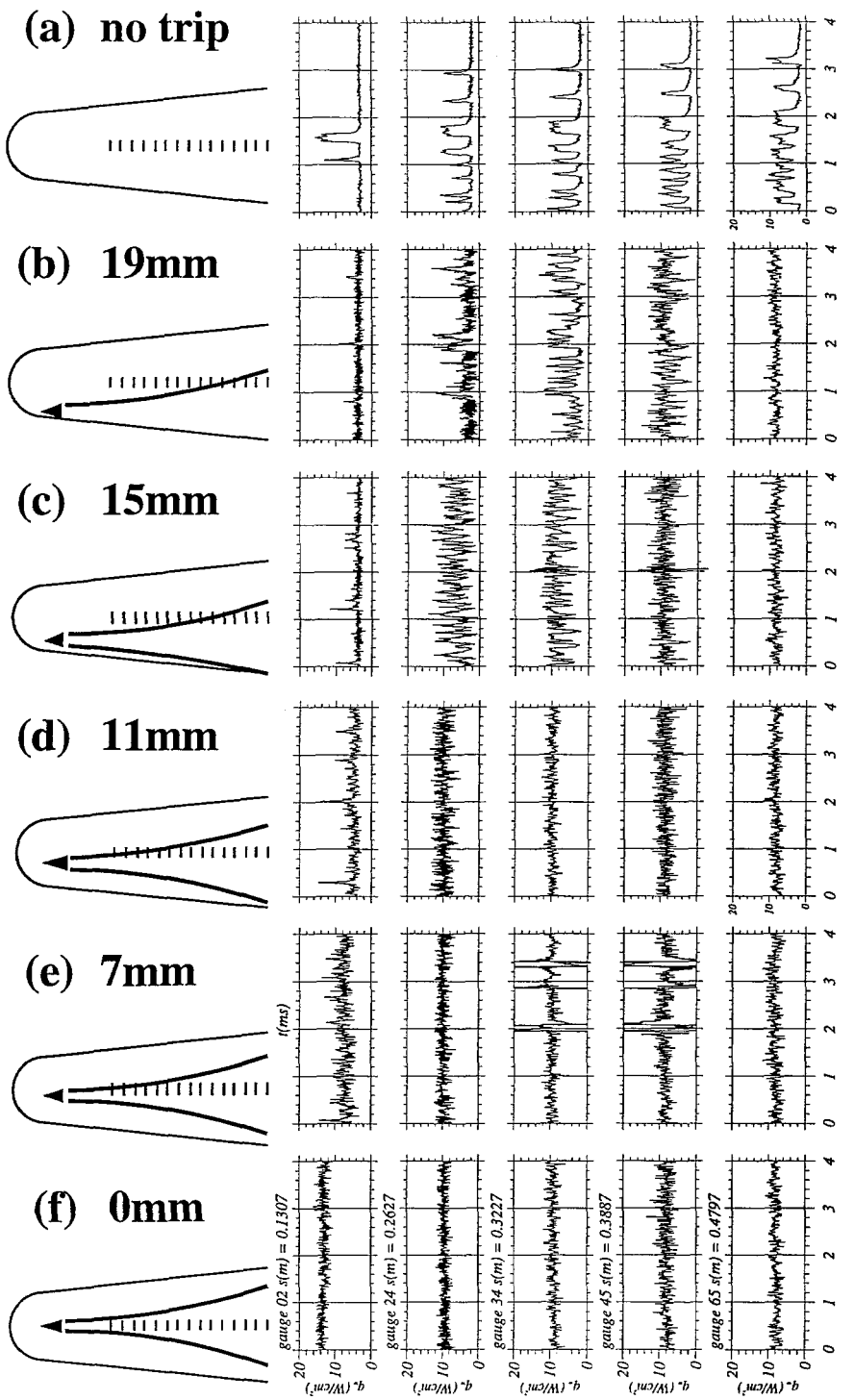


Figure 8.13: Time resolved heat transfer rates for six different triangular trip studies; test cases, from top to bottom are: no trip, 19mm circumferential separation, 15, 13, 7 and 0mm. Basic test geometry is 25mm nose radius tested at the high pressure operating condition.

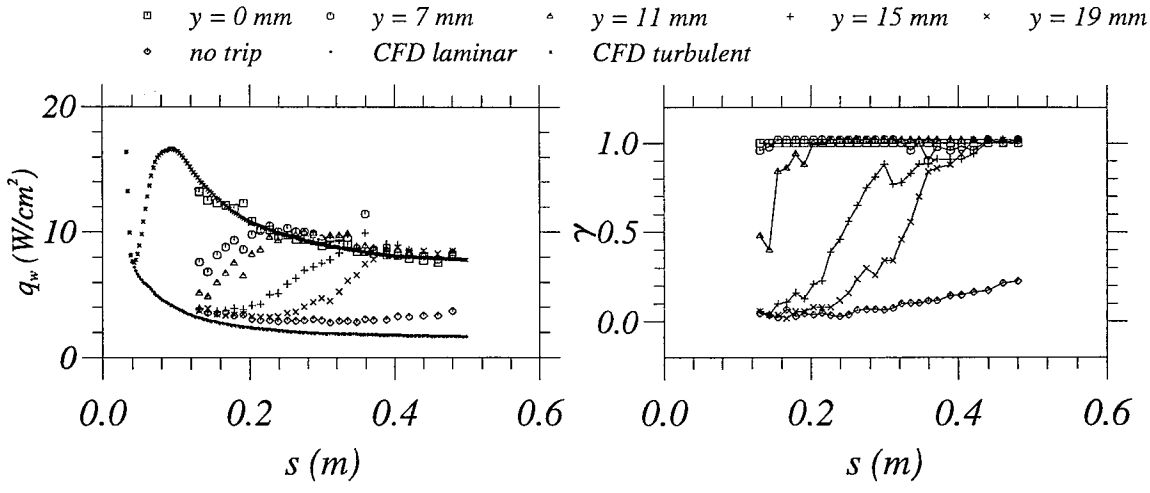


Figure 8.14: Time averaged heat transfer rates and intermittency distributions for different locations of the triangular trip, with the 25mm nose radius tested at the high pressure operating condition.

---

is increased to 11mm, (experiment (d), figure 8.13), this behaviour is extended to gauges located further downstream. Furthermore, gauge 02 is showing a fluctuating signal, which is connected with the edge intermittency process of the wedge. This is also encountered in the time resolved heat transfer traces for experiments (c) (15mm spanwise separation) and (b) (19mm separation), of figure 8.13, where the increase in circumferential spacing between the trip and the instrumentation is such that many of the gauges are wetted by the highly intermittent outer boundary of the wedge.

In figure 8.14, the time averaged heat transfer rates for the above test cases have been plotted against wetted distance. Also included are the CFD laminar and turbulent heat transfer predictions. The latter has been computed using the trip location for transition onset and a transition length of 0.05m ($2r_n$). The measured (no trip) and predicted laminar heat transfer rates can be seen to diverge with increasing wetted distance, due to the low level of intermittent turbulent activity characteristic of the reversal regime case. The 0mm separation test shows a completely turbulent heating distribution which is well predicted by the CFD. Increasing the trip to gauge circumferential separation distance causes, as stated above, the upstream gauges to exhibit intermittent or laminar heating levels, accordingly. The time resolved heat transfer signals can be used to obtain intermittency information. The intermittency

distribution can be found in figure 8.14.

The data acquired in these experiments can be used to complete a two dimensional map of both the heating rates and intermittency levels behind the trip. These are presented in figure 8.15. The local heat transfer rate and intermittency values are plotted on a streamwise and spanwise coordinate system. In total 110 data points have been interpolated to achieve the contour plots of figure 8.15 (symmetry is invoked to produce a complete heating pattern. Although sensor size poses serious limits to the method, the map compares excellently to the visualised wedge. Spreading angles measured from the plot are 5°, compared to 4° of the visualisation. Also in close agreement is the transition location. This is taken to be the point where the the two boundaries of the turbulent zone meet.

The effects of trip planform area.

In the preceding subsections, it was proposed that the vortex structures shed from the two rear corners of the trip can evolve independently and hence can undergo transition at different locations. It was found that once one vortex became turbulent, it would rapidly spread across to the neighbouring vortex and cause transition within its vortical structure by some contamination mechanism. In the series of experiments discussed below, these ideas are probed by increasing the planform area of the trips, and of consequence the spanwise distance between the rear corners. Six equilateral triangles, all of height 0.13mm, were placed on the sphere cone junction as illustrated in figure 8.16. From top to bottom in figure 8.16, the triangles' sides measure 5, 2, 4, 1, 3 and 10mm. Downstream of all six trips, wake structures are visible, by virtue of their "hotter" nature. Two types of wake structure are found. The first type, witnessed downstream of the 1, 5 and 10mm trips, is similar to the structures outlined above, (i.e. highly asymmetrical) and illustrated in figures 8.10 and 8.11. The heating patterns caused by the region of re-attached laminar flow, bounded on either side by the vortex structure can clearly be identified. The degree of asymmetry in the transitional part of the wake structure is most evident behind the 10mm trip. Indeed, the vortex structure shed from the upper tip of the trip appears to be weaker than the bottom vortex, and can be seen to attenuate within 2 to 3 nose radii downstream. The bottom vortex of this trip continues to evolve and becomes turbulent at one nose radius downstream of the sphere cone junction.

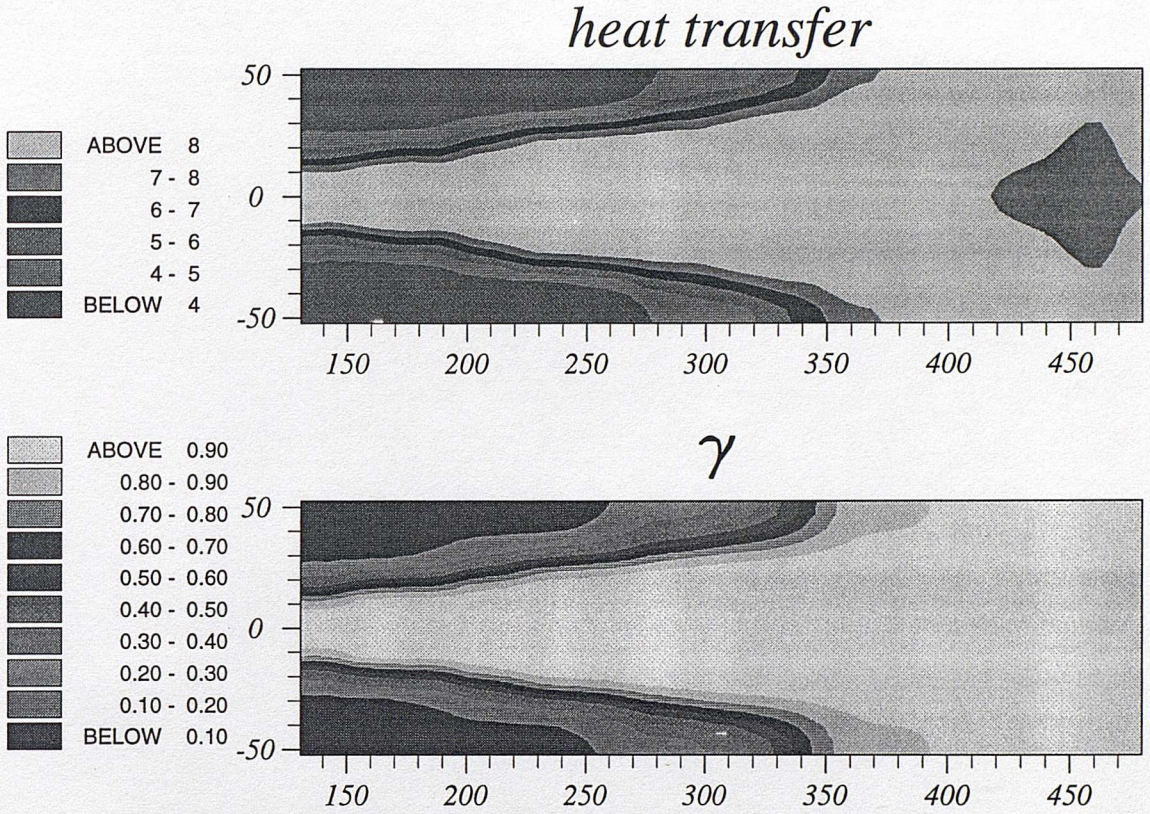


Figure 8.15: Time averaged heat transfer rates, in W/cm^2 and intermittency map with the triangular trip, with the 25mm nose radius tested at the high pressure operating condition. The distance on the x-axis is measured form the stagnation point.

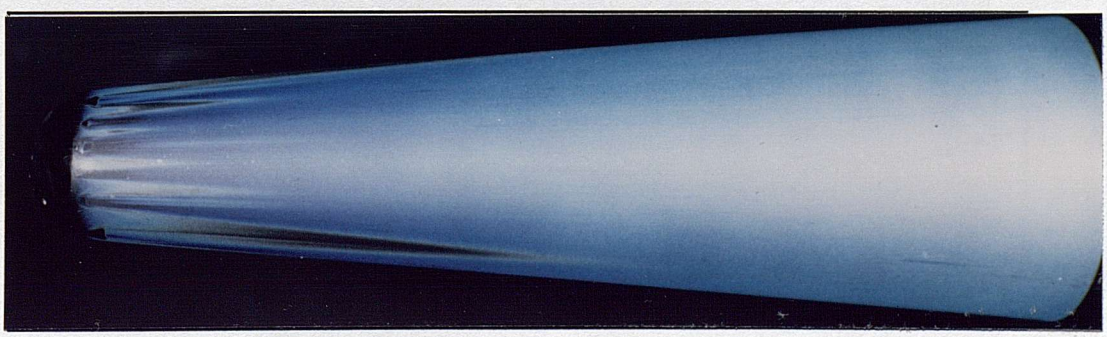


Figure 8.16: Shot 2629, liquid crystal visualisation. r_n=25mm, Re_n=1185,000.

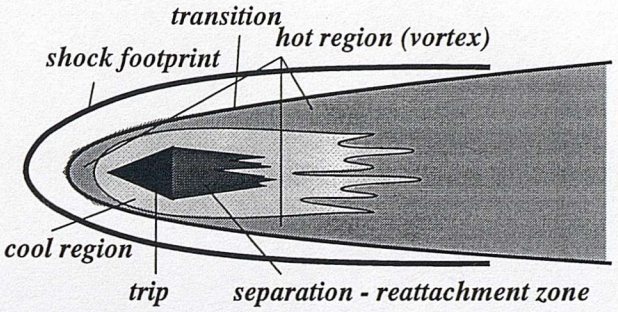


Figure 8.17: Heating patterns around the trip with protruding tip

This test was repeated three times and the surface heating patterns were captured at different times in the steady run window. In doing so, it was not only possible to confirm that the features witnessed were repeatable (as one expects from a geometrically fixed disturbance source) but also to highlight "hot" areas which may have exceeded the normal colour activity threshold. In summary, the image confirms the notion that the flow field is composed of a re-attached region bounded by two vortical structures. The heating patterns indicate that the transition processes are acting most readily upon the tip vortices. The asymmetry in the flow field shows that transition is taking place independently in the two arms.

Returning to figure 8.16, one notes that the 2, 3, and 4mm trips create a second, distinct heating pattern. The different flow field is caused by the leading edge of the trip lifting away from the surface and extending considerably into the external flow field. The protrusion of the tip causes a bow shock to form, underneath which there are signs of enhanced heating. An interpretation of the heating pattern is given in figure 8.17. The boundary layer is then expected to separate and roll up around the trip. The roll up phenomena forms a vortical structure, as depicted in figure 8.18. This vortical structure is marked by increased heating rates. Immediately downstream of the trip, the two vortices begin to grow circumferentially merging together at two to three trip lengths downstream. At this point a single wake is formed, which continues to expand in the spanwise direction. The high heating rates encountered in the wake and the elevated spreading angles suggest that the flow within it is turbulent. The exact point of transition completion is not easily identified. The strong shock process may indeed promote transition upstream of the trip itself, (observing figure 8.16, the shock can be seen to be standing a few millimetres upstream of the trip, which in

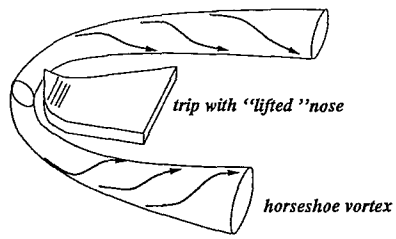


Figure 8.18: Flow field around trip with protruding tip

boundary layer terms is $\approx$ 10 δ, suggesting that the process may be initially non-linear as found in by pass transition mechanisms). Finally it is noted that this type of wedge retains a high level of symmetry.

The effect of trip location

The distributed roughness experiments indicate that the transition process is most sensitive to roughness in the supersonic region on the spherical portion of the nose. In the following section, the effect of isolated roughness in the nose and near nose region is examined. The trip geometry is an equilateral triangle, 1mm in length and 0.13mm high. In all experiments, the nose was polished prior to the application of the trips.

In figures 8.19 and 8.20, seven surface temperature distribution are shown, in each visualisation three trips are present. The trip locations for these tests are summarised in table 8.3. In visualisation 2635, figure 8.19 (a), the trips are located on the sphere cone junction. The flow structure resultant from each trip is identical in nature and presents the features described in the previous section. Immediately downstream of the trip, the presence of two vortical structures producing the axially aligned "scorch" marks can be seen. In between these lies a secondary region which is characterised by increased heating compared to the laminar base flow. The wake remains laminar for 1 nose radius length downstream (25mm circa, 60 δ), at which point it begins to exhibit turbulent behaviour characterised by the much increased spreading angle.

In shots 2636 and 2637, 8.19 (b) and (c), the trips have been moved forward on

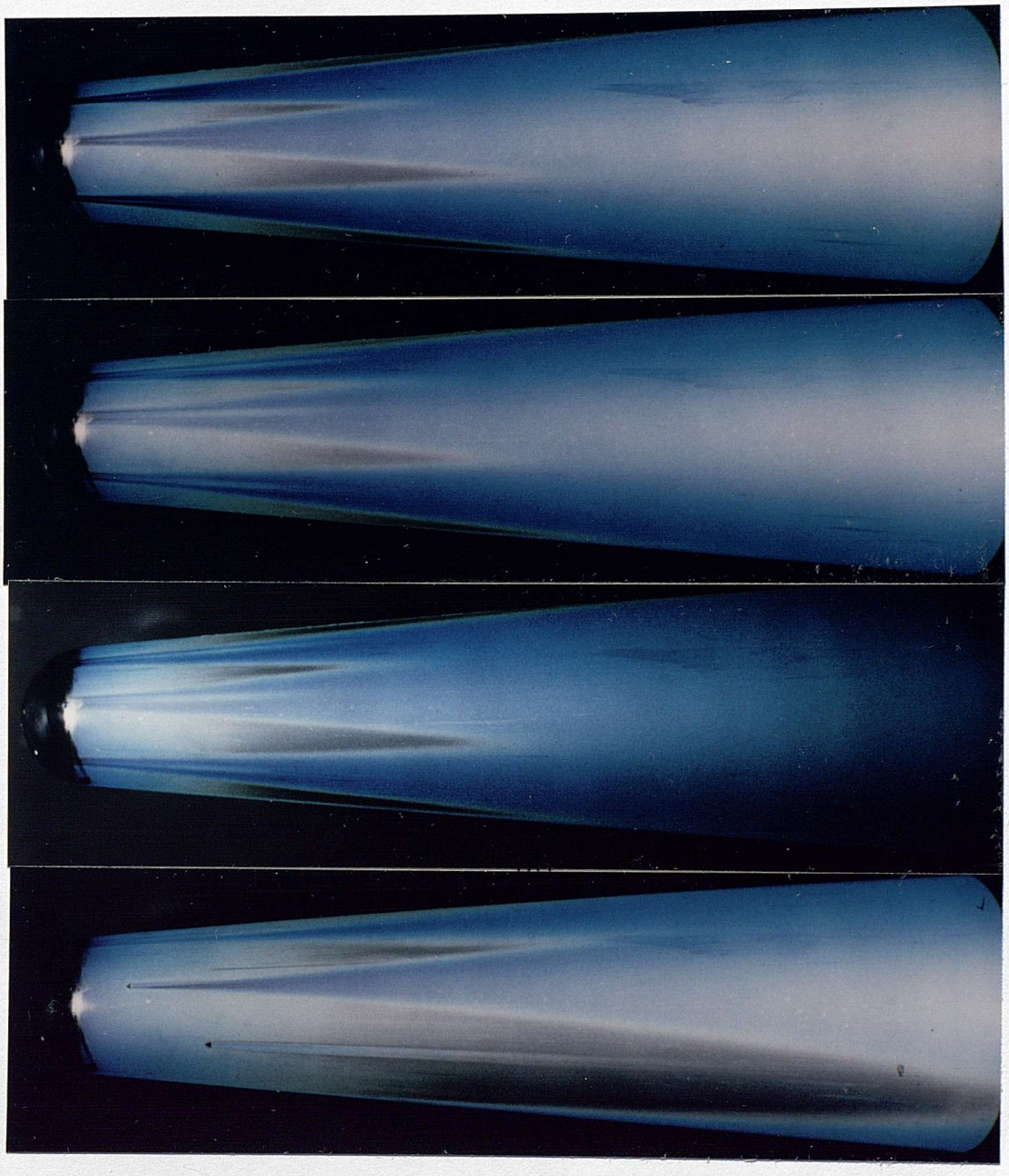


Figure 8.19: The effect of trip location, liquid crystal visualisations from runs 2635, 2636, 2637 and 2638; r_n=25mm, Re_n=1185,000.

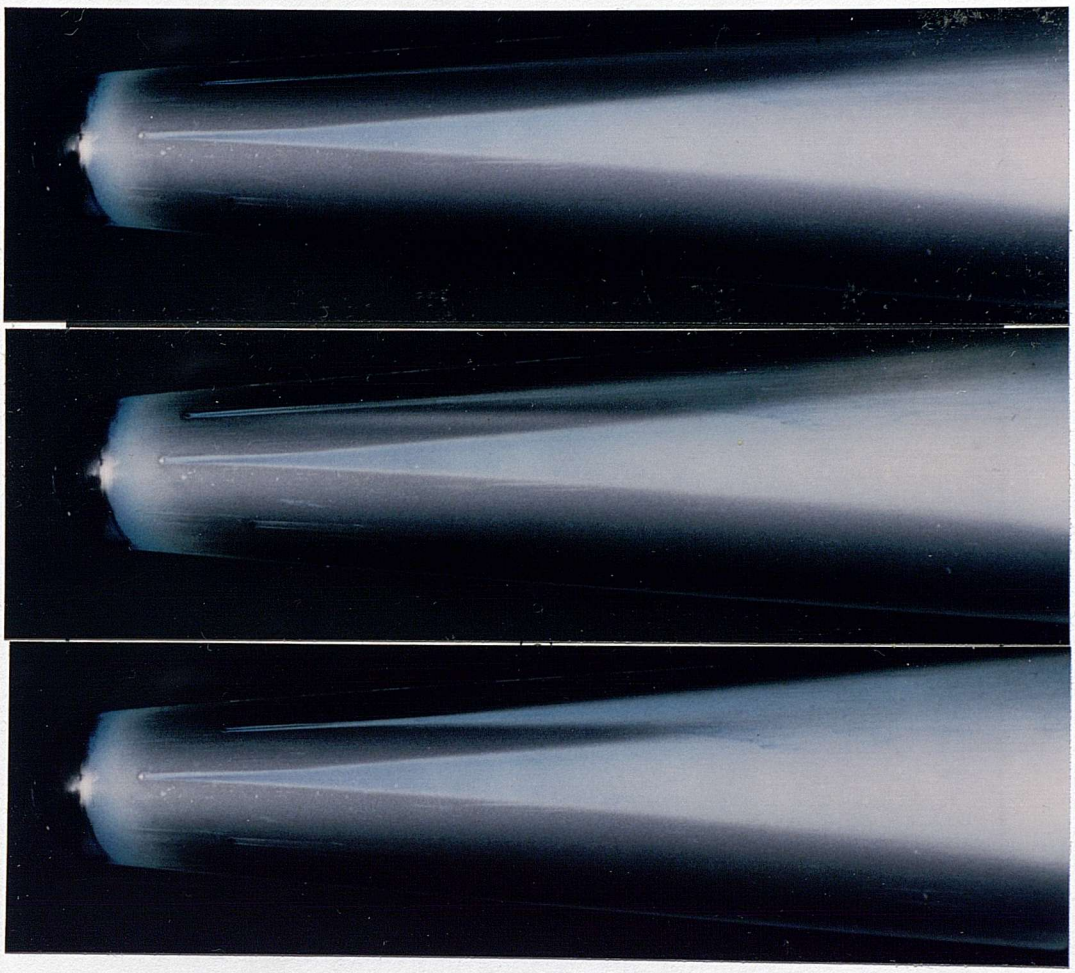


Figure 8.20: The effect of trip location, liquid crystal visualisations from runs 2640, 2641 and 2642; r_n=25mm, Re_n=1185,000.

run number	top	middle	bottom
2635	sphere-cone junction	s-c j.	s-c j.
2635	70°	70°	70°
2637	60°	60°	60°
2638	45°	s-c junction + $4/5r_n$	s-c junction + 2 r_n
2640	s-c junction+ 1 $2/5r_n$	s-c junction + $4/5r_n$	s-c junction + 2 r_n
2641	s-c junction+ r_n	s-c junction + $4/5r_n$	s-c junction + 2 r_n
2642	s-c junction+ 1 $4/5r_n$	s-c junction + $4/5r_n$	s-c junction + 2 r_n

Table 8.3: Trip location for runs 2635, 2636, 2637, 2638, 2640, 2641 and 2642

to the hemispherical portion of the nose, to 70° and 60° from the stagnation point respectively. The effect is to produce laminar wakes which in common with the wakes originating from trips at the sphere cone junction undergo transition at a distance of one nose radius downstream of this location. The main effect of moving the trips forward into the nose region is purely to increase the spanwise scale of the laminar portion of the wake. This phenomenon is linked with the greater streamline divergence encountered as the trips are brought forward into the spherical region.

In shot 2638, 8.19 (d), the top trip has been moved forward to the 40° location. The local edge Mach number is just supersonic and the boundary layer thickness comparable to the trip height. The effect on transition, contrary to expectation, is to delay the onset of turbulence in the wake to 2 - 3 nose radii downstream of the sphere - cone junction. This is the furthermost forward trip location tested in this program, and hence it is only possible to speculate on the effects of trips in the subsonic region. From the results of the 2D distributed roughness studies, it transpires that roughness is most effective in the supersonic region on the nose and that the presence of roughness purely in the subsonic region is incapable of promoting transition.

The middle trip in run 2638 is located at 2/3 of r_n downstream of the sphere-cone junction. At this location, the trip is successful in causing transition, which occurs within 2 nose radii distance of the junction. The bottom trip is placed at 2 nose radii distance from the junction. At this rearward station, the trip is not effective in promoting transition and the laminar wake decays after travelling 8 r_n.

The above visualisation indicates that, for the given trip geometry, the last effective trip location must lie somewhere between the middle and bottom trip location of image 2638. The intent of runs 2640, 2641 and 2642, figures (a), (b) and (c) figure 8.20, is to find this location. To check the repeatability of the effectiveness (or lack of) of the middle and bottom trips, the latter are kept at the same location while the top trip is moved between intermediate stations. When placed at 1.4 r_n downstream of the junction, (shot 2640), the resulting flow patterns indicate, that at the time of of image capture, the wake is laminar. In the surrounding regions there is evidence that a previous times the local temperature was in excess of the laminar background. This may indicate that earlier on in the run, the wake may have exhibited a turbulent nature, with the the associated higher heating rates and greater circumferential spreading. Indeed, one must bear in mind that the image depicts the surface tem-

perature heating pattern, rather than the instantaneous heating rate, q_w, hence, the presence of events which have since ceased to exist can still be detected, (figure 7.19 i(left) shows a possible heat transfer time signal for such a phenomenon).

The top trip is located at one nose radius downstream of the junction in shot 2641, (b) figure 8.20. In this test, the top trip is producing a laminar wake. Again, there is an area of increased heating surrounding the wake. This suggests that at earlier stages of the run, the wake may have been turbulent, i.e. the historical presence of a turbulent wedge.

In the final image of this sequence, figure 8.20 (c), the top trip has been moved further downstream to a distance equal to 1.8 nose radii downstream of the junction. This is the most downstream station tested in the intermediary region and rather counter-intuitively, the trip produces a turbulent wedge. Upon inspection, it is seen that the laminar portion of the wake is apparently being attenuated with distance downstream but at 4 nose radii distance, it becomes turbulent. It is also noted, that in this series of tests, the transition behaviour of the bottom and middle trips, which were kept at the same locations, remained consistent.

In table 8.4. the results have been summarised. The information is also presented as a a graph of transition location against trip origin, shown in figure 8.9. The graph clearly shows that the trips become less effective for s<0.02m and s >0.08m.

trip location w.r.t junction	-40°	-25°	-15°	0	$2/3r_n$
s(m) from apex	0.019	0.026	0.031	0.037	0.054
transition location w.r.t junction	3 r_n	1 r_n	1 r_n	1 r_n	2 r_n
s_{tr}(m) from apex	0.112	0.062	0.062	0.062	0.087

trip location w.r.t junction	$1r_n$	$1.4r_n$	$1.8r_n$	$2r_n$
s(m) from apex	0.062	0.072	0.082	0.087
transition location w.r.t junction	laminar	laminar	$4r_n$	laminar
s_{tr}(m) from apex	n/a	n/a	0.137	n/a

Table 8.4: Transition behaviour against trip location

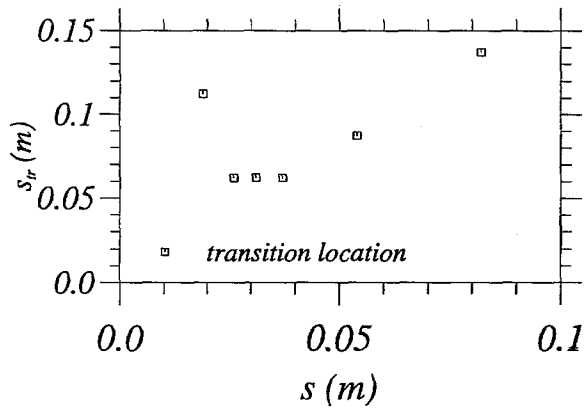


Figure 8.21: Transition behaviour for a 0.13mm high trip, on the 25mm cone, tested at the high pressure operating conditions.

8.3.2 Sand grain roughness elements

Four sand grains have been placed on the sphere-cone junction in figure 8.22. The elements are of overall dimension less than 0.2mm, which is comparable to the boundary layer height. The model nose has been polished and the liquid crystal paints extend no further forward than the sphere-cone junction, in order to reduce the roughness environment. The surface heating patterns of figure 8.22 indicate that the unperturbed regions of the boundary layer flow are laminar. Downstream of each roughness element a wake is formed. The wakes have a higher heating rate than the surrounding laminar base flow. The uppermost, central and the lowest wake show little spanwise divergence for a distance of one nose radius downstream, after which the circumferential spreading angle increases to circa 4 ° , which combined with the natural divergence of the conical flow causes the wakes to spread rapidly and eventually merge at some station downstream. The flow immediately downstream of the trip is believed to be laminar and transition to turbulence is again connected with the location at which the wake suddenly changes its spreading angle. Due to the small spanwise scale of the laminar portion of the wake, very little detail can be seen. Close inspection shows that the transition location is not constant for the three turbulent wedges and varies between 1/2 and 1+1/2 nose radii downstream. This difference in transition location is believed to be connected in geometric irregularities between the trips.

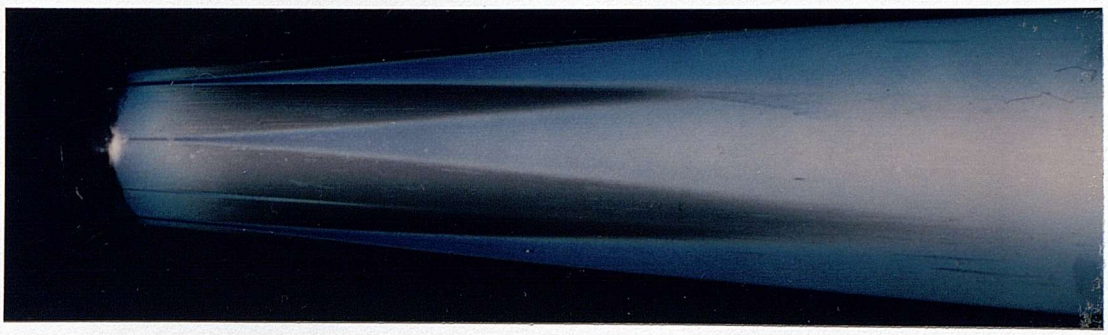


Figure 8.22: Liquid crystal surface temperature visualisation from run 2644. Four sand grain roughness elements are located on the sphere-cone junction; r_n=25mm, Re_n=1185,000.

Of particular interest is the one wake which has remained laminar. Inspection after the run indicated that the roughness element was removed (probably in the initial stages of the run) and that only residual roughness was left, associated with the glue used to fix in place the trip. The roughness connected with the glue does not provide sufficient disturbance source to promote transition and the wake decays within five nose radii.

Quantitative measurements in the wake of the sand grain

Experiments with the instrumented model were performed in which the circumferential location of the trip element was varied with the respect to the array of gauges. In total, 27 gauges are monitored at streamwise distances between s=0.131m and s=0.49m. At this location, the wake is already turbulent and has a circumferential width in excess of 20mm, the local gauge resolution. The data for the six experiments performed are given in figure 8.23. Here the time resolved heat transfer rates are plotted against time (in ms) for five selected gauges, for each of the six experiments. Experiment (f) corresponds to the case where the roughness element is located directly upstream of the gauges, i.e. a circumferential separation of 0mm. The heat transfer rates for this case are turbulent for all the gauges monitored, with the characteristic high levels of heating and signal RMS.

Increasing the circumferential spacing to 7mm, figure 8.23 (e), causes gauge 02 to

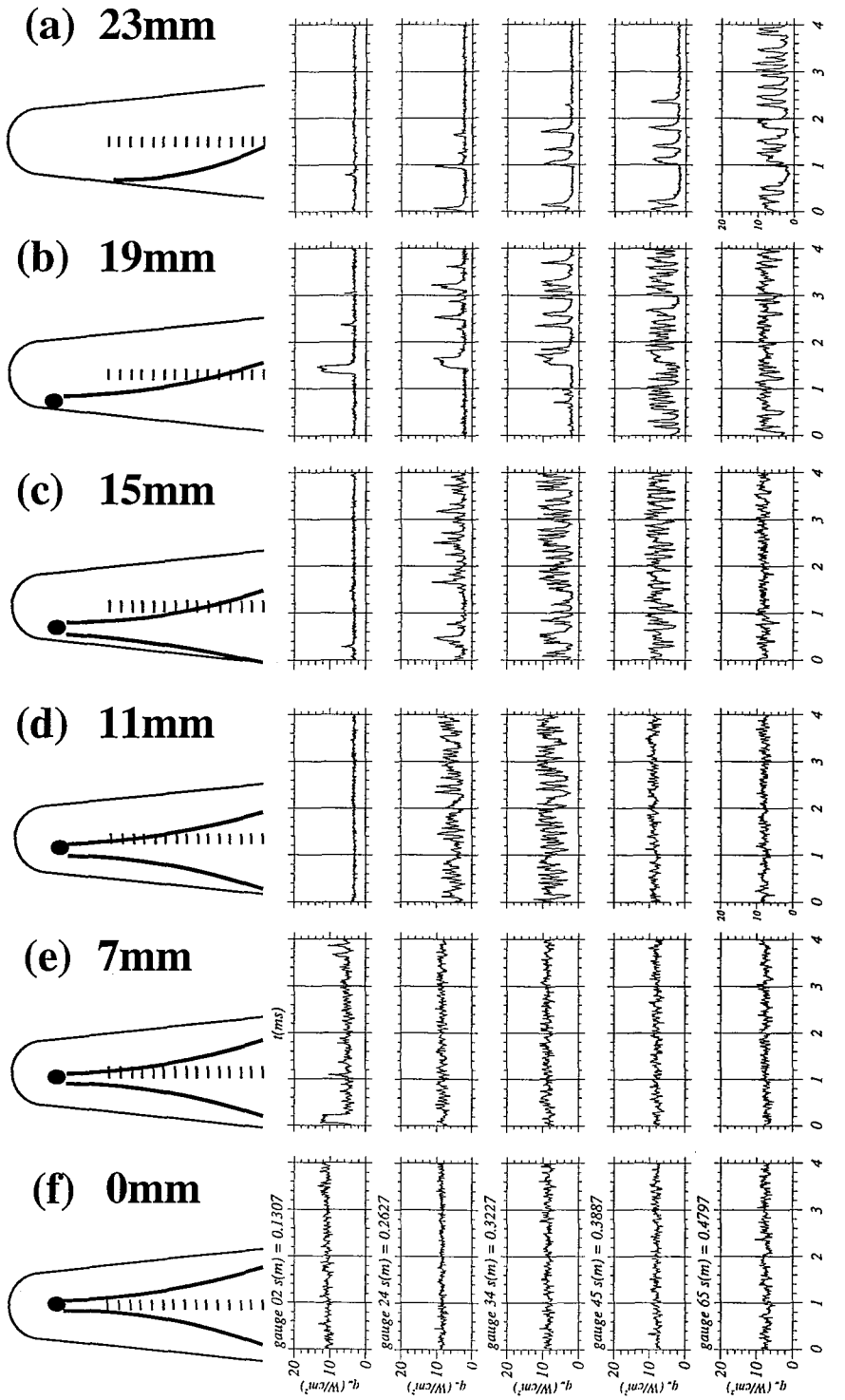


Figure 8.23: Time resolved heat transfer rates for five different sand grain trip studies, with the 25mm nose radius tested at the high pressure operating condition.

remain outside the turbulent wake. The gauge is wetted by the unperturbed regions of the boundary layer, which exhibit a transitional nature, with the passage of what must be "natural" reversal events at t=0.1ms, t=3.4 ms and t=3.6m. Moving downstream to gauge 24, it can be seen now that it is wetted by a turbulent boundary layer in a continuous fashion, indicating that it is completely encompassed by the wake. Obviously, the gauges located further downstream, 34, 45 and 65 are also engulfed by the turbulent portion of the wake.

In case (d) of figure 8.23, the separation has been increased to 11mm. The effects of the wake are not evident at gauge 02, but can be now witnessed downstream of gauge 24. Here, the process is highly intermittent due to the edge intermittency associated with the outer boundaries of the wake. This edge intermittency is still detectable at gauge 34, but the two most downstream gauges plotted indicate that they are wetted by turbulent flow. Likewise considering the 15mm circumferential separation case, (case (c), figure 8.23), it can be seen that the intermittent region is extending over most of the gauges, with exception of the most upstream ones, which are outside the domain of influence of the trip. When the separation is increased to 19mm, the edge of the wake first wets the gauges at s=0.36m, and the time trace of gauge 45, located at 0.39m) shows the typical intermittent nature. Of interest for this particular case is the appearance of a a reversal regime event at 1.4ms, 0.3ms in length, showing the characteristic rapid switch from the laminar level to the turbulent value and the tail off back to the laminar heat rates.

In the last experiment of this series, figure 8.23 (a), the trip - gauge separation has been increased to 23mm. This corresponds to an angular separation in excess of 50° , and the the experiments indicate that the wake only begins to wet the array of sensors at 0.4m downstream, where only the effects of the intermittent edge are present. This is echoed in the time resolved trace for gauge 45, (s=0.48m) where the signal can be seen to be transitional. The transitional activity witnessed on the gauges further upstream is not connected with the wake but with the natural reversal regime spot formation processes.

The time resolved information presented in figure 8.23 has been used to obtain the time averaged heat transfer distribution shown in figure 8.24. Also included in this plot are the laminar and turbulent heat transfer predictions obtained with CFD and the "no trip" case presented previously in figure 8.13. The CFD laminar predic-

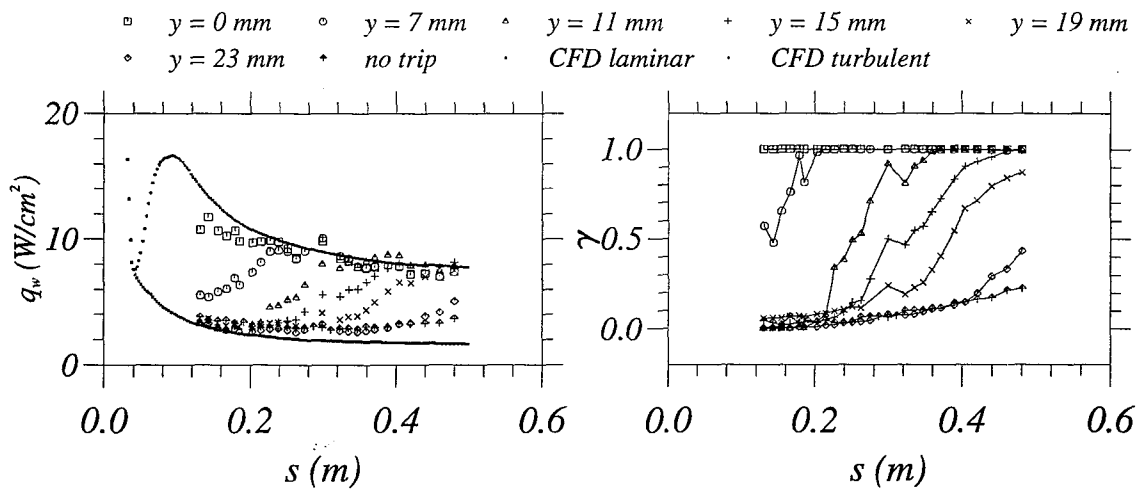


Figure 8.24: Time averaged heat transfer rates and intermittency distributions for different locations of the spherical trip, with the 25mm nose radius tested at the high pressure operating condition.

---

tion and measured time averaged heat transfer rate for the no trip case are not in agreement due to the low level of transitional activity encountered for this case. The turbulent CFD closely predicts the measured rates for the 0mm separation case, indicated with the square symbols in figure 8.24. Decreasing the amount of separation, causes the location at which the effects of the turbulent wedge are fist witnessed to move progressively downstream. Also of interest are the intermittency distributions. Again, it is seen that the transition location is progressively moving upstream as the roughness element is brought progressively closer to the array of gauges.

The data of figure 8.24 can also be used to create contours of heat transfer and intermittency plotted against axial and spanwise distance. The data has been interpolated and symmetry invoked to produce the "full" pattern, shown in figure 8.25. The heating patterns show good qualitative agreement with the visualisation of figure 8.22, except in the upstream regions, where the effect of sensor length is most important. The intermittency map shows a central region of turbulent boundary layer flow, the estimated spreading angle of which is 9 ° . The estimates include the effects of streamline divergence.

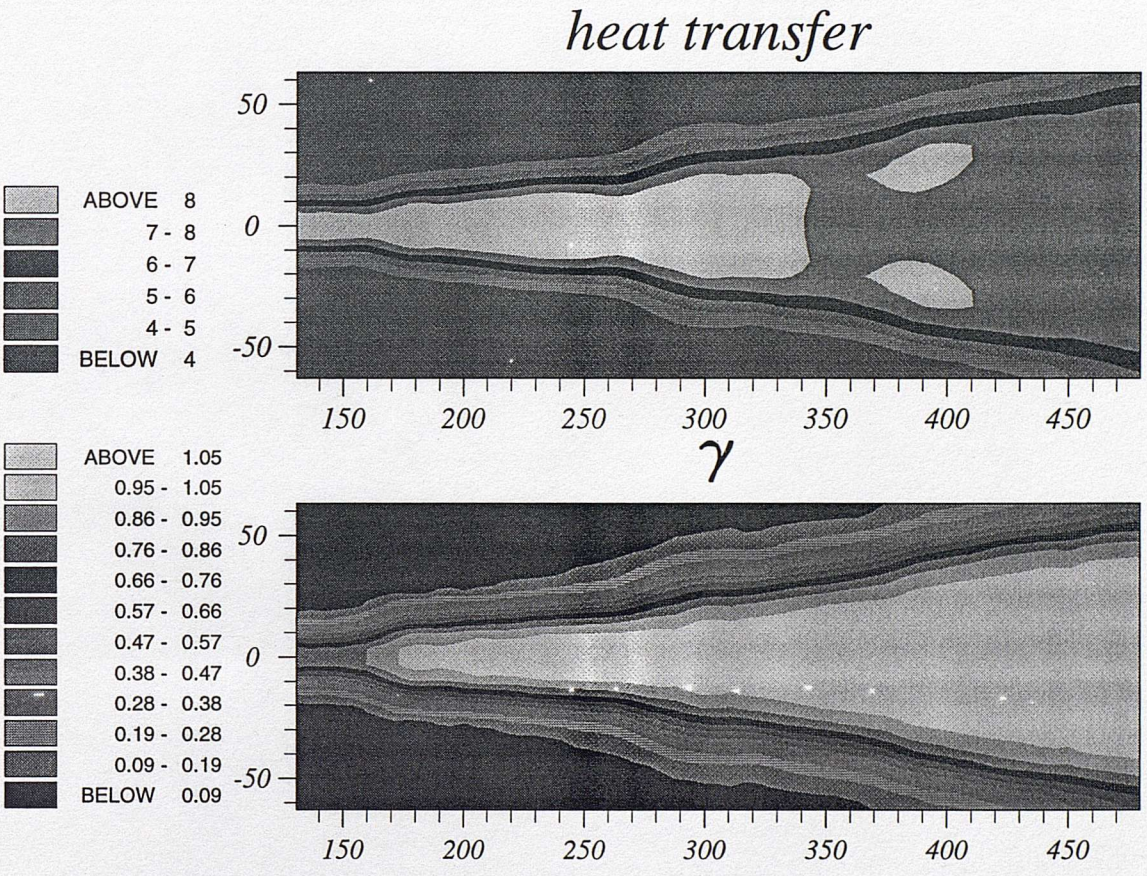


Figure 8.25: Time averaged heat transfer rates and intermittency map with the grain of a sand trip, with the 25mm nose radius tested at the high pressure operating condition.

8.4 2D annular trips

The final trip geometry tested is the annular trip, which extend completely around the model circumference. The trips are 0.13mm in height and 5mm wide. Three experimental configurations have been tested. In configuration (a), figure 8.26, the annular trip is located at the sphere cone junction. In experiment (b), the trip is located two nose radii downstream from the sphere cone junction, (s=87mm), and in the final configuration studied, two trips have been located at 87mm, again illustrated in figure 8.26 (c). The effects have been studied using the instrumented model. A selection of time resolved heat transfer traces for five gauges at different axial locations is shown for each of the cases in figure 8.26. The heat transfer traces indicate that the annular trip is successful in promoting transition when located at the sphere cone junction. The time signals for case (a) show the typical high levels of heating and signal RMS expected for turbulent flow. Moving the annular trip further downstream (b), significantly reduces the efficiency of the trip in promoting transition. Indeed, analysing the heat transfer distribution for gauge 02, it can be seen that the trace is intermittent with extensive regions of laminar flow. Further downstream, gauges 24, 34, 45, it can be seen that the level of intermittent activity increases such that by gauge 65, the boundary layer is believed to be turbulent. Adding a further annular band 5mm downstream of this band increasing the efficiency of the tripping mechanism, (case (c)), such that the flow over the entire array of gauges is turbulent.

The visualisation experiments performed with triangular, 3D elements, illustrated previously, indicated that at a location s=87mm the trip did not provide sufficient disturbance input to promote transition. Here, it has been shown that the 2D annular trip is capable of promoting transition, and hence it would appear, that the annular trip is a more effective boundary layer destabilisation mechanism than the single isolated 3D element. However, if an array of 3D trips were used, aligned in the spanwise direction, their efficiency in promoting transition would almost certainly increase due to interaction between the individual wakes.

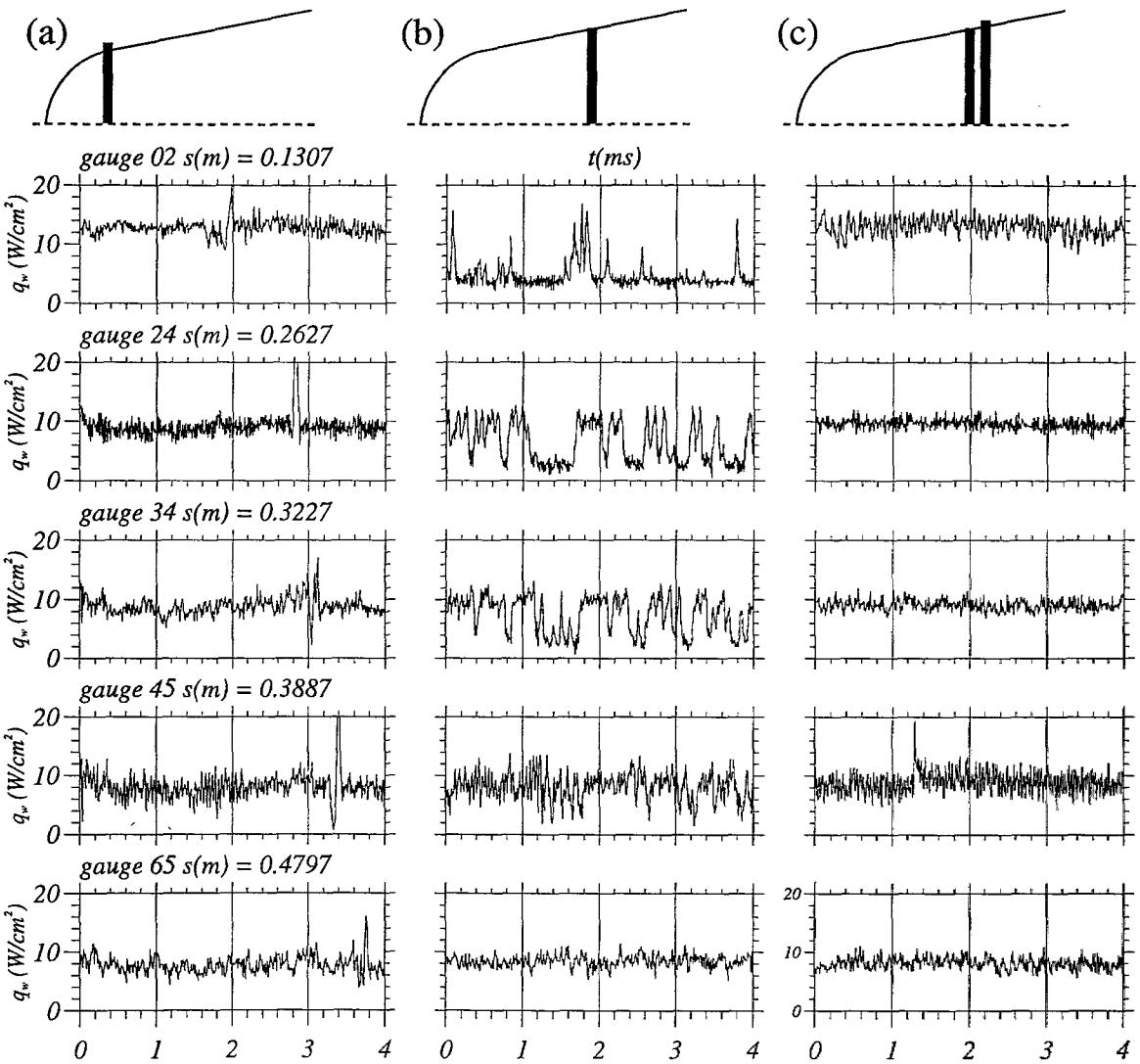


Figure 8.26: Time resolved heat transfer rates for 2D "band" trips with the 25mm nose radius tested at the high pressure operating condition.

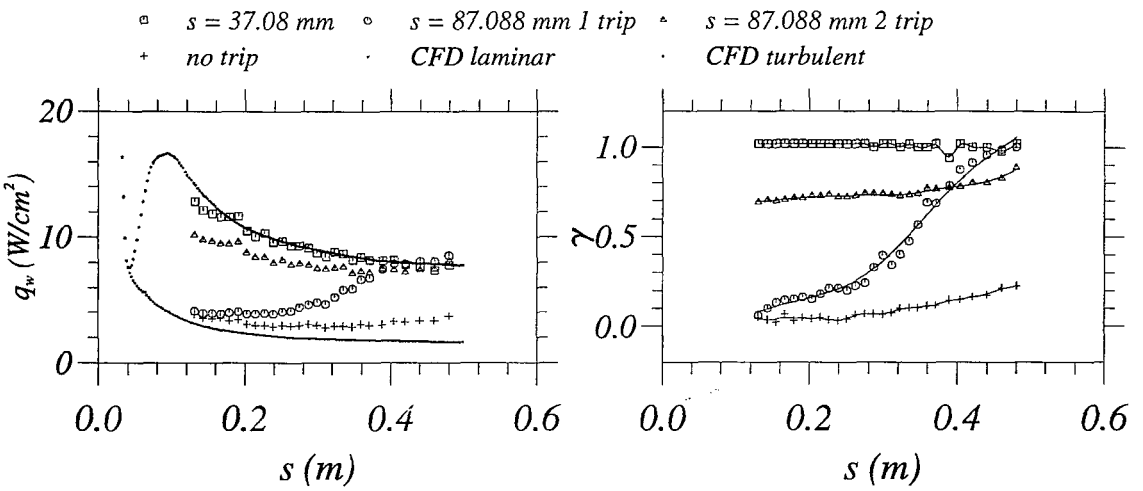


Figure 8.27: Time averaged heat transfer rates and intermittency distributions for different locations of the 2D triangular trip, with the 25mm nose radius tested at the high pressure operating condition.

8.5 Concluding remarks

In the chapter, the boundary layer sensitivity to roughness in the transition reversal regime was investigated using a variety of boundary layer tripping devices. The experiments were performed with the 25mm nose at the high pressure operating conditions. The effects of distributed roughness was explored. The liquid crystal paints were deposited in such a manner as to produce spherical particles of 50 μm in diameter uniformly coating the surface. In this fashion, they paints were found to produce axially aligned wake structures. These were spatially anchored by the bigger particles of the paint located in the hemispherical nose region, and underwent transition characterised by a change in circumferential spreading angle within $Re_s = 4 \times 10^6$. Experiments indicated that the boundary layer was most sensitive to roughness in the supersonic flow regions on the nose.

Triangular trips with height comparable to the boundary layer thickness were also investigated. Visualisation indicated that the flow separated around the trip and rolled up to form two vortical structures in correspondence of the trip's rear corners. By varying the trip planform area, it was ascertained that the two vortical structures evolved independently and transition could occur in one structure first and then

spread to contaminate the other. Spreading angles were measured. Quantitative measurements downstream of transition indicated that the wake is characterised by a central fully turbulent region surrounded by an intermittent border. The data was used to create heat transfer and intermittency maps downstream of the trip. The effect of trip location was studied and it was found that the most effective regions for promoting transition are located in the supersonic regions on the nose and the near nose regions.

A sand grain trip was tested. The wake flowfield was found to be symmetrical and transition occurred within $Re_s = 5 \times 10^6$. Spreading angles were estimated. Quantitative measurements were performed in the wake flow field and maps of intermittency and heat transfer given.

The 2D annular trips were found to produce transitional or turbulent boundary layers at the sensor measurement locations. The findings indicate that the annular trip may be a more effective destabilisation mechanism.

Chapter 9

Conclusions

9.1 Summary

The aim of this study was to obtain information regarding kinetic heating at hypersonic speeds, in particular for transitional boundary layers. The introductory remarks made at the beginning of this thesis commented on the need for continued research into hypersonic transition, in particular, for fundamental investigations in which the governing parameters are isolated and as far as possible investigated individually. The parameters chosen to study were nose bluntness and roughness and of special importance was to understand how they governed events occurring in the transitional region.

The test model used was a 5 ° semi-angle cone, 0.8m in length, with a set of twelve interchangeable nose pieces ranging from sharp to 25mm in radius. The testing was conducted in the Mach 9 Imperial College hypersonic gun tunnel. A full test section calibration was performed at all three working conditions and has been reported in this thesis. Three calibration methods were used and gave excellent agreement for the estimated Mach number, freestream static and total pressures. Problems were encountered in the estimation of the total temperature and further work may be required.

For thirty-one configurations, each distinguished by a different nose Reynolds number, the surface heat transfer rate distribution was obtained using thin film gauges. For

$Re_n < 100{,}000$, it was found that transition onset and completion were dramatically delayed with increasing nose Reynolds number, in accordance with the results of many others workers. This regime is denoted the small bluntness transition regime. For $Re_n > 400{,}000$, the transition onset location moves forward to the near nose regions. The measured transitional activity remained low over the entire model length and transition completion was not witnessed. This regime is called the transition reversal regime. Both transition regimes overlap for $100{,}000 < Re_n < 400{,}000$, where both mechanisms race to promote transition.

Subsequent experiments explored in greater detail the transition mechanism of the small bluntness regime. Visualisation of the transition front showed a high degree of axi-symmetry and no sensitivity to roughness. The transition process is governed by the formation and growth of transitional events. Intermittency has been computed and follows the universal form, showing a great similarity to measured sub- and supersonic distributions. The evolution of other properties through the transitional region also show a great similarity with the results obtained at other speeds.

Increasing nose blunting promotes the efficiency of the reversal regime transition mechanism. Experiments have shown that in the reversal regime transitional events are formed in the near nose region and are convected downstream. The temporal formation frequency of the events is linked to the severity of the roughness environment, but is an order of magnitude below the formation frequency of the small bluntness regime. A case is detailed in which both mechanisms are occurring concurrently, with the small bluntness regime transition onset location located downstream of the reversal regime onset location. The experiments indicated that the small bluntness mechanism was responsible for the completion of transition. The turbulent event passage frequency was monitored and showed a marked increase in correspondence of the onset of small bluntness transition mechanism. Cross correlations have indicated that the reversal regime structures evolve as they move downstream, however correlation between sensors rapidly deteriorates in the small bluntness transitional region. The leading and trailing edge speeds have been evaluated for ten reversal regime events, and average estimates are 94 % and 63% of the edge velocity respectively. Mean event speeds have deduced from the cross correlations and from CSD measurements. These vary between 70 - 80 % of the local edge velocity.

Experiments in the reversal regime showed that increasing the level of roughness leads

to an increased event formation rate. Due to the velocity differential between event leading and trailing edges, events can merge and form continuous bursts of sustained turbulence.

The role of roughness was investigated further using a selection of boundary layer tripping devices. Surface heating patterns obtained with liquid crystals were used in conjunction with thin film measurements to analyse the behaviour of the boundary layer.

Distributed roughness elements of 50 μm in diameter, were found to cause wake structures aligned in the streamwise direction. These wakes underwent transition in the near nose regions and the circumferential spreading angle was found to increase, allowing individual wakes to merge. The greatest boundary layer sensitivity to this sort of roughness environment was found in the supersonic region on the hemispherical nose.

Triangular and quasi spherical trips elements were also employed. The visualisation indicated that the flowfield immediately downstream of these trips is laminar and presents a highly organised structure, most possibly dominated by vortical structures shed from the trip. In the case of the triangular element, these structures are shed from the trip's rear corners. Transition occurs readily within these wakes, and the turbulent region downstream in characterised by an increased circumferential spreading angle, estimated to be between 4 - 6 $^\circ$. Quantitative measurements downstream of transition indicated that the wake is characterised by a central fully turbulent portion and an outer region which is found to be intermittent. Using the triangular trip element, the sensitivity of the boundary layer was explored at various streamwise locations, both on the hemispherical portion on the nose and along the conical portion of the frustum. Results highlighted the supersonic nose region and the near nose regions as the most sensitive to tripping.

The final trip geometry investigated was the two dimensional annular band, which proved to more successful at destabilising the boundary layer than the triangular trips element at comparable locations downstream of the nose region.

Remarks on facility dependence

In conclusion, the issue of facility dependence of the results remains to be addressed. The main emphasis of this work was to investigate the evolution of transitional events after their inception, rather than to make direct predictions concerning transition onset; hence the facility dependence effects are of weaker significance. Furthermore, a substantial part of this study concentrates upon roughness induced transition behaviour. As this is shown to be the leading mechanism promoting transition, the severity of the tunnel disturbance has little importance and again it is felt that the results are facility independent.

9.2 Further work

This study has highlighted many areas of interest, therefore there are many ideas which the author feels are worthwhile pursuing. In particular, a module has already been constructed with sensors aligned in the spanwise direction. In order to permit spanwise measurements at a variety of streamwise locations, it was decided to use a blunt cylinder configuration. The blunt cylinder presents all the flow features of interest, but provides a more flexible test bed. This model capitalises heavily on existing hardware, and testing with the module has already commenced. At present circumferential information for naturally occurring events and for a tripped case has been obtained by H. Wijensinghe as part of his undergraduate final year dissertation. The initial results are extremely encouraging and further analysis, using the tools developed as part of this study will yield valuable information concerning transition event dynamics.

Other avenues include measurements within the boundary layer. At present, fine wires probes are being developed to obtain total temperature measurements. Decreasing the wire diameter should allow the instantaneous measurement of fluctuating quantities, and the detection of the passage of transition events. Combining this information with the streamwise and spanwise measurements, will allow a fully three dimensional picture of the event to be created. Furthermore, usage of the probe in the time averaged manner in the freestream will allow a further estimation of the freestream total temperatures, resolving any uncertainties connected with the present estimate.

Chapter 10

References

Adams N. and Kleiser L. (1993)
Numerical simulation of fundamental breakdown of a laminar boundary layer at Mach 4.5. AIAA 93-5027, Proc. of AIAA/DGLR fifth international aerospace planes and hypersonic technologies conference. Munich, Germany. 1993.

Baldwin B.S. and Lomax H. (1978)
Thin layer approximation and algebraic model for turbulent separated flows. AIAA 78-0257. 1978.

Bartlett R.P., Edwards A.J. and Hillier R. (1979)
Development and calibration of a total temperature probe for the Imperial College aeronautics department gun tunnel. IC Aero rep. 79-02. Imperial college, London. June 1979.

Ben-Artzi M. and Falcovitz J. (1983)
A high resolution upwind scheme for quasi 1D flows. Proc. of the Euler workshop. INRIA, SIAM. 1983.

Ben-Artzi M. and Falcovitz J. (1984)
A second order Godunov type scheme for compressible fluid dynamics. J. of Comp. Physics, Vol. 55, No. 1, pp. 1-32. July 1984.

Billig F.S. (1967)
Shock wave shapes around spherical and cylindrical nosed bodies. J. of. Spacecraft and Rockets, Vol. 4, No. 6, pp. 822-823. June 1967.

Bogdan L. (1964)
High temperature, thin film resistance thermometers for heat transfer measurement. NASA CR 26. National aeronautics and space administration. April 1964.

Brinich P.F. and Sands N. (1957)
Effect of bluntness on transition for a cone and a hollow cylinder at Mach 3.1. NACA TN 3979, National advisory committee for aeronautics. Feb. 1957.

Cantwell B., Coles D. and Dimotakis P. (1978)
Structure and entrainment in the plane of symmetry of a turbulent spot. J. Fluid Mech., Vol. 87, part 4, pp. 641-672. 1978.

Charbonnier J. and Boerrigter H. (1993)
Contribution to the study of gap induced boundary layer transition in hypersonic flow. AIAA 93-5311. Proc. of AIAA/DGLR fifth international aerospace planes and hypersonic technologies conference. Munich, Germany. 1993.

Chen F.J., Malik M.R. and Beckwith I.E. (1989)
Boundary layer transition on a cone and flat plate at Mach 3.5. AIAA Journal, Vol. 27, No. 6, pp. 687-693. June 1989.

Chen F.J., Wilkinson S.P. and Beckwith I.E. (1993)
Gortler instability and hypersonic quiet nozzle design. J. Spacecraft and Rockets, Vol. 30, No. 2, pp.170-175. March-April 1993.

Clark J.P., Jones, T.V., Ashworth D.A. and LaGraff J.E. (1992)
Turbulent spot development in a Mach 0.55 flow. Paper 21.1, Vol. 1. Proc. of Boundary layer transition and control, Cambridge, U.K. April 1991.

Clark J.P. (1993)
D.Phil. University of Oxford. 1993.

Cook W.J. and Felderman E.J. (1966)
Reduction of data from thin film heat transfer gauges: a concise numerical technique. AIAA Journal, Vol. 4, No. 3, pp. 561-562. March 1966.

Cole D. and Savas 0. (1980)
Interactions for regular patterns of turbulent spots in a laminar boundary layer . Proc. of the IUTAM symp. on laminar turbulent transition. 1980.

Corrsin S. and Kistler A.L. (1955)
Freestream boundaries of turbulent flows. NACA. rep. 1244. National advisory committee for aeronautics. 1955.

Culotta S. and Richards B.E. (1970)
Methods for determining conditions in real nitrogen expanding flows. VKI TN 58. Von Karman institute, Belgium. Feb. 1970

Denman P.A. (1990)
Ph.D. thesis. University of London. 1990.

Doorly D.J. and Smith F.T. (1992)
Initial value problems for spot disturbances in incompressible or compressible boundary layers. J. of Engineering Mathematics, Vol. 26, pp. 87-106. 1992.

Dhawan S. and Narasimha R. (1958)
Some properties of boundary layer flow during the transition from laminar to turbulent motion. J. Fluid Mech., Vol. 3, pp. 418-436. 1958.

Emmons H.W. (1951)
The laminar turbulent transition in a boundary layer. Part 1. Journal of Aerospace Sci., Vol. 18, No. 7, pp. 490-198. July 1951.

Edney B.E. (1967)
Temperature measurements in a hypersonic gun tunnel using heat transfer methods. J. Fluid Mech., Vol. 27, part 3, pp. 503-512. 1967.

Edwards A.J. (1981)
Boundary layer studies at hypersonic speeds. Ph.D. thesis, University of London. 1981

Elfstrom G.M. (1971)
Hypersonic turbulent separation. Ph.D. thesis. University of London. 1971.

Ericsson L.E. (1974)
Correlation of attitude effects on slender vehicle transition. AIAA Journal, Vol. 12, No. 4, pp. 523-529. April 1974.

Ericsson L.E. (1988)
Effect of nose bluntness and cone angle on slender vehicle transition. AIAA Journal, Vol. 26, No. 10, pp. 1168-1174. October 1988.

Ericsson L.E. (1990)
Reply by author to K.F. Stetson, Reader's forum. AIAA Journal, Vol. 28, No. 7, pg. 1337. July 1990.

Fay J.A. and Riddell F.R. (1958)
J. Aeronautical. Sci., Vol. 25, No. 2, pp. 73-85. Feb. 1958.

Fischer M.C. and Weinstein L.M. (1972)
Cone transitional boundary layer structure at M=14. AIAA Journal, Vol. 10, No. 5, pp. 699-701. May 1972.

Gutmark E., and Blackwelder R.F. (1987)
On the structure of a turbulent spot in a heated laminar boundary layer . Experiments in fluids, Vol. 5, pp. 217-229. 1987.

Hall R.M., Obara C.J., Carraway D.L., Johnson C.B., Wright R.E. Jr., Covell P.F. and Azzay M. (1991)
Comparisons of boundary layer transition measurement techniques at supersonic Mach numbers. AIAA Journal, Vol 29, No. 6, pp. 865-871. June 1991.

Hedley T.B. and Keffer J.F. (1974)
Turbulent/non-turbulent decisions in an intermittent flow. J. Fluid Mech., Vol. 64, part 4, pp. 625-644. 1974.

Heffner K. and Arnal D. (1994)
Leading edge bluntness effects on laminar turbulent boundary layer transition on a cooled flat plate at Mach 7. ESA SP 367, pp. 485-490. Feb. 1995. Proc. of The 2nd. European symp. on aerothermodynamics for space vehicles, ESTEC, Noordwijk, The Netherlands. Nov. 1994.

Henshall B.D., Schultz D.L (1959)
Some notes on the use of resistance thermometers for the measurement of heat transfer rates in shock tubes. ARC C.P. 408. Aeronautical research council, 1959.

Herbert T. and Esfahanian V. (1992)
Stability of hypersonic flow over a blunt body. AGARD CP 514, paper 28-1. Proc. of 70th fluid dynamics panel meeting and symposium: theoretical and experimental methods in hypersonic flows. Turin, Italy. May 1992.

Hillier R. (1996)
The generalised Riemann problem. M.Sc. lecture notes. Imperial College, London. 1996.

Hillier R., Kirk D.C., Sell M. and Soltani S. (1992)
Studies of hypersonic viscous flows. AGARD CP 514, paper no. 32-1, Proc. of 70th fluid dynamics panel meeting and symposium: theoretical and experimental methods in hypersonic flows. Turin, Italy. May 1992.

Hillier R., Kirk D. and Soltani S. (1993)
Computational and experimental study of kinetic heating at hypersonic speeds. AIAA 93-5022, Proc. of AIAA/DGLR fifth international aerospace planes and hypersonic technologies conference. Munich, Germany. 1993.

Hilsenrath J. and others. (1960)
Tables of thermodynamic and transport properties of air, argon, carbon dioxide, carbon monoxide, nitrogen, oxygen and steam. Pergamon Press. 1960

Jones T.V. (1989)
Private communication to Sell M. Cited in Sell 1992.

Kachanov Y.S. (1994)
Physical mechanisms of laminar boundary layer transition . Ann. Rev. Fluid Mech., Vol. 26, pp. 411-482. 1994.

Keyes F.G (1952)
The heat conductivity, viscosity, specific heat and Prandtl numbers for thirteen gases. Project squid TR. 37. M.I.T., Cambridge, Mass., USA. 1952

Kendall J.M. (1975)
Wind tunnel experiments relating to supersonic and hypersonic boundary layer transition . AIAA Journal, Vol. 13, No. 3, pp. 290-299. March 1975.

Klebanoff P.S. and Tidstrom K.D (1959)
Evolution of amplified waves leading to transition in a boundary layer with zero pressure gradient. NASA TN D 195. National aeronautics and space administration. September 1959.

Kirk D. (1993)
Hypersonic turbulent boundary layer . Ph.D. thesis. University of London. August 1993.

Lees L. and Lin C.C. (1946)
Investigation of the stability of the laminar boundary layer in a compressible fluid. NACA TN 1115. National advisory committee for aeronautics. Sept. 1946.

Lin Z.B. and Harvey J.K. (1987)
An experimental study of the hypersonic turbulent boundary layer on a cold slender cone. AIAA paper 87-1513. June 1987.

Mack L.M. (1964)
The stability of the compressible laminar boundary layer according to a direct numerical simulation. AgardoGraph 97, Part 1, pp 329-389. 1964

Maddalon D.V. and Henderson A. Jr. (1968)
Boundary layer transition on sharp cones at hypersonic Mach numbers. AIAA Journal, Vol. 6, No. 8, pp. 424-431. March 1988.

Mallinson S.G. (1996)
Private communication. 1996.

Martellucci A., Maguire B.L. and Neff R.S. (1972)
Analysis of flight test transition and turbulent heating data. Part 1 - Boundary layer results. NASA CR 129045, National aeronautics and space administration. Nov. 1972.

Matsui T. (1980)
Visualisation of turbulent spots in the boundary layer along a flat plate in a water flow. Proc. of the IUTAM symp. of laminar turbulent transition. 1980.

Maulard J. (1968)
Les fluxmetres thermique a temperature superficielle pour tubes a choc. Rech. Aer., No. 126, p. 39. Sept. 1968.

Mee D.J. and Goyne C.P
Turbulent spots in boundary layers in a free-piston shock tunnel flow. Proc. 21st. Int. Shock Wave symp., Pasadena, Cal., USA. July 1995.

Millevoi C. (1993)
Adaption of GODVIS to deal with non-uniform initial conditions. IC Aero rep. Imperial College, London. Sept. 1993

Morkovin M.V. (1969)
Critical evaluation of transition from laminar to turbulent shear layers with emphasis on hypersonically travelling bodies. AFFDL TR 68 149. Air force flight dynamics laboratory AFB, OH, USA. 1969.

Morrisette E.L., Stone D.S. and Whitehead A.H. Jr. (1969)
Boundary layer tripping with emphasis on hypersonic flows. Viscous drag reduction. 1969.

Nagamatsu H.T., Sheer R.E. and Graber B.C. (1967)
Hypersonic laminar boundary layer transition on 8 foot long, 10 ° cone, M=9.1-16. AIAA Journal, Vol. 5, No. 7, pp. 1245-1252. July 1967.

Narasimha R. (1957)
On the distribution of intermittency in the transition region of a boundary layer . J. Aero. Sci. Vol. 24, pp. 711-712. Sept. 1957.

Narasimha R. (1985)
The laminar turbulent transition zone in the boundary layer . Prog. Aerospace Sci., Vol. 22, pp. 29-80. 1985.

Narasimha R., Devasia K.J., Gururani G. and Badri Narayanan M.A. (1984)
Transitional intermittency in boundary layers subjected to pressure gradient. Experiments in fluids, Vol. 2, pp. 171-176. 1984.

Needham D.A., Elfstrom G.M. and Stollery J.L. (1970)
Design and operation of the Imperial College number 2 hypersonic gun tunnel. I.C. Aero rep. 70-04. Imperial College, London. May 1970.

Netterfield M.P. (1988)
Hypersonic cavity flows. Ph.D. thesis. University of London. 1988.

Netterfield M.P. and Hillier R. (1989)
Experiment and computation in hypersonic flows. AIAA 89-1842. Proc. of AIAA 20th fluid dynamics, plasma dynamics and lasers conference, Buffalo New York, USA. June 1989.

Owen F.K. (1970)
Transition experiments on a flat plate at subsonic and supersonics speeds. AIAA Journal, Vol. 8, No. 3, pp. 518-523. March 1970.

Owen F.K., Horstman C.C., Stainback P.C. and Wagner R.D. (1975)
Comparison of wind tunnel transition and freestream disturbance measurements. AIAA Journal, Vol. 13, No. 3, pp. 266-269. March 1975.

Potter J.L. and Whitfield J.D. (1960)
Effects of unit Reynolds number , nose bluntness, and roughness on boundary layer transition . AEDC TR 60 5, Arnold engineering development centre. March 1960.

Potter J.L. and Whitfield J.D. (1962)
Effects of slight nose bluntness and roughness on boundary layer transition in supersonic flows. J. Fluid Mech., Vol. 12, pp 501-535. 1962.

Prodromou P. and Hillier R. (1991)
Computation of unsteady nozzle flows. Proc. of the 18th symposium on shock waves.

Reshotko E. (1969)
Stability theory as a guide to the evaluation of transition data. AIAA Journal, Vol. 7, No. 6, pp. 1086-1093. June 1969.

Reshotko E. (1976)
Boundary layer stability and transition . Ann. Rev. Fluid Mech., Vol. 8, pp. 311-349. 1976.

Reshotko E. (1990)
Hypersonic stability and transition . Proc. of workshop on hypersonic flows for reentry problems, Antibes, France. Jan. 1990.

Richards B.E. and Stollery J.L. (1966)
Further experiments on transition reversal at hypersonic speeds. A.R.C. 27 772, Aeronautical research council. Feb. 1966.

Rotta N.R. and Zakkay V. (1968)
Effects of nose bluntness on the boundary layer characteristics of conical bodies at hypersonic speeds. Astronautica Acta, Vol. 13, pp. 507-516. 1968.

Sankaran R., Antonia R.A., Bisset D.K. and Sokolov M. (1991)
Flow patterns and organisation within a turbulent spot. Physics of fluids, Vol. 3, No. 6, pp. 1560-1571. 1991.

Schneider S.P. (1995)
Improved methods for measuring laminar-turbulent intermittency in boundary layers. Exp. in fluids, Vol. 18, pp. 370-375. 1995.

Schneider S.P. and Haven C.E. (1995)
Quiet flow Ludwieg tube of high speed transition research. AIAA Journal, Vol. 33, No. 4, pp. 688-693. April 1995.

Schubauer G.B. and Skramstad H.K. (1948)
Laminar boundary layer oscillations and transition on a flat plate. NACA rep. 909. National advisory committee for aeronautics. 1948.

Schubauer G.B. and Klebanoff P.S. (1955)
Contributions on the mechanics of boundary layer transition . NACA TN 3489. National advisory committee for aeronautics. 1955.

Schubauer G.B. and Klebanoff P.S. (1956)
Contributions on the mechanics of boundary layer transition . NACA rep. 1289. National advisory committee for aeronautics. 1956.

Schultz D.L. and Jones T.V. (1973)
Heat transfer measurements in short duration hypersonic facilities. AgardoGraph 165. 1973.

Sell M. (1992)
Hypersonic blunt cone aerodynamics. Ph.D. Thesis, University of London. 1992.

Skinner G.T. (1961)
Calibration of thin film gage backing materials. ARS Journal, Vol. 31, pp. 671-672. 1961.

Sims J.L. (1964)
Tables for supersonic flow around right circular cones at zero angles of attack. NASA SP-3004. National aeronautics and space administration. 1964.

Smith D.R and Hillier R. (1995)
Computation of hypersonic viscous flows in adverse pressure gradients. Sixth international conference on computational fluid dynamics. Lake Tahoe, USA. Sept. 1995.

Soltani S. (1993)
Hypersonic separated flows. Progress Report 5. Aeronautics department, Imperial College, London. May 1993.

Soltani S. (1994)
Private communication. May 1984.

Softley E.J., Graber B.C. and Zempel R.E. (1969)
Experimental observation of transition of the hypersonic boundary layer . AIAA Journal, Vol. 7, No. 2, pp. 257-263. Feb. 1969.

Sreenivasan K. (1985)
On the fine scale intermittency of turbulence. J. Fluid Mech., Vol. 151, pp. 81-103. 1985.

Stetson K.F. (1960)
Boundary layer transition on blunt bodies with highly cooled boundary layers. J. Aerospace Sci., Vol. 27, No. 2, pp. 81 - 91. Feb. 1960.

Stetson K.F. (1990)
Comments on "Effect of nose bluntness and cone angle on slender vehicle transition". AIAA Journal, Vol. 28, No. 7, pp. 1336-1337. July 1990.

Stetson K.F. and Rushton G.H. (1967)
Shock tunnel investigation of boundary layer transition at M=5.5. AIAA journal, Vol. 5, No. 5, pp. 899-906. May 1667.

Stetson K.F., Thompson E.R., Donaldson J.C. and Siler L.G. (1983)
Laminar boundary layer stability experiments on a cone at Mach 8, part 1: sharp cone. AIAA 83-1761. Proc. of AIAA 16th fluid and plasma dynamics conference, Danvers, Mass, USA. July 1983.

Stetson K.F., Thompson E.R., Donaldson J.C. and Siler L.G. (1984)
Laminar boundary layer stability experiments on a cone at Mach 8, part 2: blunt cone. AIAA 84-0006. Proc. of AIAA 22nd aerospace sciences meeting, Reno, Nevada, USA. Jan. 1984.

Stetson K.F., Thompson E.R., Donaldson J.C. and Siler L.G. (1985)
Laminar boundary layer stability experiments on a cone at Mach 8, part 3: sharp cone at angle of attack. AIAA 85-0492. Proc. of AIAA 23nd aerospace sciences meeting, Reno, Nevada, USA. Jan. 1985.

Stetson K.F., Thompson E.R., Donaldson J.C. and Siler L.G. (1986)
Laminar boundary layer stability experiments on a cone at Mach 8, part 4: on unit Reynolds number and environmental effects. AIAA 86-1087. Proc. of AIAA/ASME 4th fluid mechanics, plasma and lasers conference, Atlanta, GA, USA. May 1986.

Stetson K.F., Thompson E.R., Donaldson J.C. and Siler L.G. (1988)
On hypersonic transition testing and prediction. AIAA 88-37916. 1988.

Stetson K.F., Thompson E.R., Donaldson J.C. and Siler L.G. (1989)
Laminar boundary layer stability experiments on a cone at Mach 8, part 5: tests with a cooled model. AIAA 89-1895. Proc. of AIAA 20th fluid mechanics, plasma dynamics and lasers conference, Buffalo, New York, USA. June 1989.

Stuckert G. and Reed H. (1992)
Linear stability of supersonic cone boundary layers. AIAA Journal, Vol. 30, No. 10, pp. 2402-2410. Oct. 1992.

Sutherland W. (1895)
Phil. mag., Vol. 40, pg. 421. 1895.

Van Ingen J.L. (1956)
A suggested semi-empirical method for the calculation of the boundary layer transition region. VTH 71 & VTH 74. Dept. of Engineering, Delft, The Netherlands. 1956.

Van Leer B. (1979)
Towards the ultimate conversation difference scheme. A second order sequel to Godonuv's method. J. Comp. Physics, Vol. 32, pp. 101-136. 1979.

Vidal R.J. (1962)
Transient surface temperature measurements. CAL rep. 114. Cornell aeronautical laboratory, Inc. March 1962.

Wendt V., Kreplin H. and Hohler G. (1993)
Planar and Conical boundary layer stability experiments at Mach 5. AIAA 93-5112, Proc. of AIAA/DGLR fifth international aerospace planes and hypersonic technologies conference. Munich, Germany. 1993.

Wygnanski I., Sokolov M. and Friedman D. (1976)
On a turbulent spot in a laminar boundary layer . J. Fluid Mech., Vol. 78, part 4, pp. 785-819. 1976.

Zanchetta M.A. and Hillier R. (1994)
Laminar turbulent transition at hypersonic speeds: the effects of nose blunting. ESA SP 367, pp. 207-212. Feb. 1995. Proc. of The 2nd. European symp. on aerothermodynamics for space vehicles, ESTEC, Noordwijk, The Netherlands. Nov. 1994.

Zanchetta M.A. and Hillier R. (1995)
Boundary layer transition on slender blunt cones at hypersonic speeds. Proc. 21st. Int. Shock Wave symp., Pasadena, Cal., USA. July 1995. (to be published)

Appendix A

Derivation of p_c/p_∞

Essential to the success of the calibration exercise described in chapter 3, is the ability to relate the measured cone pressure, p_c, to the freestream static, p_∞. In the approach used in this study, the inviscid and viscous contributions are considered separately, such that the ratio of wall pressure to static pressure is expressed as:

$$\frac{p_c}{p_\infty} = \frac{p_c}{p_{(c,inv)}} \times \frac{p_{(c,inv)}}{p_\infty} \tag{A.1}$$

For a given semi cone angle, the inviscid surface pressure, $p_{(c,inv)}$, will depend purely on Mach number:

$$p_{(c,inv)}/p_\infty = F_1(M_\infty) \tag{A.2}$$

The measured pressure, p_c, will be affected by viscous interaction and the relationship can be expressed as:

$$p_c/p_{(c,inv)} = F_2(\bar{\chi}) \tag{A.3}$$

where $\bar{\chi}$ is the viscous interaction parameter, given by

$$\bar{\chi} = \frac{M_\infty^3}{\sqrt{Re_s}}\sqrt{C} \tag{A.4}$$

and Re_s is the Reynolds number based on chord length and C is the "Chapman - Rubesin factor" expressed as:

$$C = \frac{\rho_w \mu_w}{\rho_e \mu_e} \tag{A.5}$$

In this approach, CFD predictions are used to determine both the variation of inviscid cone pressure with Mach number, (the function F_1 in equation A.2) and the variation

of induced pressure with χ, (the function F_2 in equation A.3). The computations were performed at Mach numbers between 8 and 9, using both the viscous and inviscid options in the code. A summary of the inviscid test conditions and results are listed in table A.1.

Test case	1	2	3
M_∞	8	8.5	9
$p_{(c,inv)}/p_\infty$	2.600	2.783	2.977
$p_{(c,inv)}/p_\infty$ [Sims (1964)]	2.628	2.833	3.037

Table A.1: Freestream conditions for the inviscid computations used in the determination of $p_{(c,inv)}/p_\infty$ for a 7° semi - angle cone.

The values from Sims are given for comparison and are obtained by linear interpolation from his data at $M_\infty = 8$ and 10, with cone semi angles of 5° and 7.5°. Close agreement is found between the present CFD results and his data. It is possible to fit a first order curve such that the inviscid wall pressure at any Mach number in the calibration range is given by:

$$p_{(c,inv)}/p_\infty = 2.972 + (M_\infty - 9.0) * 0.378 \tag{A.6}$$

Four viscous computations were performed at the conditions listed in table A.2. The predicted surface pressures are plotted against wetted Reynolds numbers in figure A.1. The pressures are tending asymptotically to the respective inviscid value listed in table A.1. Using the corresponding value of $p_{(c,inv)}/p_\infty$ for each case, the function $p_c/p_{(c,inv)}$ is plotted against χ in figure A.2. Following the suggested form for F_2 for weak interactions, a linear fit is used to describe the behaviour of $p_c/p_{(c,inv)}$ as a function of χ:

$$\frac{p_c}{p_{(c,inv)}} = 1 + A\chi \tag{A.7}$$

with $A = 0.045$. Combining equations A.6 and A.7, the expression linking wall pressure and freestream static pressure as a function of Mach number and Reynolds number for the 7° cone geometry is obtained.

$$\frac{p_c}{p_\infty} = \frac{p_c}{p_{(c,inv)}} \times \frac{p_{(c,inv)}}{p_\infty} \tag{A.8}$$

$$= (1 + 0.045\chi) \times (2.972 + (M_\infty - 9.0) * 0.378) \tag{A.9}$$

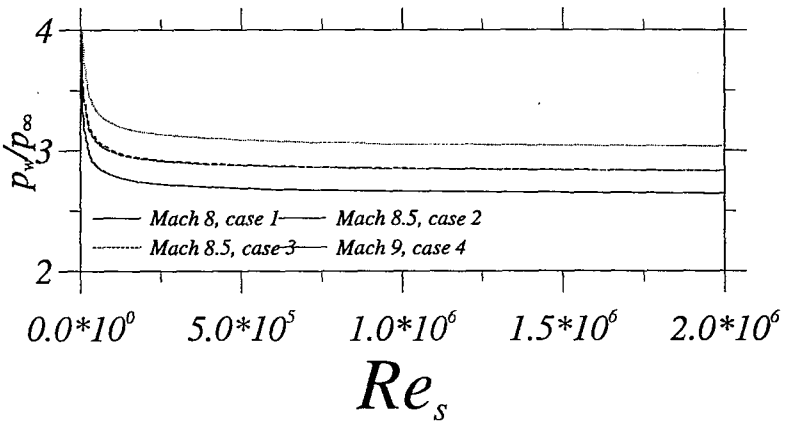


Figure A.1: Wall pressure against Reynolds number based on wetted distance for four viscous computations.

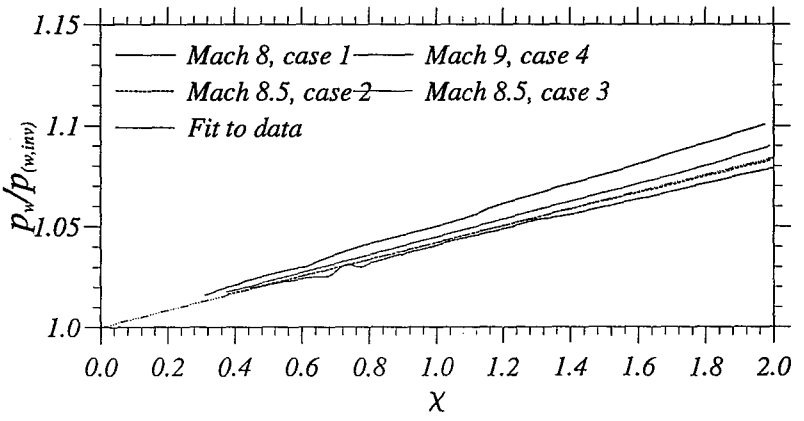


Figure A.2: Ratio of viscous wall pressure to inviscid wall pressure against viscous interaction parameter for four computations.

Test case	1	2	3	4
M_∞	8	8.5	8.5	9
Re_∞	50×10^6	50×10^6	50×10^6	50×10^6
$T_{0,\infty}$ $(°K)$	825.24	1030.00	923.91	1028.56
T_∞ $(°K)$	59.80	66.67	59.80	59.80
p_∞ (N/m^2)	3002.38	3327.86	2825.82	2668.84
ρ_∞ (Kg/m^3)	0.1707	0.1698	0.1697	0.1518

Table A.2: Freestream conditions for computations used in the determination of χ.